



HAL
open science

Subduction interface roughness and megathrust earthquakes: Insights from natural data and analogue models

Elenora van Rijsingen

► **To cite this version:**

Elenora van Rijsingen. Subduction interface roughness and megathrust earthquakes: Insights from natural data and analogue models. *Tectonics*. Université Montpellier; Università degli studi Roma Tre, 2018. English. NNT: 2018MONTG033 . tel-01954639

HAL Id: tel-01954639

<https://theses.hal.science/tel-01954639>

Submitted on 13 Dec 2018

HAL is a multi-disciplinary open access archive for the deposit and dissemination of scientific research documents, whether they are published or not. The documents may come from teaching and research institutions in France or abroad, or from public or private research centers.

L'archive ouverte pluridisciplinaire **HAL**, est destinée au dépôt et à la diffusion de documents scientifiques de niveau recherche, publiés ou non, émanant des établissements d'enseignement et de recherche français ou étrangers, des laboratoires publics ou privés.

Rome, 2018

A dissertation submitted to:
UNIVERSITÀ DEGLI STUDI ROMA TRE
Scuola dottorale in Scienze della Terra
&

UNIVERSITÉ DE MONTPELLIER

Ecole Doctorale Sciences de la Terre et de l'Eau

Subduction Interface Roughness and Megathrust Earthquakes

Insights from Natural Data and Analogue Models

PRESENTED BY

Elenora van Rijsingen

SUPERVISED BY

Francesca Funicello

Serge Lallemand

Fabio Corbi

Michel Peyret

JURY

Susan Bilek

Matthias Rosenau

Stefano Mazzoli

Giacomo Prosser

Diego Perugini

Giovanna Cultrera

Francesca Funicello

Serge Lallemand

New Mexico Tech

GFZ Helmholtz Centre Potsdam

Università degli Studi di Napoli Federico II

Università degli Studi della Basilicata

Università di Perugia

INGV

Università degli Studi Roma Tre

Université de Montpellier

Reviewer

Reviewer

Examiner

President of the Jury

Examiner

Examiner

Thesis advisor

Thesis advisor

*“Nothing in life is to be feared,
it is only to be understood”*

Marie Skłodowska-Curie

Acknowledgements

It is often said that doing a PhD is a lonely process, but looking back on the past three years, I can only think of all the people that have supported me in any way, and therefore directly or indirectly contributed to the final result of three years of hard work: this Thesis. This section is therefore a tribute to all the people who have been there for me over the years: my supervisors, colleagues, family, old friends, and many new friends.

When starting your PhD, it is hard to imagine that at some point, the day will come that you finish your work, and that everything is written down, or even published. I suppose many people start their PhD with some sort of fear, being overwhelmed by the huge amount of work that awaits them and the reputation of obtaining a doctoral degree (the idea that a PhD is supposed to be hard). 'How am I ever going to do this?', is a question that dominates our minds. Now, looking back, I fully agree with Marie-Sklodowska-Curie, who said: 'Nothing in life is to be feared, it is only to be understood. Now is the time to understand more, so that we may fear less'. I am not sure hearing these words would have changed my perspective three years ago. I guess there are some things that you need to learn the hard way. The PhD is a journey, not only a scientific one, but also a personal one. And it is the support system that plays a very important role in that personal journey.

First of all, my main PhD supervisors, Francesca and Serge. There have been many moments that I realized how incredibly lucky I have been with you as my advisors. It has not always been easy to communicate, given our different cultural backgrounds, personalities and expectations, but your devotion to help me bringing this project to a successful end means a lot to me.

Francesca, you are a scientific mom, as you have been to all your *angels*. You have successfully 'raised' all of us to being independent researchers, by guiding us in all the facets of the PhD, but never telling us exactly what to do, and giving us lots of freedom. One thing you have emphasized over the years is that life is much more than work, and that despite the large task of the PhD, we should go out, have fun, and celebrate life. Having this freedom meant a lot to me, because it gave me the opportunity to make these past years not only about the PhD, but turn it into an adventure, discovering new places and making new friends. I am confident that this way of life contributed to the final result of this PhD, since I believe getting a PhD is not about how many hours you work, it is about allowing yourself to become creative and approach a problem from different perspectives.

Serge, I would sometimes jokingly refer to you as a walking encyclopedia, but this comes from the huge respect I have for your impressive amount of knowledge about subduction zones, all over the world. It often made me realize how little I know and how much is still ahead of me, but it also encouraged me to ask you anything. The fact that you took all my questions and suggestions seriously made me feel as a very valued member of our team, rather than the unexperienced student that I actually was. Also your guidance in the beginning of the PhD, when I honestly didn't know very well what I was doing, helped a lot. By giving me some specific assignments, I could start tackling the big task step by step, and obtain the skills, knowledge and confidence that I needed to be more independent further on in the PhD.

And finally, both your efforts to work through all the bureaucracy, both on the Italian and French sides, to allow me to have two degrees, means a lot. I am proud to say that I obtained my PhD both at Roma Tre University and the University of Montpellier.

Then, my other supervisors, Fabio and Michel. Thank you so much for your help with analyzing and processing the data, always providing solutions and ideas to make things work in either GMT or Matlab, and for providing valuable suggestions for improving the work. Also Diane and Arnaud, thank you for your support and always constructive feedback regarding the natural data study. Thanks to Stephane Dominguez, who taught me a lot about both analogue modelling and working with GMT during the first year of the PhD, and provided valuable feedback about the analogue modelling part in Rome. I also want to thank Stephane Arnal, for all his efforts to create the SubQuake website, as well as Anne for creating the logo. And of course all the people that were involved in reviewing my work, either for the final Thesis, annual university assessments or publications: Susan Bilek, Matthias Rosenau, Stefano Mazzoli, Giacomo Prosser, Diego Perugini, Giovanna

Cultrera, Anthony Sladen, Christophe Voisin, Kelin Wang, three anonymous reviewers, Andrea Tommasi and the CREEP supervisory board, Claudio Faccenna and the Roma Tre PhD committee, and all the colleagues I discussed my research with during workshops and conferences.

Regarding the indirect contributors to this Thesis, I would like to start with two important colleagues and friends: Silvia and Anita. I can confidently say that you two were my best friends and most important moral support in Italy and France.

Silvia, besides all your help and support regarding the Italian life (for which I am eternally grateful!), your presence in the office with me defined my experience in Rome. It should not be underestimated how much it helps to always have someone to talk to, asking for advice, or simply blowing off steam. We had so much fun working together in the lab, having chats over coffee, going to conferences together and much more, and I really hope we can continue this in the future. *Ti voglio troppo bene* :)

Anita, I remember when I first visited the University in Montpellier, you reached out to me right away and from what I remember, we have been friends since. Your office was conveniently located right in front of mine, which made it very easy to find each other for a coffee break, lunch or just a small chat. You are such a happy, talented and caring person, and I am very glad that we could share our PhD experiences, although I am a bit sorry we only spent one year together in Montpellier. I am very happy that you found a position in Luxembourg, which makes it even easier to keep seeing each other in the future. I look forward to it!

Then, of course, the people who know me best and have always supported me: My parents and sister. You were the people who were most involved in the difficult parts of these past years and I can honestly say that I could not have done this project without you. It is not easy being far away from each other, not being able to come over when things get hard, but it means so much to me how you have supported me over the years. Even without the scientific knowledge, you have given me very valuable advice for successfully finishing this PhD. And more importantly, you supported me in managing life as a Dutchie in Southern Europe, which has been an interesting, but sometimes very challenging adventure. *Dankjulliewel!*

I also want to thank the rest of my family (grandparents, cousins, uncles and aunts) for being involved, visiting me, and sending lots of love from the Netherlands.

And last, but not least, I want to thank all my friends and colleagues that have played a role in my life over the past three years. First, my fellow CREEPers, with whom I shared many nice experiences during courses, workshops and conferences as part of our project. It was an honor to be your president! A special mention to Alida, Manuel, Simon and Gianluca, with whom I became good friends. You are amazing people and I very much hope we stay in touch! Then the new friends that I made over the years: Anna, Anna, Ai, Giorgia, Kate, Marieaude, Isabell, Aliaa, Marielle, Ulrike, Becky, Ulla, and Leona. All amazing and inspiring women, from all over the world! And of course all the friends from the Netherlands that I have stayed in touch with, and who always cleared their schedule for me when I was in the Netherlands: Marloes, Jorieke, Annemarieke, Christine, Suzanna, Yael, Maarten, Anniek, Maartje, Eva, Anne, Sebas, Anniek, Wanda, Julia, Veerle, Caroline, Laurette and Jasper. I haven't seen most of you that often over the past years, but every time we met it was like old times. I am very grateful for having so many dear friends back home. *Heel veel liefs!*

Table of Contents

<i>Abstract</i>	13
<i>Résumé</i>	14
1. Introduction	17
1.1. Preface	18
1.2. Thesis outline	20
2. The Subduction Megathrust: What do we know?	23
2.1. Seismicity in subduction zones	24
2.2. Earthquakes along the subduction megathrust	25
2.2.1. The seismogenic zone	25
2.2.2 Seismic vs. Aseismic Behavior	25
2.2.3 Rate and State Variable Friction Laws	26
2.2.4 The Asperity Model	27
2.3. Subduction parameters in relation to megathrust seismicity	29
2.4. Earthquake recording and slip inversion	30
2.4.1. Magnitude scales	30
2.4.2. Rupture distributions	32
2.5. Analogue models and megathrust seismicity	32
2.5.1. Spring-slider models	33
2.5.2. Fault-block models	33
2.5.3. Seismotectonic scale models	34
2.6. Subduction interface roughness and megathrust seismicity	36
2.6.1. Seamounts	36
2.6.2. Fracture zones	37
2.6.3. Submarine ridges	38
2.6.4. Global studies	38
2.6.5. Case studies	40
2.6.5.1. Nankai	40
2.6.5.2. Ecuador	42
2.6.5.3. Costa Rica	43
3. Roughness Characteristics of Oceanic Seafloor Prior to Subduction in Relation to the Seismogenic Potential of Subduction Zones	47
<i>Abstract</i>	48
3.1. Introduction	49
3.2. Methodology used for roughness calculation	50
3.2.1. Data sources	50
3.2.2. Roughness definition	50
3.2.2.1. Roughness in the spatial domain	50
3.2.2.2. Roughness in the frequency domain	51
3.2.2.3. Roughness in a radial bandwidth	51
3.2.2.4. Roughness parameter assuming fractal model	51
3.2.2.5. Roughness assuming average model	51
3.2.2.6. Roughness uncertainties or disparities	52
3.2.3. Processing chain and choice of criteria used for seafloor roughness characterization	53
3.2.3.1. Area/Regions covered	53
3.2.3.2. Calculation steps	53
3.2.3.2.1. Extraction of the relative bathymetry	53
3.2.3.2.2. PSD calculation	54

3.2.3.2.3. Selection of frequency bandwidths	54
3.2.3.2.4. Selection of model used for calculation	55
3.2.3.2.5. Uncertainties and validity of the proxy	55
3.3. Results: 'SubRough' database	56
3.3.1. Maps	56
3.3.1.1. Discrete roughness pattern	56
3.3.1.1.1. Short wavelength roughness R_{SW}	56
3.3.1.1.2. Long wavelength roughness R_{LW}	56
3.3.1.1.3. Intermediate wavelength roughnes R_{IW}	57
3.3.1.2. Mean roughness pattern	57
3.3.2. Global analysis of roughness information along the main subduction zones	58
3.3.2.1. Definition of roughness classes to characterize subduction segments	58
3.3.2.2. Dominantly rough subduction zones	58
3.3.2.2.1. New-Guinea-Solomon-Vanuatu	59
3.3.2.2.2. Makran	59
3.3.2.2.3. Ryukyu-Nankai	59
3.3.2.3. Mixed subduction zones	60
3.3.2.3.1. IBM-Japan-Kamchatka	60
3.3.2.3.2. Tonga-Kermadec	61
3.3.2.3.3. Philippines	61
3.3.2.3.4. South Sandwich	61
3.3.2.3.5. Luzon	62
3.3.2.3.6. Andaman-Sumatra-Java-Sumba	62
3.3.2.4. Dominantly smooth subduction zones	62
3.3.2.4.1. Andes	62
3.3.2.4.2. Antilles	64
3.3.2.4.3. Central America	64
3.3.2.4.4. Alaska-Aleutian	66
3.3.2.4.5. Cascadia	66
3.3.3. The roughness of oceanic features	66
3.3.3.1. Seamounts, seamount massifs and seamount chains	66
3.3.3.2. Fracture zones	67
3.3.3.3. Aseismic and active ridges and plateaus	68
3.3.3.4. Smooth areas	68
3.4. How does seafloor roughness correlate with the state of stress in the subduction zones?	69
3.4.1. Correlation with upper plate strain	69
3.4.2. Correlation with seismic coupling	69
3.4.3. Correlation with <i>b-values</i>	70
3.5. Discussion	71
3.5.1. No specific roughness signature for fracture zones	71
3.5.2. Clear specific roughness for seamounts	71
3.5.3. Similar specific signature of seamounts and ridges at long wavelengths	72
3.5.4. To what extent can we classify the subduction zones with respect to roughness characteristics?	72
3.5.5. Smooth areas and roughness complexities	72
3.5.6. Roughness and state of stress in subduction zones	73
3.5.7. Limitations and perspectives of the study	73
3.6. Conclusion	74
4. How subduction interface roughness influences the occurrence of large interplate earthquakes	77
Abstract	78

4.1. Introduction	79
4.2. Methodology	80
4.2.1 The roughness database	80
4.2.2 The SubQuake database	80
4.2.2.1. Already available databases	81
4.2.2.2. SubQuake data compilation and classification	82
4.2.2.3. Assembling the SubQuake data into a grid	83
4.2.3 Comparison strategy	83
4.2.3.1. SubQuake grid and facing SubRough data	83
4.2.3.2. Epicenters and facing SubRough data	84
4.3. Results	85
4.3.1 SubQuake Results	85
4.3.1.1. Rupture area vs. moment magnitude	85
4.3.1.2. Epicenter location with respect to seismic asperity	90
4.3.1.3. Subduction zone classification in terms of rupture length ratio	91
4.3.2. Comparison between SubRough and SubQuake	91
4.3.2.1. Rupture Length Ratio vs. Percentage of smooth seafloor	91
4.3.2.2. Rupture areas: Specific regions	92
4.3.2.2.1. Japan-Kuril-Kamchatka	93
4.3.2.2.2. South Andes	93
4.3.2.2.3. Alaska-Aleutian	93
4.3.2.2.4. Andaman-Sumatra	93
4.3.2.2.5. North Andes	95
4.3.2.2.6. Central America	95
4.3.2.2.7. Ryukyu-Nankai	95
4.3.2.2.8. Java-Sumba	98
4.3.2.2.9. Cascadia	98
4.3.2.3. Rupture areas: Global comparison	98
4.3.2.4. Rupture areas: Comparison for different M_w groups	99
4.3.2.5. Seismic asperities	101
4.3.2.6. Epicenters	101
4.4. Discussion	102
4.4.1. $M_w \geq 7.5$ ruptures tend to occur more often on smooth subducting seafloor	102
4.4.2. $M_w > 8.5$ events are more sensitive to a smooth seafloor than lower magnitude ruptures	103
4.4.3. Short wavelength vs. long wavelength roughness	104
4.4.4. Seismic asperities correlate with smoother seafloor than ruptures in general	105
4.4.5. Possible link between rupture's nucleation and seafloor roughness	106
4.4.6. Seafloor roughness acting as a barrier to rupture propagation	106
4.5. Conclusions	107
5. Rough subducting seafloor reduces interseismic coupling and mega-earthquake occurrence: Insights from analogue models	109
Abstract	110
5.1. Introduction	111
5.2. Methods	113
5.2.1. 3D-printing seafloor roughness	113
5.2.2. Model setup and monitoring	113
5.3. Results	114
5.3.1. General model behavior	114
5.3.2. Source parameters: Rough vs. Smooth	116

5.3.3. Seismic moment vs. Duration	116
5.4. Discussion	118
5.4.1. Comparison with numerical modelling studies	118
5.4.2. Comparison with natural observations	119
5.4.3. Scenarios for subducting seafloor roughness	119
5.5. Conclusions	121
6. Conclusions	123
6.1. The role of subduction interface roughness on megathrust earthquakes	124
6.1.1. A quantification of seafloor roughness	124
6.1.2. Subduction interface roughness in relation to seismogenic behavior in subduction zones	124
6.1.3. The influence of rough subducting seafloor on the state of stress within subduction zones: Insights from analogue models	125
6.2. Suggestions for future work	127
6.2.1. Natural observations	127
6.2.2. Seismotectonic modelling	127
<i>References</i>	130
<i>Appendix</i>	144
<i>Curriculum Vitae</i>	180

Abstract

Subduction zones are known for their very large earthquakes, with observed magnitudes up to M_w 9.6, and are therefore studied extensively by the scientific community. The impact of such events on societies can be immense, as demonstrated by the recent M_w 9.1 Tohoku (2011), M_w 8.8 Maule (2010) and M_w 9.2 Sumatra (2004) earthquakes, which occurred in densely populated areas, causing terrible human and economic losses.

There is thus a strong need for a better understanding of the spatial and temporal occurrence of such devastating events. A parameter that has been proposed to control the seismogenic behavior in subduction zones is the roughness of the subduction interface. This roughness is the combined result of seafloor morphology of the downgoing plate, the addition of sediments during subduction, as well as processes that occur during subduction, such as tectonic erosion. A rough subduction interface is thought to promote, as well as hinder the occurrence of large interplate earthquakes. These contrasting theories make it challenging to reach a general consensus on the role played by subduction interface roughness in the seismicity in subduction zones. This Thesis aims to provide further insights into this relationship, based on global natural data analyses and seismotectonic analogue models.

Since the roughness at the subduction interface is often unknown, the seafloor seaward of the trench is used as a proxy for the subduction interface. The seafloor facing all subduction zones is analyzed, resulting in a roughness signal at two chosen wavelength bandwidths: the short- (12-20 km) and long (80-100 km) wavelengths. Subsequently, the roughness amplitudes associated with specific features on the seafloor, such as seamounts, fracture zones or ridges, are compared with the global trend. Results show that seamounts have much larger roughness amplitudes at both wavelengths, while ridges can only be distinguished at long wavelengths. Fracture zones cannot be distinguished from the global trend. The seafloor roughness is also used to make a comparison with parameters describing the state of stress within subduction zones. A clear correlation has been observed between high seismic coupling and relatively low roughness amplitudes, as well as between low seismic coupling and relatively high seafloor roughness amplitudes.

A more detailed comparison was done by focusing on the occurrence of large interplate earthquakes in subduction zones, based on a newly compiled earthquake database, SubQuake. This database includes spatial characteristics for $M_w \geq 7.5$ subduction interplate events that occurred since 1900. The spatial occurrence of these ruptures, as well as their seismic asperities and epicenters, are compared with the seafloor roughness on a global scale. Results show that $M_w \geq 7.5$ earthquakes occur preferentially on smooth subducting seafloor at long wavelengths. This correlation is the clearest when considering great- to giant earthquakes (i.e., $M_w > 8.5$), suggesting that a continuous smooth seafloor plays an important role in the development of such large events. Seismic asperities correspond to smoother seafloor at both wavelengths compared to rupture areas in general, while epicenters seem to correlate with slightly rougher seafloor, suggesting that the nucleation of ruptures requires different interface conditions than the ability for a rupture to propagate.

To overcome unavoidable limitations related to natural observations, such as the limited resolution or spatial coverage of the seismic imagery, or the limited sampling period, ad hoc seismotectonic analogue models have been run to study the relationship between subduction interface roughness and megathrust earthquakes as well. These models consist of a viscoelastic gelatin wedge with a 3D-printed subducting seafloor. Two seafloor roughness endmembers have been tested: a planar- and a very rough interface characterized by many large seamounts. Modelling results show that models with a rough interface have smaller earthquakes than models characterized by a smooth interface. In addition, the rough models have lower frictional interface strength and lower interseismic coupling. These results are in agreement with the results obtained in the natural data analysis.

Résumé

Les zones de subduction sont connues pour les très grands séismes qui les affectent, avec des magnitudes observées pouvant atteindre M_w 9.6. C'est pourquoi elles sont largement étudiées par la communauté scientifique. L'impact de tels événements sur la société est immense, comme en témoignent les récents séismes de M_w 9.1 Tohoku (2011), M_w 8.8 Maule (2010) et M_w 9.2 Sumatra (2004), survenus dans des zones densément peuplées, causant de terribles pertes humaines autant qu'économiques.

Il y a donc un besoin pressant de mieux comprendre l'occurrence spatiale et temporelle de ces événements dévastateurs. Un paramètre qui a été proposé pour contrôler le comportement sismogène dans les zones de subduction est la rugosité de l'interface de subduction. Cette rugosité est le résultat combiné de la morphologie du fond marin de la plaque plongeante, de l'entraînement de sédiments pendant la subduction, ainsi que des processus érosifs qui se produisent pendant la subduction. Une interface de subduction rugueuse est censée favoriser, ou au contraire inhiber la rupture des grands séismes interplaques. Ces théories contrastées rendent difficile l'obtention d'un consensus général sur le rôle joué par la rugosité de l'interface de subduction dans la sismicité des zones de subduction. Cette thèse vise à fournir des informations supplémentaires sur cette relation, basée sur des analyses globales de données naturelles et des modèles analogiques sismotectoniques.

Étant donné que la rugosité à l'interface de subduction est souvent inconnue, le fond marin au large de la fosse est utilisé ici comme substitut de l'interface de subduction. Le fond marin faisant face à toutes les zones de subduction est ainsi analysé, sous la forme d'un signal de rugosité à deux gammes de longueur d'onde choisies: les longueurs d'onde courtes (12-20 km) et grandes (80-100 km). Par la suite, les amplitudes de rugosité associées à des caractéristiques spécifiques du fond marin, telles que les monts sous-marins, les zones de fracture ou les rides, sont comparées à la tendance globale. Les résultats montrent que les monts sous-marins ont des amplitudes de rugosité beaucoup plus grandes aux deux longueurs d'onde, tandis que les rides ne peuvent être distinguées que sur de grandes longueurs d'onde. Les zones de fracture ne peuvent être distinguées de la tendance globale. La rugosité du fond marin est également utilisée pour comparer les paramètres décrivant l'état de contrainte dans les zones de subduction. Une nette corrélation a été observée entre un couplage sismique élevé et des amplitudes de rugosité relativement faibles, ainsi qu'entre un faible couplage sismique et des amplitudes relativement élevées de la rugosité du fond marin.

Une comparaison plus détaillée a été réalisée en se concentrant sur les grands séismes de subduction, par le biais d'une base de données sismique nouvellement compilée, SubQuake. Cette base de données comprend les caractéristiques spatiales des séismes interplaques de $M_w \geq 7,5$ survenus depuis 1900. L'occurrence spatiale de ces ruptures, ainsi que les aspérités sismiques et les épicentres associés, sont comparés à la rugosité des fonds marins à l'échelle mondiale. Les résultats montrent que les séismes de magnitude $\geq 7,5$ se produisent préférentiellement face à des fonds marins peu rugueux à grande longueur d'onde. Cette corrélation est la plus évidente lorsque l'on considère les mégaséismes de $M_w > 8,5$, ce qui suggère qu'un fond marin lisse et continu joue un rôle important dans le développement de ces grands événements. Les aspérités sismiques correspondent à des fonds marins plus lisses à faible et grande longueur d'onde comparées aux zones de rupture en général, alors que les épicentres semblent corrélés à des fonds marins légèrement plus rugueux, suggérant que la nucléation des ruptures nécessite des conditions d'interface différentes.

Pour surmonter les limitations inévitables liées aux observations naturelles, telles que la résolution ou la couverture limitée de l'imagerie sismique ou encore la trop courte période d'échantillonnage, des modèles sismotectoniques ad hoc ont été utilisés pour étudier la relation entre la rugosité de l'interface de subduction et les mégaséismes. Ces modèles consistent en un coin de gélatine viscoélastique chevauchant une plaque

rigide rugueuse en subduction. Grâce à des impressions 3D, deux rugosités extrêmes de la plaque en subduction ont été testées: une interface plane et une très rugueuse caractérisée par de nombreux « monts sous-marins ». Les résultats de la modélisation montrent que les modèles à interface rugueuse génèrent des séismes plus petits que les modèles caractérisés par une interface lisse. De plus, les modèles rugueux présentent une résistance frictionnelle plus faible et donc un couplage intersismique plus faible. Ces résultats sont en accord avec les résultats obtenus à partir de l'analyse des données naturelles.

1. Introduction

1.1. Preface

The largest earthquakes on Earth occur within subduction zones, areas where oceanic lithosphere is recycled as it sinks within the underlying mantle. The downgoing movement of the subducting plate can cause stress accumulation along the shallow contact interface with the overriding plate: the subduction megathrust. When these stresses are eventually released, earthquakes with magnitudes (M_w) up to 9.6 may occur, with disastrous consequences for populations in those areas. Both the damaging effects of ground shaking as a consequence of seismic waves travelling through the Earth, as well as the effects of associated tsunami waves, can disrupt complete societies.

Since the 1970's, it has been relatively quiet in terms of great ($M_w > 8.5$) subduction earthquakes. This changed in 2004, when a M_w 9.0 earthquake ruptured the Andaman-Sumatra subduction interface over a distance of 1500 km. Together with the associated 15-30m-high tsunami waves, this event killed over 200.000 people, making it one of the deadliest earthquakes ever. Also the 2005 Sumatra earthquake (M_w 8.6), the 2010 Maule event (M_w 8.8) and the 2011 Tohoku earthquake (M_w 9.1) had large impacts on society. In particular the latter, since a $M_w > 8$ earthquake along the Japan trench was not anticipated by the scientific community, especially not with such extremely high slip values, ranging up to 60 meters in some places (Stein & Okal 2011; Yue & Lay 2013).

This brings us to the question that has troubled scientist for a long time: why do some subduction zones host such large and devastating events, while other regions show moderate seismicity? Due to the large impact subduction earthquakes may have on societies, there is a strong need for a better understanding of the spatial occurrence of megathrust events. For many decades, scientists have been trying to unravel which subduction parameters mainly influence the potential of a subduction zone to host large earthquakes. Parameters such as plate age and convergence velocity (Ruff & Kanamori 1980; Peterson & Seno 1984; Jarrard 1986), trench sediments (Ruff 1989; Heuret et al. 2011; Heuret et al. 2012; Scholl et al. 2015; Brizzi et al. 2018), upper plate strain (Heuret et al. 2011; Heuret et al. 2012; Schellart & Rawlinson 2013), fore-arc structure (Song & Simons 2003; Wells 2003), trench length and seismogenic zone width (Pacheco & Sykes 1992; Hayes et al. 2012; Schellart & Rawlinson 2013; Brizzi et al. 2018) and along-dip curvature of the downgoing plate (Bletery et al. 2016) have all been investigated.

Nowadays, the segmentation of the subduction interface into areas that promote rupture occurrence and areas that may limit them, following the asperity model (Byerlee 1970; Scholz & Engelder 1976; Lay & Kanamori 1981), is thought to mainly affect the overall potential of a subduction segment to host great-to giant earthquakes. Ruptures that can propagate easily over large (i.e., trench-parallel) distances have the ability to grow larger, and, therefore, become more destructive. Geometrical irregularities along the interface (i.e., the interface roughness) could create heterogeneities in seismogenic behavior, and, in turn, a segmentation of the subduction interface, as initially suggested by Kelleher & McCann (1976). Hence, the role of the subduction interface roughness, or individual topographical features on the seafloor, such as seamounts or ridges, has been studied extensively, but has not yet led to a general consensus (e.g., Das & Watts 2009).

Many studies focus on the role of a single topographic feature on rupture propagation, either suggesting that it has facilitated the occurrence of an earthquake (e.g., Cloos 1992; Scholz & Small 1997; Von Huene et al. 2000; Abercrombie et al. 2001; Husen et al. 2002; Bilek et al. 2003; Das & Watts 2009; Müller & Landgrebe 2012; Bell et al. 2014; Landgrebe & Müller 2015), or that it has acted as a barrier and therefore limited rupture occurrence and propagation (e.g., Kodaira et al. 2000; Robinson et al. 2006; Mochizuki et al. 2008; Wang & Bilek 2011; Geersen et al. 2015; Marcaillou et al. 2016). The contrasting observations from these studies are perhaps the result of some limitations related to observing local natural phenomena. The instrumental seismic record is limited to ~ 100 years, which is very little compared to the recurrence time of great earthquakes, that can range from several decades to many centuries (McCaffrey 2008). On top of that, each subduction zone has unique characteristics in terms of structure, geometry and rheology (e.g., Heuret et al. 2011; Kopp 2013), meaning that not each region might behave in a similar manner. Also the limitations

in terms of measuring and imaging techniques (e.g., GPS, or seismic reflection studies) make it challenging to understand the processes that occur along the subduction interface, since the seismogenic zone is usually located off the coast and at large depths (e.g., 11-51-km-depth; Heuret et al. 2011).

Hence, modelling studies that focus on the mechanics of subducting rough seafloor (e.g., Ritz & Pollard 2012; Yang et al. 2013; Ruh et al. 2016; Zielke et al. 2017), as well as global observational studies that do not have the disadvantage of dealing with possibly very local phenomena (e.g., Morgan et al. 2008; Wang & Bilek 2014; Bassett & Watts 2015a), are crucial for obtaining a better understanding of the processes that occur when rough seafloor subducts and how this influences the seismogenic potential of a specific region. This Thesis aims to clarify the role played by the subduction interface roughness in triggering interplate seismicity and tries to address some unanswered questions:

- Can we quantify the definition of rough and smooth seafloor?
- What happens in terms of stress distribution when rough and smooth seafloor subducts?
- How does seafloor roughness relate to seismic coupling in subduction zones?
- At what spatial scale does seafloor roughness play a role in subduction thrust fault seismicity?
- Does subduction interface roughness in general limit or facilitate the occurrence of large- to great earthquakes?
- How does the roughness of the interface relate to spatial characteristics of megathrust ruptures, such as the hypocenter and the seismic asperity?
- Is the effect of roughness on a single rupture different from the long-term effect on seismic behavior, e.g., over multiple seismic cycles?

1.2. Thesis outline

This Thesis addresses the abovementioned questions by using a dual approach, which involves the analysis of natural data on a global scale and analogue seismotectonic models. These two approaches complement each other, since the natural data analysis takes into account data from all current subduction zones, which each have their own complexities, while the analogue models use a more simplified approach, but allow isolating a single parameter and testing its influence over multiple seismic cycles. The Thesis is structured in four parts.

An overview of the state-of-the-art is given in Chapter 2, which includes some basic concepts of seismotectonics (sections 2.1. and 2.2), followed by an overview of subduction parameters that may play a role in the seismic potential of individual regions (section 2.3.). The subsequent sections 2.4 and 2.5 review the advances that have been made in earthquake recording and slip inversions, and analogue modelling of seismotectonics, respectively. The last part of Chapter 2 focuses specifically on subduction interface roughness, presenting the state-of-the-art and zooming into three specific, well-studied regions: Nankai (Southwest Japan), Ecuador and Costa Rica (section 2.6).

Chapter 3 contains the first part of the natural data analysis, in which the seafloor roughness is quantified on a global scale and compared with the state of stress in subduction zones. Although several studies already analyzed the seafloor bathymetry in a (semi-)quantitative way for some specific regions (Morgan et al. 2008; Bassett & Watts 2015a), a homogeneous and worldwide estimate of the seafloor roughness prior to subduction is still missing. Here, the calculation of seafloor roughness not only accounts for the absolute distribution of the elevation, but also for the relative deviation of elevation around its mean value. The roughness seaward of the trench is assumed to be a reliable proxy for the roughness at the subduction interface and is provided at several spatial wavelengths. To better understand the degree of roughness that is associated with specific topographic features on the seafloor, such as seamounts, fracture zones or ridges, the roughness measurements for these features are compared with the global, average trend. Based on the new quantitative seafloor roughness data, all subduction segments are described in detail, reviewing the roughness variations along the trench in relation to the presence of topographic features. Finally, since continuous, along-trench, measurements of roughness are now available, a comparison with several subduction parameters compiled by Heuret et al. (2011) is performed.

In order to perform a more detailed comparison with the roughness estimates presented in Chapter 3, a global database, SubQuake, for $M_w \geq 7.5$ earthquakes has been compiled (Chapter 4). This database contains spatial rupture characteristics for 182 subduction megathrust earthquakes that occurred since 1900. To better understand how subduction interface roughness influences rupture evolution (e.g., nucleation, propagation, arrest), not only the rupture area, but also the epicenter and if available, the region of the largest displacement (i.e., the seismic asperity) are considered. These spatial characteristics are then compared in a quantitative way with the roughness data seaward of the trench. As a first step, the SubQuake and SubRough databases can be compared region by region, by simply looking at the along-trench length of the subduction zone that has ruptured over the past 117 years, in relation to the percentage of low-roughness amplitude measurements. Then, a more detailed analysis is performed, where an algorithm selects the roughness data facing either rupture areas, no rupture areas, seismic asperities or epicenters.

The natural data analyses presented in Chapters 3 and 4 provide important insights in the first-order relationships between seafloor roughness and the state of stress within subduction zones, as well as spatial rupture characteristics. However, the seismic record of the SubQuake database (i.e., 117 yr), in combination with the fact that the SubRough database is based on a proxy of the subduction interface roughness, pose some limitations on this analysis. This Thesis therefore also contains an analogue modelling study (Chapter 5), which allows analysis of the relationship between subduction interface roughness and megathrust earthquakes over multiple seismic cycles and may provide more insights in the mechanisms that occur when rough seafloor subducts. Viscoelastic gelatin wedge models, developed by Corbi et al. (2013) are used, but now upgraded with a 3D-printed subduction interface. The models consist of a gelatin wedge (i.e., the

analogue of the overriding plate), that is underthrust by a rigid aluminum plate (i.e., the analogue of the subducting plate). The 3D printed seafloor and a plastic sheet together make up the subduction interface and have velocity-weakening and velocity-strengthening behavior, respectively. To gain clear insights in the effect of subducting rough seafloor with respect to a smooth seafloor, two endmember interfaces are used: a planar interface and a very rough interface characterized by many large seamounts.

Finally, in Chapter 6 the results from the natural data analyses (Chapters 3 and 4) are compared with the outcomes of the analogue models (Chapter 5) and discussed with respect to the already existing literature, with the aim to answer the questions presented in the preface. In addition, new questions that have emerged from this Thesis will be discussed, as well as future perspectives related to the study of intraplate seismicity. Chapters 3, 4, and 5 are structured as papers already published or to be submitted. This format bears possible, but unavoidable duplications.

2. The Subduction Megathrust: What do we know?

2.1. Seismicity in subduction zones

Subduction zones are regions where oceanic plates sink below another plate and are being recycled into the Earth's mantle. The main driver for the process of subduction is the pull of the subducting slab of oceanic lithosphere, which has a larger density and therefore a larger gravity than the surrounding mantle (Elsasser 1971; Forsyth & Uyeda 1975; Hager 1984; Davies & Richard 1992). This sinking of cold lithosphere into the mantle is responsible for many processes and associated hazards, such as arc volcanism due to thermal and chemical modification of the mantle, as well as the release of large amounts of seismic energy (Figure 2.1). Earthquakes can occur both within the downgoing- and overriding plate during subduction, but also along the interface between both plates (i.e., the subduction interface).

Seismic events that occur within the subducting slab (i.e., intraslab earthquakes) can occur as deep as the 660 km discontinuity and are the result of slab morphology and rheology in combination with mechanical forces. The negative buoyancy of the slab and resistance to penetrate into the lower mantle causes buckling, and therefore bending and

unbending of various parts of the slab (e.g., Engdahl & Scholz 1977; Myhill 2013). In addition, volume reductions occur due to phase changes when the relatively cold slab passes through transition zones in the mantle (Kirby et al. 1996). Also buoyancy forces due to thermal and/or compositional anomalies play a role in the mechanical forces responsible for (deep) intraslab seismicity. Besides intraslab seismicity at intermediate- (i.e., 70-300 km) and deep depths (i.e., 300-660 km), earthquakes also occur in the shallow regions of the slab (i.e., < 70 km). These earthquakes are referred to as outer rise events and are associated with the bending of the slab and the state of stress along the subduction interface (i.e., coupled or uncoupled; Christensen & Ruff 1983).

Subduction seismicity also occurs in the overriding plate, where upper plate deformation causes shallow earthquakes (i.e., < 70 km). These events mainly occur arcward of the seismic front (i.e., the trenchward limit of seismicity; House and Jacob, 1983), and can have focal mechanisms that reflect the state of stress within the overriding plate (Byrne et al. 1988). Extensional settings due to e.g. back-arc

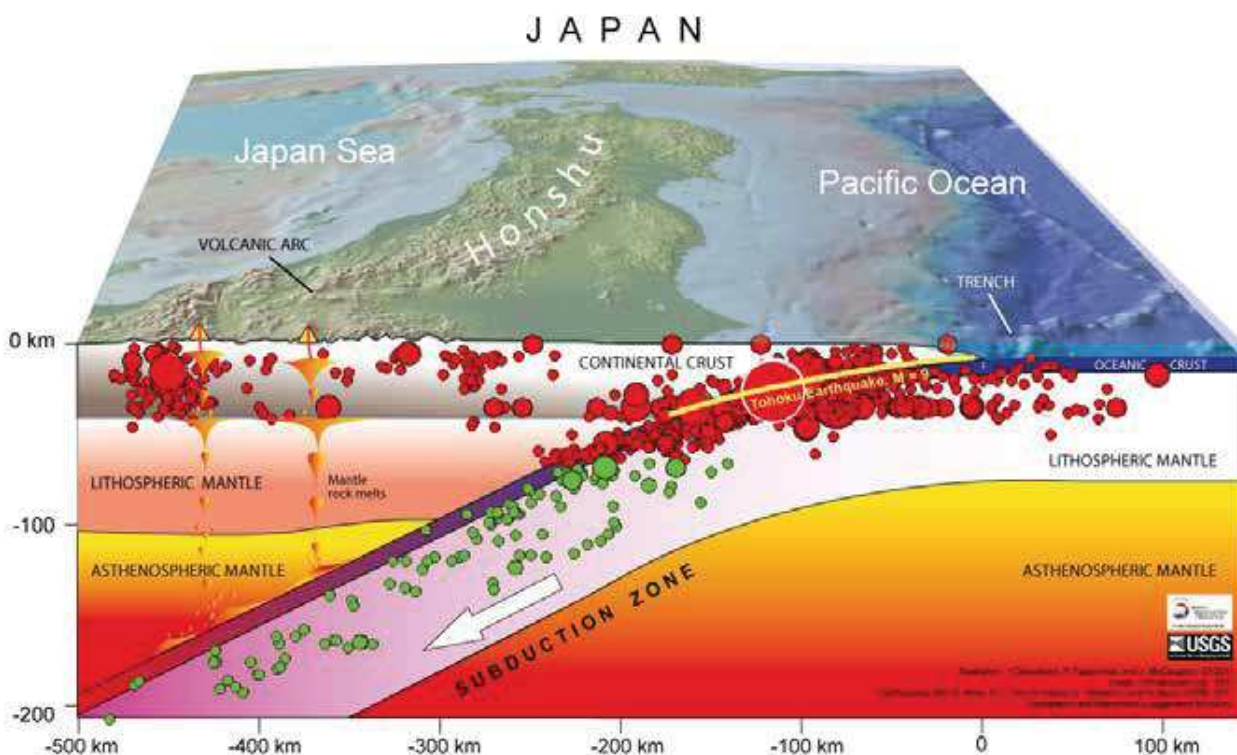


Figure 2.1. Schematic representation of the Japan Subduction zone, where the 2011 MW 9.1 Tohoku event occurred. Shallow earthquakes (< 70 km) are indicated by the red dots, while intermediate earthquakes (> 70 km) are portrayed in green. The seismogenic zone is indicated by the yellow line. Image source: Earth Observatory Singapore. Earthquake data come from the USGS.

spreading could cause displacement along normal faults, while a compressional setting causes the opposite.

The largest and therefore most dangerous earthquakes in subduction zones occur along the subduction megathrust, the shallow interface between the subducting- and overriding plates. These events are the result of frictional resistance between the two plates and are called interplate earthquakes (e.g., Scholz et al. 1986). During the movement of the downgoing slab, the interface can stay locked (i.e., it sticks) and therefore accumulate strain. During this locking, the overriding plate above the coupled area (i.e., the forearc) moves with the downgoing plate in a landward direction. When the

system can no longer accumulate any strain, the forearc moves back towards its original position (i.e., it slips), resulting in an earthquake. Since during such an event, the overriding plate moves up with respect to the downgoing plate, all events that occur along the subduction interface are thrust events.

This stick-slip type behavior of earthquakes along the subduction interface follows the so-called seismic cycle, where stresses on a fault are repeatedly built up over long periods of time (i.e., the interseismic stage), and then are rapidly released during an earthquake (i.e., the coseismic stage). After the coseismic stage, aftershocks may occur to further relax the system (i.e., the postseismic stage) before the steady-state build-up of stresses starts again.

2.2. Earthquakes along the subduction megathrust

2.2.1. The seismogenic zone

Interplate earthquakes occur along the shallow part of the subduction interface, also called the seismogenic zone. It extends from a depth of 11 ± 4 to 51 ± 9 km and has an in-depth width of 112 ± 40 km (Heuret et al. 2011).

The downdip limit of the seismogenic zone appears to be mainly controlled by temperature. Between temperatures of probably 350-450°C, a transition of full great earthquake rupture to no motion occurs, where 450°C corresponds approximately with the 'brittle-ductile' transition (Hyndman 2007). It seems that ruptures cannot nucleate, but may still extend within this 350-450°C transition zone. In some cases, the downdip rupture extent does not reach this transition zone and occurs shallower along the subduction thrust fault. It is proposed that the intersection of the subduction thrust with the forearc Moho could also form the downdip limit of the seismogenic zone. The fore-arc mantle may be serpentinized, which makes it very unlikely for earthquakes to nucleate below the forearc Moho (Ruff & Tichelaar 1996; Wada & Wang 2009; Heuret et al. 2011).

The main control of the updip limit of the seismogenic zone is most likely a variation in the

material along the subduction thrust fault (e.g., Oleskevich et al. 1999). In the most shallow part, accreted sediments are usually still unconsolidated, which makes them too weak to accommodate a buildup of stresses. At larger depth, the subducting plate is overlain by crystalline crust, which has a much larger strength. Also temperature plays a role in the position of the updip limit of the seismogenic zone. A good correlation has been found between the thermal state of the incoming oceanic plate and the depth of the updip seismogenic limit defined by microearthquakes (Harris & Wang 2002; Spinelli & Saffer 2004; Norabuena et al. 2004). The temperature associated with the updip limit of the seismogenic zone is 100-150°C. The physical mechanism explaining this temperature controlled limit is still debated, but possible explanations could be silica and carbonate diagenesis and consolidation changes of permeability that control pore-fluid pressure. Recent studies argue that ruptures could have propagated all the way to the trench, and that therefore an updip limit of the seismogenic zone is not always present (Sladen & Trevisan 2018).

2.2.2 Seismic vs. Aseismic Behavior

Within the seismogenic zone, stick-slip behavior occurs (e.g., Marone & Scholz 1988). Stress and strain accumulate during the interseismic period

(“stick”) and subsequently fail in a catastrophic manner (“slip”), creating an earthquake. This unstable sliding along the subduction thrust fault is called seismic behavior. On the other hand, the convergence between the subducting and overriding plate can also be accommodated by stable sliding, named aseismic behavior, or creep. This happens for example when temperatures are high or strain rates are low (Brace & Byerlee 1966). Here, there is no locking between the two plates and they slowly slide past each other. Aseismic behavior occurs outside the limits of the seismogenic zone, since here the conditions are not favorable for stick-slip behavior to occur. In addition, this aseismic behavior can also occur within the seismogenic zone, with patches that behave seismic, surrounded by areas that behave aseismic. The physical properties of each specific subduction thrust fault determine how much of the convergence is accommodated by seismic- and aseismic behavior. This can be quantified using the term ‘seismic coupling’. This is the amount of displacement that has been accommodated by earthquakes in relation to the total convergence between the two plates within the same time frame (e.g., Davies & Brune 1971; Peterson & Seno 1984; Pacheco et al. 1993).

2.2.3 Rate and State Variable Friction Laws

In order to better understand when a surface behaves seismic or aseismic, scientists have been trying to describe the process of frictional sliding along a pre-existing fault plane by using empirical friction laws. In the original stick-slip model (Brace & Byerlee 1966; Rabinowicz 1951), two different types of friction are considered: static friction μ_s and dynamic friction μ_d . The static friction is the ratio of shear- to normal stress which has to be reached

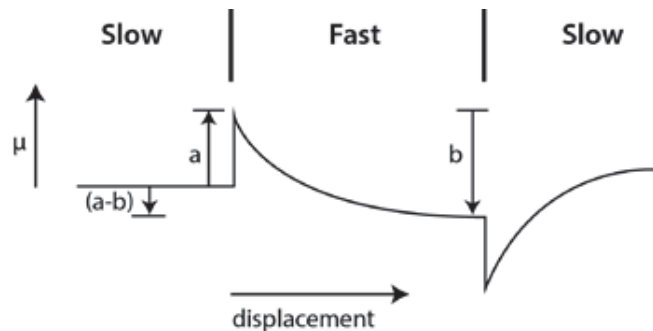


Figure 2.2. Schematic representation of rate and state parameters a and b while applying different sliding velocities. Figure modified from Scholz (1998).

to initiate sliding on a surface, while the dynamic friction is a lower friction value which holds after the initiation of the sliding (the friction is lower because the contacts are younger). When friction values drop from static to dynamic, a dynamic instability may occur, resulting in seismic slip.

Later on, new insights showed that μ_s increases with contact time between two surfaces (Dieterich 1972) and that μ_d varies with sliding velocity (Scholz et al. 1972; Scholz & Engelder 1976). The dynamic friction can exhibit velocity weakening (i.e., μ_d decreases with increasing slip velocity) over a wide range of sliding velocities (i.e., from cm/s to m/s; Tsutsumi & Shimamoto 1997), but also velocity strengthening (i.e., μ_d increases with increasing slip velocity), which is thought to be related to factors like frictional heating or rock type, but is still poorly understood (Marone 1998).

In the attempt to relate static and dynamic friction parameters, the rate and state variable friction (RSV) laws were introduced (Dieterich 1979; Ruina 1983). They aim to describe the process of stick-slip friction, which needs slip-weakening to initiate unstable sliding, as well as the healing process that is needed to re-strengthen the fault again between consecutive events.

The Dieterich-Ruina or ‘slowness’ law is commonly the most used form of the RSV friction laws because it is in best agreement with experimental data (Scholz 1998; Beeler et al. 1994):

where τ is the shear stress and σ is the effective normal

$$\tau = \left[\mu_0 + a \ln \left(\frac{V}{V_0} \right) + b \ln \left(\frac{V_0 \theta}{D_c} \right) \right] \bar{\sigma}$$

stress (applied normal stress minus pore pressure). V and V_0 are the slip velocity and a reference velocity, respectively. A steady state friction coefficient at $V=V_0$ represented by μ_0 , and D_c describes the critical slip distance (i.e., the slip necessary to renew surface contacts). The variables a and b are material properties and their values relative to each other are used to describe the frictional behavior. The state variable θ evolves according to:

The parameters a and b can be determined in friction

$$\frac{d\theta}{dt} = 1 - \frac{\theta V}{D_c}$$

experiments by applying a sudden increase in sliding velocity, after which velocity is decreased again to its initial value (Figure 2.2). With an increase in sliding rate, the friction increases by a (i.e., the ‘direct effect’), followed by a decrease in friction by b (i.e., the evolutionary effect).

Whether a frictional instability (resulting in unstable sliding) will occur, depends on the combined parameter $(a - b)$. If $(a - b) \geq 0$, the material will be velocity-strengthening, and therefore slide in a stable way (i.e., creep). When $(a - b) < 0$, velocity-weakening behavior will occur, resulting in either an unstable, or conditionally stable regime (depending on material properties such as stiffness k , critical slip distance D_c and a and b). Seismic slip can be initiated in the unstable regimes, but not in the stable regimes due to the velocity-strengthening behavior. In the conditionally stable regimes, ruptures cannot nucleate, but they can propagate through these regimes when initiated in a neighboring unstable regime (Scholz 1998).

2.2.4 The Asperity Model

The distribution of seismic and aseismic regimes does not only vary along dip (i.e., seismic in the seismogenic zone and aseismic at shallower- and deeper levels; section 2.2.2.), but also within the seismogenic zone. The asperity model, first proposed by Byerlee (1970) and further developed by Scholz & Engelder (1976) and Lay & Kanamori (1981), discusses the presence of high strength regions along a fault plane, the so-called asperities, that hold the two sides of a fault together. The nature of these asperities could be related to variations in geometrical orientation or frictional strength heterogeneities, but is still debated (e.g., Wang & Bilek 2014). Asperities along a fault are the regions that will rupture in an unstable way during seismic events, catching up with the surrounding (conditionally) stable regions that behave in a creeping manner. Asperities are therefore thought to be velocity-weakening, while surrounding stable regions, also called barriers, are likely to be velocity-strengthening. Great ruptures are thought to occur during simultaneous rupture of multiple asperities (i.e., asperity synchronization; Lay & Kanamori 1981; Corbi et al. 2017), while smaller ruptures may occur when only one asperity ruptures. The interaction between asperities depends on the

local stress distribution, as well as on the presence of stress barriers that may segment the interface.

Lay and Kanamori (1981) divided all subduction zones into four categories, based on rupture length (e.g., great ruptures have rupture length > 500 km, while large ruptures have rupture lengths of 200-500 km). Category 1 subduction zones (e.g., Southern Chile) are characterized by regular great (i.e., rupture length > 500 km) earthquakes, category 2 regions (e.g., Western Aleutians) have variable rupture lengths, with an occasional great rupture, category 3 regions (e.g., Kurile Islands) are characterized by regular ruptures over limited areas, with no occurrence of great ruptures, and category 4 regions (e.g., Marianas) do not host any large earthquakes. These four categories can be described following the asperity model, focusing on the distribution and interaction of asperities (Figure 2.3). Regions that follow the Chile-type behavior are thought to have a rather homogeneous asperity distribution, making it easy for the asperities to synchronize and therefore rupture together during great events. When asperities are slightly smaller, but still quite homogeneous, great ruptures are thought to occur only occasionally, which is the case for the second category. Subduction zones in the third category are thought to have numerous smaller asperities and

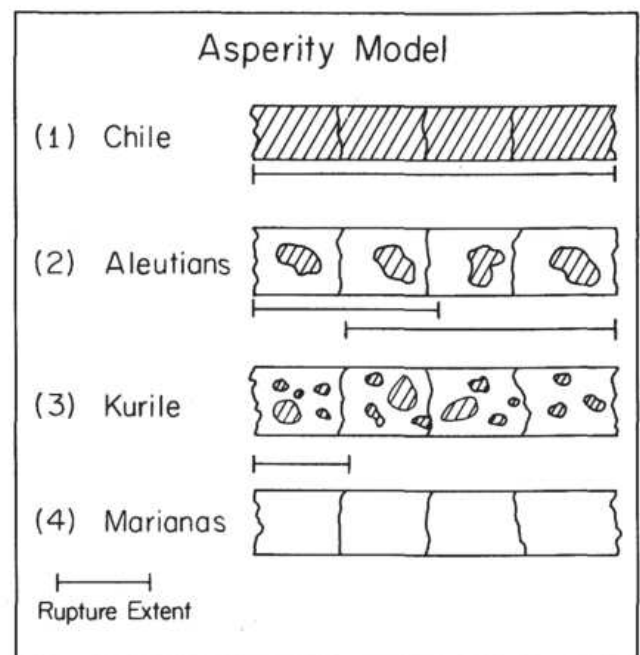


Figure 2.3. The Asperity Model showing asperity distributions for the four subduction zone categories defined by Lay and Kanamori. Figure taken from Lay and Kanamori (1981).

therefore a more heterogeneous stress distribution. Here, asperities are less likely to communicate with other asperities and therefore rupture together in great ruptures. Regions that follow the Mariana-type do not have asperities and therefore behave mainly aseismic.

These four categories are useful for comparing different subduction zones in terms of asperity distribution and associated seismicity, but the proposed distributions of frictional heterogeneity are still very general. More knowledge about the

along-dip variety of seismic behavior (e.g., tsunami earthquakes or slow earthquakes) has been acquired over the years (e.g., Bilek & Lay 1998; Bilek & Lay 1999; Bilek & Lay 2002; Lay & Bilek 2007; Lay et al. 2012), hence calling for an updated description of the subduction interface. Lay (2015) analyzed all great earthquakes since 2004 and came up with a schematic representation of both the along-depth variations in seismic behavior, as well as the general spatial heterogeneity as proposed by Lay and Kanamori (1981; Figure 2.4).

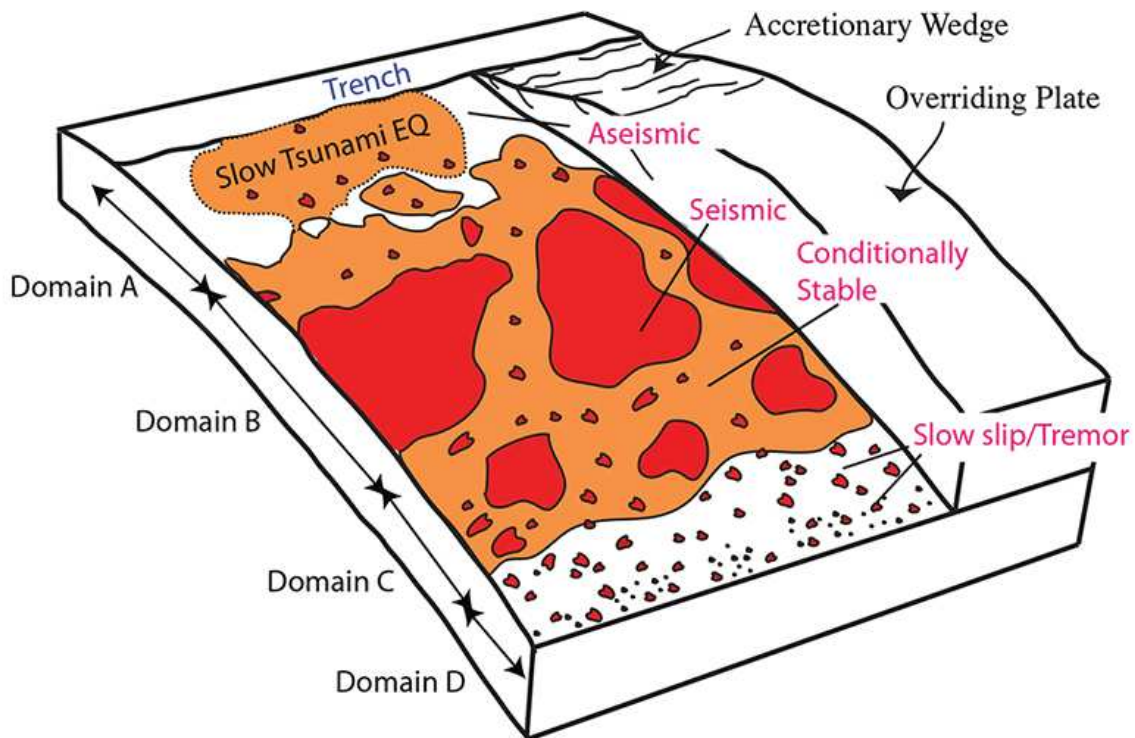


Figure 2.4. Schematic representation of the subduction interface, including along-dip variations in seismogenic behaviour represented by four different domains and a general spatial heterogeneity (in all directions). Domain A is the near trench regions, where tsunami earthquakes or anelastic deformation and stable sliding occur; Domain B represents the central megathrust where large slip may occur along large unstable patches; Domain C is the down-dip domain with patchy, smaller scale regions of stable sliding surrounded by conditionally stable areas; Domain D is the transitional domain that only exists for some (young) subduction zones, where slow slip events, low frequency earthquakes (LFEs) and seismic tremor can occur. Figure taken from Lay et al. (2015).

2.3. Subduction parameters in relation to megathrust seismicity

Subduction zones behave both seismically and aseismically (see section 2.2.), depending on the physical characteristics of each individual region. Lay and Kanamori (1981) proposed different sizes and distributions of asperities along the subduction megathrust (i.e., different distributions of seismic and aseismic regions) that could explain the observed difference in seismicity. However, the physical mechanism responsible for this variety of seismic and aseismic regions, and therefore the possibility of a rupture to grow larger, remains a subject of debate (e.g., Wang & Bilek 2014). Many parameters have already been proposed, such as the convergence velocity, age of the downgoing plate, the amount of sediments that enter the trench, or the upper plate strain (e.g., Ruff & Kanamori 1980; Ruff 1989; Heuret et al. 2012).

By using a multivariate regression analysis, they found that convergence velocity and plate age showed a strong correlation with strength of coupling (based on moment magnitude M_w of the past 100 years): young and fast subduction zones seemed more prone to host large megathrust earthquakes. This trend was confirmed by several other studies (e.g., Peterson & Seno 1984; Jarrard 1986), although a strong correlation between large earthquakes and convergence rates was questioned as well (McCaffrey 1994). In addition, Peterson and Seno (1984) showed that subduction segments with similar ages, but belonging to different subduction zones, could have different moment release rates, suggesting that the age of the lithosphere is not the dominant factor and other parameters might play a role as well. The occurrence of more recent $M_w > 9.0$ Sumatra (2004) and Tohoku (2011) events changed the perspectives on the role of plate age and convergence rate even more, since the convergence velocity in the Sumatra subduction zone is thought to be low (e.g., Stein & Okal 2007; Gutscher & Westbrook 2009; Heuret et al. 2011; Stein & Okal 2011), and the lithosphere at the Japan trench has an age > 120 million years (Müller et al. 2008; Bletery et al. 2014).

Since then, many studies have attempted to uncover which other subduction parameters play a role in the occurrence of large megathrust events (Figure 2.5). Ruff (1989) compared the amount of trench sediments (i.e., excess trench sediments vs. a horst and graben structure at the trench) with the occurrence of great earthquakes, suggesting that

subduction zones with excess trench sediments are more prone to host great megathrust earthquakes. Heuret et al. (2011; 2012) quantified the amount of trench sediments at 44 subduction segments and statistically compared this with maximum earthquake magnitude (M_{wmax}). They find that regions with a sediment thickness > 1 km, have an average M_{wmax} of 8.4, showing that the amount of sediment at the trench links to regions that are more prone to host large interplate earthquakes. More recent studies confirm these findings as well (e.g., Scholl et al. 2015; Brizzi et al. 2018), showing statistically that high magnitude earthquakes are more prone to occur on well-sedimented subduction zones. However, a question that still needs to be answered, is how the amount of sediments at the trench relates to the sediments at the subduction interface (Heuret et al. 2012; Lallemand et al. 1994; von Huene & Lallemand 1990).

Another parameter that was highlighted by the statistical analysis of Heuret et al. (2011; 2012) is the upper plate strain, which can be either compressional, neutral, or extensional. It was initially thought that compressive upper plate strain would promote the occurrence of large earthquakes, due to the higher coupling and stronger stress accumulations that are associated with it (Ruff & Kanamori 1980). Heuret et al. (2011) showed however, that instrumentally recorded $M_w > 8.5$ megathrust events are most often associated with neutral back-arc regimes, and only secondary with compressional regimes. They argue that even though stress accumulation is larger in compressional regimes, the propagation and therefore growth of ruptures might be easier in settings with neutral upper plate strain.

Also the structure of the fore-arc seems to correlate with the seismogenic behavior of the subduction thrust fault (Song & Simons 2003; Wells 2003). Low gravity anomalies have been spatially correlated with areas of high coseismic slip (i.e., seismic asperities), suggesting that the geological fore-arc structure is related to the distribution of seismic and aseismic patches along the subduction thrust fault. The fore-arc structure offshore Northeast Japan has been analyzed with residual topography and gravity anomalies to understand how it influenced the 2011 Tohoku rupture (Bassett et al. 2016). Results reveal a clear southwest-northeast-striking boundary, which is thought to be a continuation of the onshore

Median Tectonic Line and seems to correlate with a sharp north-to-south reduction in seismogenic behavior.

Since an earthquake's magnitude mainly depends on rupture area and therefore the potential for a rupture to grow, geometrical parameters like trench length or seismogenic zone width are thought to play a role as well (Pacheco & Sykes 1992; Hayes et al. 2012; Schellart & Rawlinson 2013). Longer trench lengths and wider seismogenic zones contribute to the potential of a rupture to grow large, but only if the interface itself is homogeneous enough to allow rupture propagation. Bletery et al. (2016) showed that the along-dip curvature of the downgoing plate plays a role in rupture propagation as well. Highly curved interfaces create a more heterogeneous strength pattern, making it more difficult for ruptures to grow, while more planar interfaces are more homogeneous, allowing ruptures to propagate more easily.

Besides the large scale curvature of the downgoing plate, smaller variations in the geometry of the subduction interface (i.e., seafloor features such as seamounts, ridges and plateaus) are thought to affect its seismogenic behavior as well (e.g., Das & Watts 2009; Wang & Bilek 2014). This so-called seafloor roughness is related to previously mentioned parameters like sediment thickness and structure of the forearc. Sediments have a smoothing effect and can therefore modify the interface geometry, while the structure of the forearc is thought to reflect the geometrical structure at the interface and can therefore be used as an indicator of the structures at the subduction interface (e.g., Bassett & Watts 2015). The roughness of the interface is currently thought to be one of the key parameters for promoting or impeding the occurrence of large megathrust events (see section 2.6).

2.4. Earthquake recording and slip inversion

In order to study the influence of subduction parameters on the size and spatial occurrence of megathrust earthquakes, it is important to constrain their magnitude, location and slip distribution as detailed as possible. Scientists have been trying to record earthquakes for centuries, with the strongest developments over the past 150 years (Dewey & Byerly 1969).

The very first seismoscope was invented by the Chinese philosopher Chang Hêng in 132 A.D. and was able to indicate both the occurrence of earthquakes, as well as the azimuths of their origins from the observer (Needham 1959). In the eighteenth century, simple seismoscopes were designed to measure the timing and character of ground motion of earthquakes. The first earthquake recordings however, happened at the end of the nineteenth century, with the invention of instruments that could record earthquake ground motion as a function of time: the seismographs (Dewey & Byerly 1969). In the following paragraphs, the evolution of earthquake magnitude scales (2.4.1.) and rupture distributions (2.4.2.) since the beginning of the 20th century will be discussed.

2.4.1. Magnitude scales

The first classifications of earthquakes according to their strength or magnitude, were without the use of instrumental data and are referred to as the seismic intensity scales (e.g., the modified Mercalli intensity scale, which is still used nowadays; Wood & Neumann 1931). The first quantitative magnitude scale was proposed by Richter (1935) and is called the local magnitude (M_L). By plotting the logarithm of the maximum seismogram amplitude as a function of epicentral distance, Richter was able to compare different earthquakes quantitatively. However, by doing this, he fixed certain parameters that are specific for the type and the location of the seismograph he used (i.e., a Wood Anderson Torsion seismograph in Southern California). Therefore, the local magnitude was not suitable for worldwide application. A more widely applicable scale was the surface wave magnitude scale (M_S), which uses seismograms at teleseismic distances (i.e., > 2000 km) and is therefore particularly useful for large earthquakes (Gutenberg 1945a; Duda & Nuttli 1974). A downside of the M_S scale is that it only works for earthquakes shallower than 100 km. This problem

is solved with the body wave magnitude scale (M_B), which considers a ratio of body wave amplitude (A) and period (T) as a function of epicentral distance, rather than amplitude alone as was done for previous magnitude scales (Gutenberg 1945b).

However, the M_L , M_S and M_B scales are all said to saturate at large magnitude and each work best for a specific range of earthquakes (e.g., based on depth or size). With the aim to have one magnitude scale that can be used for all earthquakes, the moment magnitude (M_W) scale was introduced (Kanamori 1977; Hanks & Kanamori 1979; Kanamori 1983).

This scale is based on the seismic moment (M_0), a measure of a rupture's size that can be determined very accurately from seismograms (Kanamori 1983), but also from rupture area (A), average slip (D) and the shear modulus (μ):

Consequently, the seismic moment can be converted

$$M_0 = \mu AD \text{ (in Nm)}$$

into a moment magnitude following this equation:

$$M_W = \frac{2}{3} \log_{10}(M_0) - 6.06$$

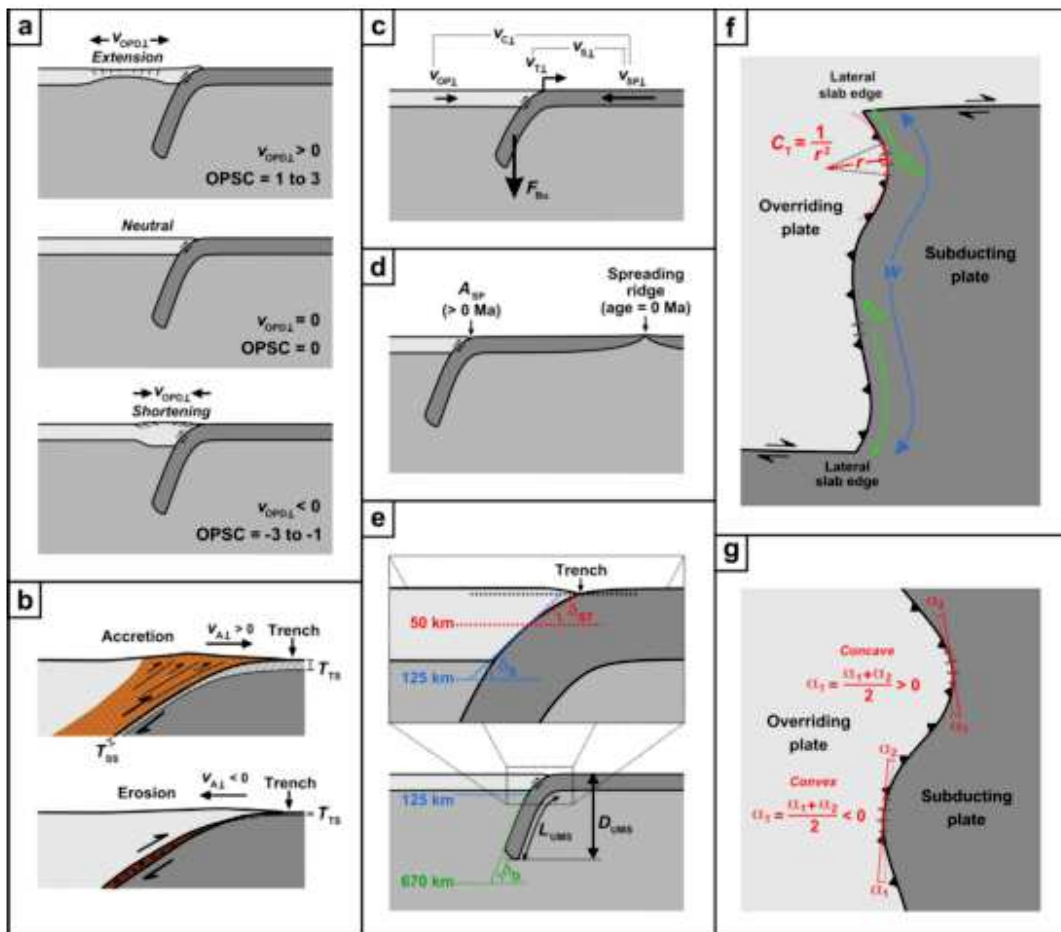


Figure 2.5. Schematic overview of various subduction parameters that have been investigated for their potential role on megathrust seismicity (Schellart and Rawlinson, 2013). (a) Strain regime in the overriding plate (extensional, neutral or compressional). (b) Accretional vs. erosional margin and trench sediment thickness. (c) Absolute and relative velocities of both subducting and overriding plate. (d) Subducting plate age at the trench. (e) Dip angles of the subduction megathrust, shallow- and deep slab. (f) Slab width, lateral slab edge distance and trench curvature. (g) Trench curvature angle. Figure taken from Schellart and Rawlinson (2013). Detailed explanations of the parameters in the figure can be found in the original version.

2.4.2. Rupture distributions

Besides a rupture's magnitude, a description of its spatial occurrence (i.e., a contour describing the area of a rupture) and slip distribution (i.e., indicating how the slip is distributed within this area) are necessary for determining what influences the occurrence of (large) megathrust events. The detail in which these parameters can be constrained varies considerably over time, since during most of the 20th century data were sparse and the means for obtaining a slip distribution from any kind of data (e.g., seismic, geodetic or tsunami data) were very different from what we are used to nowadays.

Before the implementation of the World Wide Standardized Seismograph Network (WWSSN) in 1963, earthquake rupture zones were mainly determined by using aftershocks which occurred within 24 hours of the main shock (Kowalik et al. 2005; Duong et al. 2009). When seismic data became more globally available, seismograms were used to investigate the seismic moment release distribution and slip during large earthquakes (Bilek 2007). The first earthquake whose spatial distribution was quantitatively described, was the 1960 MW 9.6 Chile event. Rupture length and velocity were determined by analyzing surface waves on long-period seismograms (Benioff et al. 1961; Press et al. 1961). In the 1970's, seismologists started to systematically analyze a rupture complexity by solving slip inversion problems that determine the slip on an assumed fault plane (e.g., Ide 2007). This assumed fault plane

was divided into several rectangular subfaults and by using the least-squares method the amount of slip for each subfault could be determined (Trifunac 1974).

In the years following these first models, new procedures were proposed to better reveal the heterogeneity of the seismic source and improve our understand of earthquake physics (e.g., Kikuchi & Kanamori 1982; Olson & Apsel 1982). The onset of geodetic measurements by using satellites in the 1990's initiated the use of joint inversion models (i.e., using both seismic and geodetic data) to determine final slip (e.g., Ide 2007; Mai & Thingbaijam 2014). Joint inversion models aim to match all observations, developing a more comprehensive image of the rupture process. This can be done by using all data simultaneously (i.e., seismic, geodetic, tsunami), or by taking an iterative approach where one dataset is used to construct an initial model that will be used for further inversions based on the remaining data (Mai & Thingbaijam 2014).

Nowadays, slip inversions are the most widely used method to determine spatial (and sometimes temporal) rupture characteristics, such as the slip distribution at depth. Due to larger and denser networks of seismometers and GPS (Global Positioning System) stations, ruptures can now be studied in more detail. A consequence of both the improved technologies and the inversion methods however, is that for recent earthquakes, many different finite fault models co-exist, often showing different slip distribution solutions (e.g., Lay 2017).

2.5. Analogue models and megathrust seismicity

Analogue models aim to reproduce geodynamic processes at convenient length- and time scales. By using simplified rheologies, geometries and boundary conditions, they represent simplified versions of their natural prototypes. Analogue models overcome several limitations with respect to direct observations to the Earth: 1) many natural processes occur on timescales of millions of years, and therefore much longer than the human life span; 2) not all processes can be observed easily, due to their large scale or the fact that they occur deep inside the Earth; 3) with natural observations only a snapshot of the Earth can be seen, not revealing

previous or future events.

Such limitations also arise when observing seismic processes in nature. Timescales vary from seconds during earthquake rupture, to days of aftershock activity, to years of postseismic relaxation and finally to hundreds of years when considering multiple seismic cycles. On top of that, many earthquakes occur at tens of kilometers depth, making it difficult for scientists to determine what happens along fault interfaces before, during and after seismic rupture. Since numerical models are based on empirical relations, and not always provide unique

solutions (e.g., slip inversions, section 2.4.2.), the use of physically self-consistent analogue models for studying seismic processes provides an important contribution to our understanding of the physics of earthquakes.

The first attempts to experimentally model earthquakes were done by (Reid 1911), who used jelly models and natural observations following the 1906 San Francisco earthquake to formulate the elastic rebound theory (i.e. an earthquake occurring as a result of elastic rebound of accumulated strain in the rocks on both sides of a fault; Wood 1912). In the decades that followed, new developments in seismology, experimental rock mechanics and the rise of the plate tectonics theory in the 1960's led to a better understanding of where and how earthquakes mainly occur. Different types of analogue models were used to model rupture processes (e.g., Burrige and Knopoff, 1967; Brune 1973; Heslot et al. 1994; Voisin et al. 2007; Lu et al. 2009; Rosenau et al. 2009; Corbi et al. 2011; Corbi et al. 2013; Caniven et al. 2015; Reber et al. 2015) resulting in the more advanced seismotectonic scale models that are performed nowadays. The different experimental approaches that have been used so far to study seismogenic processes will be discussed below. A complete overview of the developments in analogue earthquake modelling is given by Rosenau et al. (2017).

2.5.1. Spring-slider models

The simplest models for studying earthquake mechanics are spring-slider models, in which the frictional and elastic components are separate elements of the set-up. A generic fault interface is represented by a block-basement interface, while a spring with its stiffness represents the elasticity of the system (Burrige & Knopoff 1967; Baumberger et al. 1994; Vargas et al. 2008). After the first spring-slider models presented by Burrige and Knopoff (1967), many other studies used this type of modelling to investigate earthquake dynamics. King (1975, 1991, 1994) created a circular chain of spring sliders, which he used to study earthquake predictability and slip variability over various cycles. The influence of fundamental parameters like spring stiffness, loading velocity and slider mass were studied by Heslot et al. (1994), while more recent studies focused on the effect of external forcing (Varamashvili et al. 2008)

and the onset of frictional instability (Popov et al. 2012).

An important limitation of classical, spring-slider models is related to the rigidity of the slider. When the slider is rigid, shear stresses are distributed evenly across the block-basement interface, resulting in very homogeneous loading and release and therefore characteristic earthquakes (Rosenau et al. 2017). In nature, ruptures tend to be more complex, showing areas of high and low energy release (i.e., due to a heterogeneous stress distribution related to asperities and barriers along the interface; section 2.2.4). Multiple slider-systems have been introduced to overcome this limitation (Burrige and Knopoff, 1967; King 1991, 1994), resulting in more complex slip and recurrence patterns. Other advanced versions of the spring-slider model include a deformable slider (i.e., plastic rather than rigid; Reber et al. 2015), but also models related to rock friction experiments (e.g., axial loading or ring-shear tests) exist. Granular materials, such as glass beads or other synthetic faults gauges, are used as rock analogues in shear, rotation and axial compression apparatuses (e.g., Nasuno et al. 1998; Mair et al. 2002; Schulze 2003; Anthony & Marone 2005; Alshibli & Roussel 2006; Rubinstein et al. 2012; Scuderi et al. 2015).

2.5.2. Fault-block models

Another analogue approach to study earthquake dynamics is the fault-block model. Here, the ability of the model to store elastic energy is not represented by an external spring (as in the spring-slider model), but is included in the properties of the fault blocks. Models that adopt this set-up therefore have a stronger resemblance with fault-bounded crustal blocks in nature. Fault block models all consist of two blocks that are uniformly loaded, normal to their interface, and sheared against each other (Rosenau et al. 2017).

Blocks in fault-block models can have the same material, such as gelatin (e.g., Reid 1911) foam rubber (e.g., Brune 1973; Archuleta & Brune 1975) or rock (e.g. Lockner et al. 1991; Zang et al. 2000; Thompson et al. 2005; Thompson et al. 2006; Thompson et al. 2009), but can consist of two different materials as well (e.g., gel sliding on glass: Baumberger et al. 2003; rubber on rough substrate: Hamilton & McCloskey 1997, 1998; Schallamach

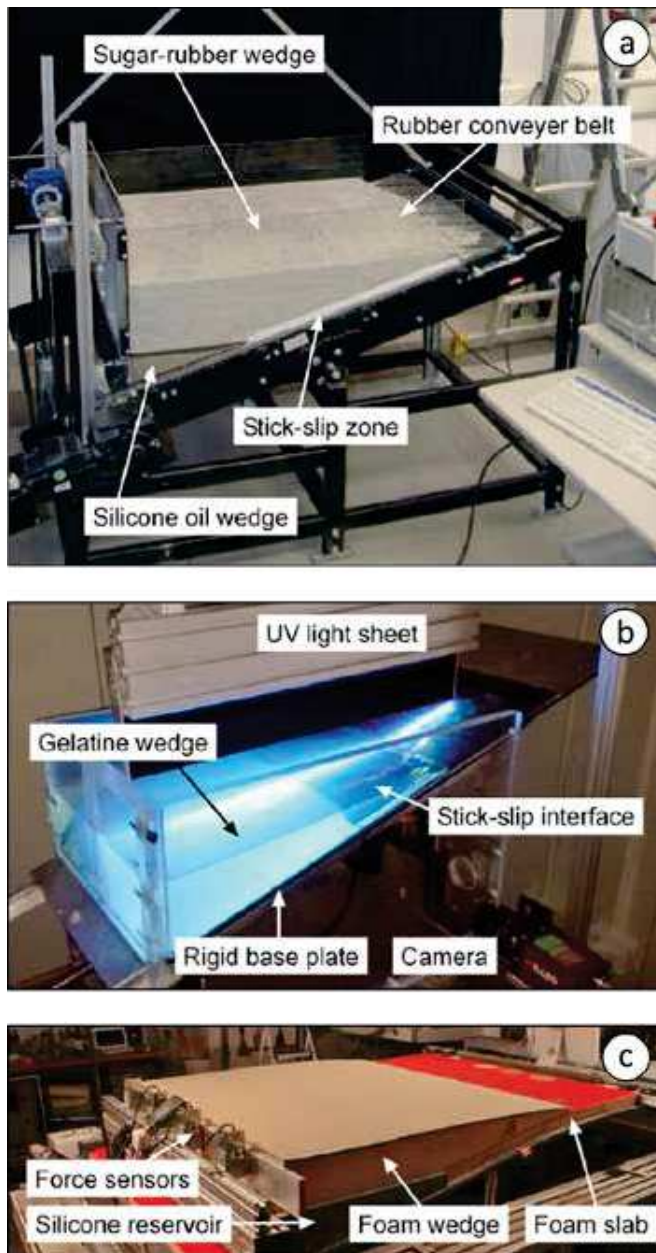


Figure 2.6. Overview of seismotectonic scale models as discussed in the text. a) Rosenau et al., 2009. b) Corbi et al., 2013. c) Dominguez et al., 2015. Figure modified from Rosenau et al., 2017.

1971). By varying the material, the desirable rheological response of the system can be acquired (e.g., purely elastic with rubber, or viscoelastic with polyvinylalcohol – PVA; Schallamach 1971 and Namiki et al. 2014, respectively), as well as the preferred monitoring time (e.g., slower rupture time and therefore longer monitoring time with softer materials; e.g., Baumberger et al. 2003; Yamaguchi et al. 2011; Latour et al. 2013).

2.5.3. Seismotectonic scale models

More advanced and realistic compared to the previously discussed spring-slider- and fault-block models, are the seismotectonic scale models. The emerge of these models is related to new developments in monitoring techniques, such as digital image correlation (e.g., Adam et al. 2005) that allowed more detailed measurements of model deformation (i.e., scaling from decimeters to meters in nature) and therefore the study of single seismic events. Seismotectonics scale models are used to study seismogenic fault behavior over many orders of magnitude in timescale and include a realistic depth-dependence of the pressurization of the fault (i.e., lithostatic pressure).

Another advantage of these models is the reasonably scaled elasticity with the natural prototype. Where materials like sand or other rigid particles are useful for studying long-term tectonic processes in the brittle regime, their elastic moduli appear to be too high for realistically studying elastic deformation (Klinkmüller et al. 2016). To still meet the scaling rules (Hubbert 1937), seismotectonic scale models require materials with elastic moduli that are several orders of magnitude lower. Compliant solids such as foam rubber (Caniven et al. 2015) or gelatin (Corbi et al. 2013) can be used, as well as the addition of elastic particles such as rubber pellets (Rosenau et al. 2009).

A major challenge of analogue modelling of earthquakes involves the slow strain accumulation in interseismic periods, with respect to the relatively fast train release during coseismic stages. Timescales range from seconds (strain release) to thousands of years (strain accumulation) in nature, and milliseconds to minutes in the laboratory, resulting in large variations in velocities, up to twelve orders of magnitude. To overcome this, seismotectonic scale models make use of non-linear timescaling (Rosenau et al. 2009; Rosenau et al. 2017).

There are various approaches for seismotectonic scale models, the first one being developed by Rosenau et al. (2009; Figure 2.6a). They introduce a quasi-two-dimensional analogue for the subduction megathrust, featuring rate- and state dependent elastic-frictional plastic and viscoelastic material properties that is scaled for gravity, inertia, elasticity,

friction and viscosity. In their models, a granular elastoplastic wedge made up of a mixture of sugar and rubber pellets represents the overriding plate, underthrust by a less compliant conveyor belt representing the subducting plate. A velocity-weakening material (i.e., rice) was used to define the seismogenic zone at the base of the wedge. With this setup, the seismotectonic evolution of subduction forearcs has been simulated (Rosenau et al. 2009), as well as the influence of great- to giant megathrust events on local tsunami runup (Rosenau et al. 2010). Another approach to model rupture dynamics along the subduction megathrust, has been presented by Corbi et al. (2013; Figure 2.6b). A viscoelastic gelatin wedge (i.e., the overriding plate) overlies a rigid, aluminum plate (i.e., the subducting plate). The seismogenic zone at the base of the wedge is represented by sandpaper that has velocity weakening characteristics, bounded by a plastic sheet up- and down-dip that behaves velocity strengthening. Experiments can be monitored from both side- (Corbi et al. 2013) and topview (Corbi et al. 2017a&b) with Particle Image Velocimetry (Sveen 2004). The viscoelastic gelatin wedge in these models is less stiff than the granular elastoplastic wedge used by Rosenau et al. (2009). Although from a scaling point of view, the granular wedge would be more appropriate, the gelatin wedge allows slower rupture velocities, which improves the observability of the ruptures. The models developed by Corbi et al. (2013) have been used to study the role of subduction velocity and the width of the seismogenic zone on the seismogenic behavior (Corbi et al. 2017a), as well as the synchronization of asperities on the interface (Corbi et al. 2017b).

A third, and most recent approach was developed by Caniven et al. (2015) to study strike-slip fault

earthquakes and seismic cycles in a brittle-ductile crust. A visco-elasto-plastic multi-layered rheology is used, consisting of an elastic block (polyurethane foam) floating on a viscoelastic material (silicone oil) and covered by brittle plastic analogue material (silica-powder-graphite mix). This multi-layered approach allows the simulation of brittle-ductile coupling, post-seismic deformation and far field stress transfer. By varying the normal stress distribution from uniform to non-uniform, variable seismic behavior was observed, ranging from irregular earthquake cycles and earthquake clustering, to more characteristic earthquakes, respectively (Caniven et al. 2017). Based on this strike-slip experimental setup, a similar multilayered approach has been developed to model the subduction megathrust Dominguez et al. (2015; Figure 2.6c).

Even though all the seismotectonic scale models mentioned here have some general limitations (e.g., the effects of temperature, fluids and poroelasticity are not included), they provide an important contribution to a better understanding of earthquake physics. In contrast to numerical models that need strong assumptions on the physical laws involved and need to be discretized, these analogue models are physically self-consistent and happen in a time and space continuum. However, a better coupling between analogue and numerical models in the future will be beneficial for the seismotectonic modelling community. In addition, improved monitoring techniques and the development of new analogue materials will play an important role in the development of more realistic seismotectonic scale models (Rosenau et al. 2017).

2.6. Subduction interface roughness and megathrust seismicity

As introduced in paragraph 2.2.3, the roughness of the subduction interface is thought to play a role in the distribution of high- and low strength regions along the interface (i.e., the asperity model; Lay & Kanamori 1981), and therefore affect a megathrusts potential to host large- to mega-earthquakes. This subduction interface roughness does not only result from the roughness of the seafloor that enters a subduction zone, but also depends on the amounts of sediments that enter the subduction zone, and processes that may alter the roughness during subduction (e.g., tectonic erosion). A first relationship between bathymetric features on the seafloor and megathrust seismicity was proposed by Kelleher & McCann (1976). They observed that shallow earthquakes were generally smaller and less frequent at locations where bathymetric rises entered the subduction zone, which they related to the larger buoyancy of these areas that modifies the subduction process.

Since then, the topic of seafloor roughness and megathrust earthquakes has been addressed by many studies. Improved methods for slip inversions (e.g., Mai & Thingbaijam 2014; Ye et al. 2016; Hayes 2017), the increased coverage and precision of GPS stations (e.g., Métois et al. 2012), technological advances in marine geophysics (Das & Watts 2009; Kopp 2013), but also the occurrence of relatively many $M_w > 8.5$ events over the past decades (e.g., Stein & Okal 2007; Stein & Okal 2011; Lay 2015) all contributed to a better understanding of this relationship. Most studies that address the role of seafloor roughness on rupture dynamics focus on the role of a single topographic feature, sometimes even considering a single seismic event. They often show how a subducting seamount, fracture zone, or submarine ridge locally influences the seismogenic behavior, or the coupling between the subducting and overriding plate. It is difficult to extrapolate results of these studies to a general model that explains what happens when rough seafloor subducts. More global studies, that consider the role of rough seafloor in general, and in various subduction settings, provide additional insights in a first-order relationship between seafloor roughness and seismicity in subduction zones. Below, the most important studies will be discussed, first providing an overview of studies that focus on the role of specific topographic features (e.g., seamounts, fracture zones, ridges; section 2.6.1. to 2.6.3), after

which several global, more general approaches will be discussed (section 2.6.4). Finally, an overview for three well-studied regions will be given, showing the complexity of the problem, but also the large trench-parallel variability in seismogenic behavior within a single subduction zone (section 2.6.5.).

2.6.1. Seamounts

Seamounts are among the most abundant features on the bottoms of the Earth's oceans (Kim & Wessel 2011) and are therefore often studied in relation to subduction interplate seismicity. Seamounts are active or extinct isolated underwater volcanoes with variable heights (small: $h < 1\text{ km}$; intermediate: $1\text{ km} \leq h < 3\text{ km}$; large: $h \geq 3\text{ km}$) that can be easily distinguished within the seafloor topography.

The first link between seamounts and megathrust earthquakes was made by Cloos (1992), who noted that the relative abundance of subducting seamounts is proportional to the relative numbers of earthquakes with different magnitudes. He therefore proposed that seamounts act as asperities, being jammed against the overriding plate, and subsequently trigger earthquakes when they are sheared off their base. The theory of seamounts acting as asperities is proposed as well by Scholz

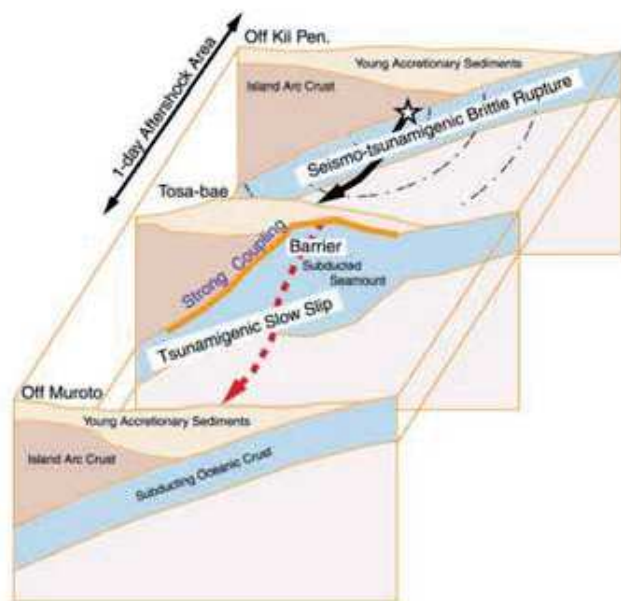


Figure 2.7. Schematic diagram of the proposed rupture process of the 1946 Nankaido earthquake. Figure taken from Kodaira et al., 2000.

& Small (1997), who suggested that an increase of normal stress related to seamount subduction will locally increase the seismic coupling along the interface.

There are several natural examples of seamounts acting as asperities along the subduction interface (von Huene et al. 2000; Abercrombie et al. 2001; Husen et al. 2002; Bilek et al. 2003; Das & Watts 2009; Bell et al. 2014). Von Huene et al. (2000) proposed that seamounts associated with the Fisher Seamount Chain offshore Costa Rica enter the subduction zone, where they act as asperities for moderate to large ($M_s = 6.4 - 7.0$) earthquakes. Both Kodaira et al. (2000) and Husen et al. (2002) have identified a subducting seamount along the subduction interface (off Nankai and Costa Rica, respectively) and associate it with strong seismic coupling. Husen et al. (2002) argued that as a result of this local increase in coupling, the seamount will act as an asperity, while Kodaira et al. (2000) argued the opposite: the seamount acting as a barrier (Figure 2.7). Also a subducting seamount in the Java subduction zone leads to various theories (Abercrombie et al. 2001; Bilek & Engdahl 2007; Shulgin et al. 2011). Masson et al. (1990) described the presence of several subducting seamounts near two previous earthquakes and proposed a link between the seamounts and the rupture characteristics of these two events. Abercrombie et al. (2001) performed a slip inversion for a later M_w 7.8 (1994) and found a region of high slip on one of the previously identified subducting seamounts. They interpreted this area as a locked patch (i.e., an asperity) in an otherwise decoupled subduction zone. This is supported by Bilek & Engdahl (2007), but contradicted by Shulgin et al. (2011), who imaged the crustal structure offshore Eastern Java and did not recover any direct evidence for the presence of bathymetric features within the subduction zone. In the Hikurangi margin, a subducting seamount has been associated with the 1947 tsunami earthquakes that occurred along the east-coast of the North Island, New Zealand (Bell et al. 2014). It is proposed that subducted seamounts could play a role in the nucleation of complex low-velocity ruptures (up to $M_w \sim 7$) that enhance tsunami waves and therefore cause larger seismic hazards.

In contrast to the abovementioned examples, seamounts are also believed to have acted as a barrier to rupture propagation (Kodaira et al.

2000; Mochizuki et al. 2008; Geersen et al. 2015; Marcaillou et al. 2016). While Kodaira et al. (2000) proposed a barrier-effect due to a local increase in coupling where a seamount subducts, other studies argue that a decrease in coupling associated with seamount subduction forms a local barrier. Based on earthquake activity over an 80-yr period around a well imaged subducting seamount in the southern part of the Japan Trench, Mochizuki et al. (2008) concluded that the seamount was behaving mainly aseismically, probably caused by fluid-rich sediments that are entrained with the seamount. Earthquakes might therefore be stopped on top of the seamount or in its wake, while stress concentrations in front of the seamount might initiate large ruptures. Also Geersen et al. (2015) suggest low coupling in regions where seamounts subduct, therefore limiting rupture propagation. They used swath bathymetry and seismic reflection to study the seafloor and overriding plate in Northern Chili and observed underthrusting seamounts along the plate interface. Several of these seamounts correlate with the southward and up-dip arrest of the 2014 Iquique earthquake and are located within low coupled regions.

Wang & Bilek (2011) aimed to answer the question of seamounts acting as asperities or barriers and presented a conceptual model for seamount subduction. Based on sandbox experiments by Dominguez et al. (1998a; 2000), who demonstrated the development of a fracture network during seamount subduction, Wang and Bilek proposed that seamounts subduct mainly aseismically. The complex structure and heterogeneous stresses of the fracture network promote small earthquakes and aseismic creep, but provide unfavourable conditions for the generation and propagation of large ruptures. Several numerical modelling studies regarding seamount subduction confirmed these findings (Yang et al. 2013; Ruh et al. 2016).

2.6.2. Fracture zones

Besides the effects of subducting seamounts on a megathrusts seismogenic behavior, other topographic features have been linked to megathrust seismicity as well. Robinson et al. (2006) analyzed the rupture evolution of the 2001 M_w 8.4 Peru earthquake, showing the rupture slowing down when

it reached a fault patch that acted as a barrier. This barrier was interpreted to be a fracture zone, possibly a northeastern extension of the Nazca Fracture Zone. Also Carena (2011) investigated the role of oceanic fracture zones along the South American trench, in this case focusing on the initiation and extent of several great and giant earthquakes. Here, fracture zones are portrayed as steep steps on the seafloor that will cause stress concentrations and therefore increased mechanical coupling. It is suggested that this higher coupling results in longer recurrence times and larger slip compared to the adjacent flats that have lower mechanical coupling. The effect of fracture zones intersecting with the subduction interface was investigated also globally (Müller & Landgrebe 2012). It was shown that fracture zone – subduction zone intersection regions are linked

with epicenters of 13 of the 15 largest ($M_w \geq 8.6$) earthquakes, suggesting some sort of relationship.

2.6.3. Submarine ridges

In addition to fracture zones, also submarine ridges have been associated with megathrust events. Christensen & Lay (1988) focus on the Louisville Ridge in the Tonga Subduction zone and suggest that strong interplate coupling north of the intersection between the Tonga-trench and the Louisville Ridges resulted in the 1982 M_w 7.5 thrust event. Spence et al. (1999) investigated the rupture evolution of the 1996 M_w 7.7 Peru earthquake, which occurred within the southern half of the subducting Nazca ridge, with aftershocks clustered within the northern half of the Nazca ridge, showing that the ridge does not subduct aseismically. In contrast, a subducting ridge in the Solomon subduction zone caused a minimum in slip during the 2007 M_w 8.1 Solomon earthquake, while large slip occurred on both sides of the ridge (Chen et al. 2009; Furlong et al. 2009). Contreras-Reyes & Carrizo (2011) discuss several subducting topographic highs along the South-American margin and show that the Northern Chile seismic gap roughly coincides with the subduction of the Iquique Ridge (Figure 2.8). The 1995 Antofagasta event occurred to the south of this ridge, and is bounded by the Tal-Tal Ridge in the south. On the other hand, the 2007 Tocopilla earthquake correlates spatially with the southern part of the Iquique Ridge, making the relation between the ridge and its seismogenic behavior rather complex. The Chile Rise in the southernmost part of the South-American margin is thought to have acted as a barrier to the 1960 M_w 9.6 earthquake, which ruptured over a distance of 1,000 km, passing several subducting fracture zones, and ending near the Chile Rise. Also Sparkes et al. (2010) focused the South-America-Nazca plate margin, investigating rupture limits of thirteen historic great earthquakes. They showed a strong correlation with subducted topography with relief > 1,000m, such as the Juan Fernandez Ridge.

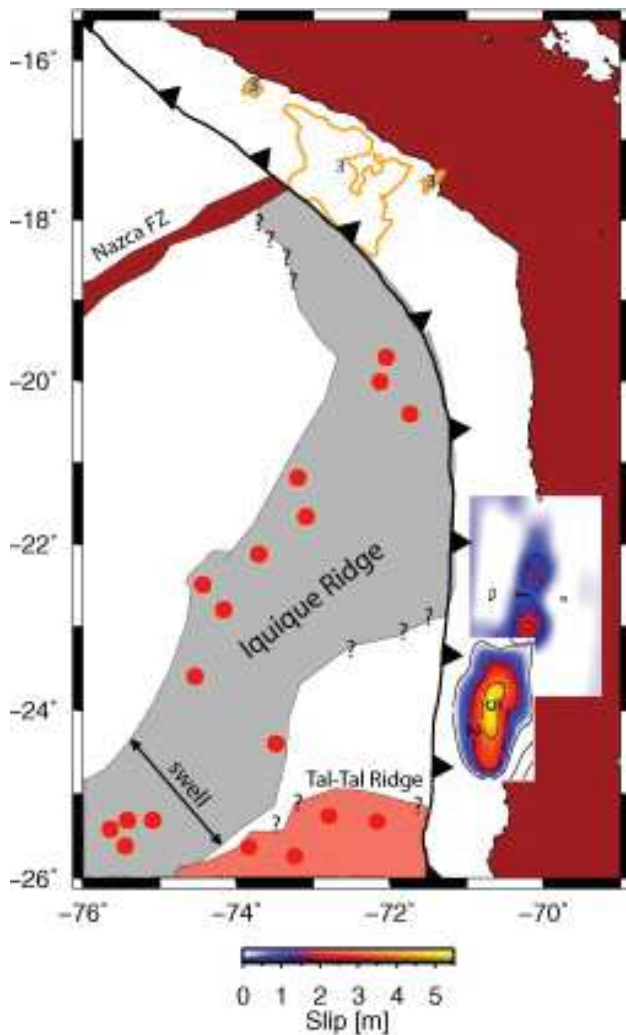


Figure 2.8. Fault slip models for the 1995 Antofagasta and 2007 Tocopilla earthquakes, with respect to the Iquique- and Tal-Tal Ridges. Red dots indicate large seamounts. Figure taken from Contreras-Reyes & Carrizo (2011).

2.6.4. Global studies

The abovementioned examples show many different roles of subducting features on rupture dynamics, not leading to a general consensus. To better constrain a first-order relationship between seismogenic behavior and subduction interface roughness, global

studies can be useful. With this in mind, Morgan et al. (2008) quantified the seafloor roughness and forearc basin size associated with 30 large earthquakes ($M_w \geq 7.7$) and studied the effect that the shape and size of bathymetric features have on earthquake magnitude. They used a semivariogram analysis, which is a way to describe the spatial correlation of the bathymetry by measuring how depth varies as a function of the spatial distance between depth data points. The results of their study show that the size of subduction zone earthquakes relates to the degree of roughness on the incoming plate, but to a lesser extent to the forearc roughness. When plotting the roughness of the incoming plate versus moment magnitude for the 30 studied events, a decline in magnitude can be observed. Morgan et al. (2008) also mentioned the role of subducting sediments, that may have a smoothing effect on the interface.

A more qualitative approach was chosen by Das & Watts (2009) who reviewed the rupture history of four great subduction earthquakes and their relationship with bathymetric features on the subduction plate. As already shown by the examples given in section 2.6.1., they observe that the effect of these bathymetric features on the rupture dynamics differs quite a bit for each event. When comparing the amount of slip within a rupture area with the location of subducting feature, they observed high slip at the (supposed) location of a seamount within the 1986 Andreanof rupture area, while a low slip regions was observed at the location of a geometrical barrier within the 2001 Peru rupture area. They argued that this is related to the stage of the seismic cycle an earthquake occurs in, since they believe eventually the entire plate boundary has to “catch-up” and therefore rupture at some point. Therefore, Das and Watts concluded that while subducting plate morphology and rupture dynamics may be linked, there is no universal relation between regions of high- and low slip and specific bathymetric highs and lows on the seafloor.

In a similar manner as Das and Watts (2009), a qualitative review was performed by Wang & Bilek (2014), but now more focused on the seismogenic behavior of (large) subduction zone segments, rather than single events. Wang and Bilek reviewed the seismicity and degree of creeping (based on geodetic observations) for subduction zones or segments

where extremely rugged seafloor is subducting. They concluded that creep is the predominant mechanism for the subduction of rough seafloor and that it is very unlikely that such regions will host great- to giant earthquakes. Also seamounts are thought to generally stop large ruptures from propagating, therefore acting as barriers, although they may be associated with small to medium sized earthquakes. Wang and Bilek (2014) elaborated on their previously proposed mechanism for seamount subduction (Wang & Bilek 2011), suggesting that very rugged subduction seafloor subducts in a ‘break-through’ manner, thereby severely fracturing and deforming the overriding plate and giving rise to heterogeneous stress distributions (Figure 2.9). They highlighted that the creep-like behavior resulting from this (sometimes accompanied by small to medium sized earthquakes), cannot be described as stable or unstable friction along a single contact interface.

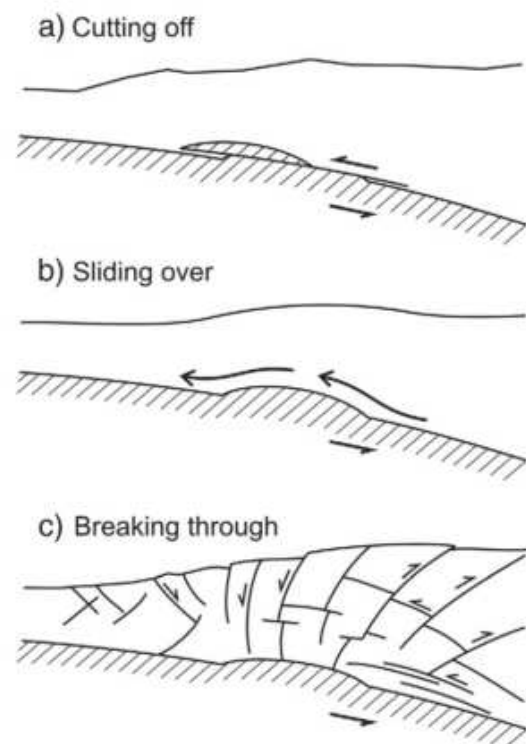


Figure 2.9. Proposed scenarios of seamount subduction by Wang and Bilek (2011; 2014). (a) “Cutting off”: The top part of or the seamount is sheared off. (b) “Sliding over”: The upper plate frictionally slides over the seamount without severe internal damage. (c) “Breaking through”: The seamount forces its way through by severely damaging its surrounding and itself. The final scenario is considered most realistic according to Wang and Bilek. Figure taken from Wang and Bilek (2014).

The most recent global study covering the topic of seafloor roughness and megathrust seismicity has been performed by Bassett & Watts (2015a), who computed residual bathymetric and gravimetric anomalies for all major subduction zones, after removal of the long wavelength topography and gravity field. This computation was done on both sides of the trench (600 km on each side), with the aim to place new constraints on where subducting topographic features might be present within seismogenic zones. Over 200 residual bathymetric anomalies have been identified within subduction fore arcs, like subducted seamounts (up to 17 km from the trench), fracture zones (up to 200 km from the trench) and submarine ridges (variable expressions due to trench-normal variations in rigidity and deformation of the overriding plate). Since the morphological expression and spatial distribution of subducting seamounts does not show indications for wholesale decapitation and accretion of the seamounts, the majority is likely to subduct intact. Bassett and Watts (2015) associated both subducting seamounts and ridges with reduced levels of megathrust seismicity and proposed that the ‘breaking through’ model (Wang & Bilek 2011; Wang & Bilek 2014) might also be applicable to subducting ridges. The flanks of such ridges usually have higher degrees of roughness, explaining the tendency for ruptures to terminate near these flanks.

2.6.5. Case studies

2.6.5.1. Nankai

The Philippine Sea Plate is a relatively small diamond-shaped plate that subducts below southwest Japan (i.e., the Nankai trench) and the Ryukyu trench along its northwestern side, and in the southwest below the Philippines. It is underthrust by the Pacific Plate in the East (forming the Izu-Bonin- and Mariana trenches) and by the Eurasian Plate along its central western margin (forming the Luzon trench). The Philippine Sea Plate contains quite a few topographic features, from which several are currently subducting into the Ryukyu-Nankai trench. The longest feature is the Kyushu-Palau ridge, an aseismic ridge of ~2600 km, trending N-S in the middle of the plate, but bending towards the northwest, where it runs sub-perpendicular with respect to the Nankai Trench. South of the Kyushu-Palau ridge lies the ADO region, consisting of the Amami Plateau, the Daito Ridge

and the Oki-Daito Ridge that are all thought to have originated in an Island Arc setting (Nishizawa et al. 2014). North of the Kyushu-Palau Ridge, in the Shikoku Basin, lie the Kinan Seamount chain, oriented perpendicular to the Nankai Trench and the old volcanic Zenisu ridge, orientated sub-parallel to the trench (Lallemant et al. 1989; Park et al. 2004).

In terms of seismicity, the Nankai Trench is probably one of the best-known subduction segments, since historical records of large earthquakes go back to 684 AD. In the 1400 years since then, nine cycles of earthquakes have occurred. The Nankai interplate section, which extends for 530 km from Shikoku Island in the West to the Tokai district in the East, is divided into fault segments A-D, from west to east (Ando 1975; Satake 2015; Figure 2.10). In every cycle, all segments are ruptured, either in a pair of earthquakes that occur within a relatively short time interval, or within one large rupture. The most recent cycle occurred in the 1940’s, with the 1944 Tonankai (M_w 8.1) event rupturing segment C (referred to as the Tonankai segment) in the east and the 1946 Nankaido (M_w 8.3) event rupturing the segments A

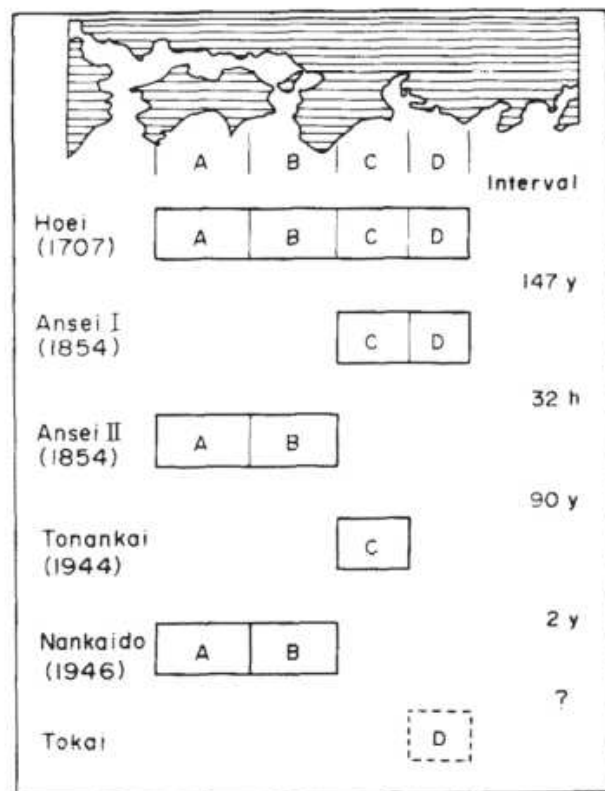


Figure 2.10. Schematic representation of earthquake cycles along the Nankai trench. Figure taken from Ando, 1975.

and B in the west. Since the most eastern segment D (referred to as the Tokai segment) has not ruptured during these two events, it is thought to be the next fault segment that will rupture (Ando 1975). The cycles before the 1944 and 1946 events include the Ansei I and II events in 1854, which ruptured segments C and D (Ansei I, MW 8.4) and A and B (Ansei II, MW 8.4), and the 1707 Hiei event (estimated magnitude 8.6) that ruptured all segments at once and used to be the largest known earthquake in Japan, before the occurrence of the 2011 Tohoku event along the Japan Trench (Figure 2.10).

The two most recent events have been investigated with respect to the roughness along the interface (e.g., Kodaira et al. 2000; Park et al. 2004; Yamamoto et al. 2013; Yokota et al. 2016). Due to conflicting results concerning the 1946 Nankaido rupture area (i.e., the rupture area based on geodetic data is much larger than the one based on seismic data), Kodaira et al. (2000) used ocean-bottom seismographs in this region to better understand the rupture processes.

This revealed the presence of a large-scale subducted seamounts of 50-km wide and 13 km thick, most likely part of the seaward Kinan Seamount Chain (Yamazaki & Okamura 1989; Kobayashi et al. 1995). The presence of this seamount in the rupture area is used to explain the previously proposed two-phase rupture of the 1946 Nankaido event: brittle rupture in the eastern part and slow slip in the west (Kato et al., 1997; Cummins et al., 1999). Kodaira et al. (2000) proposed an increase in coupling where the seamount subducts, causing a barrier-type effect of the seamount. Seismo-tsunamigenic brittle rupture in the East is stopped by the seamount, resulting in only tsunamigenic slow slip that propagated towards the west.

Further towards the east, Park et al. (2004) used seismic reflection and refraction data to confirm the presence of a previously proposed subducted ridge parallel to the Zenisu ridge seaward of the trench (Lallemand et al. 1992a; Okino & Kato 1995; Le Pichon et al. 1996). Their data indeed revealed the presence

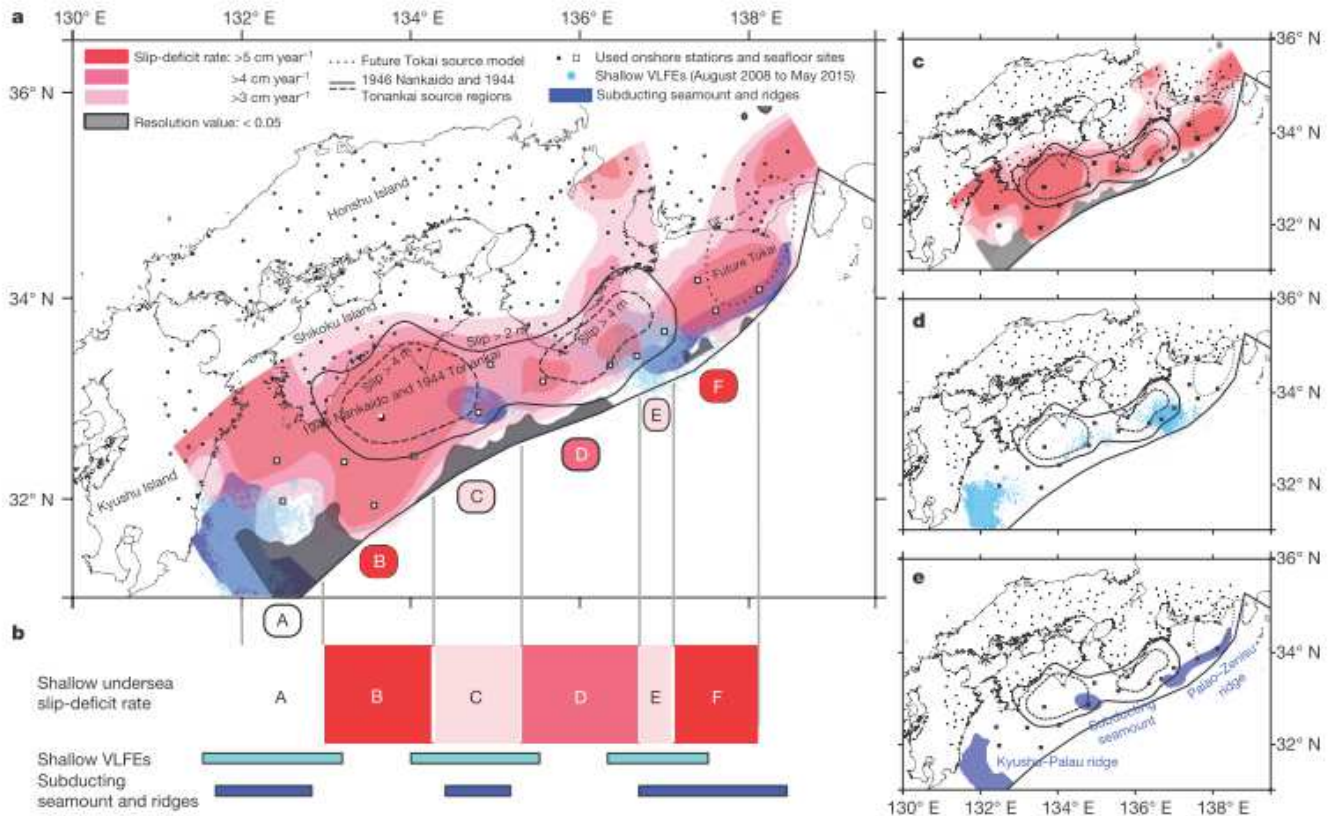


Figure 2.11. Spatial slip deficit rate (SDR) distribution by Yokota et al. (2016). a) SDR distribution, overprinted by locations of subducting features (shaded dark blue) and VLFE's (light blue dots). b) Schematic representation of along-trench variations in seismogenic behavior. c-e) Individual plots of SDR, VLFE's and subducting seamounts and ridges. Figure taken from Yokota et al. (2016).

of the subducted Paleo-Zenisu ridge, spanning the outer-ridge region of the Tonankai segment (C), as well as the inner slope region in the Tokai segment (D). The ridge is roughly 200 km-long, 20-30 km-wide and has a maximum height of 2.5 km, all very similar to the Zenisu ridge located seaward of the trench. The Paleo-Zenisu ridge is located along the seaward edge of the 1944 coseismic rupture area, which led Park et al. (2004) to suggest a barrier-type role of the ridge, preventing the 1944 rupture to propagate further towards the trench.

A third feature that has been imaged along the Nankai subduction interface, is the continuation of the Kyushu-Palau Ridge further to the west. Yamamoto et al. (2013) used 3D seismic tomography data to identify the precise location of the subducted Kyushu-Palau Ridge, by focusing on the difference in crustal thickness between the ridge and the surrounding normal oceanic plate. Since the location of past large earthquakes (e.g., the 1707 Hōei, the 1946 Nankaido and the 1968 Hyuganada events) does not extend into the region where the Kyushu-Palau Ridge is subducting, Yamamoto et al. suggested that it acts as a barrier to rupture propagation. The presence of continuous very low frequency earthquakes (VLFE's) activity above the ridge strengthens this theory.

To better understand the role that the above-mentioned subducting features play in the Nankai subduction zones, Yokota et al. (2016) analysed the Nankai subduction segment in terms of slip deficit rates. They aimed to obtain total seafloor geodetic information, by means of a broad-scale seafloor observations network that uses both GPS and acoustic ranging (GPS-A) techniques. They compare the spatial distribution of slip deficit rates (i.e. the degree of coupling) with the location of subducting geological features, such as the Kyushu-Palau Ridge, the Kinan Seamount and the Paleo-Zenisu ridge (Figure 2.11). Their results show that regions where these features subduct have low slip deficit rates, but also coincide with the occurrence of shallow VLFE's. Yokota et al. (2016) suggest that the subduction of the features generates the VLFE's, which in turn causes the lower slip deficit rates (i.e., a lower coupling between the plates). In the Nankai region, the subducting features therefore seem to act as a barrier to earthquake propagation, which is in line with the break-through model of Wang and Bilek (2011,2014).

2.6.5.2. Ecuador

Along the Ecuadorian segment of the North-Andes subduction zone, the Neogene Nazca plate underthrusts the northeastward-escaping North Andean Sliver (Pennington 1981; Yepes et al. 2016) with a velocity of 4.7 cm/yr (Nocquet et al. 2014). The most prominent feature entering the subduction zone is the Carnegie ridge in the central part, a hotspot trace up to 2-km-high and formed by the eastward motion of the Nazca Plate (Sallarès et al. 2005). Towards the north, the Malpelo Ridge (most likely a fragment of the Cocos Ridge further north; (Lonsdale & Klitgord 1978; Gardner 1992), the extinct Malpelo Rift and the associated Yaquina Through can be clearly seen in the morphology of the seafloor (Gutscher et al. 1999). A smaller feature on the seafloor is the Atacames seamount chain, which lies immediately north of the Carnegie Ridge. It contains four 1 to 1.5-km-high seamounts, from which the southernmost one is located at the trench (Collot et al. 2005).

Several large ($M_w \geq 7.5$) earthquakes have occurred along the Ecuadorian margin, of which the largest took place in 1906 (M_w 8.8). It had a rupture length of approximately 500 km, running from north Ecuador to southern Bolivia. It's rupture area was partially reactivated during four successive events from south to north, in 1942 (M_w 7.8), 1958 (M_w 7.7) and 1979 (M_w 8.2; Beck & Ruff 1984; Swenson & Beck 1996). In 2016, a M_w 7.8 event took place, which has been investigated in detail by Nocquet et al. (2016). By combining historical seismological data, present-day geodesy data and dense local observations of the 2016 event, they were able to reconstruct the strain budget since the great 1906 earthquake. They observed that the 2016 event ruptured two patches along the interface that were locked prior to the earthquake, most probably overlapping the 1942 rupture area. The accumulated slip deficit since 1942 however, is smaller than the coseismic slip during the 2016 earthquake, which led Nocquet et al. (2016) to consider the existence of supercycles along the Ecuadorian margin. From historical records, it is known that there were no large earthquakes in the centuries before the great earthquake in 1906, suggesting a mode of temporally clustered earthquakes, separated by periods of seismic quiescence.

How this seismic activity relates to the roughness at the plate interface is only studied in a few places, where the subduction interface has been imaged with seismic reflection data, swath bathymetry and/or 2-D wide-angle seismic data (Marcaillou et al. 2016; Collot et al. 2017). A double-peaked seamount along the North Ecuadorian subduction interface, probably belonging to the Atacames seamount chain, was imaged by Marcaillou et al. (2016). They observed an uplifted and highly fractured margin segment in this region, associated with seismic quiescence and GPS modeled low interseismic coupling (Figure 2.12; in agreement with the model proposed by Wang and Bilek, 2014). This region of low seismic coupling terminates downdip the seamount, near the 1942 M_w 7.8 earthquake rupture area. Marcaillou et al. (2016) therefore suggested that the Atacames seamount triggered the 1942 earthquake ahead of its leading flank, as proposed by Mochizuki (2008) as well.

Collot et al. (2017) imaged a region below La Plata Island (coinciding with the southern half of the subducting Carnegie ridge) that had been identified as a 80 km x 55 km locked asperity (Vallée et al. 2013; Chlieh et al. 2014; Nocquet et al. 2014) to learn more about the structural nature of this locked region. They identified a broad 55 km x 50 km, 1.5-2-km-high, low height-to-width ratio, multi-peaked, sediment-bare, shallow subducted oceanic relief, that is most likely responsible for the locally high coupling that has been observed. This observation is the contrary of what has been observed by Marcaillou et al. (2016): low coupling where the Atacames seamount subducts. The findings of Collot et al. (2017) support the model proposed by Scholz and Small (1997), who stated that seamounts locally increase interplate coupling (section 2.6.1.). However, even though these observations would suggest the occurrence of a $M_w > 7$ event, there is no record of large earthquakes in this area for several centuries. Also, regular seismic swarms have occurred in this area during the last 40 years, and since 2010, frequent slow slip events have been recorded. This suggests that the rough subducting seafloor might actually cause heterogeneous interplate friction (following the model of Wang and Bilek, 2014) within the locked patch. To explain the difference in interseismic coupling with subducting oceanic relief along the Ecuadorian subduction segment (i.e., high coupling at the oceanic relief below La Plata Island

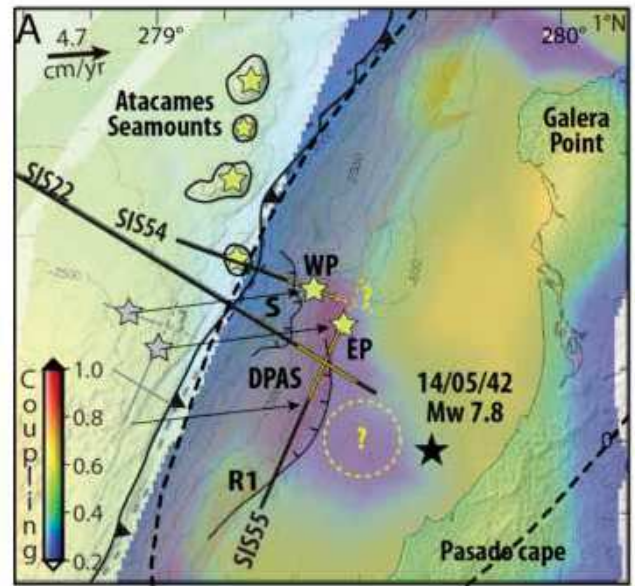


Figure 2.12. Interseismic coupling along the subduction interface (from Chlieh et al., 2014). Yellow stars indicate the western and eastern peaks, WP and EP, of the subducted Atacames seamount. The flanks of the seamount are indicated by the plain yellow lines. The 1942 earthquake epicenter and rupture zone are indicated by the black star and dashed ellipse, respectively. Figure is modified from Marcaillou et al., 2016.

vs. low coupling where the Atacames seamount subducts), Collot et al. (2017) referred to the height-to-width ratio of the oceanic relief in relation to the subduction channel thickness. When there is no detectable subduction channel, a subducted relief that is broad, highly jagged, and with a low height-to-width ratio, could favor interplate coupling at the seamount scale. Regions with larger height-to-width ratios (such as the subducting Atacames seamount) might have a more bulldozing effect, fracturing and weakening the margin, and therefore promoting weaker interplate coupling.

2.6.5.3. Costa Rica

In central America, the Cocos plate subducts below the Caribbean plate with a velocity of ~ 83 mm/yr (DeMets et al. 2010). The Costa Rica segment of the Central America trench is particularly interesting, since the Nicoya and Osa peninsula's are located much closer to the trench compared to other coastlines in subduction zones, which places them right above the seismogenic zone (Kyriakopoulos & Newman 2016; Schwartz & DeShon 2007). Offshore Costa Rica, several features on the seafloor can be

easily recognized, such as the Fisher Seamount and the Quepos plateau in the central part of the trench, as well as the Cocos ridge further south. Also the roughness at the interface is known quite well from seismic reflection studies (e.g., Von Huene et al., 2000). This makes this location a very suitable area for trying to understand how the subducting seafloor roughness might play a role on the seismicity of the region.

Von Huene et al. (2000) divided the Costa Rican trench into several different segments, based on the morphological features on the seafloor: the Nicoya segment, located below the Nicoya peninsula, the Osa segment, located below the Osa peninsula, and the Quepos segment, which represent the region in between the Nicoya and Osa segments (Figure 2.13). The seafloor of the Nicoya segment is the smoothest of the three, being covered by a 500 m of sediments (von Huene et al. 1995). The adjacent Quepos segment is characterized by many small seamounts, which range in size from 1.5-2 km height and 10-20 km width (Ranero & von Huene 2000). Also the Quepos plateau and the Fisher seamount are located within this segment. The Osa segment is where the 200-300 km wide Cocos Ridge is entering the trench and is believed to be moderately smooth (Bilek et al. 2003).

By simply looking at the forearc topography for each of these segments, a relationship with the morphology of the subduction interface can already be observed. The forearc of the Quepos segment is characterized by a highly irregular topography, containing furrows and scarps that have been linked to tunneling of subducting seamounts (von Huene et al. 2000; Ranero & von Huene 2000), while the continental slope in front of the Osa segment shows very little topographic relief.

When comparing the seismic coupling and the occurrence of previous earthquakes along the Costa Rican trench, some clear differences can be observed as well. (Protti et al. 1995) showed that the largest megathrust events in this region ($M_w > 7.5$) have historically occurred along the Nicoya segment, where relative smooth seafloor enters the trench. In the Quepos segment, facing the central part of Costa Rica, events with maximum

magnitude of $M_w 7$ have occurred, and were linked to the subduction of small seamounts, which were thought to promote the occurrence of characteristic, relatively small earthquakes (Bilek et al. 2003). Where the thickened oceanic crust belonging to the Cocos Ridge is subducting, intermediate-magnitude events occurred (M_s up to 7.4), sometimes showing a relatively complex rupture pattern (Bilek et al. 2003). Protti et al. (1995) suggested a strong coupling for the Nicoya segment, a low coupling for the Quepos segment, where the many small seamounts are thought to reduce the coupling, and intermediate coupling for the Osa segment.

On September 5th 2012, a $M_w 7.6$ interplate event occurred below the Nicoya peninsula. Since large earthquakes ($M_w > 7$) have occurred in this region approximately every 50 years (the latest being a $M_w 7.7$ in 1950), this event was anticipated (Protti et al. 2014). Due to the systematic occurrence of megathrust events in this area, many studies have aimed to determine the degree of locking of the interface by using global positioning system (GPS) data and microseismicity (Feng et al., 2012; Ghosh et al., 2008; Newman et al., 2002; Norabuena et al., 2004, Schwarz & DeShon 2007). They identified a locked region with an along-strike width of 60 km near the coastline of Central Nicoya. The 2012 event occurred in the heart of this locked patch, even though its magnitude ($M_w 7.6$) was slightly lower than anticipated (i.e. $M_w 7.7-7.8$; Protti et al. 2014). This could be related to a smaller MW 6.9 event that occurred in 1978 and accounts for 16% of the accumulate strain energy since the 1950 $M_w 7.7$ earthquake (Protti et al. 2014). Therefore, a locked area may remain offshore, having the potential for a future large aftershock.

Even though the subduction interface below the Nicoya segment has been thought to be smooth (e.g., von Huene et al., 2000), a recent study by Kyriakopoulos and Newman (2016) suggests the location of a topographic high that resists further subduction at the location of the previously locked patch and the occurrence of the 2012 Nicoya event. This finding raises new doubts on the question whether subducting topography will act as an asperity or a barrier to megathrust earthquakes.

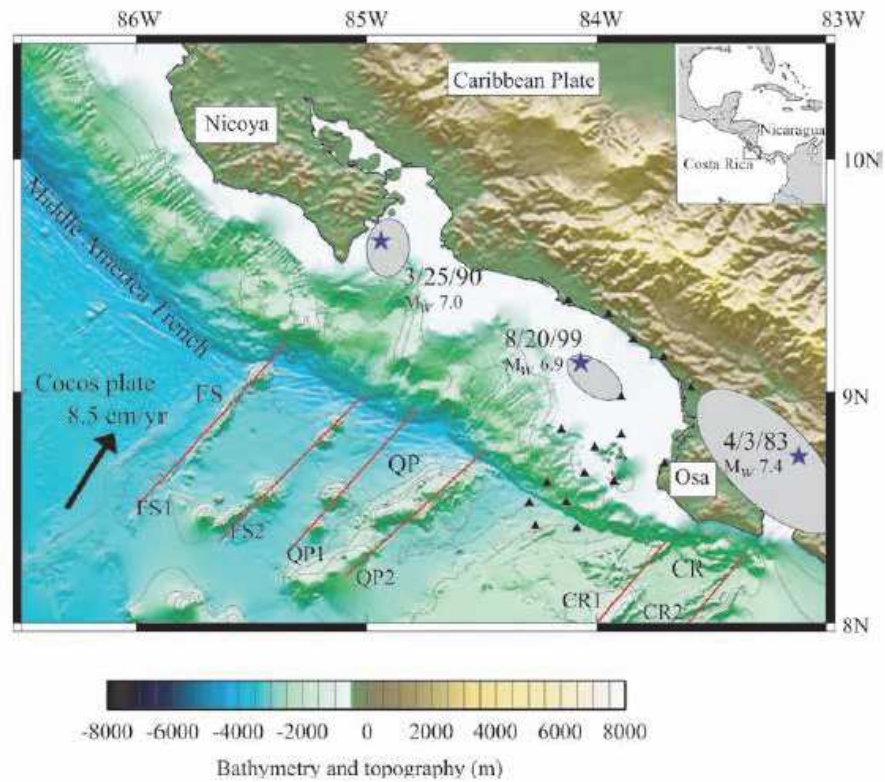


Figure 2.13. Map of the Cocos Plate subducting below Costa Rica. Bathymetry and topography are indicated by the colors, subducting features are indicated (FS = Fisher Seamount, QP = Quepos Plateau, CR = Cocos Ridge). Figure has been taken from Bilek et al. (2003).

3. Roughness Characteristics of Oceanic Seafloor Prior to Subduction in Relation to the Seismogenic Potential of Subduction Zones

Published as:

Lallemand, S., Peyret, M., van Rijnsingen, E., Arcay, D., & Heuret, A. (2018). Roughness characteristics of oceanic seafloor prior to subduction in relation to the seismogenic potential of subduction zones. *Geochemistry, Geophysics, Geosystems*, 19. <https://doi.org/10.1029/2018GC007434>

Abstract

We have developed a new approach to characterize the seafloor roughness seaward of the trenches, as a proxy for estimating the roughness of the subduction interface. We consider that abrupt elevation changes over given wavelengths play a larger role in the seismogenic behavior of the subduction interface than the amplitude of bathymetric variations alone. The new database, SubRough, provides roughness parameters at selected spatial wavelengths. Here, we mainly discuss the spatial distribution of short [12-20 km] and long wavelength [80-100 km] roughness, R_{SW} and R_{LW} respectively, along 250 km-wide strips of seafloor seaward of the trenches. Compared with global trend, seamounts show distinct roughness signature of much larger amplitudes at both wavelengths, whereas aseismic ridges only differ from the global trend at long wavelengths. Fracture zones cannot be distinguished from the global trend, which suggests that their potential effect on rupture dynamics is not the consequence of their roughness, at least not at these wavelengths. Based on R_{LW} amplitude, segments along subduction zones can be defined from rough to smooth. Subduction zones like the Solomons or the Ryukyus appear dominantly rough, whereas others like the Andes or Cascadia are dominantly smooth. The relative contribution of smooth versus rough areas in terms of respective lateral extents probably plays a role in multi-patch rupture, and thus in the final earthquake magnitude. We observe a clear correlation between high seismic coupling and relatively low roughness and conversely between low seismic coupling and relatively high seafloor roughness.

3.1. Introduction

Many studies have emphasized the role of subducting topography in the initiation, propagation and termination of ruptures of large to mega-earthquakes. As early as in the late eighties, Ruff (1989), based on a limited database, suggested that smooth seafloor associated with excess trench sediment favored large ruptures. Soon after, Cloos (1992) proposed that subducting seamounts were likely candidates for large earthquake triggers. Based on additional marine observations and physical modeling, alternative processes have been proposed involving multiple seismogenic behaviors depending on the type of subducting topographic features (Cloos 1992; Scholz & Small 1997; Gutscher et al. 1999; Dominguez et al. 2000; Kodaira et al. 2000; Abercrombie et al. 2001; Bilek et al. 2003; Robinson et al. 2006; Morgan et al. 2008; Mochizuki et al. 2008; Konca et al. 2008; Bilek et al. 2009; Das & Watts 2009; Sparkes et al. 2010; Wang & Bilek 2011; Carena 2011; Métois et al. 2012; Yang et al. 2012; Müller & Landgrebe 2012; Kopp 2013; Wang & Bilek 2014; Landgrebe & Müller 2015; Bassett & Watts 2015a&b; Geersen et al. 2015; Henstock et al. 2016; Marcaillou et al. 2016), the trench sediment thickness (Jarrard 1986; Ruff 1989; Heuret et al. 2012; Scholl et al. 2015), the state of stress within the upper plate (Jarrard 1986; Heuret et al. 2012; Schellart & Rawlinson 2013), the possible occurrence of tectonic erosion (Sage et al. 2006; Bilek 2010b; Scholl et al. 2015), the friction, normal stress and fluid pressure along the subduction interface (Ruff 1992; Scholz 1998; Ranero et al. 2008; Saffer & Tobin 2011; Chlieh et al. 2011; Corbi et al. 2011; Lin et al. 2013; Saillard et al. 2017) or the geometry or kinematics of the subduction zone (Jarrard 1986; Uyeda 1987; McCaffrey 2008; Gutscher & Westbrook 2009; Schellart & Rawlinson 2013; Bletery et al. 2016). Some of these studies argue that along-trench segments exhibiting low topographic roughness at long spatial wavelength should be prone to propagate ruptures over large distances, and consequently, be the location of very large earthquakes. On the other hand, subducting highs may – in some circumstances – act as strong patches where stress builds up and suddenly releases or – in other circumstances – act as a barrier to rupture propagation.

Global seafloor roughness characterization intending to compare the data with subduction zone seismicity has already been performed using two different techniques or approaches. Morgan et al. (2008)

have used semi-variograms built in the spatial domain along 10 subduction segments (on both sides of the trench) which they later compare with 30 $M_w \geq 7.7$ earthquake events. They concluded that the geomorphology of the subducting seafloor and forearc constrain the earthquake size. Bassett and Watts (2015a&b) have computed and analyzed the residual bathymetric and gravimetric anomalies after removal of the long-wavelength topography and gravity field from subduction zones. In the same manner as Morgan et al., they examined both sides of the trench but at larger distances (600 km on each side instead of ~ 100 km for Morgan et al.). They observe that subducted features have contrasting expressions in the arc and forearc. Subducting seamounts for example have similar morphological expressions as unsubducted ones, but only at slab depths less than 17 km. Subducting aseismic ridges can be traced in the forearc with a gradual reduction in morphologic expression. In some cases, the authors are able to correlate their signal with the down-dip limit of co-seismic slip and strong interplate coupling. Pre-existing crustal structures over the margin like faults or lateral variations in rigidity significantly influence the seismogenic behavior (Bassett et al. 2016) and superimpose on the subducting seafloor contribution.

However, a homogeneous and worldwide estimate of the oceanic plate roughness prior to subduction is still missing. In this study, we have developed a new database, called SubRough, based on a spatial frequency analysis, which aims at providing a simple and synthetic quantification of the seafloor roughness, which is supposed to play a role in the seismogenic behavior of the subduction interface. Our approach is designed to study the seismogenic effect of subducted reliefs, that may have a dual influence on seismicity, as a function of their characteristic spatial scale. Because there are very few places in the world where we have access to a detailed mapping of the subduction interface, we have decided to use the bathymetry seaward of the trench as a proxy of the currently subducting topography along the seismogenic plate interface. Such an approach has been successfully applied to specific ruptures by (Das & Watts 2009), which appear to be controlled by the subducting seafloor topography.

We will first explain the novelty of the methodology used for roughness characterization. Then, we

will present the SubRough dataset and interpret the roughness signal with regard to the expected seismogenic character, focusing on specific features like seamounts, ridges or fracture zones. We will evaluate to which extent the seafloor roughness controls the state of stress in subduction zones. We will finally discuss the limits and potentials of our approach, and propose some extensions of

this work which we believe are worth exploring. A detailed correlation of seafloor roughness with the seismogenic behavior along subduction zones is studied in a companion paper by van Rijsingen et al. (2018).

3.2. Methodology used for roughness calculation

We have applied the following criteria while constructing the SubRough database:

1. Quantifying discrete seafloor roughness for all oceanic subduction zones;
2. Defining homogeneity, in both spatial coverage and resolution, in the processed elevation dataset, even if higher bathymetric resolution is available for some regions;
3. Ascribing a limited number of roughness parameters corresponding to different relevant spatial scales for the purpose of studying large earthquake rupture dynamics;

3.2.1. Data sources

Even if high-resolution bathymetric data are available for some specific areas, we used the General Bathymetric Charts of the Oceans (GEBCO) database, released in 2014 (Smith & Sandwell 1997; Sandwell et al. 2002; Becker et al. 2009; Weatherall et al. 2015) to match the constraint of working at a global scale. This database is gridded at 30" arc (~1 km) interval. It is a combination of high-resolution (km-scale) measurements obtained by echo-sounding from ship survey and lower resolution (typically > 10 km) measurements from satellite gravity anomalies. Its vertical accuracy is on the order of a few hundred meters while its global resolution is estimated to 12.5 km (Smith & Sandwell 1997). Our estimate of the vertical error between high and low resolution data is ~ 100 m, based on statistics performed on residual bathymetry when subtracting swath-mapping data acquired onboard R/V L'Atalante in 1996 and in 2017 from GEBCO database (standard deviation is 117 m for ACT data east of Taiwan and 55 m for GARANTI data west of Guadeloupe). Since the database contains about 10% of high-resolution data over our

zones of interest, we have decided not to take them into account and only provide roughness estimates at wavelengths longer than 12 km for homogeneity over all subduction zones.

3.2.2. Roughness definition

The roughness of a surface can be defined as the deviation of its elevation around a mean value. Keeping in mind both the global data resolution and the final objective of providing a limited number of roughness parameters characterizing the ability of the subduction interface to produce large earthquakes, we have elaborated the following technique.

3.2.2.1. Roughness in the spatial domain

In this study, we consider that abrupt elevation changes over short and longer distances likely play a larger role in seismicity initiation, propagation and arrest, than the elevation values (bathymetry) themselves. One may hypothesize that, if the energy released is sufficient, a rupture can propagate, whatever the mean elevation is, as long as no topographic gradient threshold is met. We thus focus on the roughness of the topography R_{Ω} in meters, which is defined as the deviation (rms) of its elevation z around its mean value \bar{z} within a given spatial domain Ω (equation (3.1), see Text A3.1 in the appendix for more details).

$$R_{\Omega} = \left(\int_{\Omega} (z - \bar{z})^2 d\Omega \right)^{1/2} \quad (3.1)$$

A classical way to estimate this disparity is to perform

an autocorrelation of z in the spatial domain. For efficiency, we move the autocorrelation function of the elevation into the frequency domain via Fourier transform, leading to the power spectral density (PSD).

3.2.2.2. Roughness in the frequency domain

Given that the total energy of one signal is the same in both the spatial and frequency domain, one can define the roughness in the frequency domain R_f using equation (3.2), where f_x and f_y are the frequencies in the x and y directions (see Text A3.1 in the appendix for more details).

$$R_f = \left[\iint_0^{+\infty} PSD(f_x, f_y) df_x df_y \right]^{1/2} \quad (3.2)$$

3.2.2.3. Roughness in a radial bandwidth

Some authors like Dunham et al. (2011) also define a “bandwidth roughness”, which only takes into account the contribution of one specific frequency band (or wavelength band) to the complete deviation of the signal around its zero mean value, either considering specific directions or radial frequencies (see Text A3.1 in the appendix for more details). In this study, we will mainly use radial frequencies (Figure 3.1), by implicitly assuming that the bathymetry deviation is isotropic. The radial frequency bandwidth roughness $R_{\Delta f}$ can be written as:

$$R_{\Delta f} = \left[\int_{f_{min}}^{f_{max}} PSD(f) df \right]^{1/2} \quad (3.3)$$

3.2.2.4. Roughness parameter assuming fractal model

In order to regularize roughness values, we have the choice to fit discrete PSD measurements with different models. One of them takes into account the fractal structure of topography. It has been shown that global topography on Earth can be considered as a fractal object, i.e., the distribution of elevation is similar, regardless of the scale (Turcotte 1992; Renard et al. 2013). It means that the PSD of topography exhibits a power-law dependence on radial frequency (e.g., Fox & Hayes 1985; Voss 1988; Huang

& Turcotte 1989; Huang & Turcotte 1990; Turcotte 1997):

$$PSD(f) \propto |f|^{-(\beta+1)} \quad (3.4)$$

In a log-log plot, $(\beta+1)$ is the slope (in absolute value) of the theoretical dependence of PSD values on radial frequency (dotted line in Figure 3.1). This exponent can also be expressed in terms of other parameters that are commonly used in the literature, such as the fractal dimension (see Text A3.1 in the appendix for more details).

Using this fractal model, the roughness parameter defined by equation (3.3) for a given radial wavelength bandwidth $R_{\Delta\lambda/fractal}$ and for $\beta > 0$ becomes:

$$R_{\Delta\lambda/fractal} = \left[\frac{C}{\beta} \right]^{1/2} (\lambda_{max}^{\beta} - \lambda_{min}^{\beta})^{1/2} \quad (3.5)$$

where C is a constant and $\lambda = 1/f$ is the spatial wavelength. It can be visualized directly in a log-log representation where the PSD between two wavelengths is approximated by a regression line (bold green line in Figure 3.1).

3.2.2.5. Roughness assuming average model

Another, simpler model to fit the PSD is the average over a given frequency bandwidth. Using the fractal or average model for estimating the roughness generally leads to similar results. Indeed, the PSD exhibits a clear fractal structure almost everywhere. We find a mean slope value (over all the subduction segments) of 2.9, which is similar to what is generally found for topography (e.g., intermediate frequencies in Perron et al. 2008). Nevertheless, we often notice a slightly steeper bending of the PSD graph at high frequencies (typically $\lambda \leq 10$ km). This pattern has already been reported (e.g., Perron et al. 2008). By contrast, a slight reduction in spectral slopes at long wavelength is observed even if no prior detrending step is performed (see bold green line with respect to black dotted line in Figure 3.1). Moreover, we found a few areas characterized by large variance within particular frequency bands, thus revealing local topography patterns that do not fit with a regional fractal model. In the case of limited frequency bandwidth or limited number of discrete

measurements, it appears that the PSD function may be more reliably approximated by the mean value within the considered frequency band (blue lines in Figure 3.1). Although this approach seems, at least in principle, less integrative than the fractal approach, in practice, it appears to be steadier for narrow wavelength intervals, since the fractal hypothesis may not be valid everywhere.

Using the average model, the roughness parameter in equation (3.3) for a given radial wavelength bandwidth $R_{\Delta\lambda/mean}$ becomes:

$$R_{\Delta\lambda/mean} = [\overline{PSD}]^{1/2} \left(\frac{1}{\lambda_{min}} - \frac{1}{\lambda_{max}} \right)^{1/2} \quad (3.6)$$

where $[\overline{PSD}]$ is the mean value of PSD over the wavelength band $[\lambda_{min}, \lambda_{max}]$.

3.2.2.6. Roughness uncertainties or disparities

On top of the data resolution discussed above, there are several ways to compute the uncertainty of roughness estimators. The simplest one consists in using the standard deviation of the PSD values σ_{PSD} over some frequency bands when applying the average approach (see Text A3.1 in the appendix for details). The second one consists in estimating the standard deviations of the slope and intercept when using the fractal approach but is less easy to derive. We have thus implemented a third approach adapted to both average and fractal models, and which relies on the determination of the variance of roughness values over several spatial orientations. This technique is also a way to measure the robustness of the radial/isotropic approach as well

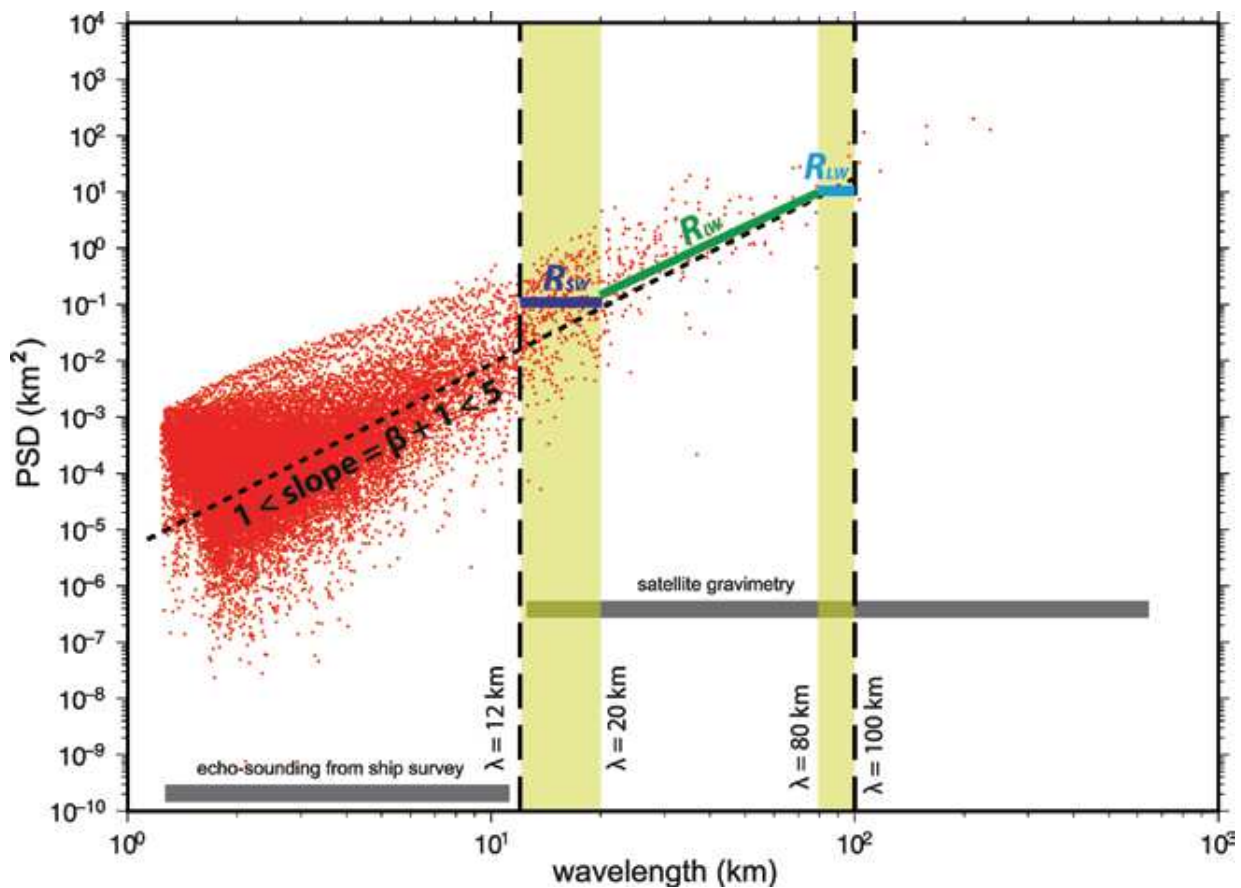


Figure 3.1. Example of a typical power spectral density graph. Each red point represents one PSD (f) value. The linear regression through this log-log graph represents the fractal model that best fits the PSD function. The fractal model can be estimated over different frequency bands (1–100 km for the dotted black line, 20–80 km for the green line). Mean PSD values over the wavelength bands (12–20 km) and (80–100 km) are shown in dark and light blue, respectively. Because echo sounding from ship survey are rather sparse in the General Bathymetric Charts of the Oceans database, a uniform analysis over all the subduction zones requires considering only wavelengths longer than 12 km (spatial resolution of the satellite gravimetry). PSD = power spectral density.

as to complement the roughness database with more detailed information related to orientation. We thus systematically performed the roughness calculation along 12 different orientations, with 15° wide opening each, to cover the $0\text{-}180^\circ$ azimuth range. The variance over the 12 orientations constitutes a good proxy for roughness disparity. Roughness estimates for specific orientations are briefly treated in the supplementary material (Figure A3.1). Throughout the rest of this paper, we will only consider radial bandwidth roughness estimators $R_{\Delta\lambda/mean}$ or $R_{\Delta\lambda/fractal}$.

3.2.3. Processing chain and choice of criteria used for seafloor roughness characterization

3.2.3.1. Area/Regions covered

Since the currently subducting topography is generally unknown, we assume that the bathymetry of oceanic plates, a few hundreds of kilometers seaward of the trench, is a reasonable proxy for modeling the roughness of the subduction interface. The roughness analysis has been performed over most oceanic subduction zones. We have not paid much attention to narrow subduction systems or those where continental crust is significantly involved. Based on the location of oceanic trenches from Heuret & Lallemand (2005), we have selected a 400 km-wide strip of seafloor bathymetry 10 km seaward the trench (Figure 3.2). In many locations, a thick pile of sediment fills the trench and smooths the seafloor before entering the subduction zone. Since we generally do not know how much of the trench fill is scraped off at the margin's front, we avoid being too close to the trench, where trench fill may alter the roughness estimate. Including this 10 km-wide seafloor strip into our calculations would contribute for only $1/40$, i.e., 2.5% of our results (4% if when focusing on a 250 km-wide strip). In the same way, we do not explore too far away from the trench where direct comparison with the current seismogenic zone behavior becomes very uncertain.

3.2.3.2. Calculation steps

3.2.3.2.1. Extraction of the relative bathymetry

The roughness mathematical definition requires

that the elevation distribution is a realization of a stationary random field (i.e., spatial stochastic process). We thus first model and remove the plate bending contribution from the bathymetric database. To do so, we average bathymetric profiles spaced by 10 km, perpendicular to the trench (Figure 3.3), over a sliding 500 km-long trench-parallel window. Beforehand, seamounts are masked using the database of Kim and Wessel (2011), even though their contribution vanishes in the averaging process. Additionally, we also manually mask the main ridges and continental platforms in order to preserve their large scale topographic signature from the averaging process. When the lateral extent of the subduction segment is smaller than 500 km, the averaging process is performed over the whole segment. This approach is similar to the one used by Bassett & Watts (2015a). Once this mean reference bathymetry is obtained (Figure 3.3c), it is subtracted from the real bathymetry, leading to what is called hereafter the relative bathymetry, whose statistical

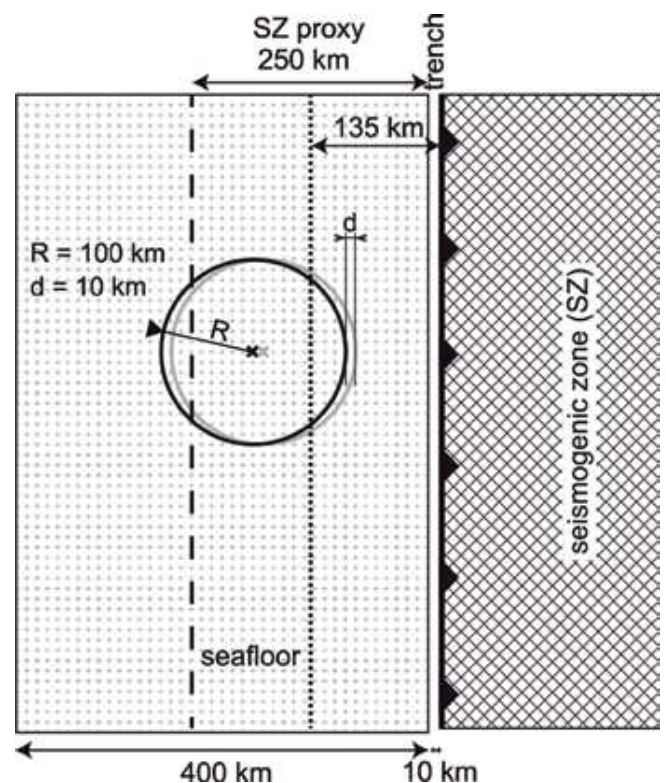


Figure 3.2. Schematic view of processing. The region of interest is a strip along the trench, 400 km wide, located 10 km seaward of the trench. The power spectral density (and roughness) calculation is performed on a circular window (100-km radius). This analysis is done over a uniform spatial grid with 10-km spacing as shown by the dots filling the study area.

mean in the study area is zero (Figure 3.3d).

3.2.3.2.2. PSD calculation

The relative bathymetry dataset is projected into a local Cartesian coordinates system, i.e., Conic Lambert projection whose origin and standard parallels are adapted to the studied subduction zone. The PSD mapping is performed over all subduction segments discretized by a 10 km square grid (Figure 3.2). We use a circular sliding window with a radius of 100 km compatible with the width of the strips and allowing for analyzing the seafloor roughness up to a maximum wavelength of 200 km. A local planar detrend is performed in order to remove the null frequency component of the relative bathymetry that, at this small spatial scale, would have not been eliminated in the reference bathymetry. The PSD is calculated on the full-resolution GEBCO dataset (30'' \approx 1 km) even though only wavelengths higher than 12 km are further retained in our roughness analysis as they correspond to the resolution of the bathymetry derived from satellite gravity anomalies (Figure. 3.1).

3.2.3.2.3. Selection of frequency bandwidths

The longest investigated wavelength is given by the diameter of the sliding window, i.e., 200 km. In practice, the longer the wavelength is, the fewer the samples are (Figure 3.1). Thus, considering only wavelengths typically longer than 100 km may lead to unstable results. Keeping in mind these limitations (better sampling between 12 and 100 km wavelengths within a larger dataset ranging from 1 to 200 km), the choice of wavelength band limits for roughness calculation is somewhat arbitrary. We aim at discriminating the contribution of various topographic features, whose typical elevation and spatial extent are different, to the global roughness of the subducting plate. When considering short wavelengths, we expect to be sensitive to elevation changes induced by the presence of fracture zones, or isolated small seamounts. When looking at the longest wavelengths available in our analysis, we are blind to such small topographic patterns, but sensitive to larger ones like ridges, large seamounts or aggregates of smaller objects like seamount chains for example. Finally, we suggest to use frequency bands that approximately fit the typical dimensions of these classes of topographic objects whose role in earthquake nucleation and rupture propagation/ending are expected to be very different. In addition, we have limited the number

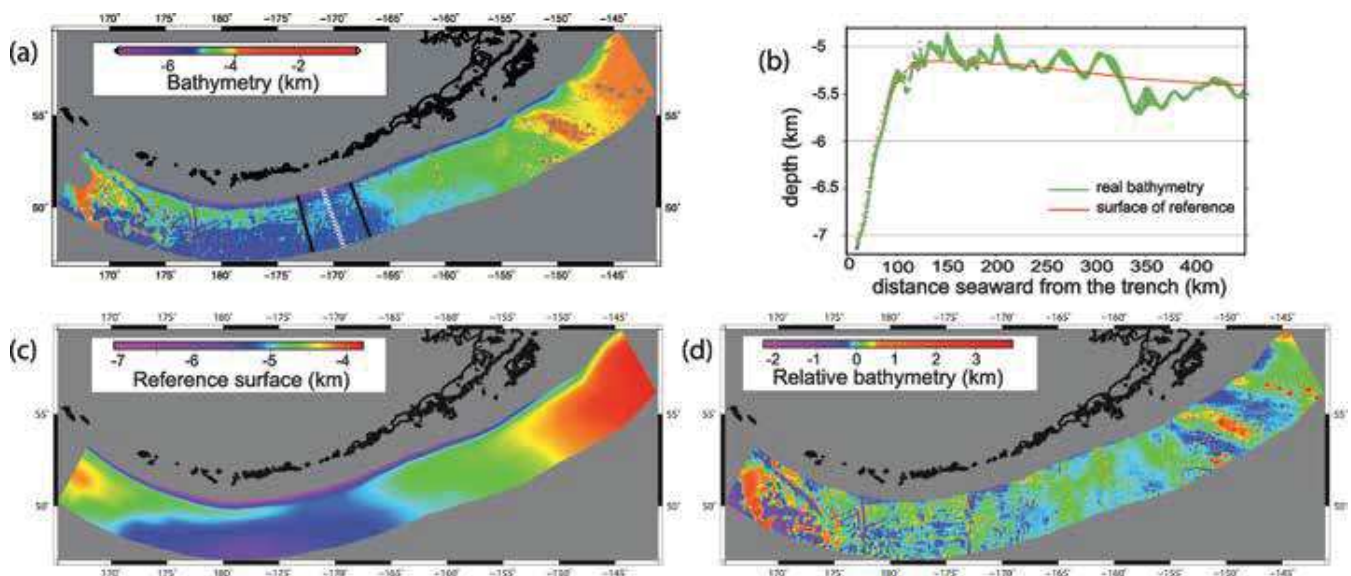


Figure 3.3. Example of plate bending removal along the Aleutians. (a) Real bathymetry from GEBCO_2014. For estimating the reference surface at white dotted profile, averaging is performed over all profiles perpendicular to the trench that lie between the two black profiles that are 500 km away from each other. Seamounts (in gray) are removed from the bathymetric data set before processing. (b) Elevation (in green) along the white dotted profile shown in (a) and mean elevation over neighboring profiles (in red). (c) Reference surface over the Aleutians. Note the fit to the curvature close to the trench. (d) Relative bathymetry defined as the real bathymetry minus the reference surface.

of roughness parameters for practical reasons. After comparing many frequency bandwidths, we finally chose to work at three significantly different scales: short wavelengths between 12 and 20 km, intermediate wavelengths between 20 and 80 km and long wavelengths between 80 and 100 km.

3.2.3.2.4. Selection of model used for calculation

Even though it is less integrative, we have mentioned above that the average model better fits the “real data”, especially when considering narrow frequency bandwidths. In this study, we show the roughness values for the narrow wavelength bands [12km, 20km] and [80km, 100km] obtained with the average model (Equation (3.6)), while the fractal model is used for estimating the roughness over the larger frequency band at intermediate wavelengths, i.e., between 20 and 80 km (Equation (3.5)).

Hereafter, we adopt the following notation:

$$\begin{aligned} R_{HF} &= R_{SW} = R_{\Delta\lambda/mean} && \text{in the range (12-20 km)} \\ R_{LF} &= R_{LW} = R_{\Delta\lambda/mean} && \text{in the range (80- 100 km)} \\ R_{IF} &= R_{IW} = R_{\Delta\lambda/fractal} && \text{in the range (20-80 km)} \end{aligned}$$

where R_{HF} , R_{LF} and R_{IF} refer to roughness estimates at high, low and intermediate frequencies, respectively, and R_{SW} , R_{LW} and R_{IW} refer to roughness estimates at short, long and intermediate wavelengths, respectively.

3.2.3.2.5. Uncertainties and validity of the proxy

Assuming that isotropic PSD are valid, the uncertainty on the roughness values can be estimated using the standard deviation of the PSD in the average model (Equation (A3.7) in Text A3.1 in the appendix). We typically get values of $\sigma_R \sim 100$ m in the 12-20 km wavelength bandwidth and ~ 200 m in the 80-100 km bandwidth. Ninety-five percent of these uncertainties remain below 250 m and 450 m for the 12-20 km and 80-100 km bandwidths, respectively. More relevant is the applicability of using the seafloor roughness seaward of the trench as a proxy of the subduction interface roughness landward of the trench. Ideally, one should compare the roughness seaward and landward of the trench in regions where the morphology of the seismogenic zone is well constrained. Unfortunately, such imagery down to a depth of typically 50 km is not available. We

thus statistically explored the roughness anisotropy in all spatial directions or the roughness similarity normal to the trench versus other directions within a distance of 400 km off the trenches.

We have computed the roughness in the same way as described above but for 12 different orientations spanning 360°. For each orientation, the PSD is limited to samples aligned along this orientation (within a few degrees). Then, we estimate the deviation of these 12 anisotropic PSD where high values mean that our hypothesis of isotropy is locally likely to be wrong. We found that these deviations have the same order of magnitude as the deviations estimated above at high frequency, but slightly higher at low frequency. They generally do not exceed ~ 250 m at short wavelengths (150 m on average) and 900 m at long wavelengths (400 m on average). Indeed, as expected, this deviation may be much higher for a few specific regions made of major oriented-topography (for example, the Louisville seamount chain off Tonga). Typically, in Japan-Kuril trenches, 15% of the studied area exhibit a clear oriented structure, as the Joban seamount chains or the fracture zone south of it at both wavelengths, or the southern trench-parallel bending-related normal faults at high frequency (Figure A3.1 in the appendix).

We have also computed the similarity of the roughness spatial distribution pattern when estimated either close to the trench or ~ 200 km seaward further. To do so, we have divided the 400 km-wide studied strip into two 200 km-wide trench-parallel strips, one closest to the trench and the other seaward. Then, every 1° along all subduction zones, we select a 200 km along-trench wide zone on each strip (centered on the node of analysis) and perform a correlation between these two roughness spatial distributions weighted by the total roughness energy. This latter normalization makes the correlation sensitive to the similarity of roughness spatial distribution regardless of the global amplitude. Nevertheless, similar results are obtained with non-normalized correlation. Such an analysis provides both a quantification of the similarity of the roughness estimation perpendicular to the trench, and an indication of a possible better correlation following an oblique direction (see Figure A3.2 in supplementary material). By doing so, we estimate the degree of similarity between both 200 km-wide strips and validate our proxy concept.

The test shows that (1) in most cases the correlation is actually the best in a direction normal to the trench, (2) the fit in normalized-roughness spatial distribution exceeds 80%, and (3) surprisingly it is slightly better for R_{SW} than R_{LW} except for the Sunda trench. To sum up, the roughness of the seafloor prior to subduction appears to be mainly isotropic and displays, statistically, a better similarity in shape with surrounding strips in the trench-normal direction.

Mass transfers occurring in the shallow part of the subduction interface, such as sediment offscraping or upper plate removal by subduction accretion (von Huene & Scholl 1991; Lallemand et al. 1994), may alter the interplate roughness as estimated before subduction. However, numerous observations indicate that the roughness still persists despite the various subduction regimes. This is attested for example by the scars left by the subducting

seamounts in the forearc in the Nankai or Hikurangi Troughs or Costa-Rica trench (Kodaira et al. 2000; von Huene et al. 2004; Pedley et al. 2010), or by the observation of subducting seamounts revealed by detailed seismic imagery like beneath the Ecuadorian margin (Marcaillou et al. 2016; Collot et al. 2017) or even at greater depths like beneath the Sumatran margin (Singh et al. 2011). Wang and Bilek (2014) detailed how the subducting seafloor roughness and sediment thickness are important in the seismogenesis. It has also been proposed that the directivity in the tremor sources along the Nankai seismogenic interface were guided by striations at the bottom of the upper plate resulting from paleo-seamounts underthrusting (Ide 2010). Therefore, we are confident that the seafloor roughness measured immediately seaward of the trench well represents the one immediately landward, even if significant misfits may locally be observed.

3.3. Results: 'SubRough' database

3.3.1. Maps

3.3.1.1. Discrete roughness pattern

The global maps of the discrete distribution of the three roughness estimates R_{SW} , R_{LW} and $R_{LW'}$ over the entire set of subduction zones are provided in the appendix (Figures A3.3 to A3.5, respectively).

3.3.1.1.1. Short wavelength roughness R_{SW}

R_{SW} mapping (Figure A3.3) highlights bathymetric gradients at high frequencies. Therefore, 95% of R_{SW} values vary in the range [0-300 m] with a mean around 145 m (median ~100 m). It clearly illustrates how heterogeneous the seafloor bathymetry is, and why there may be no single rule for a rupture to initiate and propagate along the subduction interface. Some gentle aseismic ridges like Carnegie, Nazca or Ninety-East are not clearly expressed in the roughness signal because almost all their spectral signatures lie at wavelengths longer than 20 km. Other large features are better highlighted, like the Obruchev Rise east of the Emperor-seamount chain, the Iquique Ridge off North Chile, the Oki-Daito Ridge

south of Kyushu, the East-Pacific Rise off Mexico or the Nazca-Pacific spreading center off South Chile. Hence, ridges with similar global pattern may have different structure at small scale. Seamounts as small as the ones belonging to the Kinan seamount chain off southwest Japan, whose mean size is about 20-30 km in diameter and ~1 km in height, clearly appear with $R_{SW} > 250$ m. Most fracture zones are detected along their surface trace in R_{SW} signal but only a few of them, like the Grijalva Fracture zone off Guayaquil Gulf in Ecuador, exhibit a linear trend. Many of them, even the largest ones, like the Luzon-Okinawa Fracture zone south of the Ryukyus, are not discernible, i.e., having a non-linear signature.

3.3.1.1.2. Long wavelength roughness R_{LW}

R_{LW} mapping (Figure A3.4) provides an image of the long wavelength component of elevation changes. Ninety-five percent of R_{LW} values fall in the range [0-1500 m] with a mean around 485 m (median ~250 m). It is a good indicator for topographic changes at large spatial scale. It highlights the main large features that may segment trenches, such as the Louisville Ridge segmenting the Tonga from the Kermadec trenches,

the Palau-Kyushu Ridge between the Nankai Trough and the Ryukyu Trench, the Ogasawara Plateau between the Izu-Bonin trench and the Mariana Trough or the Emperor seamount chain between Kamchatka and W-Aleutians trenches. Some fracture zones marked by a pronounced topography are well defined at these wavelengths such as the Investigator FZ south of Sumatra or the Barracuda FZ east of Guadeloupe. Low R_{LW} regions corresponding to sediment fans off Cascadia or Andaman for example immediately appear in this mapping.

3.3.1.1.3. Intermediate wavelength roughness R_{IW}

R_{IW} generally mimics the R_{LW} pattern with a larger amplitude, given the fact that PSD are integrated over a wider wavelength interval. Indeed, roughness amplitudes increase with increasing wavelength, but also with enlarged wavelength bandwidths. Ninety-five percent of RIW values vary in the range 0-1500 m with a mean around 635 m (median \sim 430 m). Since the fractal approach integrates all wavelengths from 20 to 80 km (Figure A3.5), it is a good technique for mapping objects of intermediate size, namely seamounts, seamount aggregates or spreading ridges. In most cases, R_{IW} follows the trend of short- or long-wavelength roughnesses with

a mean amplitude about 30% larger than the one of R_{LW} as a result of larger wavelength bandwidth contributions. This observation strengthens our choice to describe the roughness with only two short and long wavelengths parameters. It should be noted that the roughness signal is necessarily dominated by the largest wavelengths up to 80 km. In a few cases, some oceanic features are better defined at intermediate than at short or long wavelengths. R_{IW} mapping brings complementary information with respect to R_{SW} and R_{LW} along the Aleutian, Cascadia and Ryukyu trenches for example.

3.3.1.2. Mean roughness pattern

In addition to the discrete dataset over a 10-km spatial grid, it may be useful to have access to mean roughness values along trenches for first-order roughness evaluation and correlation with other subduction parameters (see section 3.4). We have thus averaged the roughness values over a 250 x 250-km squared area facing each trench node issued from Heuret et al.'s (2011) database, i.e., every \sim 200 km along the trench. Figure A3.6 (in the appendix) shows the results in two map views for R_{SW} and R_{LW} . Averaged values are available online in the SubMap database (<http://www.submap.fr>).

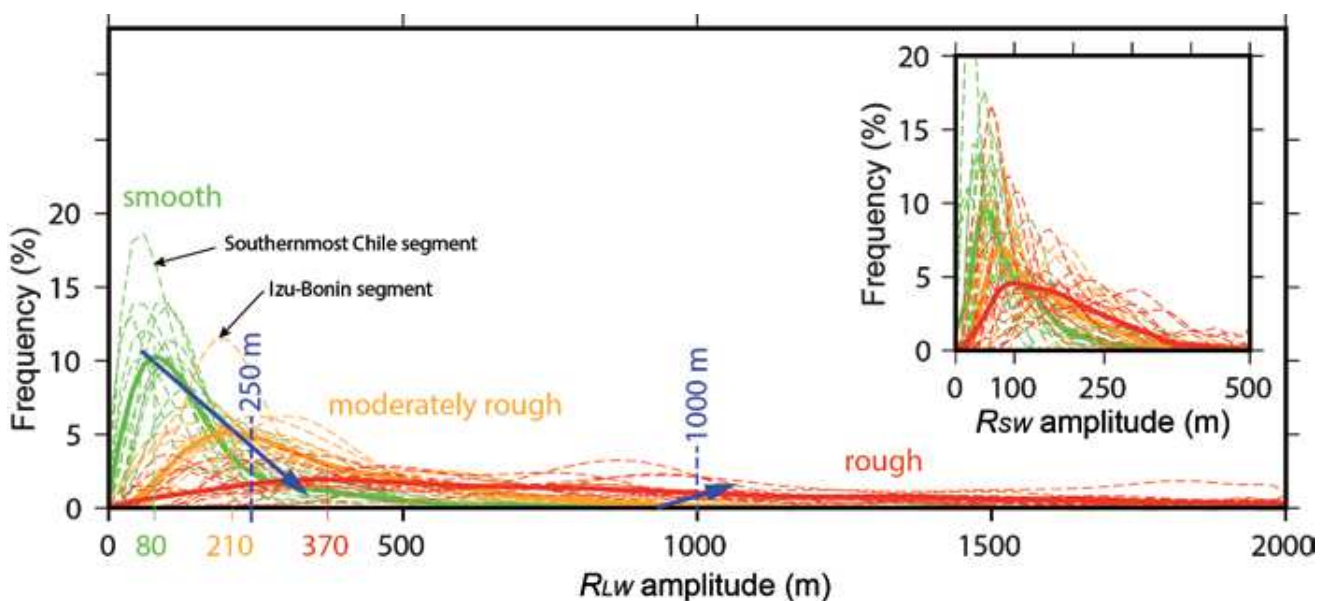


Figure 3.4. Histograms of R_{SW} and R_{LW} for the three main classes of subducting seafloor. Each dashed line represents a trench segment. The plain lines are synthetic distribution averaging the roughness distributions of all segments within a class. The data set used for the statistics considers the 250-km-wide strip close to the trench. Note that the histograms dispersion within the same class is low for R_{LW} and high for R_{SW} . The blue arrows illustrate the change in roughness distribution from the smoothest class to the roughest.

3.3.2. Global analysis of roughness information along the main subduction zones

In this section, we examine the lateral variations of R_{SW} , R_{IW} and R_{LW} with respect to the relative (residual) bathymetry, at mid-distance between the trench and the seaward boundary of the 250 km-wide strip (i.e., 135 km from the trench, by averaging data along a 2-km-wide band, see Figure 3.2). Since the general trend of R_{IW} and R_{LW} signals is often the same, except for a few small offsets in their respective peaks, we will not describe R_{IW} to rather focus on R_{SW} and R_{LW} . It should be taken into account that roughness values, even if plotted along a transect, were acquired in a spatial domain within a 100-km-radius sampling circle, so that there could be significant differences between the relative (residual) bathymetry sampled along a 2-km-wide band far from the trench and the roughness peaks and lows sampled over a 200-km-wide area.

3.3.2.1. Definition of roughness classes to characterize subduction segments

Most subduction zones exhibit lateral variations in terms of subducting seafloor roughness. We have thus decided to first characterize the seafloor prior to subduction segment by segment. We have defined our segmentation by taking into account only the 250-km-wide strip close to the trenches in order to optimize the proxy with the subduction plate interfaces. Since we observe a great dispersion of the R_{SW} data and a better coherence for R_{LW} , we have identified seafloor segments based on R_{LW} characteristics only. We define segments larger than 400 km (along-strike), long enough to generate $M_w > 8.5$ earthquakes, except at trench edges where shorter segments may be considered. We then define three classes depending on the percentage of R_{LW} amplitudes less than 250 m and the percentage exceeding 1,000 m (see arrows in Figure 3.4):

1. The “rough” segments which exhibit a significant proportion of $R_{LW} > 1,000$ m (from 14% up to 77%) as well as a limited proportion of $R_{LW} < 250$ m (less than 27%).
2. The “smooth” segments characterized by more than 58% of $R_{LW} < 250$ m (up to 100%) and less than 5% of $R_{LW} > 1,000$ m.
3. The “moderately rough” segments are intermediate and do not verify the above criteria

except one short segment seaward of the Izu-Bonin Trench which matches the “smooth” criteria but whose mode (200 km) better fits the moderately rough class (see Figure 3.4).

The R_{LW} histograms of all segments are plotted in Figure 3.4 with the mean histogram obtained for each class in bold. Peak values of R_{LW} for each class are respectively 80 m, 210 m and 370 m for smooth, moderately rough and rough. Standard deviation increases drastically from smooth to rough. We validate a posteriori the two roughness thresholds 250 m and 1,000 m used to define the three roughness classes (blue arrows in Figure 3.4). The R_{SW} histograms (see inset within Figure 3.4) are more scattered but globally follow the same trend as R_{LW} .

Figure 3.5 illustrates the respective segment lengths and classes along most subduction zones. We did not perform any statistics for the Mediterranean region as well as along some narrow subduction zones in South-East Asia, because the length of the segments is too short either because the subduction zones themselves were too narrow or because continents were involved in the subduction.

Table 3.1 provides a quantitative description of most subduction zones as a function of the different classes of seafloor segments (Figure 3.5). From the respective contribution of each class, we propose a classification of subduction zones within three groups, spanning from “dominantly rough” (Solomons or Makran) to “dominantly smooth” (Andes or Cascadia). We classify the subduction zones facing moderately rough segments (South Sandwich) or showing strong lateral variations (Izu-Bonin-Mariana-Japan-Kamchatka or Luzon) in the “mixed” group. Typical examples selected among each group are presented in Figures 3.6 and 3.7. All other subduction zones are displayed in the supporting information (Figures A3.7 to A3.12).

3.3.2.2. Dominantly rough subduction zones

These trenches are dominated by prominent unsubducted oceanic features, if not already subducting, with more than 14% of $R_{LW} > 1,000$ m. We have systematically masked the subducting continental seafloor, as well as areas above sea level from the roughness dataset in regions like in

the Solomons because we consider that collision processes are out of the scope of our study.

3.3.2.2.1. *New-Guinea-Solomon-Vanuatu*

The Australian plate subducting beneath New Guinea, New Britain, Solomon Islands and Vanuatu, consists of a mosaic of oceanic features including fragments of continental crust as well as oceanic basins, arcs, plateaus, troughs and spreading centers. This 3,450-km-long subduction zone is probably facing the roughest morphology of all modern subduction systems. Indeed, all roughness parameters reach their highest recorded values there: 46% of the area characterized by $R_{LW} > 1,000$ m, 75% with $R_{LW} > 500$ m, 4% with $R_{LW} < 250$ m. The roughness profile shown in Figure 7a has been masked each time the subducting plate emerges, as well as at both ends of the subduction system where the Trobriand Platform and the Loyalty Ridge subduct, but also in the middle of the trench where the Pocklington Rise and the Rennell Ridge are also subducting. Oceanic basins, i.e., Solomon Sea, Woodlark, Santa Cruz and North Loyalty basins, exhibit lower roughness values than oceanic reliefs, but are still rough, with $R_{LW} > 250$ m, except in very restricted areas of the Woodlark and North Loyalty Basins (Figure 3.6a). Among the

various oceanic reliefs, the D'Entrecasteaux Zone – a double-ridge mountain chain - is known to subduct beneath and subsequently causes the uplift of Esperitu Santo Island (Vanuatu) (Collot et al. 1985; Fisher et al. 1991).

3.3.2.2.2. *Makran*

The Oman Sea seafloor subducting at the 850-km-long Makran trench shares the same characteristics as the seafloor off the Solomon Islands. The Oman region to the west and the Owen Fracture Zone to the east are major subducting features responsible for 43% of $R_{LW} > 1,000$ m. However, the triangular shaped Oman Basin (Figure A3.7), which is quite narrow at a distance of 135 km from the trench and widens toward the trench, shows very low R_{LW} values.

3.3.2.2.3. *Ryukyu-Nankai*

The Philippine Sea Plate subducts along its northwestern side along the 2,300-km-long Ryukyu and Nankai trenches. Both the northern end of the Luzon volcanic arc colliding with the Taiwan orogen and the Gagua Ridge – a former fracture zone (Deschamps et al. 1998) – contribute to the very

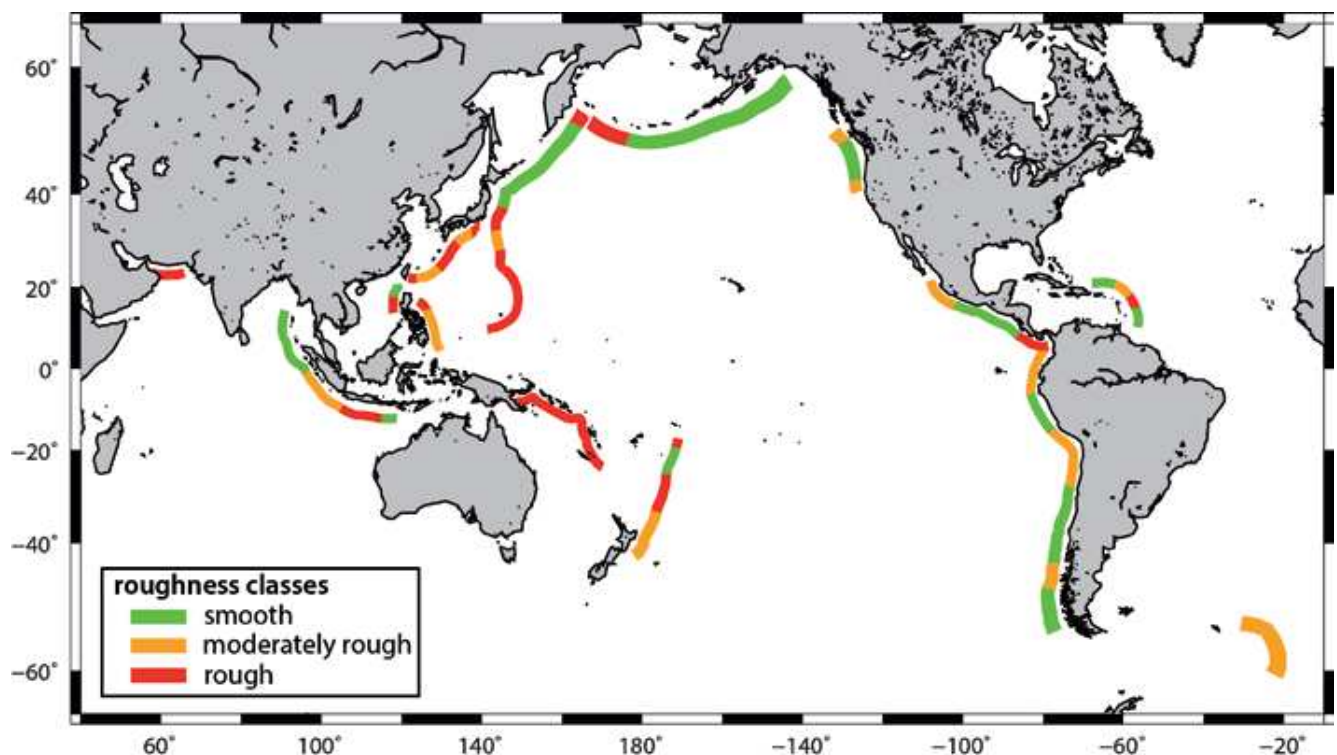


Figure 3.5. Plot of the seafloor segments seaward of most subduction zones, according to their roughness class.

high level of both RSW and R_{LW} (77 % of $R_{LW} > 1,000$ m, see Figure A3.7 and rough termination in Figure 3.5). The Amami-Daito-Oki-Daito (ADO) region - remnants of a Mesozoic arc complex - is prominent along the residual bathymetry profile and marked by very high values of RSW and R_{LW} (45 % of $R_{LW} > 1,000$ m, rough segment in Figure 3.5). South of the ADO region, the complex fabrics of the West Philippine Basin is reflected in the morphology, thanks to the thin sedimentary cover, increasing roughness parameters to significant levels: up to 250 m for RSW and more than 250 m for R_{LW} . This segment is considered as moderately rough. North of the ADO region, the Kyushu-Palau Ridge, a remnant of the proto-IBM arc, marks the transition between the Ryukyu segment where the West Philippine Basin subducts and the Nankai segment off southwest Japan where the Shikoku Basin subducts. This basin, classified as moderately rough (Figure 3.5), fringes the Nankai Trough. It locally exhibits very low R_{SW} and R_{LW} , despite some intermediate-size seamounts (Koshu and Kinan seamounts) present in its central part (see section 3.3.3.1. for further details of these seamounts). Several indications of subducting

features similar to these seamounts (Kodaira et al. 2000) or extent of the Gagua and Kyushu-Palau Ridges (Dominguez, et al. 1998a; Park et al. 2009; Lallemand 2016) underneath the margin were reported.

3.3.2.3. Mixed subduction zones

These trenches are characterized by a subducting seafloor either moderately rough or showing lateral variations, i.e., rough segments adjacent to smooth or moderately rough ones.

3.3.2.3.1. IBM-Japan-Kamchatka

Typically, this 6,250-km-long subduction zone is composed of a rough southern part where the old Mesozoic Pacific seafloor subducts along the 3,500-km-long IBM Trench and a northern, essentially smooth, part extending from northern Japan, along the Kurils to the Kamchatka Trench (Figure 3.6b).

The Caroline Ridge and the Ogasawara Plateau, both characterized by $R_{LW} > 1,000$ m, are major features

Groups	Trenches	Classes		
		Smooth (%)	Moderately rough (%)	Rough (%)
Dominantly Rough	New Guinea-Solomon-Vanuatu	0	0	100
	Makran	0	0	100
	Ryukyu-Nankai	0	46	54
Mixed	Tonga-Kermadec	23	35	42
	Philippines	0	79	21
	South Sandwich	0	100	0
	Luzon	46	0	54
	Java-Sumatra-Andaman	47	28	25
Dominantly Smooth	IBM-Japan-Kamchatka	48	8	44
	Antilles	55	24	21
	Central America	51	25	24
	Aleutians	81	0	19
	Andes	51	49	0
	Cascadia	61	39	0

Table 3.1. Classification of the seafloor areas prior to subduction into three groups from the roughest to the smoothest, based on the respective proportion of segments in each class.

that control the Mariana Trench shape at both south and north terminations (e.g., Wallace et al. 2009). Numerous seamounts, scattered all along this trench segment, boost the roughness values around 250 m for R_{SW} and above 1,000 m for R_{LW} . Low roughnesses ($R_{SW} < 100$ m and $R_{LW} < 250$ m) are also observed over a few hundreds of kilometers on both sides of the Ogasawara Plateau (Figures 3.6b and 3.7b). As mentioned in section 3.3.2.1, the 480-km-long segment north of the Ogasawara Plateau (Figure 3.5) has been classified as moderately rough because of its RLW mode around 200 m, even though it also fits the smooth class criteria (73% of $R_{LW} < 250$ m, Figure 3.4).

Most of the Lower Cretaceous Pacific seafloor, subducting beneath Kuril and northern Japan island arcs, presents a rather smooth, moderately hilly morphology characterized by $R_{SW} \approx 100$ m and 65% of $R_{LW} < 250$ m (mode ≈ 110 m) over almost 2,000 km compared with the total length of the Japan-Kuril-Kamchatka Trench: 2,750 km. The lowest R_{LW} values are recorded off Tohoku, northern Honshu. Both R_{SW} and R_{LW} increase significantly, up to 300 m and 2,000 m respectively, south of the Japan Trench where the Joban and Takuyo seamount chains obliquely intersect the trench (Figure 3.7b). The extension of the seamount chain beneath the Japan margin has been demonstrated by seismic imaging (Lallemand et al. 1989; Mochizuki et al. 2008). Near the northern termination off Kamchatka, R_{LW} increases up to 1,000 m over the Meiji Guyot and Obruchev Rise, which belong to the Hawaii-Emperor hotspot seamount chain.

3.3.2.3.2. Tonga-Kermadec

The 3,400-km-long Tonga-Kermadec subduction system (Figure A3.8) is segmented at the latitude of the Louisville hotspot chain, which consists of a seamount chain associated with R_{SW} up to 250 m and R_{LW} up to 2,900 m. North of its intersection with the trench, the Pacific seafloor off the Tonga archipelago, even significantly offset by bending-along-strike-normal faults, exhibits rather low roughness values (78% of $R_{LW} < 250$ m with a mode of ~ 70 m along the 720 km long smooth segment), except at the two edges where huge seamounts (Capricorne and Osborn seamounts) enter the trench (Figure 3.5). The Louisville Ridge has been detected, up to 60-km arcward from the trench, beneath the Tonga

margin based on residual bathymetry by (Bassett & Watts 2015a). It is known to have severely damaged the Tonga Trench during its southward creeping (Pelletier & Dupont 1990; Lallemand et al. 1992b). The seafloor off the Kermadec Islands, south of Louisville seamount chain, is characterized by elongated seamounts and ridges producing high amplitudes of R_{SW} , up to 250 m, and R_{LW} , up to 1,200 m (Figure A3.8). A sharp step is crossed near 36°S coinciding with the northern limit (scarp) of the Hikurangi Plateau. Despite its elevation above the abyssal plain, the plateau is rather flat with several scattered seamounts on top increasing the level of roughness ($R_{SW} < 100$ m, $R_{LW} < 500$ m). Some of them have profoundly damaged the Hikurangi margin (Collot et al. 2001; Lewis et al. 1998; Lewis et al. 2004; Pedley et al. 2010). These subducting seamounts may explain the dominant creeping behavior along the Hikurangi subduction interface according to Gao and Wang (2014). At the southern end, the profile abuts against the E-W-trending shallow Chatham Rise.

3.3.2.3.3. Philippines

The West Philippine Basin Eocene oceanic crust subducts beneath the Philippine archipelago along the 1,550-km-long Philippine Trench. The middle subducting segment facing South Leyte and the North Mindanao islands is moderately rough with $R_{SW} < 100$ m and 34% of $R_{LW} < 250$ m (Figure A3.9). The southern part of the subducting seafloor (Palau Basin) is locally rougher when crossing the Mindanao Fault but still classifies as moderately rough. The seafloor becomes rougher in the north as the result of ridge-plume interaction in the Eocene (Deschamps & Lallemand 2002; Ishizuka et al. 2013), with R_{LW} up to 2,000 m where the Benham Rise intersects the trench.

3.3.2.3.4. South Sandwich

The South America oceanic crust subducts along the 1,200-km-long South Sandwich trench (Figure A3.9). Despite numerous fracture zones branched onto the close South America-Antarctica spreading center, roughness parameters never exceed 400 m for R_{LW} (except at the northern edge approaching the South Georgia Rise) and 300 m for R_{SW} . With 54% of $R_{LW} < 250$ m and only 1% of $R_{LW} > 1,000$ m, it is close to belong to the smooth class but we still classified it

as moderately rough (Figure 3.5, Table 3.1).

3.3.2.3.5. Luzon

The Chinese Platform subducts beneath Taiwan along the northernmost part of the 1,200-km-long Luzon Trough (Figure A3.9). We did not process the northern part where continental crust collides with the Luzon volcanic arc.

South of the continental talus, where the South China Sea oceanic seafloor subducts, we observe that the northern part, supplied by sediments coming from Taiwan, is very smooth with both R_{SW} and $R_{LW} < 100$ m (75% of $R_{LW} < 250$ m), while the southern part off Luzon Island is extremely rough. The high roughness values (RSW up to 300 m and R_{LW} up to 2,500 m; 26% of $R_{LW} > 1,000$ m) are associated with the subducting Scarborough seamount chain, which aligns along the N80°-trending fossil spreading center. Wang & Bilek (2014) discussed the roughness of the igneous crust, almost concealed by the sediment cover in the northern “smooth” part, considering that once most of the sediment cover is scraped off at the front of the upper plate, the subducting seafloor may become rugged and promote creeping along the subduction interface.

3.3.2.3.6. Andaman-Sumatra-Java-Sumba

As the IBM-Japan-Kamchatka subduction zone, the seafloor facing the 5,100-km-long Andaman-Sumatra-Java-Sumba subduction zone is segmented into smooth segments off the Andaman Islands and between the Java and Sumba islands, and rough segments especially south of Java (Figure A3.10). The morphology is extremely smooth off the Andaman Islands and northern Sumatra, over about 1,000 km of seafloor with both R_{SW} and $R_{LW} < 100$ m, mainly as the result of high sediment supply from the Bengal fan (70% of $R_{LW} < 250$ m, R_{LW} mode ≈ 40 m). Only the N-S-trending Ninety-East Ridge overhangs the abyssal plain at a distance from the trench with R_{LW} up to 800 m, fringing the trench without being subducted yet (Moeremans & Singh 2014).

To the south, off central and southern Sumatra, numerous north-south trending fracture zone reliefs, like the 97°E or the Investigator fracture zones, contribute to higher roughness amplitudes, especially at long wavelengths, as the oceanic sedimentary cover becomes thinner (29% of $R_{LW} <$

250 m, 33% of $R_{LW} > 500$ m). Similar roughness patterns have been observed from seismic reflection and gravity data in the seismogenic zone beneath the margin (Henstock et al. 2016). This segment has been classified as moderately rough (Figure 3.5). The 1,140-km-long southern segment of the Sunda trench, off Java, is characterized by a rough subducting seafloor. From west to east, we distinguish the Christmas Island, the Roo Rise and the Australian Rise, all associated with 25% of $R_{LW} > 1,000$ m (Figure 3.5 & A3.10). Surprisingly, most of the RSW values do not exceed 100 m, whereas only 8% of $R_{LW} < 250$ m, attesting that oceanic feature wavelengths are larger than 20 km. The 440-km-long easternmost segment, abutting against the Australian Rise, presents smooth characteristics with 58% of $R_{LW} < 250$ m.

3.3.2.4. Dominantly smooth subduction zones

This group of trenches exhibits more than 58% of $R_{LW} < 250$ m together with a maximum of 5% of $R_{LW} > 1,000$ m (Figure 3.4 and Table 3.1).

3.3.2.4.1. Andes

The 7,350-km-long Andean Trench (Figure 3.6c) shows strong lateral variations in the morphology of the subducting seafloor alternating moderately rough segments with longer smooth ones. In Figure 3.7c, we have divided this long subduction system into two segments on both sides of the Arica bend: a North Andes segment 3,300 km long and a South Andes segment 4,050 km long.

Starting from the north, off Colombia, Ecuador, and northernmost Peru, the Nazca Cenozoic seafloor is very irregular with plume-derived ridges (Malpelo and Carnegie), troughs (Yaquina T.) and fracture zones (e.g., Grijalva, Alvarado, Sarmiento ridges) producing moderately high roughness values (22% of $R_{LW} < 250$ m, 4% of $R_{LW} > 1,000$ m). Off the Peru Trench, the seafloor is smoother (95% of $R_{LW} < 250$ m) with both R_{SW} and $R_{LW} \approx 100$ m except across the sharp Mendaña and Nazca fracture zones ($R_{LW} \approx 250$ m) and the 300-km-wide Nazca Ridge ($R_{LW} \approx 500$ m). Interestingly, the two main aseismic ridges, i.e., Carnegie and Nazca, culminating at about 1,600 m above the surrounding seafloor, have a relatively small roughness signature, especially at short wavelengths. These major features are known

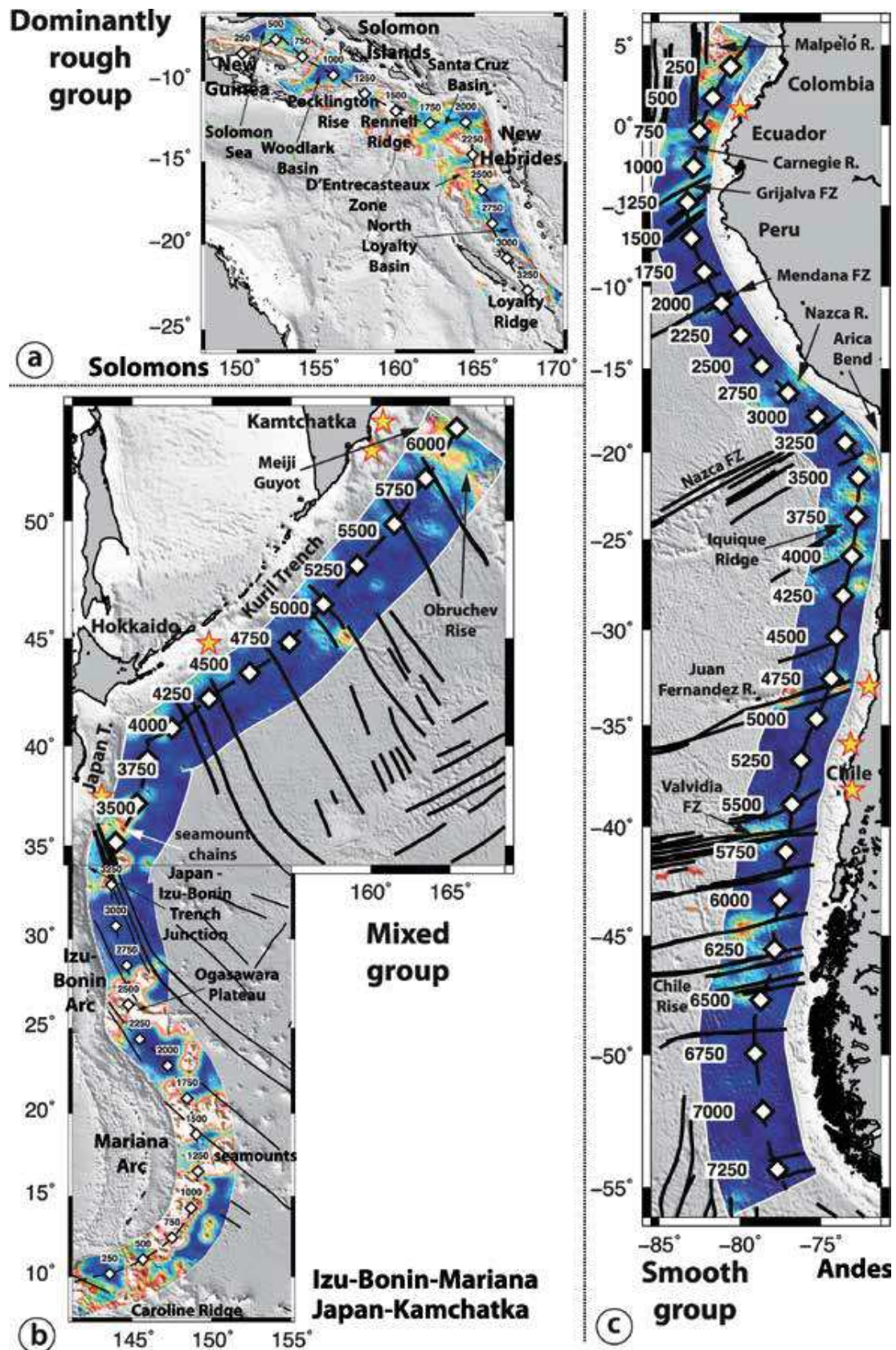


Figure 3.6. R_{LW} maps representative of the three groups of subduction zones. (a) Dominantly rough group with Solomons, (b) mixed group with Izu-Bonin-Mariana-Japan-Kamchatka, and (c) dominantly smooth group with the Andes all at the same scale. The along-strike profiles of Figure 3.7, obtained at a distance of 135 km from the trench are plotted as a black dashed line. Diamonds are plotted every 250 km in order to facilitate the comparison with the main features on the profiles.

to extend beneath the margin as well as volcanic massifs on the flanks of the Carnegie Ridge observed on both sides of the (Gutscher et al. 1999; Gutscher et al. 2000; Marcaillou et al. 2016; Collot et al. 2017).

South of the Arica bend, the Nazca seafloor becomes locally rougher with several scattered seamounts on both sides of the Iquique Ridge, showing values comparable to those in the northernmost Andes (R_{SW} up to 250 m, 33% of $R_{LW} < 250$ m and R_{LW} up to 1,000 m). Similar seamounts were detected, based on multichannel seismics imagery, into the subduction channel landward of the trench. They are suspected to have controlled interplate coupling and seismic rupture in the 2014 Iquique earthquake area (Geersen et al. 2015). South of this moderately rough area and over 1,780 km, the seafloor shows short wavelengths oceanic fabric (R_{SW} and 82% of $R_{LW} < 250$ m) sometimes punctuated by the Juan Fernandez seamount chain (R_{LW} up to 700 m). Then, the moderately rough segment of the Chile Rise and young fracture zones (i.e., Mocha, Valdivia, Chiloe) boosts the roughness values up to 500 m for long wavelengths and 250 m for short wavelengths (41% of $R_{LW} < 250$ m). The continuation of those features, as well as the variable thickness of the subduction channel, beneath the Chile margin has been investigated by (Contreras-Reyes et al. 2010). They have noted a probable tectonic control of the 1960 and 2010 Chiloe and Maule giant earthquakes. South of the trench-trench-ridge triple junction, the Antarctica seafloor smooths again drastically over 770 km showing the lowest roughness values of the Andean trench near 100 m for both R_{SW} and R_{LW} (100% of $R_{LW} < 250$ m). Finally, the seafloor along the Chile trench is probably one of the most extended (total of 3,730 km long) smooth subducting seafloor in the world.

3.3.2.4.2. Antilles

The Cretaceous Atlantic seafloor is subducting beneath the Caribbean Plate from Hispaniola Island to Trinidad along the 2,200-km-long Puerto-Rico and Lesser Antilles trenches (Figure A3.11). Similar to the Tonga Trench, where strong plate bending does not increase roughness, we observe a smooth seafloor along the 560-km-long segment north of Puerto-Rico, characterized by extremely low roughness values (both R_{SW} and $R_{LW} < 100$ m, 69% of $R_{LW} < 250$ m). Then, R_{LW} increases off Saint Martin, Antigua and

Barbuda (500-km-long moderately rough segment, 34% of $R_{LW} < 250$ m), reaching a maximum of 1,200 m off Guadeloupe where fracture zone ridges like Barracuda and Tiburon intersect the trench (360-km-long rough segment, 13% of $R_{LW} < 250$ m and 21% of $R_{LW} > 1,000$ m). Those ridges extend far beneath the Lesser Antilles accretionary wedge and arc basement, as seen on seismic reflection profiles (Laigle et al. 2013). The seafloor smoothens again off Barbados Island in the south, partly as a consequence of the Orinoco sediment supply, with extremely low roughness values similar to those off Puerto-Rico (600-km-long smooth segment, 69% of $R_{LW} < 250$ m). R_{LW} increases at the southern end near the Demerara Plateau and at the northern end at the vicinity of the Bahamas Bank.

3.3.2.4.3. Central America

The Neogene Cocos Plate, subducting beneath Central America along the 3,450-km-long Middle America trench, is limited to the north by the East Pacific Rise and highly tectonized young seafloor (Rivera fracture zone and massif), and to the south by the Cocos Ridge originating from the Galapagos hotspot, and the Panama fracture zone (Figure A3.11). The seafloor facing Central America has been divided into three segments (Figure 3.5).

The 970-km-long northern segment is moderately rough with 34% of $R_{LW} < 250$ m, up to 1,200 m near the Rivera Massif. The main middle segment, 1,930-km-long, is globally smooth with 88% of $R_{LW} < 250$ m, up to 600 m close to the Tehuantepec Ridge, a major fracture zone branched onto the East Pacific Rise. North of that ridge, R_{SW} maintains a high level up to 250 m north (Figure A3.11). The smoothest section, about 1,100 km wide with $R_{SW} < 100$ m and $R_{LW} < 250$ m, is observed south of the Tehuantepec Ridge off Guatemala, El Salvador, Nicaragua and northern Costa-Rica. Northwest of the Cocos Ridge, offshore Costa-Rica, several scattered conical seamounts are observed seaward and landward of the trench. They produce embayments in the small accretionary wedge and remarkable scars into the forearc as they subduct far from the trench (von Huene et al. 1995; von Huene et al. 2000; Dominguez et al. 1998a; Dominguez et al. 2000; Ranero & von Huene 2000). The 980-km-long southernmost segment includes the Cocos Ridge and the Panama fracture zone. We consider it as a rough segment characterized by 18%

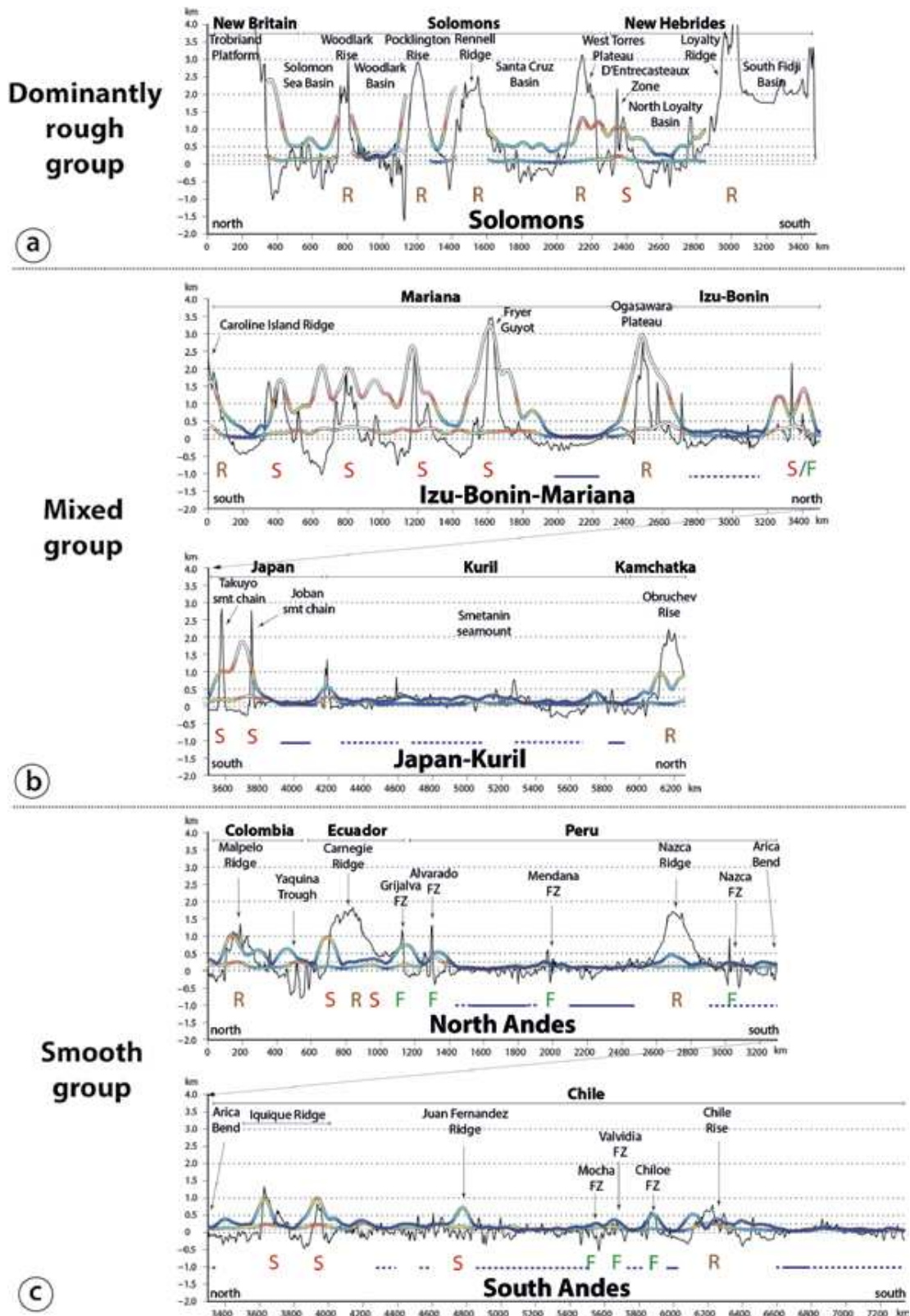


Figure 3.7. Along-strike profiles of representative subduction zones for each group appearing in Figure 3.6. Profiles show the relative bathymetry (black line), acquired at a distance of 135 km seaward of the trench (see Figure 3.2) and associated R_{SW} and R_{LW} . Thin horizontal dotted lines are rulers at 0, 100, 250, 500, 1,000, 2,000, and 3,000 m. S = location of major seamounts or seamount chains or seamount massifs. R = location of major aseismic or active ridges. F = location of major fracture zones. Continuous dark blue lines below the profiles indicates the very smooth regions characterized by R_{SW} and $R_{LW} < 100$ m. The dotted dark blue lines outline areas with moderately smooth seafloor, for example, R_{SW} and $R_{LW} < 250$ m.

of $R_{LW} > 1,000$ m and 12% of $R_{LW} < 250$ m.

3.3.2.4.4. Alaska-Aleutian

The Pacific seafloor, which subducts beneath the 3,750-km-long Alaska-Aleutian Trench, is globally smooth except in its western portion (Figure A3.12). This 730-km-long westernmost segment coincides with the northern termination of the Hawaii-Emperor seamount chain at the junction between the Kamchatka and Aleutian trenches. There, the seafloor is very irregular including the Detroit Tablemount, the SW Aleutian and the Aleutian Rises. R_{LW} reaches values as high as to 1,300 m whereas R_{SW} may exceed 250 m along this rough segment (15% of $R_{LW} > 1,000$ m and 14% of $R_{LW} < 250$ m).

The rest of the seafloor subducting to the east over more than 3,000 km maintains a high level of R_{SW} up to 250 m while R_{LW} decreases below 500 m due to the presence of several N-S-trending fracture zones (Rat and Amlia for example). The lowest roughness values are measured off the Eastern Aleutians and the Western Alaska Peninsula. Only the Sirius seamount, south of Shumagin margin, interrupts the low roughness level ($R_{LW} < 250$ m) of this ~1400-km-wide area. Both R_{SW} and R_{LW} increase again south of Kodiak Island in response to the presence of the Patton and Giacomini seamounts. This long segment is undoubtedly smooth as it shows 85% of $R_{LW} < 250$ m (Figure 3.5).

3.3.2.4.5. Cascadia

The 400-km-wide central part of the very young Juan de Fuca Plate subducting beneath British Columbia, Washington and Oregon states is extremely flat, as it is filled by the large Nitinat and Willapa sediment fans. R_{SW} and R_{LW} values are very low (< 100 m) compared with those on both northern and southern segments of this 1,200-km-long subduction zone. Indeed, the oceanic fabric, including a spreading center and fracture zones (e.g., Mendocino and Sovanco FZ with R_{SW} up to 500 m) covered with fewer sediment, explains the irregular seafloor morphology there. Interestingly, R_{SW} exceeds R_{LW} in amplitude over some oceanic features like the Explorer and Juan de Fuca Ridges, the Blanco and the Mendocino Fracture Zones. We classified the 780-km-long middle segment as extremely smooth (98% of $R_{LW} < 250$ m) and the two short (250 km long each) edge segments as moderately rough (48% of

$R_{LW} < 250$ m).

3.3.3. The roughness of oceanic features

Main categories of oceanic features such as seamounts, ridges or fracture zones are noted along profiles in Figures 3.7 and A3.8 to A3.12 as S, R and F, respectively. These features are known for contributing to the seismogenic behavior along the subduction interface. Here, we will examine their roughness signature before subduction with respect to the global roughness pattern (Figure 3.8 and Table 3.2).

3.3.3.1. Seamounts, seamount massifs and seamount chains

Seamount are extremely abundant on oceanic plates and cover a great variety of morphological aspects. They are often isolated with various sizes and shapes. Eighty-three per cent of detected seamounts are less than 3 km high, more or less conical, sometimes truncated. Those higher than 3 km are generally re-shaped by rift zones, flank collapses, sub-aerial erosion by the waves or reef development (Dominguez et al. 1998b; Wessel 2001; Kim & Wessel 2011). Figure 3.8 shows the R_{SW} and R_{LW} pattern over seamounts with respect to the global roughness pattern. We have analyzed all roughness values from the 10-km-spaced grid inside the seamount contours as defined by Kim and Wessel (2011) within the 250-km-wide strip along the trenches. As expected, the mean roughness is higher than the global trend (mean $R_{SW} = 234$ m instead of 144 m; mean $R_{LW} = 909$ m instead of 490 m; mean $R_{TW} = 1,380$ m instead of 634 m, see Table 3.2). However, it appears that the difference from the global trend is particularly clear when looking at short wavelengths on the density plot in Figure 3.8. Seamounts also appear as aggregates or massifs, like the Rivera Massif off Mexico, the Atacames seamounts on the northern flank of the Carnegie Ridge (Marcaillou et al. 2016), or chains like the Koshu or Kinan seamount chains south of the Nankai Trough, the Joban seamount chain subducting in the Japan Trench, or the Iquique Ridge off north Chile (Figures 3.6, 3.7, A3.7 & A3.11). In those cases, the seamount size is typically 2 to 3 km high and 15 to 50 km in diameter. Their roughness signal ranges from 200 to 300 m for R_{SW} and from 400 to 2,000 m

for R_{LW} . The long wavelength roughness amplitude is sensitive, not only to the seamount morphology itself, but also to the surrounding morphology over a wider area.

Many ridges like the Louisville Ridge, the Juan Fernandez Ridge, the D'Entrecasteaux Zone or the Kashima seamount chain, are composed of aligned large-size seamounts either originating from hotspots or controlled by major faults (Figures 3.6, 3.7 & A3.8). Their signature is thus anisotropic, as any seamount chain like the Scarborough seamount chain off Luzon or the Joban seamount chain. Seamounts taller than 3 km have a strong signal especially on R_{LW} .

3.3.3.2. Fracture zones

Fracture zones often appear as linear features that can be followed over hundreds or thousands of kilometers. They clearly extend into the subducting slabs and are often supposed to affect the seismic behavior of the plate interface (Das & Watts 2009; Carena 2011; Müller & Landgrebe 2012). Taken all together and investigating an area located 10 km away on each side of the fracture zones, their

roughness signal does not differ much from the global seafloor one (Figure 3.8): mean $R_{SW} = 141$ m instead of 144 m and mean $R_{LW} = 394$ m instead of 490 m. In most cases, due to their spatial extent and their low elevation gradients, the fracture zone contribution to roughness is not significantly different from its vicinity. In a few cases, the oceanic crust age contrast, and vertical offset, across the fracture zone are enough to produce a significant difference in elevation, for example, 500 m across the Grijalva FZ off Ecuador or the Mindanao FZ off the Philippines. Such a morphological step is marked by $R_{LW} = 700$ -1,000 m (Figures 3.6, 3.7 & A3.9), since this parameter is very sensitive to slope gradients, but such a case is very rare. Some fracture zones – generally named ridges - have been the locus of localized deformation and rise, as the Gagua Ridge east of Taiwan, the Owen Fracture Zone off Makran (Figure A3.7) or the Barracuda Ridge off Lesser Antilles (Figure A3.11). In those cases, R_{LW} ranges from 1,000 to 2,000 m. The maximum is reached at the Owen FZ because the ridge evolved in a transtensional context and is now bordered by pull-apart basins as the Dalrymple Trough (Rodriguez et al. 2013), increasing the slope gradient.

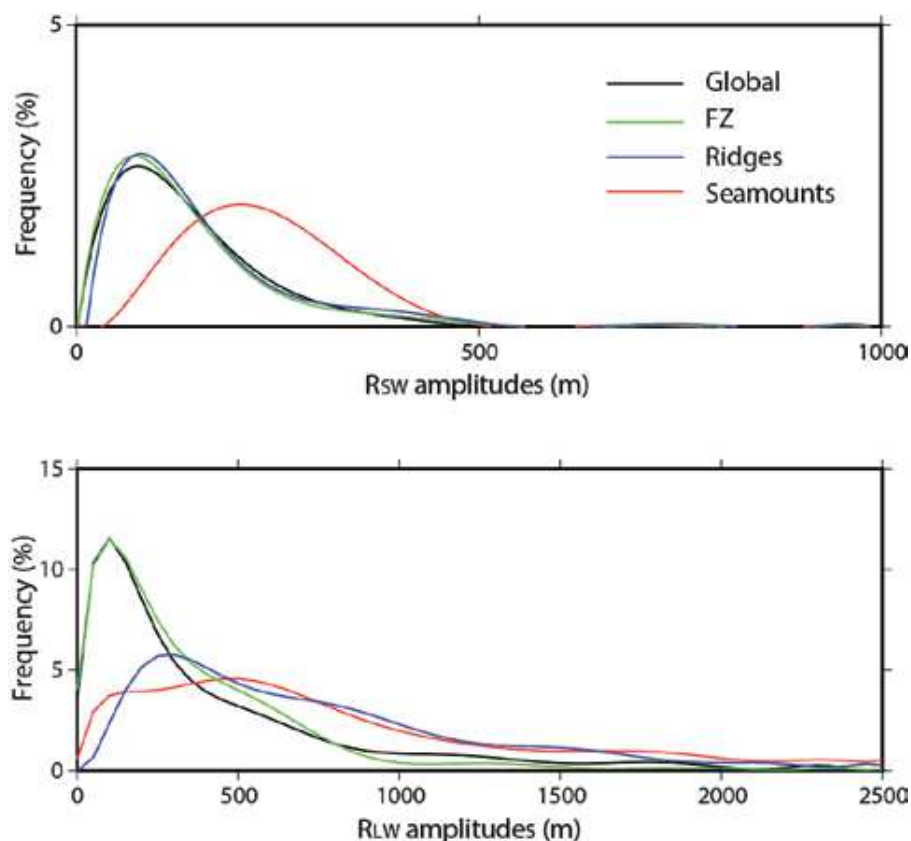


Figure 3.8. Distribution of roughness values among the global data set (in black) or sub datasets (in color) corresponding to major oceanic features.

3.3.3.3. Aseismic and active ridges and plateaus

Here, we consider all elongated prominent features as well as plateaus other than fracture zones or seamount chains. As for seamounts, the mean roughness values of these features are higher than for global seafloor, especially for long wavelengths: mean R_{SW} = 163 m instead of 144 m and mean R_{LW} = 835 m instead of 490 m. The maximum R_{LW} amplitude – typically 600-1,000 m - is generally observed along the flanks of the Hikurangi Plateau, Cocos, Carnegie, Malpelo, Obruchev or Ninety-East Ridges when their width is larger than 100-200 km (Figures 3.6, 3.7, A3.8, A3.10, A3.11 & A3.12). Narrower features like the Kyushu-Palau Ridge, Amami Plateau, Daito Ridge, Pocklington Rise or SW Aleutian Ridge share similar signals with seamounts, i.e., high R_{SW} and R_{LW} (Figures 3.6, 3.7, A3.7 & A3.12). Active ridges like the Chile, the Juan de Fuca or the Gorda Rises (Figures 3.6, 3.7 & A3.12) show higher R_{SW} up to 250 m because of the high bathymetric signal frequency but no or few anomalies in R_{LW} .

3.3.3.4. Smooth areas

Continuous smooth areas are outlined in Figures

3.6, 3.7 and A3.7 to A3.12. Plain lines correspond to regions with both R_{SW} and R_{LW} less than 100 m, that is, very smooth regions, whereas dotted lines highlight regions with both R_{SW} and R_{LW} less than 250 m, that is, smooth regions compared to their surroundings. Among the smoothest regions (R_{SW} and $R_{LW} < 100$ m), some reflect a smooth oceanic crust like off the northernmost Mariana arc (250 km of lateral extent), Porto-Rico (150 km), northern Japan (200 km), northern Kuriles (< 100 km), Eastern Aleutians (350 km), Peru (400 km on each side of the Mendana FZ), Guatemala (150 km) and Nicaragua (200 km). Other regions are smooth because of an excess of terrigenous sediment filling the trench like Andaman (400 km), northern Sumatra (400 km), Barbados (100 km), Cascadia (300 km), western Alaska (250 km), and south Chile (\approx 100 km on each side of the Chile Rise). Many smooth areas extend laterally with moderately smooth areas (R_{SW} and $R_{LW} < 250$ m) like off Middle America, southern Chile, Aleutians or Antilles. The above evaluation of the smooth area extents has been done at a distance of 135 km from the trench. The lateral extent may thus vary in the direction normal to the trench, but not drastically since the roughness values are calculated from a 200-km-wide sampling area (see Figure 3.2).

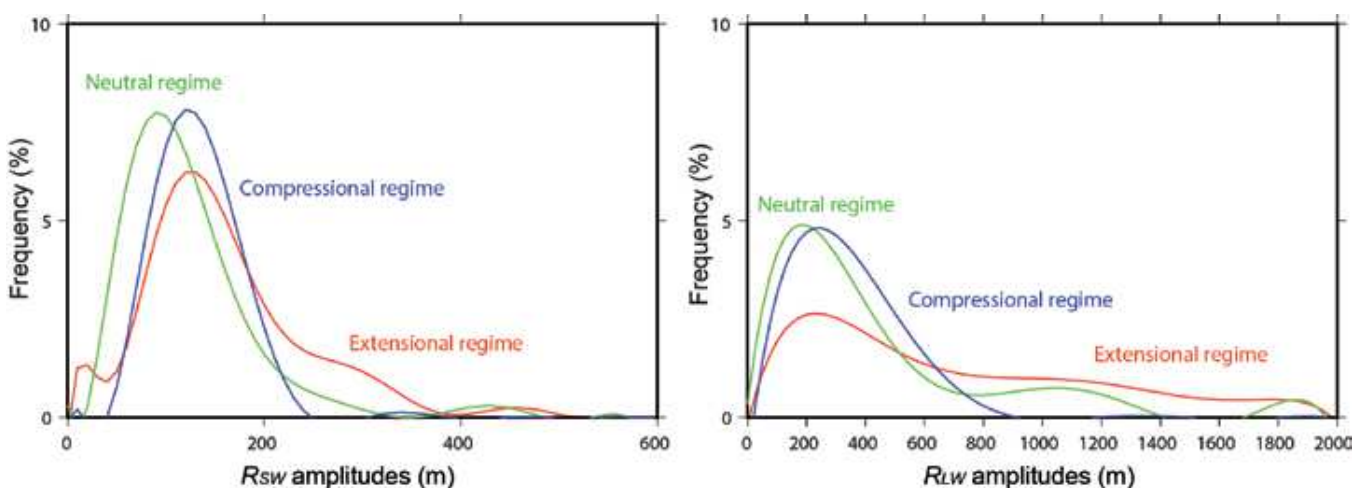


Figure 3.9. Distribution of roughness values of seafloor facing regions characterized by different upper plate strain regimes as defined by Heuret and Lallemand (2005).

3.4. How does seafloor roughness correlate with the state of stress in the subduction zones?

This study is the first step to investigate several topics such as the relationship between subduction interface roughness and seismicity, but also margin's tectonic behavior. Here, we analyze the correlation with subduction parameters, which may be potentially controlled by the roughness of the plate interface. In this respect, we have selected parameters dealing with the state of stress within the converging plates as well as the plate interface to test the influence of the plate boundary topography on it. Thus, we test three proxies of the state of stress in the subduction zone: the upper plate strain at a distance from the plate interface as defined by Heuret and Lallemand (2005), the seismic coupling as estimated by Heuret et al. (2011), and the b-value as estimated by Nishikawa and Ide (2014).

3.4.1. Correlation with upper plate strain

We have used the SubMap database (Heuret and Lallemand, 2005, <http://www.submap.fr>) to extract the upper plate strain along most subduction zone transects. Following Jarrard's study (1986), Heuret and Lallemand (2005) have estimated the strain regime of oceanic subduction zones in a semi-quantitative way based on most representative focal mechanisms of earthquakes occurring within

the upper plate at a distance from the trench, i.e., in the arc and back-arc domains. In this study, we have reduced the seven initial strain classes from highly extensional (back-arc spreading) to highly compressional (back-arc shortening) into only 3 strain classes: extensional, neutral and compressional. The strain classes estimated over 200-km-wide transects have been correlated with 200-km-wide sampled mean roughness parameters obtained along trenches (see section 3.3.1.2, Figure 3.9). With respect to neutral regimes, compressional regimes correlate with slightly higher roughness amplitudes. The main difference is observed with extensional regimes which are associated with significantly larger roughness amplitudes especially at long wavelengths.

3.4.2. Correlation with seismic coupling

Seismic coupling coefficients, that is, the ratio of the amount of seismic slip to total amount of plate convergence over about a century (e.g., Ruff & Kanamori 1983; Peterson & Seno 1984), should normally range from 0 (pure creep) to 1 (all the slip is seismic). Since it is calculated over a period which could be shorter than the recurrence time of great earthquakes, the seismic coupling coefficient may be

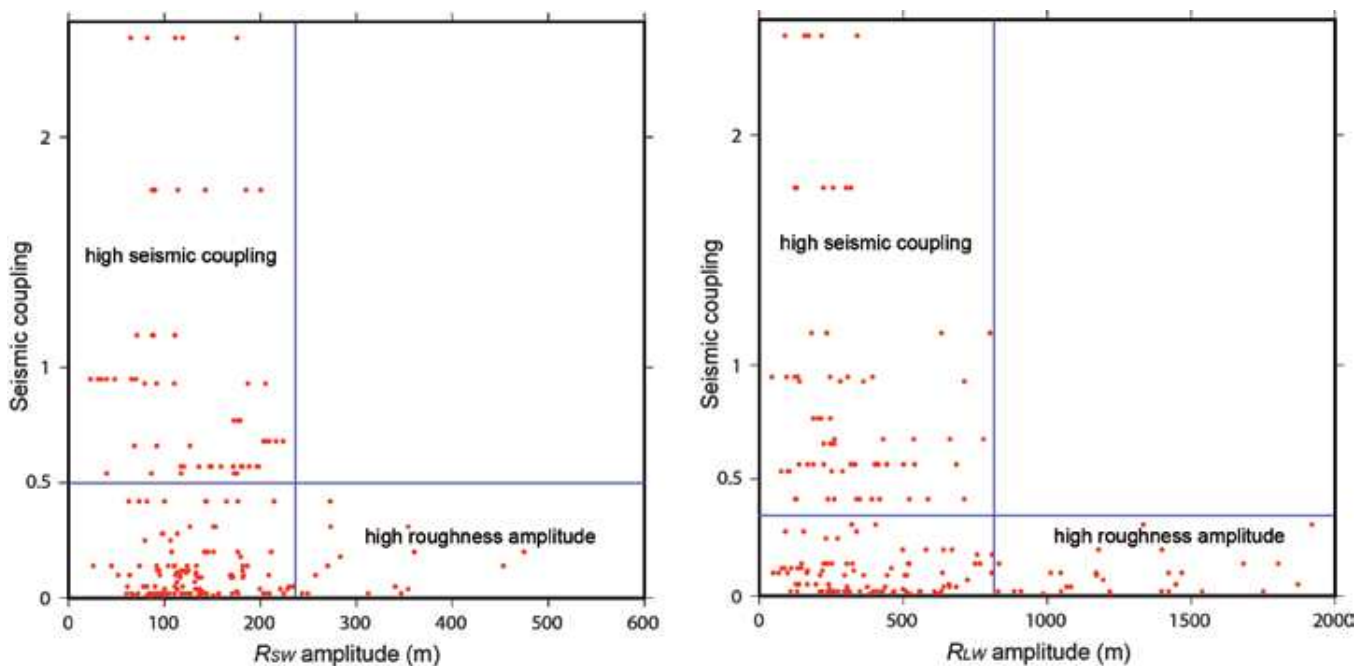


Figure 3.10. Distribution of roughness values of seafloor facing regions characterized by different seismic coupling coefficients as defined by Heuret et al. (2011).

larger than 1. We have used the values estimated by Heuret et al. (2011, www.submap.fr) based on Brune (1968) and computed over the period 1900-1975 using the Centennial catalog and 1976-2007 using the Harvard catalog, seismogenic zone dimensions deduced from seismicity analysis (Heuret et al., 2011) and a plate interface rigidity equal to 5×10^{10} N/m². The seismic coupling coefficients have been calculated over subduction segments typically 400 to 1,000 km long, whereas the roughness mean values are obtained over a distance of 200 km along trench. For that reason, the same seismic coupling value may be correlated with different mean roughness values. The cross-correlation between both R_{SW} and R_{LW} and seismic coupling is shown in Figure 3.10. It is noteworthy that high seismic coupling (> 0.5) is systematically observed for relatively small roughness amplitudes at both short and long wavelengths, respectively less than 230 m and 800 m. Reversely, relatively high roughness amplitudes ($R_{SW} > 230$ m and $R_{LW} > 800$ m) are systematically associated with low seismic coupling < 0.5 .

3.4.3. Correlation with b -values

The b value, that is, the negative slope of the power-law frequency-size distribution of earthquakes, is supposed to be correlated with the shear stress

(Gutenberg & Richter 1944): the higher the b -value, the lower the shear stress. Nishikawa and Ide (2014) have estimated the b values in 88 regions, 500 km-along-strike-wide each, where the number of seismic events (at least 100 events), issued from the Advanced National Seismic System (ANSS) catalogue from 1978 to 2009, was sufficient to estimate the completeness magnitude. They found a positive relation with the buoyancy of the subducting plate (plate age and trench depth) and no significant relation with the horizontal force balance (convergence rate and upper plate velocity). Among the 88 regions studied by Nishikawa and Ide (2014), we have been able to correlate the b -values for 70 of them where roughness data were coincident. To be coherent with the sampling area used by the authors to calculate the b -values, we have analyzed the coincident roughness over a similar trench length within a 250-km-wide strip seaward of the trench. Figure 3.11 shows that there is no significant correlation between the roughness and the b -value.

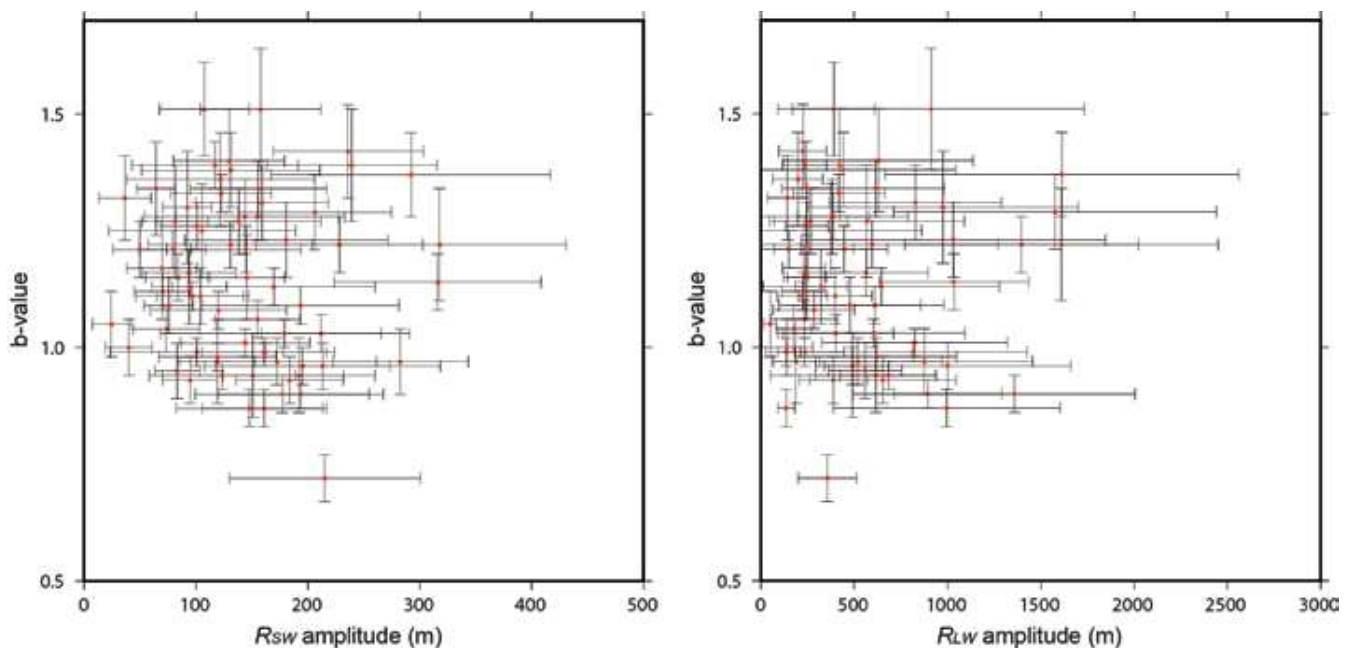


Figure 3.11. Distribution of roughness values of seafloor facing regions characterized by different b -values as calculated by Nishikawa and Ide (2014). Standard deviations of roughness values over the wide sampled areas are plotted together with those provided for the b -values.

3.5. Discussion

The sensibility of mega-earthquake rupture propagation to the amplitude and wavelength of the seismogenic subduction interface topography is still unclear. In this study, we have made the choice to focus on roughness rather than residual bathymetry, in order to better account for not only the absolute distribution of the elevation, but also for the relative deviation of the elevation around its mean value in a wide range of frequencies. In other words, we put the emphasis not only on the characterization of the subducting features themselves, but also on the topography gradient in the vicinity of the subducting features over distances comparable with those of large ruptures. This study provides a complete dataset of roughness characteristics along most oceanic subduction zones. Detailed correlations between the discrete distribution of the seafloor roughness and the seismogenic potential of the plate interface focusing on nucleation, propagation, maximum slip and arrest of the ruptures requires great attention and cannot be treated here. It is the topic of a complementary study (van Rijsingen et al. 2018).

3.5.1. No specific roughness signature for fracture zones

It is somewhat surprising that transform faults and fracture zones do not differ in their roughness signal from the global trend at both short and long wavelengths (Figure 3.8). Statistically, it means that the distribution of seafloor elevations has similar amplitudes and wavelengths as these linear features. In detail, we have observed that many of them can be traced on roughness maps: Investigator FZ, Ninety-East Ridge, Grijalva FZ for example, but in average they do not significantly differ from the background signature. The literature provides contrasting arguments regarding the effect of subducting fracture zones on earthquakes triggering. Müller and Landgrebe (2012) claim that the occurrence of great ($M_w \geq 8$) subduction earthquakes is strongly biased toward regions associated with intersections of oceanic fracture zones and subduction zones, but they also admit that those characterized by uplifted ridges are more prone to cause strong and persistent coupling in the subduction interface. Robinson et al. (2006) and Das and Watts (2009) saw a clear link between fracture zones and rupture dynamics during large earthquakes like the 1986 M_w 8.0 Andeanof Islands event, or the 2001 M_w 8.4 Peru event. In

these cases, the rupture was stalled by the fracture zones that acted as barriers. The same behavior has been observed for several other ruptures like the 2005 M_w 8.6 Sumatra event (Konca et al., 2008) or the 2010 M_w 8.8 Maule event (Contreras-Reyes et al., 2010). The lubricant role of subducting fracture zones was recently proposed for the Lesser Antilles by Schlaphorst et al. (2016), based on *b-value* studies. Here we can only conclude that for many fracture zones, we do not detect a specific signal in roughness at any wavelength from 12 to 100 km. However, their intrinsic weakness and potentially high fluid content may certainly play a role in the rupture dynamics during large earthquakes. Further investigations at wavelengths smaller than 12 km in high-resolution mapped areas should be conducted.

3.5.2. Clear specific roughness for seamounts

Seamounts lend themselves well to roughness investigations, especially at short wavelengths (Figure 3.8). Their roughness amplitude is almost twice the one of a “standard seafloor”. Numerous studies in the literature describe the role played by subducting seamounts in stopping or attenuating rupture propagation during large earthquakes off Honshu or Sumatra (e.g., Kodaira et al., 2000; Mochizuki et al., 2008; Henstock et al., 2016). In all these examples, the seamounts were relatively shallow. At larger depths, it is not excluded that subducting seamounts may behave as strong patches during moderate to large earthquakes, as proposed beneath the margin off Costa-Rica (Dominguez et al., 2000; Bilek et al., 2003). The question of the geodetic coupling associated with subducting seamounts is more debated than their role in seismogenesis, because both strong and weak interseismic coupling have been recorded above subducting seamounts on both sides of the Carnegie Ridge intersecting the north Andean subduction zone (Nocquet et al., 2016; Marcaillou et al., 2016; Collot et al., 2017). Roughness characterization thus appears to be good tool to explore its influence on the seismogenic potential as a function of amplitude or wavelength because earthquakes often nucleate close to seamounts and then propagate farther, indicating a possible control by the seamount.

3.5.3. Similar specific signature of seamounts and ridges at long wavelengths

Surprisingly, aseismic ridges cannot be distinguished from the global trend in terms of roughness at short wavelengths (Figure 3.8). This can be explained by the long wavelength of the ridges themselves, and the fact that they host both seamounts and regular seafloor. At long wavelengths, they share about the same roughness signal in average as the seamounts, covering a large range of roughness values in amplitude. Previous studies have shown that rough seafloor relief, and aseismic ridges in particular, promote creeping rather than seismic coupling (e.g., Kelleher and McCann, 1976; Wang and Bilek, 2014). The reason would be the development of a broad fracture network damaging the upper plate in a similar way as a seamount (Dominguez et al., 1998b, 2000) but at a larger scale. Looking in more detail, we often observe a clear positive signal in the roughness for narrow ridges and a very tiny signal for broad ridges (e.g., the Nazca, Carnegie or Cocos ridges, which size exceeds the window size), suggesting that narrow ridges have the same characteristics as seamounts.

3.5.4. To what extent can we classify the subduction zones with respect to roughness characteristics?

An important asset of the SubRough database is the possibility to compare any subduction zone with another. We have classified them into three groups from dominantly rough to dominantly smooth (see section 3.3.2) based on the ratio of low to high R_{LW} amplitudes over given trench segments. For practical reasons, we have proceeded trench by trench. Such sampling is somewhat arbitrary because the same trench can host rough and smooth sections, especially in the mixed group (Table 3.1, Figure 3.5). We have thus simplified the purpose in previous section 3.3.2, but the detailed description trench by trench remains valid, especially when analyzing the lateral variations in roughness amplitudes (Figure 3.6, 3.7 and A3.7 to A3.12).

3.5.5. Smooth areas and roughness complexities

The coincidence between thick trench fill and high

potential of mega-ruptures has been mentioned by several authors (e.g., Ruff, 1989; Heuret et al., 2012; Scholl et al., 2015). Assuming that the thick trench fill is mostly subducted and then smoothens the plate interface, which is not necessarily verified, authors conclude that a smooth plate boundary enhances seismic coupling and/or rupture propagation. In this study, we have made the choice to remove the contribution from the trench fill by exploring the seafloor at a distance of more than 10 km seaward of the trench, because we considered that part of or even all the trench fill material could be accreted at the front of the margin. We thus focus on the flatness of the subducting seafloor without any contribution from sediment supply in the trench (except if trench fill extends farther than 10 km away from the trench). The lateral extent of the smooth areas is indicated with horizontal lines along each profile in Figures 3.6, 3.7 and A3.7 to A3.12 (solid line if $R < 100$ m, dotted line if $R < 250$ m, see figure captions for more details). It is clear from Figures 3.7 and A3.7 that all trenches belonging to the “rough group” do not show large smooth areas, except locally (lateral extent less than 250 km) along the Mariana Trench. The smoothest seafloor is observed off Andaman, northern Sumatra, Antilles, Cascadia, Japan, Kamchatka, Eastern Aleutians, Western Alaska, Peru, Chile and Central America. Many of these regions have hosted $M > 8.5$ giant earthquakes (yellow stars in Figures 3.6, A3.10 & A3.12). The lateral extent of smooth areas should play a major role, if we consider that seamounts, ridges and fracture zones rather act as barriers or sources for rupture complexities. A recent study by Ye et al. (2018) suggested that earthquake complexity was primarily controlled by persistent geological factors. They have quantified the rupture complexity, using the excess radiated energy with respect to the minimum radiated energy expected for a similar source (REEF) for 119 $M_w > 7.0$ earthquakes. A careful comparison between REEF and roughness characteristics would allow to better characterize the nature of the permanent geological features. Corbi et al. (2017a) have demonstrated experimentally that the synchronization of slip patches to produce large events depends on the ratio of weak (barrier) to strong (asperity) patches sizes. In their analogue experiments, they observed that the barrier became permanent if its size was at least half the size of the asperities. If a link exists between the roughness of the subduction interface and its seismogenic potential (asperity vs barrier),

this might explain why the South Chile, Japan-Kuril, Eastern Aleutians-Alaska or Cascadia, where the proportion of rough to smooth lengths is often less than 0.5, are regions hosting mega-earthquakes. Further analyses are performed to better evaluate those ratios as well as the threshold values in roughness amplitudes (van Rijsingen et al. 2018).

3.5.6. Roughness and state of stress in subduction zones

It has been observed in some regions that the interseismic coupling, estimated by using geodetic measurements mainly onshore, was partly controlled by the roughness of the subduction interface (e.g., Nocquet et al., 2016; Yokota et al., 2016; Collot et al., 2017), even if no general law can be proposed between a given subducting relief type and its associated degree of coupling. We thus expected some trend by comparing the roughness characteristics of the seismogenic zone proxy with the *b-value* or the seismic coupling. The lack of correlation with the *b-value* may be due to the width of the sampled area (500 km x 250 km), which reduces the signal by averaging it (see the large error bars in R values in Figure 3.11). The correlation with the seismic coupling is more satisfying, since relatively rough subducting seafloor is always associated with low seismic coupling and high seismic coupling is always associated with relatively smooth subducting seafloor (Figure 3.10). The seismic coupling coefficient is only indicative because it depends on earthquake recurrence for very large events, which is a function of the degree of coupling and the subduction (loading) rate. It means that we underestimate the seismic coupling in slow subduction zones (like the Antilles), or in regions characterized by earthquake supercycles (Herrendorfer et al. 2015; Nocquet et al. 2016). Despite this approximation, we still observe a clear correlation between high interseismic coupling and low roughness, which is something expected if we consider that creeping is more characteristic of rough subduction interfaces, as proposed by Wang and Bilek (2014).

The subduction of prominent seamount chains, like the D'Entrecasteaux Zone (Vanuatu) or the Louisville Ridge (Tonga) has been described as synchronous with active shortening in the volcanic arc region (Collot et al., 1985; Pelletier et al., 1998;

Lallemand et al., 1990). We thus expected that large subducting features might also contribute in upper plate compressive stress. Our statistical analysis apparently does not support such correlation with upper plate stress as a rule. This may indicate that the roughness of the subducting seafloor mainly affects the nearby area of the plate interface even if it contributes in a few regions to the upper plate stress.

3.5.7. Limitations and perspectives of the study

As discussed in section 3.2.3.2.5, we are fully aware that the unsubducted seafloor is only a proxy of the seismogenic zone and does not represent its exact replica. Seafloor roughness anisotropy and mass transfers between the subducting and overriding plate during the subduction process certainly alter in some way the correlation between the two areas, subsequently diminishing the expected signal. Our computational method does not make the difference between positive and negative reliefs (Equation (3.1)). It is then possible that subducting lows like grabens will be filled by material from the upper plate during the subduction process and will finally produce a smooth subduction interface. However, such lows do not contribute much in the roughness because the reference surface, used for calculating the relative bathymetry, is estimated from a bathymetric grid where seamounts and ridges are removed, so that the positive features dominate the signal. Finally, the comparison of the seafloor roughness along most oceanic subduction zones provides a good basis for addressing numerous studies related to the dynamics of subduction. Building on the good correlation between seafloor roughness and seismic coupling, van Rijsingen et al. (2018) have performed a detailed analysis based on a newly compiled ruptures catalog for 1900-2017 $M_w \geq 7.5$ earthquakes.

3.6. Conclusion

In this study, we provide a new seafloor roughness database, called SubRough, that allow to characterize the seafloor prior to subduction along most oceanic trenches. Based on R_{LW} amplitude, we propose a classification of the seafloor segments adjacent to subduction zones from dominantly rough to dominantly smooth. The investigated regions can be used as proxies for the adjacent seismogenic zones and thus provide constraints to better understand the seismicity pattern, especially for large to great earthquakes, where rupture complexities or slip patches synchronizations often occur. Large seamounts and ridge flanks mainly contribute in the high roughness character, which in turn is associated with regions of low seismic coupling. Conversely, high seismic coupling is mainly observed in regions characterized by smooth seafloor.

4. How subduction interface roughness influences the occurrence of large interplate earthquakes

Published as:

van Rijsingen, E., Lallemand, S., Peyret, M., Arcay, D., Heuret, A., Funiello, F., & Corbi, F. (2018). How subduction interface roughness influences the occurrence of large interplate earthquakes. *Geochemistry, Geophysics, Geosystems*, 19. <https://doi.org/10.1029/2018GC007618>

Abstract

The role of seafloor roughness on the seismogenic behavior of subduction zones has been increasingly addressed over the past years, although their exact relationship remains unclear. Do subducting features like seamounts, fracture zones or submarine ridges act as barriers, preventing ruptures from propagating, or do they initiate megathrust earthquakes instead? We address this question using a global approach, taking into account all oceanic subduction zones and a 117yr time window of megathrust earthquake recording. We first compile a global database, SubQuake, which provides the location of a rupture epicenter, the overall rupture area and the region where the largest displacement occurs (the seismic asperity) for $M_w \geq 7.5$ subduction interplate earthquakes. With these data, we made a quantitative comparison with the seafloor roughness seaward of the trench, which is assumed to be a reasonable proxy for the subduction interface roughness. We compare the spatial occurrence of megathrust ruptures, seismic asperities and epicenters, with two roughness parameters: the short wavelength roughness R_{SW} (12-20 km), and the long wavelength roughness R_{LW} (80-100 km). We observe that ruptures with $M_w \geq 7.5$ tend to occur preferentially on smooth subducting seafloor at long wavelengths, which is especially clear for the $M_w > 8.5$ events. At both short- and long wavelengths, seismic asperities show a more amplified relation with smooth seafloor than rupture segments in general. For the epicenter correlation, we see a slight difference in roughness signal, which suggests that there might be a physical relationship between rupture nucleation and subduction interface roughness.

4.1. Introduction

Over the past decades, large interplate earthquakes ($M_w \geq 7.5$) in subduction zones have received a great deal of attention from the scientific community. Their high magnitudes, sometimes even exceeding $M_w 9$, make them among the most destructive earthquakes on Earth. Therefore, unravelling the mechanism and both the spatial and temporal occurrence of large megathrust earthquakes is of great importance. Why do some subduction zones frequently host such events, while others remain silent for hundreds of years? Many subduction zone parameters have been proposed to explain this (e.g., Lallemand & Heuret, 2017). It has long been thought that young and fast subducting plates were more likely to host such large events (Ruff & Kanamori, 1980), but the recent $M_w > 9.0$ Sumatra (2004) and Tohoku (2011) events have changed this perspective (e.g., Stein & Okal 2007, 2011).

Another parameter that has been proposed for several decades already, is the amount of sediments filling the trench (Brizzi et al., 2018; Heuret et al., 2012; Ruff, 1989; Scholl et al., 2015). It is shown that subduction zones with large amounts of trench sediments positively correlate with the occurrence of great interplate earthquakes. This relates to another theory which developed over the years, suggesting a negative correlation between subduction interface roughness and megathrust earthquakes (Bassett & Watts, 2015a; Das & Watts, 2009; Heuret et al., 2012; Kelleher & McCann, 1976; Kopp, 2013; Loveless et al., 2010; Sparkes et al., 2010; Wang & Bilek, 2014). Subduction interface roughness results from a combined effect of topographic features on the seafloor (e.g., seamounts, ridges or plateaus), the amount of sediments, and possible deformation processes occurring during subduction (e.g., tectonic erosion).

Numerous studies focus on the effect of topographic features on the occurrence of a single-, or several megathrust events. Some propose that subducting features like seamounts or fracture zones could act as asperities and therefore facilitate large ruptures (Cloos 1992; Scholz & Small 1997; Bilek et al. 2003; Müller & Landgrebe 2012; Landgrebe & Müller 2015), while others propose the opposite: subducting topographic highs acting as barriers to rupture propagation (Geersen et al., 2015; Henstock et al., 2016; Kodaira et al., 2000; Mochizuki et al., 2008; Robinson et al., 2006; Wang & Bilek, 2011). Due to

the discrepancy among the possible interpretations, sometimes restricted to a specific region or feature, the scientific community so far has not reached a general consensus on the relationship between megathrust earthquakes and subduction interface roughness.

Among different factors like temperature (e.g., Gutscher & Peacock, 2003; Peacock & Hyndman, 1999), or fluids (e.g., Heise et al., 2017; Ranero et al., 2008; Saffer, 2017; Saffer & Tobin, 2011; Moreno et al., 2018) that may play a role in tuning megathrust seismicity, here we focus on the potential role of subduction interface roughness on the occurrence of $M_w \geq 7.5$ events. We use a global approach, taking into account all oceanic subduction zones and a 117 yr time window of megathrust earthquakes recording. By performing a quantitative comparison, we aim to provide a first order relationship, while at the same time acknowledging that exceptions in specific regions may still exist.

This work follows up on a previous study by Lallemand et al. (2018), who provide a global database of seafloor roughness seaward of all oceanic subduction zones – SubRough - and who already made a first-order comparison with several parameters related to the state of stress in subduction zones. We extend this approach, by first providing a global database - SubQuake - for subduction megathrust earthquakes, which will then be compared in a quantitative way to the seafloor roughness seaward of the trench.

The SubQuake database lists events that occurred since 1900, detailing spatial characteristics for 182 interplate earthquakes with moment magnitude ≥ 7.5 . Since most of these earthquakes rupture a relatively large portion of the subduction megathrust (i.e., 103-105 km²; Allen & Hayes, 2017), it is not sufficient to only consider the location of a rupture's hypocenter. To better understand how the size and location of seismic ruptures relate to the subducting seafloor roughness, a more accurate description of the spatial characteristics of these ruptures is necessary. Rupture initiation, propagation direction, rupture arrest and the location of the largest displacement (i.e., the seismic asperity; e.g., Lay & Kanamori, 1981; Wang & Bilek, 2014), are all characteristics whose spatial occurrence is still poorly understood. The SubQuake database compiles information on earthquake epicenters, rupture

area contours, and if possible seismic asperity contours. The maximum possible timespan in terms of catalogue completeness (i.e., 1900 – 2017), and the global coverage of the database, make it a useful tool for studying spatial rupture characteristics with respect to many subduction zone parameters, not necessarily limited to the seafloor roughness as presented in this study. The entire database is available online via subquake.gm.univ-montp2.fr. In this paper, we first briefly present the recently compiled SubRough database (Lallemand et al.,

2018). Next, we present how the earthquake data for the new SubQuake database have been collected and discretized into an earthquake grid for each subduction zone. Then, we discuss the procedures used for the quantitative comparison with the seafloor roughness, followed by the comparison results. Finally, we discuss our main findings by looking at how they relate to the results and concepts previously published.

4.2. Methodology

4.2.1 The roughness database

For the global comparison between seafloor roughness and the occurrence of subduction megathrust earthquakes, we use the SubRough database, a parameter database estimating the seafloor roughness seaward of the trench, presented by Lallemand et al. (2018). They have developed an approach to estimate the roughness signal at different spatial wavelengths to characterize the seafloor bathymetry prior to subduction, to be used as a proxy for the roughness of the subduction interface (Figure 4.1).

From the GEneral Bathymetric Charts of the Oceans (GEBCO) database (Smith & Sandwell 1997; Becker et al. 2009; Weatherall et al. 2015), the seafloor roughness has been determined by using power spectral densities (PSD). Over a 250 km wide, trench-parallel strip, a spectral analysis has been performed by using a circular sliding window (radius of 100 km; step of 10 km). Based on the resulting PSD, two wavelength bandwidths have been selected for further analysis: a short wavelength bandwidth from 12-20 km to compute one roughness parameter (R_{SW}), and a long wavelength bandwidth from 80-100 km to compute the other parameter (R_{LW}). The choice for the R_{SW} bandwidth, the lower boundary, comes from the limited availability of high resolution (i.e., < 12 km) data in the GEBCO dataset. High-resolution measurements from ship surveys are only available for a few specific regions (i.e., only 10% of subduction trench length), while the lower resolution measurements from satellite gravity anomalies are available worldwide, with a global resolution of

12.5 km (Smith & Sandwell 1997). The choice for the R_{LW} bandwidth, the upper boundary, is related to the size of the circular sliding window used for the spectral analysis. For wavelengths longer than 100 km, the number of samples within this window decreases, which makes PSD computation at very long wavelengths less reliable.

R_{SW} and R_{LW} highlight different topographic features on the seafloor, such as small and intermediate size seamounts and fracture zones in the short wavelength roughness signals, and large seamounts, seamount chains and submarine ridges for long wavelength roughness. Their respective roles in earthquake nucleation and rupture propagation/ending are likely to be very different, which may be tested by estimating their signature in the seafloor roughness separately. Roughness amplitudes at both wavelength bandwidths are given in meters, where 95% of the R_{SW} values generally fall within the [0-300 m] range, with a mean of 145 m. For R_{LW} , 95% of the roughness values vary in the range [0-1500 m], with a mean around 485 m.

Both the short- and long wavelength roughness parameters are used in this study, to perform a global, and quantitative comparison between the seafloor roughness seaward of the trench and the occurrence of subduction megathrust earthquakes.

4.2.2 The SubQuake database

One of the biggest challenges of compiling an earthquake database covering more than 100 years, relies on the availability of the data and the disparity

in quality. Because of the lack of good global, and continuous coverage of seismometers during most of the 20th century, data are sparse and difficult to retrieve. In addition, the methods for obtaining slip distributions have improved considerably over the past decades, leading to more detailed solutions for recent events, often based on a combination of high quality seismic-, geodetic-, and/or tsunami data (e.g., Nocquet et al., 2016; Yue & Lay, 2013). In this section, we first address the already available databases that provide rupture slip distributions. Then, we discuss how we derived the earthquake's epicenters, rupture contours and seismic asperity contours, and how we accounted for the difference in quality. Finally, we explain how the data have been discretized into a rupture grid covering all subduction zones.

4.2.2.1. Already available databases

Several attempts have been made to compile a database providing information on the spatial characteristics of seismic ruptures, not in particular dedicated to subduction megathrust earthquakes

(Hayes, 2017; Mai & Thingbaijam, 2014; Ye et al., 2016). The SRCMOD database displays 364 finite fault rupture models for 169 earthquakes over a time frame of ~ 100 years. This database shows different models for the same event and displays the various methods that have been used to obtain slip distributions. Recent events are very well represented (e.g., 21 different inversion models for the 2011 Tohoku earthquake, Lay, 2017), while only very few inversion models exist for events older than 1960. Ye et al. (2016) and Hayes (2017; USGS) also gathered rupture models for different events, but chose a specific time window (1990 – present) and a consistent modelling approach. Ye et al. (2016) documented finite fault models for all $M_w \geq 7.0$ subduction interplate earthquakes from 1990 to 2015, based on global broadband body wave inversions. Hayes (2017) used finite fault models based on body- and surface wave solutions (Ji et al. 2002), and provides a complete catalogue for ruptures with $M_w \geq 7.5$ since 1990 (further referred to as the USGS database). The latter two approaches lead to a more homogeneous database, in which different events can be compared more reliably.

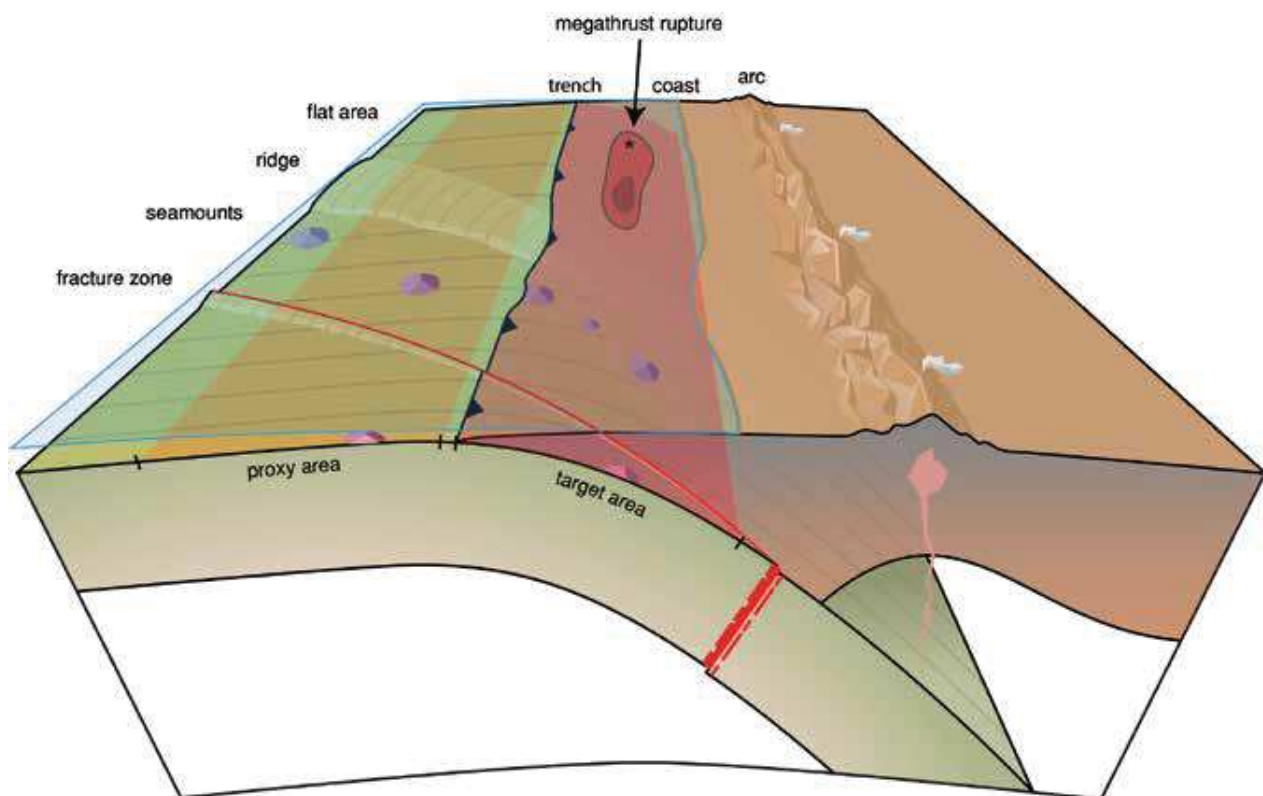


Figure 4.1. Overview of a subduction setting, indicating the area of the seafloor that is used as a proxy for the seismogenic zone (target area).

4.2.2.2. SubQuake data compilation and classification

For compiling the SubQuake database, hypocenters of $M_w \geq 7.5$ events from the recently updated ISC-GEM catalogue (Storchak et al., 2013, updated in January 2016) were analyzed to select subduction megathrust earthquakes. The selection criteria for this analysis follow from Heuret et al. (2011), which include examining the focal mechanism, hypocenter depth, fault plane orientation, and distance from the trench. If no information about the nature of the event could be found (in the case of events older than 1975), the earthquake is assumed to be a thrusting event along the subduction plate interface because of its large magnitude.

For collecting earthquake rupture contours, we rely on the SRCMOD and USGS databases, as well as on many individual publications. Before the implementation of the World Wide Standardized Seismograph Network (WWSSN) in 1963, earthquake rupture zones were mainly determined by using aftershocks. The older publications we use in this study therefore usually provide only an estimate of the rupture area. When seismic data became more abundant, people started using strong ground motions and teleseismic data to calculate slip distributions (e.g., Beck & Ruff, 1987). This did not only allow them to determine the spatial extent of the rupture area, but also gave them more insights in rupture evolution (e.g., the 1986 M_w 8.0 Andreanof Islands earthquake; Das & Kostrov, 1990).

Over the past decades, seismic inversion techniques have improved significantly, resulting in an increase in the accuracy of rupture characteristics. In addition, the ongoing development of continuous GPS measurements and InSAR data contributes to a better determination of co-seismic slip, but also allows to better monitor the coupling during the interseismic phase within subduction zones (e.g., Métois et al., 2012). However, all these new technologies and improved methods result in many different inversion models for the same seismic event, often showing different slip distribution solutions.

We therefore chose to use the USGS database as a basis for the most recent events (i.e., ≥ 1990) in order to keep the inversion method as consistent as possible. Several exceptions exist, for which we believe that another inversion model yields a more accurate representation of the slip distribution, thanks to a combination of high quality seismic and geodetic data (e.g. Sumatra 2004, Tohoku 2011, Pedernales 2016). For events older than 1990, we either relied on the SRCMOD database, or on individual publications, in which we selected rupture models as a function of the methods that were implemented. In addition, we integrated information from Bassett & Watts (2015a), who collected many rupture contours for several major subduction zones.

From the studies providing information on the slip distribution, we extracted seismic asperity regions.

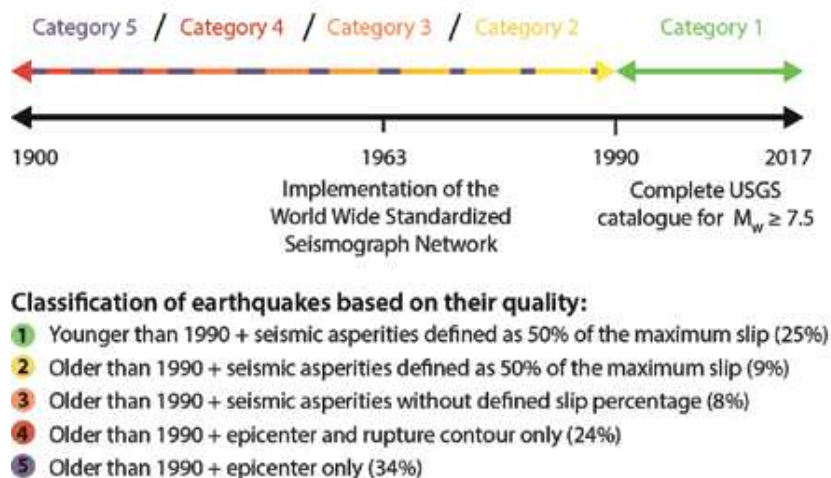


Figure 4.2. Categories of the SubQuake database. The classification is based on the age and seismic asperity definition of the event. For some events, no rupture contour data have been found, indicated by the dashed purple line (category 5). Percentage of ruptures related to the total number of events is given for each category.

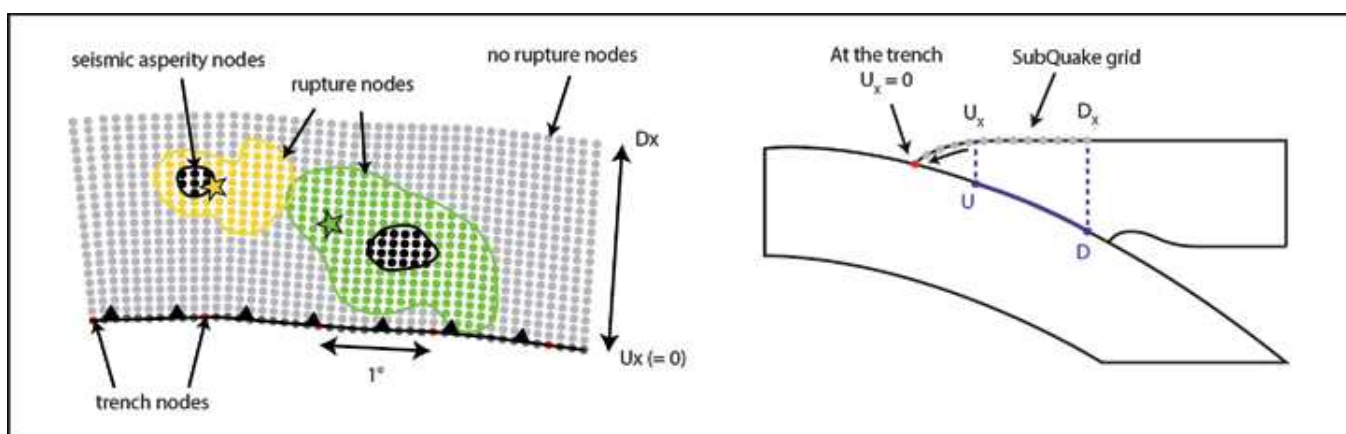


Figure 4.3. SubQuake data discretization. Trench nodes have been interpolated every 0.1° and projected in a trench-perpendicular direction, delimited by U_x and D_x , the horizontal distances to the trench from the updip (U) and the downdip limit (D) of the seismogenic zone, respectively. After reviewing the trenchward extent of the SubQuake ruptures, U_x has been set to 0. Nodes falling within a rupture or seismic asperity contour are classified as rupture (colored according to Figure 4.2 categories) and seismic asperity nodes (black). Stars depict epicenters. All remaining nodes are classified as no-rupture nodes (grey).

For the digital slip distributions provided by the USGS and SRCMOD databases, we defined seismic asperities as regions exceeding ‘50% of the maximum slip’, following the definition by Yamanaka & Kikuchi (2004). For the remaining events, we relied on the seismic asperity information given by individual studies.

All events in the SubQuake database are classified as a function of their quality (Figure 4.2). We chose to use a classification system based on the rupture age and the way its seismic asperity is defined. The age and determination method of the seismic asperity in a study adequately reflect the quality of the model, both in terms of event age and method used (e.g., old rupture models based on aftershock distributions cannot indicate a seismic asperity and therefore belong to category four). Ruptures for which we were not able to obtain any information about the rupture contour have been classified as category 5.

4.2.2.3. Assembling the SubQuake data into a grid

The SubQuake data are assembled into a grid for all subduction zones (Figure 4.3). This grid is a surface projection of the seismogenic zone, for which the trench-perpendicular extent is based on Heuret et al. (2011), who defined the horizontal distance from the trench to the updip- and the downdip limits of the seismogenic zone for all subduction zones (U_x and D_x , respectively). The node spacing (10 km) is

chosen to be the same as the one of the SubRough grid. The SubQuake rupture- and seismic asperity contours are used to assign each grid node with a specific seismic behavior, either ‘no rupture’, ‘rupture’ (taking into account the 4 different rupture categories) or ‘seismic asperity’. More detailed information about the compilation of the SubQuake grid can be found in the appendix (section A4.1).

4.2.3 Comparison strategy

A global, quantitative comparison between the SubRough and SubQuake datasets is done following two strategies: the first one is based on the SubQuake grid (for rupture- and seismic asperity contours), while the second one focuses on the location of rupture epicenters. The aim of these comparison strategies is to evaluate the presence of a rupture, seismic asperity or epicenter in the SubQuake grid and subsequently select the roughness data that face these regions seaward of the trench. Both procedures will briefly be discussed below. More detailed descriptions of the comparison algorithms can be found in the appendix (section A4.2).

4.2.3.1. SubQuake grid and facing SubRough data

The 2D SubQuake grid has been divided into 1D segments along the trench, based on the occurrence of ruptures and seismic asperities. An algorithm evaluates the presence of either rupture or seismic

asperity nodes in the continuation of every trench node, following the trench-perpendicular azimuth (Figure 4.4a and b). This results in a selection of trench segments for all three categories (i.e., no rupture, rupture and seismic asperity). Note that the no-rupture segments simply indicate regions where no $M_w \geq 7.5$ have been observed between 1900 and 2017. They should not be directly interpreted as areas where ruptures can never occur, since the recurrence time may exceed the 117 yr time window due to low subduction rates or only partial coupling.

With this segment-approach, the trench-perpendicular information of the SubQuake grid is lost, since the algorithm does not take into account the number of rupture or seismic asperity nodes found in the continuation of each trench node. However, since we use the roughness seaward of the trench as a proxy for the subduction interface, our knowledge of trench-perpendicular roughness variations is limited. We therefore mainly focus on the trench-parallel variations in subduction interface roughness.

Based on the three different types of segments, the SubRough data seaward of the trench, for both the short wavelength R_{SW} and the long wavelength R_{LW} can be selected and evaluated (see section 4.2.1 for details). For this, we use a trench-perpendicular direction for data selection, except for some regions

where we take into account the obliquity of specific linear features extending into the trench (i.e. for the Joban Seamount chain in Japan, the Louisville ridge in Tonga and the Murray Ridge in Makran). In most cases, the seafloor right in front of the trench is a good proxy for the subduction interface (Das & Watts 2009; Bassett & Watts 2015a) and the use of this proxy therefore seems a reasonable assumption for this global study. The roughness data selected for the rupture-, no-rupture-, and seismic asperity segment groups are analyzed in terms of density distribution, illustrating which roughness amplitudes are the most common.

4.2.3.2. Epicenters and facing SubRough data

All 182 epicenters have been correlated with R_{SW} and R_{LW} seaward of the trench. For each epicenter, the closest trench node has been selected based on a spherical approximation with great circles (Global Mapping Tools, Wessel et al., 2013). For these trench nodes, roughness data perpendicular to the trench are selected within a 50 km wide and 250 km long strip (i.e., taking into account the complete width of the roughness bands; Figure 4.4c). For epicenters located in regions where an oblique projection has been performed for the SubQuake grid, the same modified azimuth has been used for roughness data selection.

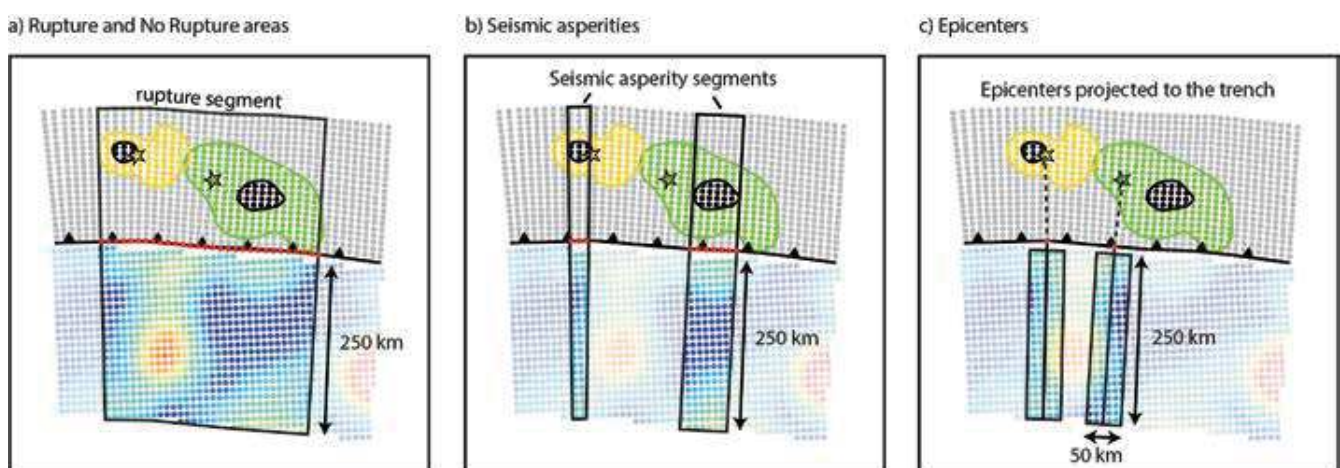


Figure 4.4. Trench segmentation and data selection as a function of seismogenic behavior: rupture and seismic asperity (a and b) and epicenters (c). Colors in the SubQuake grid (landward of the trench) represent the rupture categories (see Figure 4.2); colors on the seaward side illustrate the variety of seafloor roughness (from dark blue being smooth to red being rough). Red nodes depict the along trench segments, and stars depict epicenters.

4.3. Results

The results of this study are presented in two main sections: 1) the new global database that we compiled, and 2) the comparison with the seafloor roughness data. Regarding the SubQuake database (section 4.3.1), we discuss the location of a rupture's epicenter with respect to its seismic asperity (section 4.3.1.1.), and we classify all subduction zones according to their rupture length ratio (section 4.3.1.2). In section 4.3.2, where we show the comparison to the seafloor roughness, we first discuss a first order comparison between the rupture length ratio and the percentage of smooth seafloor for each region. Then we discuss in more detail nine regions that together represent the variety of observed seismogenic behavior, after which we study the relation between earthquake magnitude and seafloor roughness at a global scale. Finally, we show the comparison of seismic asperity segments and rupture epicenters to the seafloor roughness.

4.3.1 SubQuake Results

Table 4.1 lists all $M_w \geq 7.5$ subduction megathrust earthquakes since. From the 82 collected ruptures in our database, 45 events are category 1 ruptures, 16 category 2, 15 category 3, 44 category 4 and 62 for category 5.

4.3.1.1. Rupture area vs. moment magnitude

From the SubQuake rupture contours, rupture areas have been calculated. Figure 4.5 shows the rupture area (A) vs. moment magnitude (M_w) for all category 1-4 ruptures, including several scaling relationships (Allen & Hayes, 2017; Strasser et al., 2010; Ye et al., 2016). We have used orthogonal regression (i.e., accounting for measurement errors in both x and y directions) to find a scaling relation based on our own

data. In addition, we calculated the coefficient of determination (R^2) for each category. Both category 1 and 2 events show a good correlation between rupture area and moment magnitude ($R^2 = 0.65$ and 0.6 , respectively), while for categories 3 and 4 the correlation decreases ($R^2 = 0.27$ for cat 3; $R^2 = 0.09$ for cat 4). Events in these categories are generally older, and therefore have a larger uncertainty for both the moment magnitude and the rupture area. Category 4 rupture contours are often based on aftershock distributions and could therefore overestimate the actual rupture area (Duong et al., 2009). Since the moment magnitude relies on both the rupture area and average slip, variations in average slip that are not proportional with the rupture area can also affect the scaling relationship between rupture area and moment magnitude (e.g., up to 60 m of slip for the M_w 9.1 Tohoku 2011 event; Yue & Lay, 2013). Despite the decreasing correlation for the lower quality events, the scaling relation based on all events (cat 1-4) shows a trend similar to the scaling law provided by Allen & Hayes for earthquakes with magnitudes up to 8.6 (blue line in Figure 4.5.), which is mainly based on events younger than 1990, of which many have been used for compiling the SubQuake dataset. This indicates that the decreasing correlation for the category 3-4 events does not strongly affect the global trend.

All three $M_w > 9.0$ ruptures (i.e., M_w 9.1 Tohoku 2011, M_w 9.3 Alaska 1964 and M_w 9.6 Chile 1960) have smaller rupture areas than expected from both the linear scaling by Strasser et al. (2010) and our own scaling law, suggesting that a saturation of the rupture area might occur for very high magnitudes. A saturation of the rupture width has been suggested before (e.g., Sommerville et al., 2015; Tajima et al., 2013, Allen & Hayes, 2017), and even though rupture length can continue to increase, this rupture

Table 4.1.
List of all SubQuake events.

N°	Location	Date	M_w	Cat	Method	Author
182	Puerto Quellon, Chile	25-12-2016	7.61	1	Body / Surf	Hayes (2017)
181	Pedernales, Ecuador	16-4-2016	7.82	1	Body / HRGPS / InSAR	Nocquet et al. (2016)
180	Illapel, Chile	16-9-2015	8.23	1	Body / Surf	Hayes (2017)
179	Kokopo, Papua New Guinea	5-5-2015	7.47	1	Body / Surf	Hayes (2017)
178	Panguna, Papua New Guinea	19-4-2014	7.47	1	Body / Surf	Hayes (2017)
177	Iquique, Chile	3-4-2014	7.78	1	Body / Surf	Hayes (2017)
176	Iquique, Chile	1-4-2014	8.18	1	Body / Surf	Hayes (2017)

4. How subduction interface roughness the occurrence of large interplate earthquakes

N°	Location	Date	M _w	Cat	Method	Author
175	Costa Rica	5-9-2012	7.62	1	Body / Surf	Hayes (2017)
174	Oaxaca, Mexico	20-3-2012	7.47	1	Body / Surf	Hayes (2017)
173	Tohoku, Japan	11-3-2011	9.09	1	Body / Surf / HRGPS	Yue & Lay (2013)
172	Kepulauan Mentawai, Indonesia	25-10-2010	7.83	1	Body / Surf	Hayes (2017)
171	Northern Sumatra	6-4-2010	7.82	1	Body / Surf	Hayes (2017)
170	Maule, Chile	27-2-2010	8.79	1	Body / Surf	Hayes (2017)
169	Vanuatu	7-10-2009	7.62	1	Body / Surf	Hayes (2017)
168	Antofagasta, Chile	14-11-2007	7.73	1	Body / Surf	Hayes (2017)
167	Sumatra, Indonesia	12-9-2007	8.49	1	Body / Surf	Hayes (2017)
166	Pisco, Peru	15-8-2007	7.97	1	Body / Surf	Hayes (2017)
165	Solomon Islands	1-4-2007	8.07	1	Body / Surf	Hayes (2017)
164	Kuril Islands	15-11-2006	8.3	1	Body / Surf	Hayes (2017)
163	Java, Indonesia	17-7-2006	7.72	1	Body / Surf	Hayes (2017)
162	Tonga	3-5-2006	7.97	1	Body / Surf	Hayes (2017)
161	Sumatra, Indonesia	28-3-2005	8.62	1	Body / Surf	Hayes (2017)
160	Sumatra, Indonesia	26-12-2004	9.00	1	Body / Surf	Ammon et al. (2005)
159	Rat Islands, Alaska	17-11-2003	7.76	1	Body / Surf	Hayes (2017)
158	Hokkaido, Japan	25-9-2003	8.26	1	Body / Surf	Hayes (2017)
157	Colima, Mexico	22-1-2003	7.48	1	Body / Surf	Hayes (2017)
156	Southern Peru	7-7-2001	7.61	1	Body / Surf	Hayes (2017)
155	Southern Peru	23-6-2001	8.39	1	Body / Surf	Hayes (2017)
154	New Britain, Papua New Guinea	17-11-2000	7.77	1	Body / Surf	Hayes (2017)
153	New Ireland, Papua new Guinea	16-11-2000	7.81	1	Body / Surf	Hayes (2017)
152	Kamchatka	5-12-1997	7.76	1	Body / Surf	Hayes (2017)
151	Santa Cruz Islands	21-4-1997	7.70	1	Body / Surf	Hayes (2017)
150	Central Peru	12-11-1996	7.71	1	Body / Surf	Hayes (2017)
149	Andreanof Islands	10-6-1996	7.88	1	Body / Surf	Hayes (2017)
148	Northern Peru	21-2-1996	7.51	1	Body / Surf	Hayes (2017)
147	Kuril Islands	3-12-1995	7.88	1	Body / Surf	Hayes (2017)
146	Colima, Mexico	9-10-1995	7.98	1	Body / Surf	Hayes (2017)
145	Bougainville, Papua New Guinea	16-8-1995	7.72	1	Body / Surf	Hayes (2017)
144	Antofagasta, Chile	30-7-1995	8.00	1	Body / Surf	Hayes (2017)
143	Honshu, Japan	28-12-1994	7.73	1	Body / Surf	Hayes (2017)
142	Java, Indonesia	2-6-1994	7.76	1	Body / Surf	Hayes (2017)
141	Kamchatka	8-6-1993	7.48	1	Body / Surf	Hayes (2017)
140	Nicaragua	2-9-1992	7.63	1	Body / Surf	Hayes (2017)
139	Kuril Islands	22-12-1991	7.57	1	Body / Surf	Hayes (2017)
138	Costa Rica	22-4-1991	7.62	1	Body / Surf	Hayes (2017)
137	Mindanao, Philippines	15-12-1989	7.52	5	-	
136	Antofagasta, Chile	5-3-1987	7.54	5	-	
135	Andreanof Islands	7-5-1986	7.95	3	Body	Boyd et al. (1995)
134	Guerrero, Mexico	21-9-1985	7.54	3	Body	Ruff and Miller (1994)
133	Michoacan, Mexico	19-9-1985	7.97	2	Body / SGM	Mendoza & Hartzell (1989)
132	Valparaiso, Chile	3-3-1985	7.95	2	Body / Surf / SGM	Mendoza et al. (1994)
131	Solomon Islands	7-2-1984	7.54	5	-	

N°	Location	Date	M_w	Cat	Method	Author
130	Atacama, Chile	4-10-1983	7.63	5	-	
129	Costa Rica	3-4-1983	7.45	3	Body / Surf	Adamek et al. (1987)
128	Tonga	19-12-1982	7.47	4	Aftershocks	Christensen and Lay (1988)
127	Loyalty Islands	25-10-1980	7.45	4	Aftershocks	Tajima & Kanamori (1985)
126	Santa Cruz Islands	17-7-1980	7.73	5	-	Tajima & Kanamori (1985)
125	Santa Cruz Islands	8-7-1980	7.47	5	-	Tajima & Kanamori (1985)
124	Ecuador	12-12-1979	8.09	3	Body / Surf	Swenson & Beck (1996)
123	Oaxaca, Mexico	29-11-1978	7.75	4	Aftershocks	Singh et al. (1985)
122	Honshu, Japan	12-6-1978	7.63	2	SGM	Yamanaka & Kikuchi (2004)
121	Kuril Islands	23-3-1978	7.56	4	Aftershocks	Perez (2000)
120	Kermadec Islands	14-1-1976	7.79	4	Aftershocks	Nishenko (1991)
119	Tonga, Samoa Islands	26-12-1975	7.70	5	-	Tajima & Kanamori (1985)
118	Philippines	31-10-1975	7.50	5	-	
117	Solomon Islands, doublet (a)	20-7-1975	7.60	4	Body / Surf	Lay & Kanamori (1980)
116	Solomon Islands, doublet (b)	20-7-1975	7.60	4	Body / Surf	Lay & Kanamori (1980)
115	Kuril Islands	10-6-1975	7.50	4	Aftershocks	Schwartz & Ruff (1987)
114	Central Peru	3-10-1974	8.10	2	Body	Hartzell & Langer (1993)
113	Hokkaido, Japan	17-6-1973	7.80	3	Body	Schwartz & Ruff (1987)
112	Kuril Islands	28-2-1973	7.50	5	-	
111	Colima, Mexico	30-1-1973	7.60	3	Body	Ruff & Miller (1994)
110	Mindanao, Philippines	2-12-1972	8.00	4	Aftershocks	Acharya (1980)
109	Solomon Islands	17-8-1972	7.50	5	-	
108	Solomon Islands	26-7-1971	8.10	2	Body	Park & Mori (2007)
107	Solomon Islands	14-7-1971	8.00	2	Body	Park & Mori (2007)
106	Valparaiso, Chile	9-7-1971	7.80	4	Aftershocks	Comte et al. (1986)
105	Sumatra	21-11-1969	7.59	5	-	Tajima & Kanamori (1985)
104	Kuril Islands	11-8-1969	8.20	3	Body	Schwartz & Ruff (1985)
103	Talau, East Indonesia	30-1-1969	7.60	5	-	
102	Honshu, Japan	16-5-1968	8.20	2	Body, SGM, other	Nagai et al. (2001)
101	Nankai	1-4-1968	7.50	5	Aftershocks	Wyss (1976)
100	Santa Cruz Islands	31-12-1966	7.80	4	Aftershocks	Kelleher et al. (1974)
99	Antofagasta, Chile	28-12-1966	7.70	4	Unknown	Kelleher (1972)
98	Central Peru	17-10-1966	8.10	3	Body	Beck & Ruff (1989)
97	Vanuatu	11-8-1965	7.60	4	Aftershocks	Kelleher et al. (1974)
96	Fox Islands, Alaska	2-7-1965	7.80	4	Aftershocks	Sykes (1971)
95	Rat Islands, Alaska	4-2-1965	8.70	3	Body	Beck & Christensen (1991)
94	Puysegur	12-9-1964	7.60	5	-	
93	Alaska	28-3-1964	9.30	2	Level / Tsunami /Tri / Sea	Holdahl & Sauber (1994)
92	Kuril Islands	13-10-1963	8.50	3	Body	Beck & Ruff (1987)
91	Kyushu, Japan	26-2-1961	7.54	4	Aftershocks	Wyss (1976)
90	Central Peru	20-11-1960	7.60	5	-	Pelayo & Wiens (1990)
89	Bio-Bio, Chile	22-5-1960	9.60	2	Level / Sea	Barrientos & Ward (1990)
88	Honshu, Japan	20-3-1960	7.95	2	SGM	Yamanaka & Kikuchi (2004)
87	Kamchatka	4-5-1959	7.90	4	Unknown	Fedotov et al. (2011)
86	Kuril Islands	6-11-1958	8.40	3	Body	Schwartz & Ruff (1987)

4. How subduction interface roughness the occurrence of large interplate earthquakes

N°	Location	Date	M _w	Cat	Method	Author
85	Ecuador	19-1-1958	7.60	3	Body	Swenson & Beck (1996)
84	Guerrero, Mexico	28-7-1957	7.60	4	Body	Beroza et al. (1984)
83	Aleutian Islands, Alaska	9-3-1957	8.60	2	Body / Surf / Tsunami	Johnson et al. (1994)
82	Japan (Honshu)	29-9-1956	7.53	5	-	
81	Kermadec	27-2-1955	7.52	5	-	
80	Honshu, Japan	25-11-1953	7.90	4	Tsunami	Matsuda et al. (1978)
79	Chile	6-5-1953	7.55	5	-	
78	Kamchatka	4-11-1952	8.90	2	Tsunami	Johnson & Satake (1999)
77	Hokkaido, Japan	4-3-1952	8.10	2	Tsunami	Hirata et al. (2003)
76	Vanuatu	2-12-1950	7.90	5	-	Kelleher et al. (1974)
75	Tonga	8-9-1948	7.50	5	-	Okal et al. (2004)
74	Nankaido, Japan	20-12-1946	8.30	2	Tsunami	Baba et al. (2002)
73	New Ireland, Papua new Guinea	29-9-1946	7.68	5	-	
72	Domenican Republic	4-8-1946	7.76	4	Aftershocks	Kelleher et al. (1973)
71	British Columbia	23-6-1946	7.50	5	-	
70	Alaska	1-4-1946	8.60	4	Unknown	Sykes (1971)
69	New Britain	28-12-1945	7.50	5	-	
68	Pakistan	27-11-1945	8.10	4	Body, Level	Byrne et al. (1992)
67	Puysegur	1-9-1945	7.50	5	-	
66	Tonankai, Japan	7-12-1944	8.10	2	Tsunami	Tanioka & Satake (2001)
65	Puerto Rico	29-7-1943	7.70	4	Aftershocks	Kelleher et al. (1973)
64	Philippines	25-5-1943	7.76	5	-	Acharya (1980)
63	Coquimbo, Chile	6-4-1943	8.10	3	Body	Beck et al. (1998)
62	Central Peru	24-8-1942	8.10	4	Body	Swenson & Beck (1996)
61	Guatemala	6-8-1942	7.70	4	Aftershocks	Kelleher et al. (1973)
60	Ecuador	14-5-1942	7.80	3	Aftershocks	Swenson & Beck (1996)
59	Costa Rica	5-12-1941	7.52	4	Aftershocks	Kelleher et al. (1973)
58	Nankai	18-11-1941	8.02	5	-	
57	Andaman Islands	26-6-1941	7.60	4	Aftershocks	Bilham et al. (2005)
56	Michoacan, Mexico	15-4-1941	7.60	4	Aftershocks	Kelleher et al. (1973)
55	Mariana	28-12-1940	7.70	5	-	Okal (2012)
54	Central Peru	24-5-1940	8.20	4	Body	Beck and Ruff (1989)
53	Nicoya, Costa Rica	21-12-1939	7.59	4	Aftershocks	Kelleher et al. (1973)
52	Solomon Islands	30-4-1939	7.95	5	-	
51	Solomon Islands	30-1-1939	7.82	5	-	
50	Alaska	10-11-1938	8.30	2	Tsunami	Johnson & Satake (1994)
49	Fukushima-Oki, Japan (1)	5-11-1938	7.80	4	Tsunami	Hashimoto et al. (2009)
48	Fukushima-Oki, Japan (2)	5-11-1938	7.70	4	Tsunami	Hashimoto et al. (2009)
47	Ryukyu	16-6-1938	7.60	5	-	
46	Ryukyu	10-6-1938	7.66	5	-	
45	Japan (Fukushima-Oki)	23-5-1938	7.70	5	-	Hashimoto et al. (2009)
44	Chile	13-7-1936	7.52	5	-	
43	Philippines	1-4-1936	7.75	5	-	Acharya (1980)
42	Kepulauan Batu, Indonesia	28-12-1935	7.60	4	Body	Rivera et al. (2002)

N°	Location	Date	M _w	Cat	Method	Author
41	Solomon Islands	15-12-1935	7.60	5	-	
40	Santa Cruz Islands	18-7-1934	7.70	4	Aftershocks	Kelleher et al. (1974)
39	Mariana	24-2-1934	7.50	5	-	
38	Manila trench	14-2-1934	7.50	5	-	Duong et al. (2009)
37	Sumatra	24-6-1933	7.53	5	-	
36	Colima, Mexico	18-6-1932	7.80	4	Aftershocks	Pacheco et al. (1997)
35	Nankai	2-11-1931	7.93	5	-	
34	Solomon Islands	10-10-1931	7.95	5	-	
33	Solomon Islands	3-10-1931	7.88	5	-	
32	Honshu, Japan	9-3-1931	7.98	4	SGM	Yamanaka & Kikuchi (2004)
31	Japan	10-11-1930	7.73	5	-	
30	Maule, Chile	1-12-1928	7.70	4	Aftershocks	Beck et al. (1998); Bilek (2010)
29	Oaxaca, Mexico	22-3-1928	7.73	4	Aftershocks	Kelleher et al. (1973)
28	Vanuatu	16-3-1928	7.53	5	-	Kelleher et al. (1974)
27	Kamchatka	3-2-1923	8.40	4	Aftershocks	Johnson & Satake (1999)
26	Atacama, Chile	11-11-1922	8.30	3	Aftershocks	Beck et al. (1998)
25	Taiwan	1-9-1922	7.59	5	-	Theunissen et al. (2012)
24	Vanuatu	20-9-1920	8.15	5	-	
23	Taiwan	5-6-1920	8.23	4	Other	Theunissen et al. (2010)
22	New Britain / Solomon Islands	2-2-1920	7.81	5	-	
21	New Britain / Solomon Islands	6-5-1919	7.75	5	-	
20	Tonga	30-4-1919	8.10	5	-	Okal et al. (2004)
19	Chile	4-12-1918	7.83	5	-	
18	Kuril Islands	8-11-1918	7.79	4	Unknown	Fedotov et al. (2011)
17	Kermadec	1-5-1917	8.20	5	-	
16	Solomon Islands	1-1-1916	7.89	5	-	
15	Kuril Islands	1-5-1915	7.80	5	-	
14	Southern Sumatra	25-6-1914	7.57	4	Unknown	Natawidjaja et al. (2004)
13	Southern Peru	6-8-1913	7.74	4	Unknown	Kelleher (1972)
12	Tonga	26-6-1913	7.74	5	-	
11	Philippines	14-3-1913	7.77	5	-	
10	Mexico	7-6-1911	7.60	5	-	
9	Philippines	16-12-1910	7.61	5	-	
8	Guerrero, Mexico	30-7-1909	7.50	5	-	
7	Mexico	15-4-1907	7.80	5	-	
6	Northern Sumatra	4-1-1907	7.80	5	Other	Newcomb & McCann (1987)
5	Valparaiso, Chile	17-8-1906	8.20	4	Unknown	Bilek (2010)
4	Ecuador	31-1-1906	8.35	4	Unknown	Kelleher (1972)
3	Kamchatka	25-6-1904	7.70	5	Unknown	Fedotov et al. (2011)
2	Mexico	14-1-1903	7.69	5	-	
1	Vanuatu	9-8-1901	7.92	5	-	

Methods: Body = body waves, Surf = surface waves, SGR = strong ground motion, GPS = Global Positioning System, HRGPS = high rate GPS, InSAR = interferometric synthetic-aperture radar, Tsunami = tide gauge data, Level = leveling data based on coseismic elevation changes, Tri = triangulation data based on horizontal co-seismic displacements, Sea = data based on sea-level changes, Aftershocks = spatial distribution of smaller earthquakes that occurs in the same area, after the mainshock.

width saturation will still influence the relation between the rupture area and moment magnitude. A new, bilinear scaling law, with a hinge magnitude of 8.6, has been proposed by Allen & Hayes (2017) and has a better fit with the SubQuake data (pink line in Figure 4.5.). The scaling laws provided by Strasser et al. (2010) and Ye et al. (2016) both have different slopes compared to the regression line of this study, as well as the regression line provided by Allen & Hayes for magnitudes lower than the hinge magnitude. This could be related to the fact that they consider a single relationship between rupture area and moment magnitude over the whole magnitude range (e.g., M_w 7.0 - 9.6). Another scaling law provided by Allen & Hayes (2017; $\log_{10}(A) = -3.63 + 0.96 M_w$), where they do not take into account a hinge magnitude, is very similar to the one provided by Strasser et al. (2010). The downward shift of the Ye et al. regression line, and therefore the overall

smaller area estimation compared to other datasets, could be related to different choices in the inversion approach, or the threshold that is used to extract the rupture area from the finite-fault rupture models.

4.3.1.2. Epicenter location with respect to seismic asperity

With the seismic asperity- and epicenter data, we can evaluate how often the location of a rupture's epicenter is overlapping with the area of maximum slip. We observe that for 47% of category 1 events, the epicenter is located within the seismic asperity contour. When also considering categories 2 and 3, for which the uncertainty in both epicenter- and seismic asperity location is higher, we observe that 37% of epicenters are located within the seismic asperity.

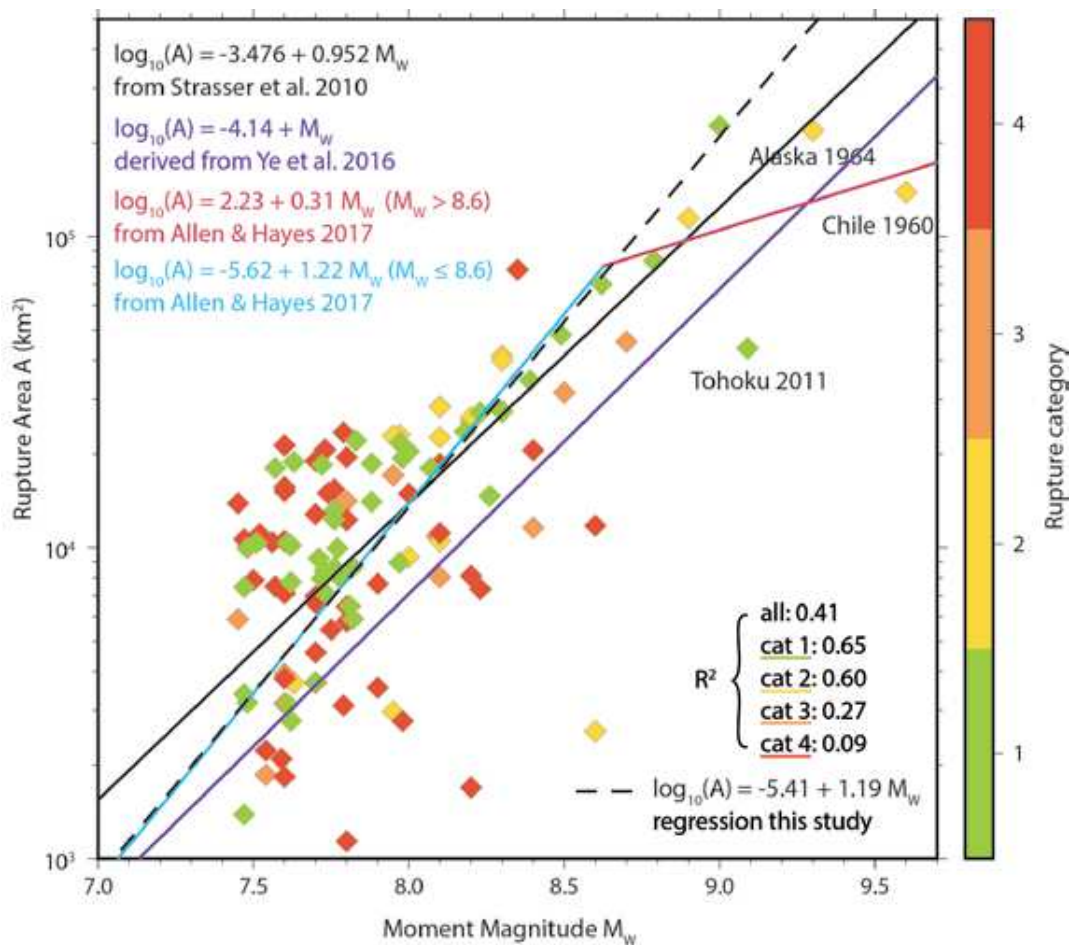


Figure 4.5. Rupture area vs. moment magnitude of the SubQuake events. Diamonds depicting individual events are color-coded as a function of their category (cf. Figure 4.2). Scaling relationships by Strasser et al. (2010) and Allen & Hayes (2017) are displayed, as well as the scaling law derived from the present study and the coefficient of determination, R^2 , for each category. Allen & Hayes provide a bilinear scaling law, with a hinge magnitude of 8.6.

4.3.1.3. Subduction zone classification in terms of rupture length ratio

In Table 4.2, the subduction zones considered in this study have been ordered in terms of rupture length ratio (RLR). Rupture percentages have been calculated based on the trench-parallel length of the rupture segments in relation to the total trench length. Since we do not take into account the category 5 ruptures when calculating this ratio, it should be seen as a minimum RLR. We defined four different classes based on the occurrence of $M_w \geq 7.5$ ruptures: high RLR (with $> 75\%$ of the trench length covered by ruptures), intermediate rupture length ratio ($25\% < \text{RLR} < 75\%$), low RLR (with $\text{RLR} < 25\%$), and finally the regions where no cat. 1-4 $M_w \geq 7.5$ ruptures have been observed. Regions that fall in the ‘high RLR’ class are Japan-Kuril-Kamchatka, South Andes, Alaska-Aleutian and Andaman-Sumatra. The regions in the ‘intermediate RLR’ class are North Andes, Central America, New-Guinea-Solomon-Vanuatu, Ryukyu-Nankai and Makran, in

order of decreasing rupture length ratio. The regions with low RLR are Java-Sumba, Tonga-Kermadec, the Antilles and the Philippines. Both the Antilles and the Philippines, but also the Makran subduction zone in the ‘intermediate RLR’ class, only contain one or two category 4 ruptures; all older than 1975. The four regions which did not host any category 1-4 $M_w \geq 7.5$ ruptures between 1900 and 2017, are Cascadia, Izu-Bonin-Mariana, Luzon and South Sandwich.

4.3.2. Comparison between SubRough and SubQuake

4.3.2.1. Rupture Length Ratio vs. Percentage of smooth seafloor

Following the classification of subduction zones based on their RLR (Table 4.2), we calculated the percentage of smooth seafloor for each region to make a first-order comparison with the RLR. Lallemand et al. (2018) used thresholds of 250 m and

Class	Region	Rupture length ratio RLR (%)	Percentage of $R_{LW} < 250$ m (%)
High Rupture Length Ratio ($> 75\%$)	Japan-Kuril-Kamchatka	96	52
	South Andes	93	67
	Alaska-Aleutian	89	69
	Andaman-Sumatra	79	53
Intermediate Rupture Length Ratio ($> 25\% \& < 75\%$)	North Andes	58	51
	Central America	53	56
	New Guinea-Solomon-Vanuatu	46	4
	Ryukyu-Nankai	29	16
Low Rupture Length Ratio ($< 25\%$)	Makran	27	22
	Java-Sumba	18	23
	Tonga-Kermadec	14	41
	Antilles	11	49
No $M_w \geq 7.5$ ruptures ¹	Philippines	10	27
	Cascadia	0	78
	Izu-Bonin-Mariana	0	19
	Luzon	0	42
	South Sandwich	0	54

Table 4.2. Subduction zone classification according to rupture length ratio. Percentages of trench length that has hosted ruptures have been calculated and organized into four categories. Percentages of long-wavelength roughness (R_{LW}) with amplitudes below 250 m are indicated for region as well. Regions indicated in bold are displayed in Figures 4.7, 4.8, and 4.9.

¹ except for several category 5 events, for which it is uncertain whether they are interplate events

1000m to identify whether an area can be considered dominantly smooth, mixed, or dominantly rough (at long wavelengths, R_{LW}). We followed the 250 m threshold to determine the percentages of smooth seafloor for each region, which are indicated in Table 4.2. When plotting the relationship between RLR and smooth seafloor (Figure 4.6), we clearly observe that regions with smoother seafloor also have higher RLR. We can distinguish two groups: the regions with $RLR > 50\%$, which all show large percentages of smooth seafloor, and the regions with $RLR < 50\%$, which show a more mixed signal in terms of smooth seafloor. We highlighted two outliers in Figure 4.6: the New-Guinea-Solomon-Vanuatu and Cascadia subduction zones, which both do not fit the general trend that we observe.

4.3.2.2. Rupture areas: Specific regions

By qualitatively comparing the SubQuake grid on the landward side of the trench and the SubRough data on the seaward side, some areas already suggest

a possible relationship between the roughness of the seafloor and the occurrence of megathrust earthquakes. Figures 4.7 and 4.8 show the SubQuake grids for the six subduction zones where the rupture length ratio is the highest, as well as three regions representative for the remaining groups of Table 4.2. Seaward of the trenches, the SubRough data at both wavelength bandwidths (i.e., R_{SW} and R_{LW}) is plotted. Individual figures for all subduction zones in Table 4.2 can be found in Figures A4.2 to A4.16 in the appendix. As can be seen in Figure 4.8, all the subduction zones with $RLR > 50\%$ face mainly smooth to moderately rough seafloor, as shown in Figure 4.6 and demonstrated as well by Lallemand et al. (2018).

Figure 4.9 shows density distributions for the long wavelength roughness signal of the subduction zones displayed in Figures 4.7 and 4.8, illustrating which roughness amplitudes are the most common for these regions. Density has been multiplied by the number of grid points in each dataset (i.e. rupture

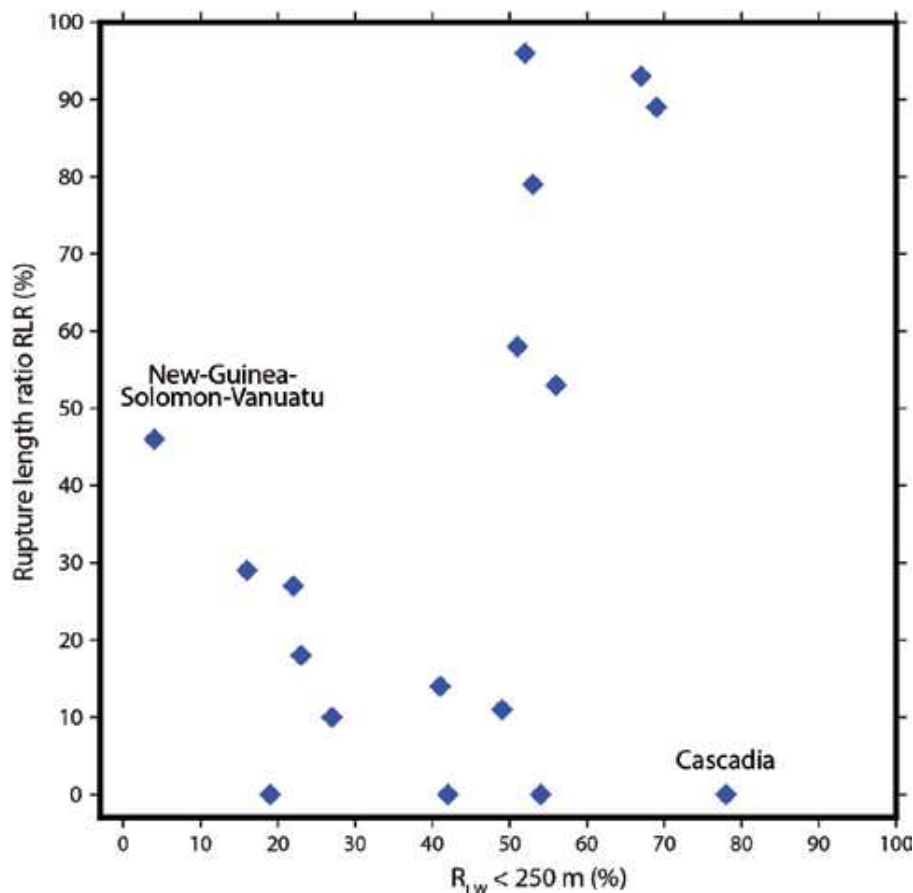


Figure 4.6. Rupture length ratio (RLR) versus percentage of smooth seafloor ($R_{LW} < 250$ m). Blue diamonds all represent one region from Table 4.2. Two outliers, New-Guinea-Solomon-Vanuatu and Cascadia, are indicated.

or no-rupture groups for each region) to obtain the count, which better highlights the size of the different groups. Density plots for the remaining regions can be found in the supporting information (Figure A4.17). The comparison between seaward roughness and interface seismicity for the subduction zones displayed in Figures 4.8 and 4.9 will be briefly discussed below, both qualitatively and quantitatively. Since the regions with very high RLR display large differences in counts between rupture- and no-rupture segments, a quantitative comparison for these specific zones is difficult. The same holds for the Java-Sumba region, where the count for the rupture segments is rather low with respect to the no-rupture segments.

4.3.2.2.1. Japan-Kuril-Kamchatka

The Japan-Kuril-Kamchatka trench has the largest rupture length ratio; 96% of the forearc has ruptured. This area is among the smoother ones, except at the two edges of the region. In the north, the subducting Emperor Seamount Chain is clearly visible in the roughness signal. This also holds for the Joban Seamount Chain in the south, offshore Japan. This chain intersects the Japan Trench with an angle of roughly 55° (measured from north) and is assumed to continue with this trend into the subduction zone (e.g., Bassett & Watts, 2015a; Nishizawa et al., 2009). The partly subducted Daiichi-Kashima seamount (Lallemand et al., 1989), and another large seamount along the plate interface (Mochizuki et al., 2008), support this assumption. When looking at the SubQuake data on the landward side of the trench, no rupture has recently occurred at the location where the Joban Seamount chain is subducting, while the Tohoku 2011 rupture (n° 173 in Figure 4.8) and the two 1938 ruptures (n° 48 and 49) all stop where the Joban Seamount chain enters the subduction zone. Another rupture, from 1953 (n° 80), has occurred south of the Joban Seamount chain, where the seafloor roughness becomes smoother again (following the 55° extrapolation trend). From the density plot (Figure 4.9a), we see that the roughness distribution for the rupture segments has a mode of ~ 125 m, and that the majority of the data fall below 250 m, confirming the smooth character of the seafloor prior to subduction.

4.3.2.2.2. South Andes

Because of its significant length, the Andean trench has been split up in two parts to facilitate quantitative comparisons, a North- and South Andes segments separated by the Arica bend. Almost all the trench length of the Southern Andes has recorded $M_w \geq 7.5$ ruptures ($> 90\%$), which are quite variable in age and magnitude. The two largest events in this area are the 1960 Bio-Bio M_w 9.6 rupture, and the 2010 Maule M_w 8.8 rupture, which both occurred in the southernmost part of the trench (n° 89 and 170 in Figure 4.8, respectively). The seafloor in front of these two rupture areas, south of the Juan Fernandez ridge, is shown to be one of the smoothest parts of the southern Andes margin (Lallemand et al., 2018). The area north of the Juan Fernandez ridge hosts relatively smaller ruptures, characterized by magnitudes mainly encompassed between M_w 7.5 and 8.0. The seafloor in front of this area is rougher than the area southwards. The density plot (Figure 4.9b) shows that the majority of the roughness amplitudes are mainly below 250 m, the mode for the roughness in front of rupture segments being around 125 m.

4.3.2.2.3. Alaska-Aleutian

Like the preceding subduction zones, the Alaska-Aleutian region has a very high rupture length ratio; $\sim 89\%$ of the trench has ruptured. Almost half of the total number of $M_w \geq 7.5$ events in this area have magnitudes that are higher than M_w 8.5. Figure 4.8 shows that the seafloor in front of the Alaska-Aleutian trench on average is very smooth. Rough features are limited to the westernmost part, like the Detroit Tablemount and the Aleutian Rise. We observe that the main R_{LW} amplitudes for rupture segments are very low (mode of ~ 100 m, Figure 4.9c). The second mode associated with rupture-segments, around 500 m, most likely results from the rough area in the west, facing the 1965 Rat Islands earthquake (M_w 8.7, n° 95 in Figure 4.8). This rupture seems to fade out towards the west. On the other side of the trench, we note that a rough domain is likely to be extended across the trench following a strong obliquity up to the area where event n° 95 stopped.

4.3.2.2.4. Andaman-Sumatra

The Sumatra-Java trench has also been divided into

4. How subduction interface roughness the occurrence of large interplate earthquakes

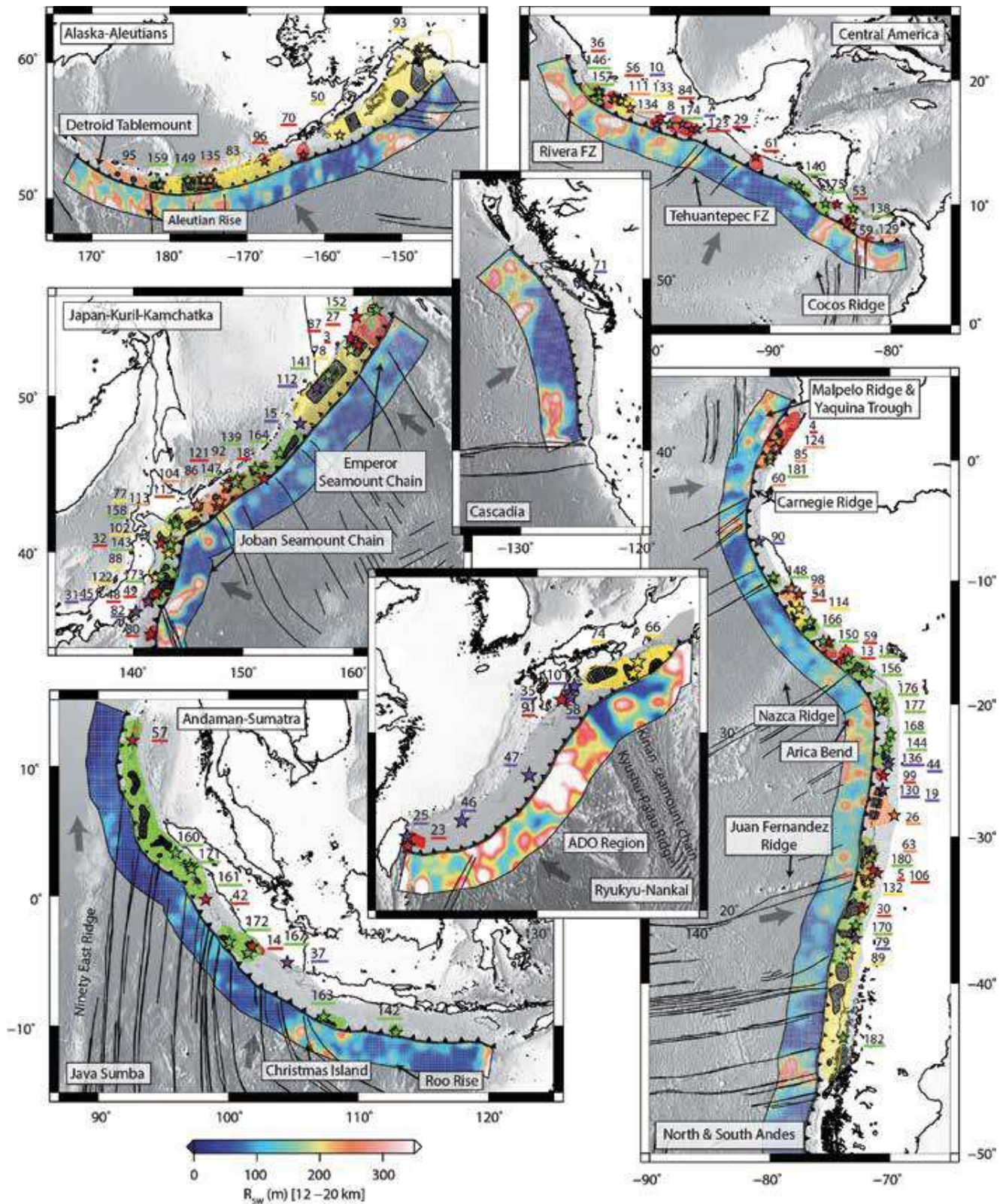


Figure 4.7. Short-wavelength roughness (R_{sw}) data and SubQuake grids for the six regions that have the highest occurrence of $M_w \geq 7.5$ interplate events and for Ryukyu-Nankai, Java-Suma, and Cascadia. Ruptures and epicenters are color-coded according to the rupture categories displayed in Figure 4.2; numbers indicate the events listed in Table 4.1. Seaward of the trench, short-wavelength roughness R_{sw} data from Lallemand et al. (2018) are plotted. Colors indicate the roughness amplitude. Seafloor features mentioned in the text are indicated. The ADO region (Ryukyu-Nankai) includes the Amami Plateau, Oki-Daito Ridge, and the Daito Ridge. Convergence directions are indicated by the dark-grey arrows.

two segments: the Andaman-Sumatra segment in the north, starting from rupture n° 167 (Figure 4.8), and the Java-Sumba segment in the south. The seafloor facing the Andaman-Sumatra trench contains very smooth patches, which alternate with rougher regions. These high roughness amplitudes are mainly caused by Ninety-East Ridge in the northwestern part of the area, almost parallel to the trench in the northernmost part and therefore not representative of the roughness of the subduction interface. The Andaman-Sumatra trench has recorded several large earthquakes: the $M_w \geq 8.5$ 2004, 2005 and 2007 ruptures, respectively n° 160, 161 and 167 in Figure 4.8. The density plot of this region (Figure 4.9d) shows the wide roughness signal observed in this area. Most of the rupture areas face very smooth seafloor, as suggested by the strong peak around a roughness amplitude of ~ 75 m. The higher roughness amplitudes characterizing rupture segments can be related to the ninety-east ridge and the rougher seafloor facing the 2007 rupture (n° 167).

4.3.2.2.5. North Andes

The part of the North Andes trench length that has ruptured (RLR $\sim 58\%$), is considerably lower than in the Southern Andes (RLR $\sim 93\%$). Right above the Arica bend, $M_w \geq 7.5$ ruptures are numerous, while in Northern Peru, a seismic gap is observed (Nocquet et al., 2014). The seafloor from the Arica bend up to this seismic gap region in Northern Peru is essentially smooth, while the seafloor in front of Ecuador and Colombia appears moderately rough (mainly because of the Malpelo Ridge, Carnegie Ridge and the Yaquina Trough). Several ruptures occurred in this part of the Andean trench, such as the M_w 8.4 1906 event in Ecuador (n° 4 in Figure 4.8). When looking at the density plot (Figure 4.9e), the distribution of the R_{LW} roughness appears to be relatively similar for the rupture- and no-rupture segments. This could be related to the rough area in the northernmost part, which might not be representative of the subduction interface roughness, since the Malpelo Ridge and Yaquina Trough are oriented sub-parallel to the trench, and therefore may not extend into the trench. Furthermore, the seismic gap in northern Peru, facing smooth seafloor seaward of the trench, enhances the similarity between the rupture- and the no-rupture curves.

4.3.2.2.6. Central America

The Central American subduction zone shows a moderate RLR, with $\sim 53\%$ of trench length that has ruptured. The seafloor in front of the trench is very smooth in the central part, while on the edges several rough areas occur (e.g., the Cocos Ridge in the southeast and the Rivera fracture zone in the northwest). The Tehuantepec fracture zone is also clearly visible in the center of the subduction zone. Many megathrust earthquakes occurred in the northern part of the Central America trench, offshore Mexico, where the roughness amplitudes significantly vary (Rivera fracture zone). Several $M_w \sim 7.5$ ruptures occur in the region where the Cocos Ridge is entering the trench, all of them being more or less limited to the ridge domain. The smooth segment in the middle, between the Cocos ridge and the Tehuantepec fracture zone, hosts very few megathrust ruptures. The density plot (Figure 4.9f) shows a somewhat higher count at low roughness for the rupture segments, but both curves follow a similar shape. For very high roughness amplitudes ($R_{LW} > 750$ m), the rupture-segment count is close to zero, while the no-rupture distribution does include roughness amplitudes higher than 750 m. This is probably related to the signal east of the Cocos ridge, where we indeed have no record of any $M_w \geq 7.5$ earthquakes in the SubQuake database.

4.3.2.2.7. Ryukyu-Nankai

Even though the Ryukyu-Nankai trench only hosts four $M_w \geq 7.5$ ruptures (not taking into account the category 5 events), they still take up 29% of the trench length ('moderate RLR' class). In terms of seafloor roughness, the area as a whole is considered rough, because several ridges with high R_{LW} amplitudes (i.e., the Kyushu-Palau Ridge, Amami Plateau, Oki-Daito Ridge and the Daito Ridge) are intersecting the trench. However, the area in front of the two largest ruptures in this region (i.e., the 1944 Tonankai and 1946 Nankaido earthquakes, n° 66 and 74 in Figure 4.8) appears to be smoother. The assumption that the roughness signature seaward of the trench can be extrapolated perpendicularly into the trench, is supported by the subducting Kinan Seamount Chain and the Kyushu-Palau ridge, since both have been imaged on the subducting interface (Kodaira et al., 2000; Lallemand, 2016; Yokota et al., 2016). It is also known that many historical earthquakes have

4. How subduction interface roughness the occurrence of large interplate earthquakes

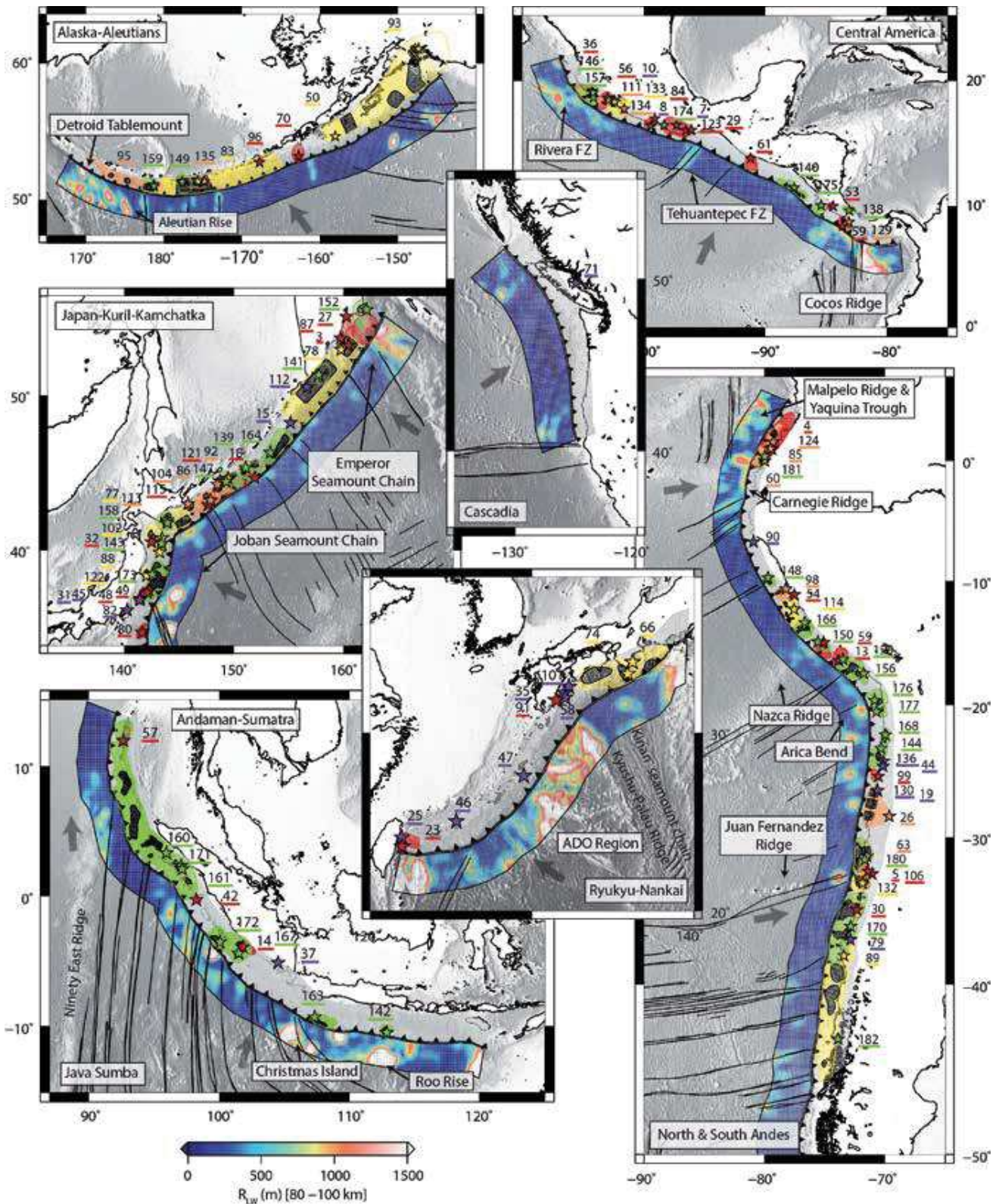


Figure 4.8. Long-wavelength roughness (R_{LW}) data and SubQuake grids for the six regions that have the highest occurrence of $M_w \geq 7.5$ interplate events and for Ryukyu-Nankai, Java-Suma, and Cascadia. Ruptures and epicenters are color-coded according to the rupture categories displayed in Figure 4.2; numbers indicate the events listed in Table 4.1. Seaward of the trench, short-wavelength roughness R_{LW} data from Lallemand et al. (2018) are plotted. Colors indicate the roughness amplitude. Seafloor features mentioned in the text are indicated. The ADO region (Ryukyu-Nankai) includes the Amami Plateau, Oki-Daito Ridge, and the Daito Ridge. Convergence directions are indicated by the dark-grey arrows.

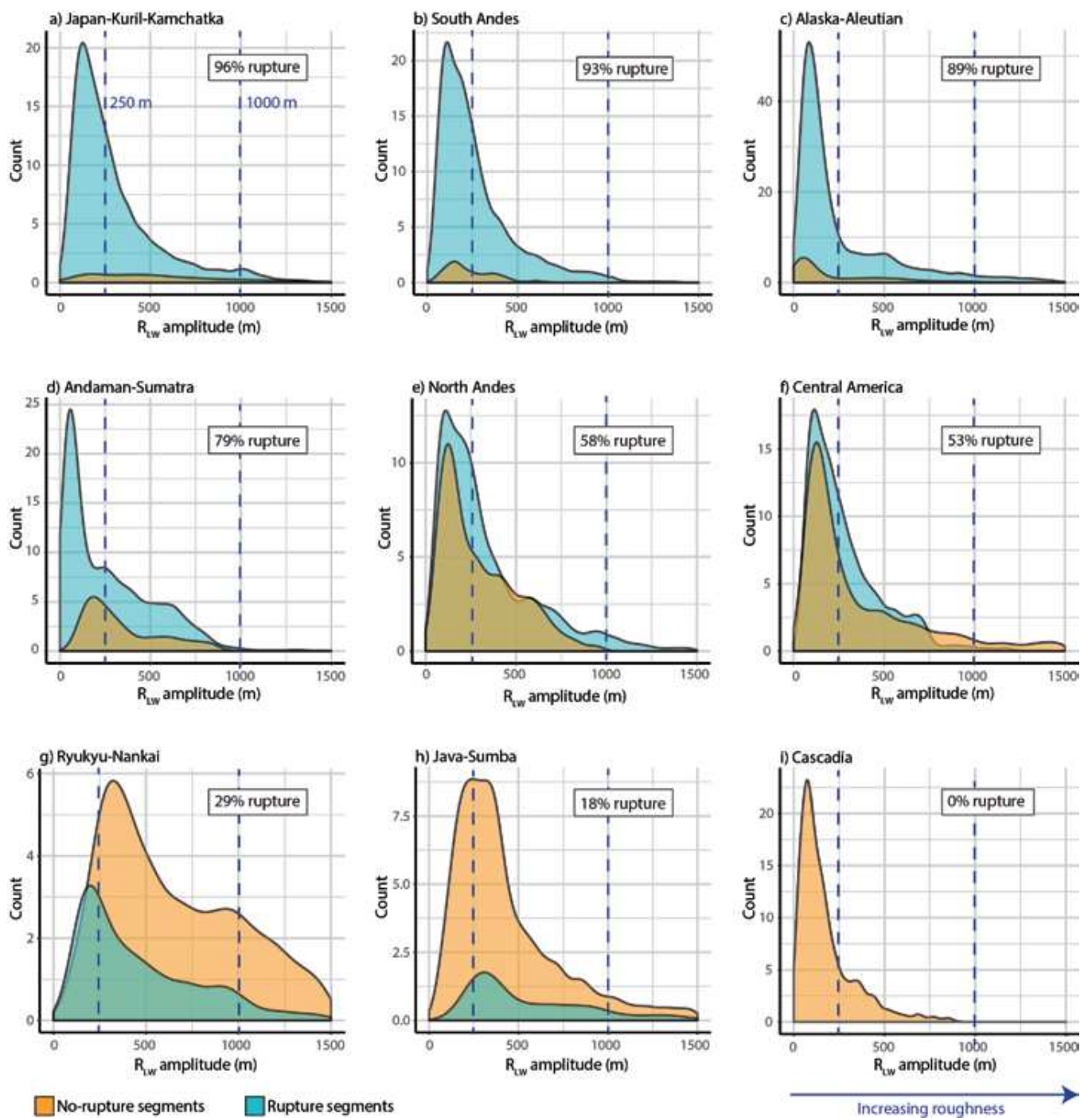


Figure 4.9. R_{LW} density plots for the nine regions mentioned in the text. Counts for long-wavelength roughness are shown with increasing roughness amplitudes (i.e., from smooth to rough). Orange and blue curves indicate the roughness data selected for the no-rupture and rupture segments, respectively. Blue dashed lines indicate the smooth and rough thresholds of 250 and 1,000 m, respectively (as introduced by Lallemand et al., 2018)

occurred in the 1944 Tonankai and 1946 Nankaido rupture areas (e.g., Ando, 1975; Satake, 2015) while the number of earthquakes in the remaining part of the Ryukyu trench is very low. These observations are in agreement with the density plot (Figure 4.9g); the no-rupture segments are mainly characterized by very rough R_{LW} amplitudes, and a relatively large part of the data exceeds the 1000 m threshold.

4.3.2.2.8. Java-Sumba

The Java-Sumba trench has a low rupture length ratio, with only 18% of the trench length that has ruptured. The two ruptures that did occur in this area had magnitudes between M_w 7.5 and 8.0 (n^o 142 and 163 in Figure 4.7). As can be seen in Figure 4.8, the Java-Sumba section is very rough, mainly because of the Roo Rise and the Christmas Island topographic highs in the central part. The density plot (Figure 4.9h) shows roughness distributions similar for the rupture- and no-rupture segments, with a mode of ~ 300 m for both distributions. The range of roughness amplitude for the two rupture segments in this region does not significantly differ from the one of the remaining areas of the trench.

4.3.2.2.9. Cascadia

The SubQuake database records only 1 event in the Cascadia subduction zone: a M_w 7.5 earthquake in 1946 (category 5). However, this event was most likely a crustal, or intraplate event (Clague 2002). The prior-to-subduct seafloor does appear very smooth, which can be seen both from Figure 4.8, as from the density plot (Figure 4.9i), which shows that the large majority of roughness data fall below 250 m. This distribution is very similar to regions with a large rupture length ratio, such as Japan-Kuril-Kamchatka and Alaska-Aleutian. Even though no interplate $M_w \geq 7.5$ events have been recorded during the past 117 years, it is widely accepted that great earthquakes have occurred before this time period (Wang & Tréhu, 2016). This is supported by coastal geological studies (Atwater 1987), marine turbidity deposits (Adams 1990; Goldfinger et al. 2012), but also by historical Japanese tsunami records (Satake 2003).

4.3.2.3. Rupture areas: Global comparison

In this section, we study all subduction zones together. Figure 4.10 shows the density plots for

the whole dataset, both for the short- and long wavelength roughness. It also displays the relative density function, which measures the offset of the two subgroups with respect to the whole dataset (a combination of both the rupture and no-rupture subsets):

$$D_{rel}(R) = D_{sub}(R) - D_{all}(R)$$

where D_{rel} is the relative density at a specific value for roughness R , D_{sub} the density for each subset (i.e., rupture vs. no-rupture) and D_{all} the density for the entire dataset.

Such a relative density plot helps visualizing the difference between the two classes of trench segments especially since often the curves are rather similar in shape. This is related to the global distribution of the roughness data, which shows that the highest densities are usually at roughness amplitudes between 50 and 150 m for R_{SW} and 0 and 500 m for R_{LW} , regardless of the rupture or no-rupture class they make part of. With the relative density plots, we highlight the offset of both the rupture- and no-rupture subsets with respect to the density signal of the entire dataset. Negative relative densities indicate that densities are lower than the overall density signal, while positive relative densities show a density increase with respect to the overall signal. Depending on the roughness amplitudes at which these variations occur, we can infer whether smooth or rough seafloor is mainly associated with rupture- or no-rupture segments. For the short wavelength roughness, we do not observe a significant difference between the rupture and no-rupture segments (Figure 4.10a and b). Regarding the long wavelength roughness, rupture segments have higher densities at low roughness amplitudes (i.e., smooth seafloor), than the no-rupture segments (Figure 4.10c and d). On the other hand, the no-rupture segments have slightly higher densities at higher roughness amplitudes. This switch in density dominance takes place at a roughness amplitude of ~ 250 m. In addition, the mode of the no-rupture class is shifted to the right with respect to the rupture class, showing a difference in R_{LW} of ~ 20 m. These results indicate that when looking at long wavelength roughness, ruptures tend to occur preferentially on smooth portions of the subduction megathrust.

4.3.2.4. Rupture areas: Comparison for different M_w groups

Another aspect of the quantitative comparison we performed, is the relationship between subduction interface roughness and varying moment magnitude. Instead of considering rupture segments (often consisting of several, partly overlapping ruptures), we now select the seafloor roughness facing each event and calculate a mean roughness value. Figure 4.11a shows mean R_{LW} vs. M_w of cat. 1 – 4 events. We observe that for decreasing roughness, the moment magnitude increases, following a power law relationship. This result is especially clear for the $M_w > 8.5$ events, which all show an average roughness lower than ~ 300 m. An exception is the

1965 Rat Island event (category 3), for which it has already been mentioned that the roughness proxy might not be entirely representative. The M_w 8.0 – 8.5 events show a wider range of average roughness values, but are all smaller than 700 m, except for the 1923 Kamchatka and 1920 Taiwan events, which are both category 4 events, and therefore less reliable. For the M_w 7.5 – 8.0 events, we see a wide range of roughness amplitudes, ranging up to 1750 m. Figures 4.11b-e show density- and relative density plots when only considering ruptures with M_w 7.5-8.5 (b & c), or $M_w > 8.5$ (d & e). For this comparison, previous rupture segments (that would switch into no-rupture segments due to the modified magnitude threshold) are excluded from the computation.

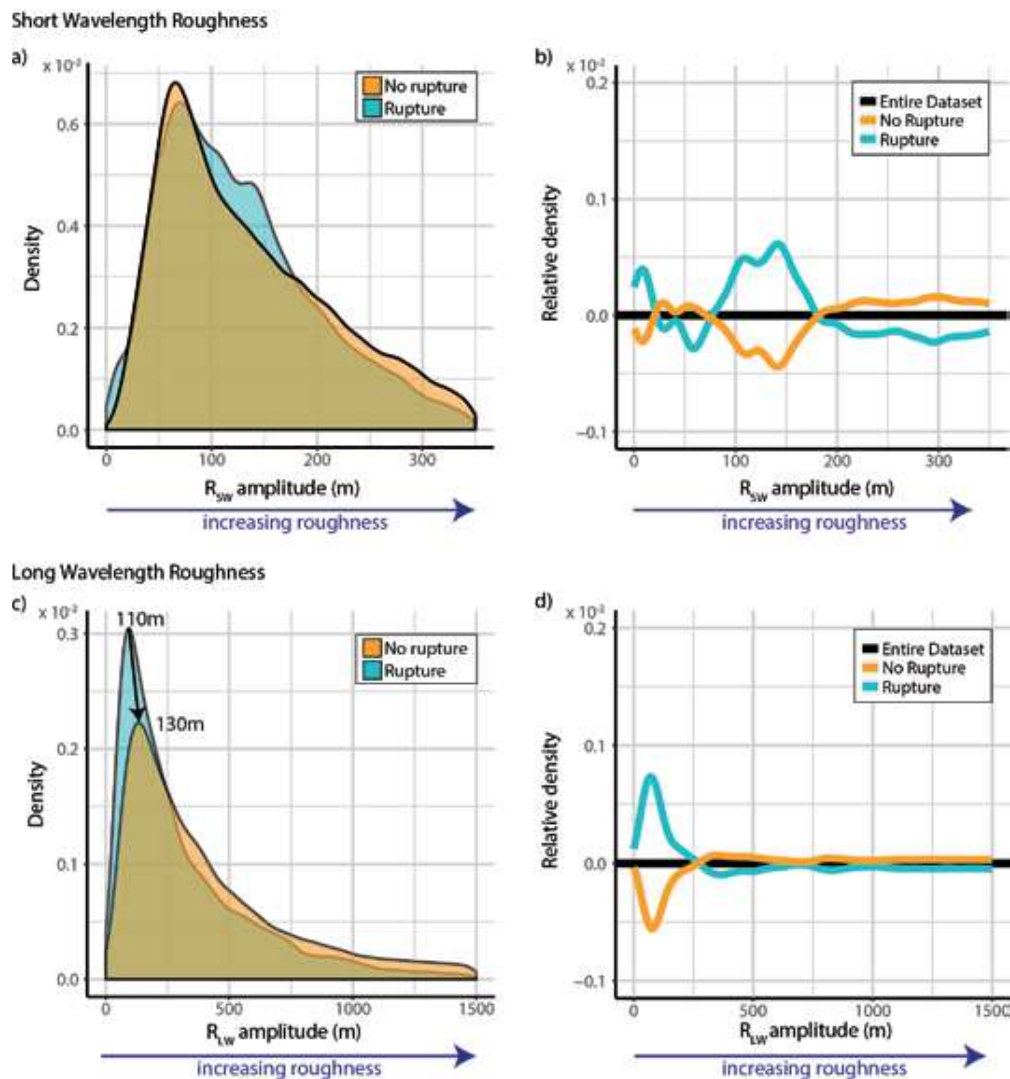


Figure 4.10. Global density distributions, taking into account all subduction zones and shown for both short-wavelength roughness (a, b) and long-wavelength roughness (c, d). Orange and blue shades indicate the roughness data selected for the no-rupture and rupture segments, respectively. Plots (a) and (c) show the density curve for increasing roughness amplitudes, from smooth (left) to rough (right). Plots (b) and (d) show the relative density, which illustrates the deviation of the two segment classes with respect to the entire data set.

4. How subduction interface roughness the occurrence of large interplate earthquakes

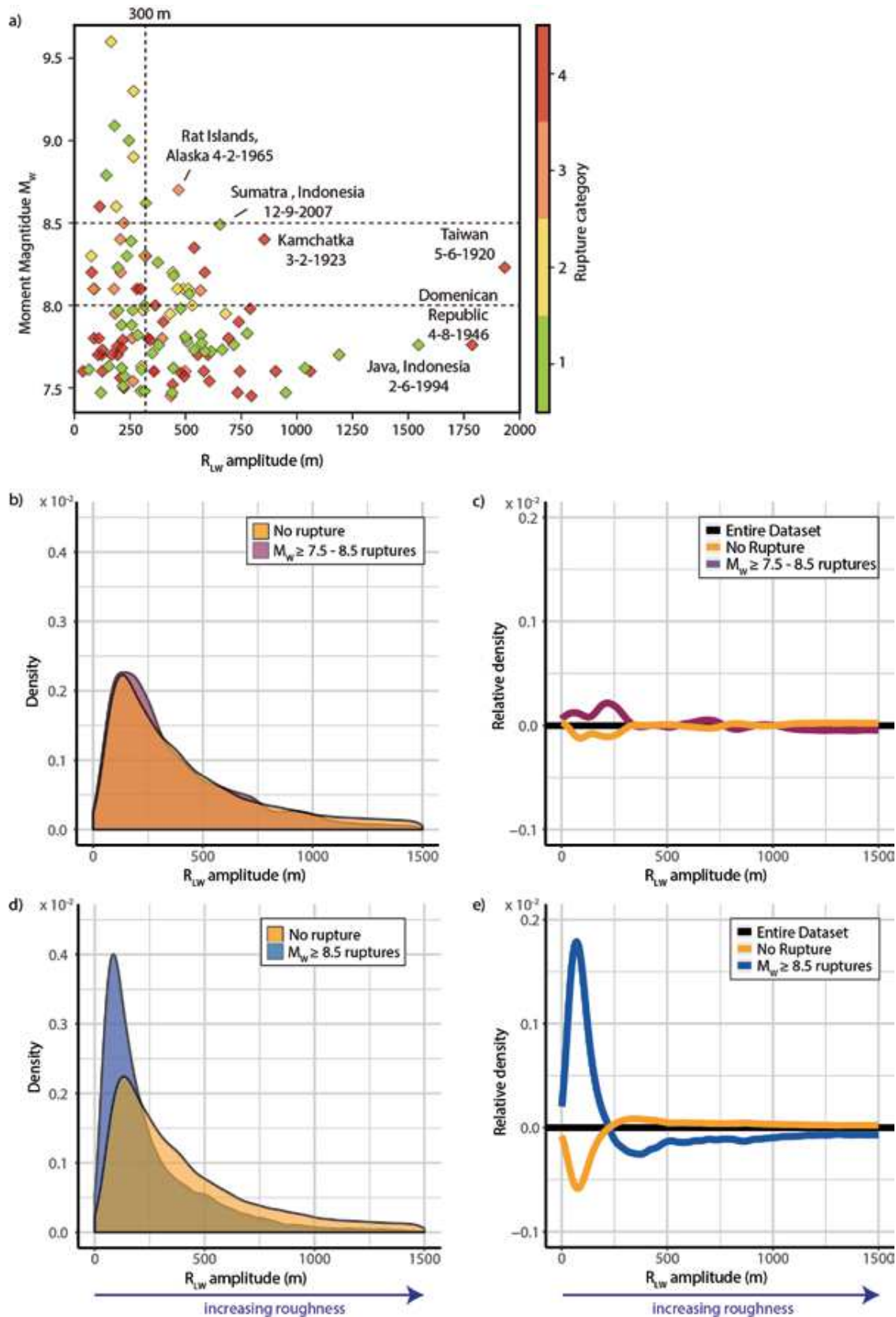


Figure 4.11. Long-wavelength roughness distribution (R_{LW}) with varying moment magnitudes. (a) Average R_{LW} for each event versus moment magnitude. Possible outliers are indicated with their name and date. Events are color-coded according to the rupture categories. Global density distribution for R_{LW} only taking into account M_w 7.5–8.5 ruptures (b), or $M_w > 8.5$ only (d), and relative density distribution (c and e, respectively) are displayed as well.

For the $M_w \geq 8.5$ ruptures, we observe a very clear difference between the roughness signals for the rupture segments with respect to the no-rupture segments. These results indicate that mainly the $M_w \geq 8.5$ ruptures are promoted by a smooth subducting interface at long wavelengths.

4.3.2.5. Seismic asperities

We now focus on the regions where the maximum slip occurred: the seismic asperities. Their roughness signal is compared to the distribution for rupture segments in general, to see if there is a difference between the maximum slip areas and remaining rupture areas. Figure 4.12 shows relative density plots for both R_{LW} and R_{SW} , highlighting the difference in roughness distribution with respect to rupture areas in general, and the roughness distribution of the entire, global dataset (black line). The reason why the signal for seismic asperity segments is compared to the signal of all rupture areas (including the seismic asperities), comes from the fact that ruptures and seismic asperities often overlap. A seismic asperity for one event, might be part of the rupture area for a second event, without being highlighted as a seismic asperity for that second event. For R_{LW} , we observe that the roughness distribution for seismic asperity segments shows the same pattern as for the rupture segments with respect to the entire dataset (i.e. higher densities at low roughness

amplitudes and lower densities at high roughness amplitudes). However, the seismic asperity signal is more amplified, indicating that the seafloor in front seismic asperities is smoother than in front of the rupture areas in general. This amplification of the signal is also seen for the short wavelength roughness, even though no clear difference in R_{SW} signal between rupture- and no-rupture areas was observed.

4.3.2.6. Epicenters

Figure 4.13 shows relative density plots for 182 $M_w \geq 7.5$ epicenters as a function of the seafloor roughness. Both for short- and long wavelength roughness, epicenters correlate with slightly rougher seafloor than average, around 125 m for R_{SW} and 600 m for R_{LW} . To test the robustness of this result, the same algorithm has been performed for 100 synthetic datasets (grey lines in Figure 4.13), each containing 182 randomly selected grid nodes instead of the real epicenters used for the original comparison. The grey lines in Figure 4.13 form an envelope that demonstrates the disparity in roughness signal that can arise from simply selecting a subset of the total dataset. The roughness distribution associated with the real epicenters of the SubQuake database falls partly outside this envelope.

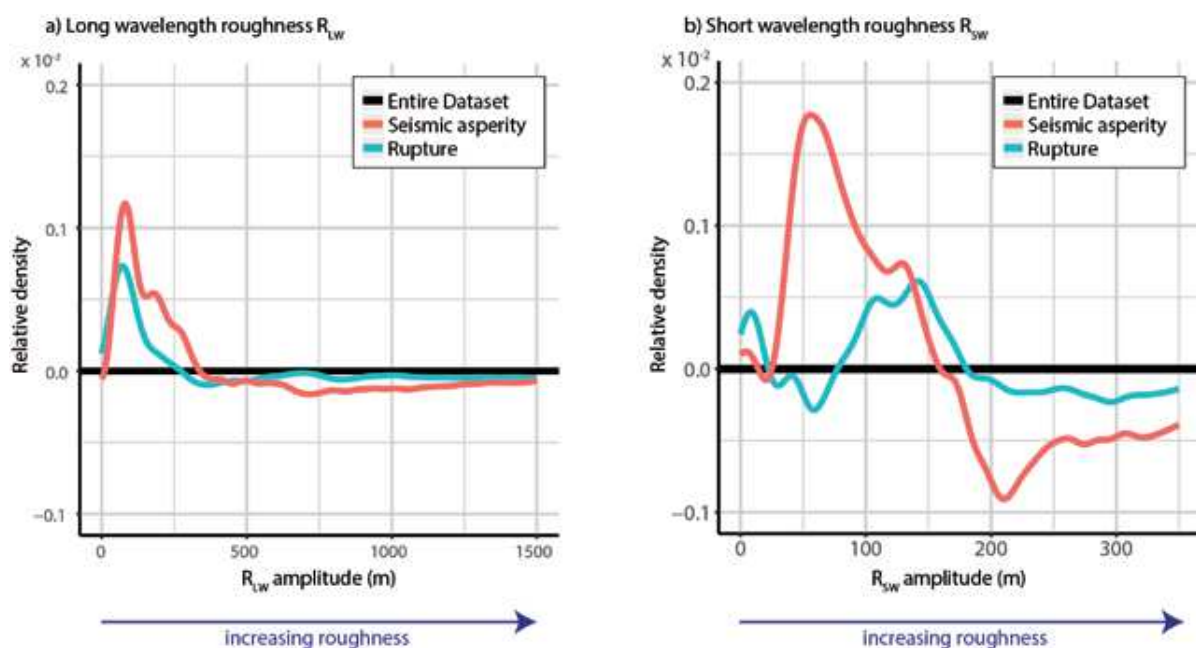


Figure 4.12. Relative density distribution for R_{LW} (a) and R_{SW} (b) for seismic asperities (pink curves) and rupture segments (blue curves) with respect to the global roughness distribution (black line).

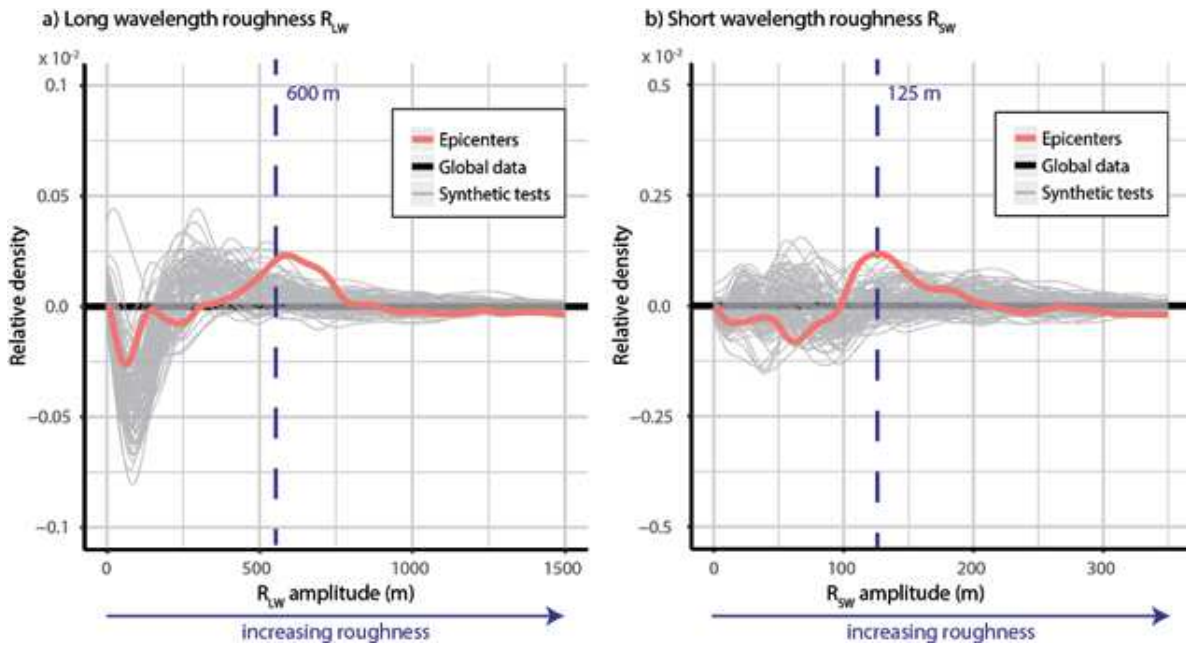


Figure 4.13. Relative density plots for roughness data selected for epicenters (pink curves) with respect to the global roughness distribution (black line), both for R_{LW} (a) and R_{SW} (b). The grey curves indicate the relative density for 100 synthetic data sets, each containing roughness data for 182 randomly selected grid nodes, which represent the “synthetic epicenters.”

4.4. Discussion

The possible relationship between the roughness of the subduction interface and the occurrence of megathrust earthquakes remains a subject of debate. So far, this relationship has not been tested by using a quantification of the seafloor roughness (Lallemand et al., 2018) and taking into account all large interplate events since 1900.

We provide a global database (SubQuake), which includes the location of the rupture epicenter, the overall rupture area and the region where the largest displacement occurs (the seismic asperity). This database is designed to perform a quantitative comparison with two roughness parameters provided by Lallemand et al. (2018): the short wavelength roughness R_{SW} (12-20 km), and the long wavelength roughness R_{LW} (80-100 km). As for many studies attempting to unravel some relevant characteristics for subduction megathrust earthquakes, the limited time record of such events may alter the results (Stein & Okal 2007, 2011). In this study we therefore tried to limit this problem by using the largest possible time window for our analysis, 1900 - 2017. We are aware that this approach raises other uncertainties, such as the decreasing quality of rupture and/or seismic

asperity contours for older ruptures. However, we show that despite these uncertainties, a first-order global trend can be observed.

Ruptures with $M_w \geq 7.5$ tend to occur more often on smooth subducting seafloor at long wavelengths, which is especially significant for the $M_w > 8.5$ events. When focusing on the seismic asperity segments, we observe that they tend to correlate better with smooth seafloor than rupture areas in general. For the epicenter correlation, we see a slight difference in roughness signals, which suggests a possible physical relationship between the nucleation of a rupture and the roughness of the subduction interface. Below, we will discuss these main findings in more detail, with respect to previous studies.

4.4.1. $M_w \geq 7.5$ ruptures tend to occur more often on smooth subducting seafloor

The fact that $M_w \geq 7.5$ megathrust events preferably occur in regions adjacent to a smooth subducting seafloor is in agreement with previous studies (Bassett & Watts, 2015a; Das & Watts, 2009; Wang & Bilek, 2014), which compared the variations in

bathymetry with the occurrence of megathrust events in a qualitative way. We show that this pattern is not only true for specific ruptures or subduction zones, but that it is a general pattern, mainly observed for long wavelength seafloor roughness (Figure 4.10 c & d). By simply looking at the overall roughness and the occurrence of megathrust events, we see that most trenches where seismic slip is spatially predominant, are also among the smoother regions (i.e., Japan-Kuril-Kamchatka, South Andes and Alaska-Aleutians). Those regions, in combination with the very rough areas where almost no $M_w \geq 7.5$ events have been observed (e.g., Izu-Bonin-Mariana), play an important role in the negative correlation between seafloor roughness and $M_w \geq 7.5$ events that we observe in this study. However, within this global trend, exceptions exist, which we briefly discuss in the following paragraphs.

One region which does not face smooth seafloor everywhere, but still hosted many seismic ruptures, among which three $M_w > 8.5$ events, is the Andaman-Sumatra trench. Many of the high roughness amplitudes observed along this trench, result from the presence of the Ninety-East ridge. Whether this Ninety-East Ridge is continuing into the subduction interface however, is questionable (Moeremans & Singh, 2014, 2015). Towards the Andaman Islands, the ridge becomes almost parallel to the trench. In this region, it is therefore possible that the seafloor in front of the trench does not provide a good proxy of the actual subduction interface roughness. Moreover, the large amount of trench sediments (Heuret et al., 2012) in this area suggests that the subduction interface could be considerably smoother than the proxy used in this study.

Several regions that do not fit the general pattern either, are the Cascadia and Antilles subduction zones, as well trench segments in Northern Peru and Central America. These areas all face smooth seafloor, especially at long wavelengths, but show very low, to no occurrence of large megathrust events. The Cascadia subduction zone has been studied extensively (Atwater 1987; Adams 1990; Satake 2003; Goldfinger et al. 2012), and it is widely accepted that previous great megathrust events have occurred along this subduction zone, the last one most likely around 1700. The recurrence time of these events is thought to be ~ 500 years (Wang & Tréhu, 2016), which explains why no interplate

events have been recorded during the past 117 years.

Regarding the smooth region in Northern Peru, Nocquet et al. (2014) used geodetic analyses to demonstrate that this area behaves mainly aseismically, indicating that even though the interface seems to be smooth, other factors play a role in the lack of seismicity. The lack in recently recorded megathrust events remains more difficult to explain for the Antilles subduction zone, as well as the central part of the Central America trench (in front of Guatemala, El Salvador and Nicaragua). In these cases, only little information on the geodetic coupling exists, which makes it difficult to infer whether the subduction interface is predominantly creeping or locking (Okal & Hartnady, 2009). Both the Puerto Rico- and the Lesser Antilles trench are thought to be only partially coupled (Manaker et al. 2008), while the Central America trench between South Mexico and El Salvador is deemed to be weakly coupled (coupling degree of ~ 0.25 , Franco et al., 2012). This low coupled Central America segment is thought to have been influenced by the subduction of the Cocos Ridge towards the southeast, that may act as an indenter against the Caribbean plate (LaFemina et al. 2009; Scholz & Campos 2012). Other possible influences on the coupling and seismogenic behavior are fluid overpressures (Saffer & Tobin 2011), and the inheritance of previous subducted features, which could have damaged the overriding plate and therefore, despite the smooth incoming seafloor, prohibit the occurrence of large events (Ranero & von Huene 2000).

4.4.2. $M_w > 8.5$ events are more sensitive to a smooth seafloor than lower magnitude ruptures

A clear result from our global analysis is the improved correlation between subduction interface roughness and megathrust ruptures with high earthquake magnitude (Figure 4.11a). When we study the relationship between only $M_w 7.5 - 8.5$ events and facing seafloor roughness, we observe almost no difference between the roughness signals for seismic event segments and for the remaining regions (Figure 4.11d & e). However, if we focus on earthquakes with higher magnitudes (i.e., $M_w > 8.5$), we see that it is mainly these largest events

that contribute to the negative correlation between megathrust earthquakes and seafloor roughness (Figure 4.11b & c). In other words, our analysis shows that the largest events are the ones that might have been mostly favored by a smooth subducting seafloor. Since the moment magnitude of an event is proportional to the rupture area, the larger the event can grow, the higher the magnitude. A smooth seafloor without any large mechanical/frictional obstacles or barriers, is therefore the ideal location for an event with the potential of becoming a great megathrust earthquake. For smaller events however, two main reasons could explain why they are not able to grow larger and reach higher magnitudes: 1) Their initial energy is too low. The relationship between the initial stages of a rupture (i.e., the rupture nucleation phase) and the final magnitude is debated. It has been proposed that larger nucleation zones should result in earthquakes with larger magnitudes (e.g., Ohnaka, 2000), whereas others argue that the nucleation size is unrelated to the final size of an earthquake (e.g., Lapusta & Rice, 2003). 2) A heterogeneous stress distribution on a fault, either due to the arrest of previous ruptures, (i.e., areas where stress has been released recently), or due to the presence of a physical barrier (e.g., a subducting seamount or ridge), could prohibit events from propagating and therefore growing any further (Corbi et al., 2017a; Lay et al., 1982). In this case, relatively small ruptures will occur more often on seafloor that is slightly rougher and therefore more heterogeneous, while smooth seafloor might facilitate great to giant earthquakes. This trend has also been observed on the laboratory scale and with numerical simulations. Goebel et al. (2017) investigated the influence of fault roughness on b-values, focal mechanisms, and spatial localization of laboratory acoustic emission (AE) events during stick-slip experiments. They observe that smooth faults promote a more homogeneous stress field and therefore larger rupture sizes when compared to rough- or fractured fault interfaces. Zielke et al. (2017) performed large-scale numerical simulations, while varying roughness and strength conditions. They show that smoother faults may generate larger earthquakes than rougher faults under identical tectonic loading conditions.

On the scale of the subduction megathrust, a clear example of the variable roughness dependency with moment magnitude can be seen along the South

Andes trench. Here, the two greatest ruptures (i.e. the 1960 MW 9.6 and the 2010 M_w 8.8, events 89 and 170 in Figure 4.7) occurred in the southernmost part of the trench, where the seafloor is continuously very smooth. Towards the north, the seafloor is characterized by smooth patches alternating with rough features and here, mainly M_w 7.5 – 8.0 ruptures occurred. The fact that $M_w > 8.5$ events are more frequently associated with a smooth seafloor, might therefore be a direct consequence of the fact that most of these very large ruptures needed continuous smooth seafloor to propagate over long trench-parallel distances and to reach these maximum magnitudes (Figure 4.14). An exception is the 2011 Tohoku event, which reached a M_w of 9.1 without propagating over large trench parallel distances, due to extremely high slips observed in the rupture area (Yue & Lay, 2013). Following the reasoning above, we would expect to see a steady correlation increase with increasing magnitudes, i.e. to observe a larger difference between roughness signals facing M_w 7.5 – 8.0 ruptures than facing the $M_w > 8.0$ ruptures. This can be seen in Figure 4.11a. However, this trend could be influenced by the larger uncertainty in the seafloor roughness proxy when considering lower magnitude events and therefore smaller rupture areas. We mainly focus on the trench-parallel correlation with the seafloor roughness, while earthquakes with $M_w < 8.0$ might not grow necessarily in the trench parallel direction (Sparkes et al. 2010). Besides this, the number of category 5 ruptures (62 events), for which we were not able to obtain a rupture contour, could influence this result. These events are mainly among the oldest events in the database, which makes their location, magnitude, but also their belonging to the subduction interface, very uncertain.

4.4.3. Short wavelength vs. long wavelength roughness

An important aspect of the correlations performed in this study is the considered wavelength of the seafloor roughness. Do all roughness wavelengths play a role in facilitating or prohibiting the occurrence of large interplate earthquakes? We do not observe a significant correlation between the short wavelength roughness (12-20 km) of the seafloor in front of the trench, when looking at segments that correlate with $M_w \geq 7.5$ megathrust ruptures vs. the remaining

length of the trench (i.e., where no ruptures have been recorded since 1900; Figure 4.10a & b). For the long wavelength roughness (80-100 km), we do observe a difference in roughness amplitudes when comparing rupture- and no-rupture segments. Several possible explanations why we do not see a similar result when looking at smaller spatial scales may be suggested: 1) It is possible that variations in seafloor roughness at shorter wavelength and therefore lower amplitudes (i.e., in the range of 0 – 350 m), are not significant enough to play a role in rupture propagation and arrest. In the Alaska-Aleutian region for example, we observe a very different roughness signal when we look at the two wavelength bandwidths (Figures 4.7 & 4.8). At long wavelengths, the roughness amplitudes are very low and the region has been therefore classified as smooth by Lallemand et al. (2018). The short wavelength roughness map however, shows much more variability in roughness, ranging up to amplitudes larger than 350 m. Despite the relatively rough seafloor at short wavelength, many $M_w > 8.0$ ruptures have occurred in this area, making it one of the regions that have a high rupture length ratio. 2) The proxy for the subduction interface roughness at short wavelength based on the seafloor bathymetric prior to subduction could be less reliable. In this

study, we assume that the seafloor seaward of the trench is a reasonable proxy for the roughness of the subduction interface. For the long wavelengths, this proxy is likely to be valid (e.g., Bassett & Watts, 2015a; Das & Watts, 2009; Kodaira et al., 2000; Mochizuki et al., 2008), but one can imagine that the shorter the wavelengths, the more difficult it is to extrapolate roughness variations over a distance of several hundreds of kilometers into the subduction interface.

4.4.4. Seismic asperities correlate with smoother seafloor than ruptures in general

From our analysis of seafloor roughness facing seismic asperities, we observed an amplification of the signal, with respect to the pattern observed for rupture segments (Figure 4.12a & b). This indicates that the seafloor in front of seismic asperities alone, is smoother than the seafloor in front of rupture areas in general. This is in line with expectations, since it seems plausible that during rupture propagation the largest amount of slip occurs where the seafloor is the smoothest, since this is where the largest coupling is expected (Contreras-Reyes et al., 2010, 2017). Surprisingly,

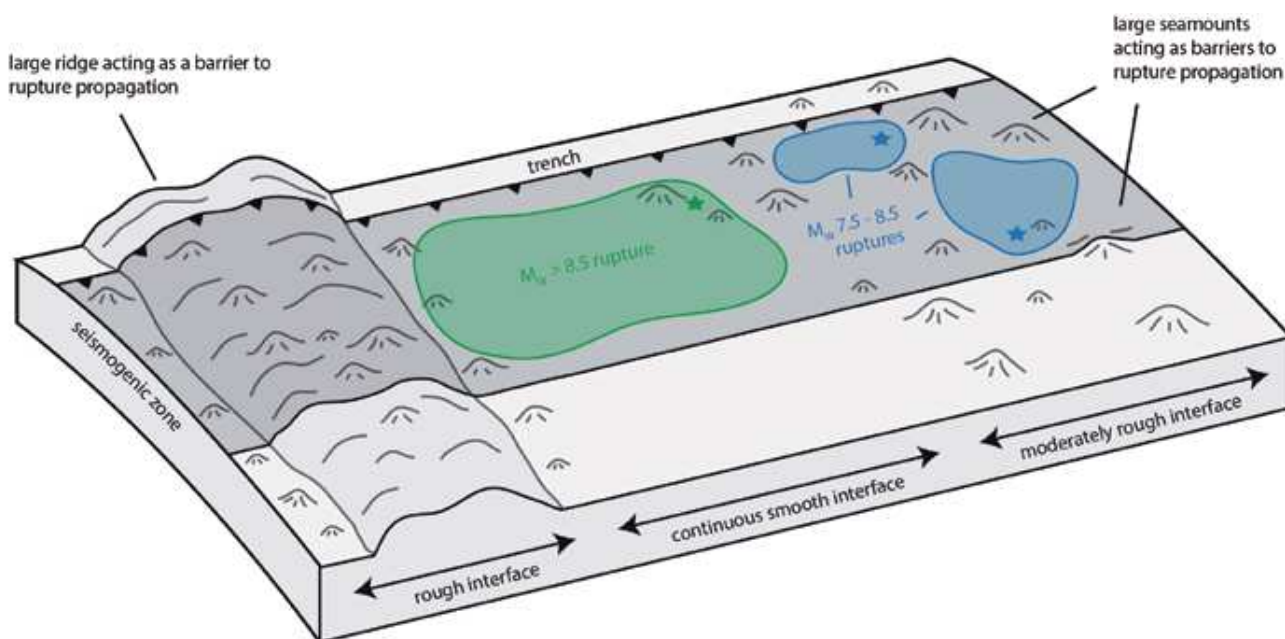


Figure 4.14. Conceptual model illustrating the main results of this study. $M_w > 8.5$ ruptures tend to occur more often on a smooth subduction interface segment, while $M_w 7.5-8.5$ ruptures might also occur on moderately rough seafloor, characterized by a mix of smooth and rough patches. Subducting features, like seamounts or ridges, might act as barriers to rupture propagation but could also be the regions where ruptures nucleate, due to the transition between a locked and creeping state of the interface.

we also observe an excess in low R_{sw} amplitudes (~50-60 m), which is not observed for the areas facing the ruptures in general. This may indicate that seismic asperities preferentially locate where the plate interface is smooth at all wavelengths. A more detailed relationship between seismic asperities and subduction interface roughness cannot be obtained by this study, since some seismic asperities might be too small for the purpose of our global analysis, and their exact location, even for recent events, remains quite uncertain (Lay 2017; Clévéde et al. 2012). Therefore, future studies, possibly more focused on the propagation of individual ruptures, are needed to confirm this (e.g., Ye et al., 2018).

4.4.5. Possible link between rupture's nucleation and seafloor roughness

As mentioned before, when studying the spatial occurrence of large megathrust earthquakes, it is important to take into account the rupture area of these events, and not just the location of their hypocenters. However, by studying solely the hypocenter location, we might gain some insights about the conditions favoring rupture nucleation. According to the rupture data compiled in this study, we see that for ~35 to ~50% of ruptures, the epicenter is located outside the seismic asperity (37% taking into account all seismic asperities, 47% for category 1 events only). This indicates that the nucleation point of an earthquake does not necessarily occur where the largest displacement takes place. Therefore, the conditions necessary for earthquake nucleation are likely to be different than the ones that favor earthquake propagation. Large events have been suggested to nucleate in the vicinity of transition between locked and creeping patches of the subduction interface (Lapusta & Rice 2003). Such transitional regions could result from a change in interface roughness, like the base of a seamount or ridge (Das & Watts, 2009). We observe that the location of a rupture epicenter correlates with a slightly rougher seafloor (compared to the average seafloor, section 4.3.2.4, Figure 4.13a & b). This result has been tested for robustness with 100 synthetic tests (see section 4.3.2.4. and supporting information). The actual epicenter data fall partly outside the envelope formed by the synthetic tests for the long wavelength roughness, suggesting that the results we obtain are robust, and might indicate a physical relationship between the nucleation of

a rupture and the roughness of the subduction interface. In regions close to subducting topographic highs, the stress conditions at the resulting transition between locked and creeping fault patches might be favorable for rupture nucleation. Of course, for this we would assume that major subducting highs would favor a dominantly creeping behavior (Wang & Bilek, 2011).

4.4.6. Seafloor roughness acting as a barrier to rupture propagation

Numerous authors have suggested that topographic features on the seafloor, like seamounts or ridges, may segment the subduction interface and arrest ruptures (Geersen et al., 2015; Kodaira et al., 2000; Mochizuki et al., 2008; Robinson et al., 2006; Wang & Bilek, 2011). Such behavior has been observed for the 2011 M_w 9 Tohoku rupture, which stopped against the Joban seamount chain towards the south (Wang & Bilek, 2014), but also for the 1960 M_w 9.6 Bio-Bio rupture, which is thought to be influenced by the subducting Chile Rise at the southernmost part of the rupture area (Contreras-Reyes & Carrizo, 2011). The southern arrest of the 2004 M_w 9 Sumatra earthquake is also thought to have been caused by a morphological high, that acted as a persistent barrier and therefore prevented the 2004 and 2005 Sumatra ruptures from occurring as one single event (Morgan et al. 2017).

Despite the many examples of subducting highs that likely played a role in rupture arrest, it is not easy to address this question in this global study. Many rupture areas in our SubQuake grid overlap, making it difficult to define the areas that may have acted as barriers to rupture propagation. An additional complexity arises from the possible change in mechanical behavior of a subducting feature over time, for example depending on the slip history of preceding events, or the mechanism that causes the barrier-type behavior (i.e., either due locally increased or decreased coupling at the subducting high; Das & Watts, 2009; Kodaira et al., 2000; Morgan et al., 2017; Wang & Bilek, 2011).

Even though we cannot address the role of subducting reliefs as barriers in detail, our results do highlight a general trend of rupture occurring preferentially on large smooth patches of the seafloor, especially

with increasing rupture magnitude. This is in line with earlier proposed models for seamount subduction, which stated that a seamount might fracture the overriding plate while it subducts, and therefore would locally prevent the buildup of stress necessary for rupture propagation (Dominguez et al., 1998; Ruh et al., 2016; Wang & Bilek, 2011, 2014). In addition, Lallemand et al. (2018) have shown that rough seafloor is associated with low values of seismic coupling (< 0.5), while smooth seafloor correlates with high seismic coupling (> 0.5). Seafloor that is characterized as rough, with many

significant topographic features, might therefore be less prone to host large- to giant earthquakes. This is what we observe in this study, as a first-order, global relationship. Besides the studies that address natural examples of subducting features and their role on the seismogenic behavior of the megathrust, modelling studies, focusing on the physical mechanism of relief subduction, are necessary to unravel the effect that a topographic high might have on the state of stress and on the coupling along the subduction interface.

4.5. Conclusions

We present SubQuake: a complete catalogue of $M_w \geq 7.5$ subduction interplate earthquakes that occurred between 1900-2017. SubQuake includes information on the rupture epicenter, rupture contour and seismic asperity contours. We use this database for a quantitative comparison with a proxy of the subduction interface roughness within a given wavelength interval (12 -100 km). From this global comparison, we can draw the following conclusions:

1. Large ($M_w \geq 7.5$) interplate earthquakes occurred preferentially in areas that are characterized by smooth seafloor. From this group, $M_w > 8.5$ earthquakes are the most sensitive to a smooth subduction interface, while for $M_w 7.5 - 8.5$ events, the difference in roughness pattern with respect to the areas that did not host any events is less clear.
2. We observe that roughness at longer wavelengths (80 – 100 km) seems the most determining for the occurrence of large- to giant subduction earthquakes. For short wavelength roughness we do not observe a clear difference in roughness signal between rupture and no-rupture areas.
3. Based on our analysis, seismic asperities tend to correlate better with smooth seafloor than rupture areas in general, both for short- and long wavelengths.
4. Our first-order comparison between rupture epicenters and seafloor roughness suggests that there might be a physical relationship between the nucleation of a rupture and the roughness of the subduction interface.

Future studies are necessary to systematically investigate the role of seafloor roughness on the coupling along the subduction interface and on the occurrence of large- to giant megathrust earthquakes. Modelling studies, both analogue and numerical, can contribute to the understanding of the role of subducting features over timescales of multiple seismic cycles. Additional natural data studies, for example focusing on the geodetic coupling of specific areas, are necessary to better understand the current state of stress in regions where rough seafloor is subducting.

5. Rough subducting seafloor reduces interseismic coupling and mega-earthquake occurrence: Insights from analogue models

In preparation for submission as:

van Rijnsingen, E., Funicello, F., Corbi, F., Lallemand, S. Rough subducting seafloor reduces interseismic coupling and mega-earthquake occurrence: Insights from analogue models.

Abstract

The roughness of the subduction interface is thought to influence seismogenic behavior in subduction zones, but a detailed understanding of how such roughness affects the state of stress along the subduction megathrust is still debated. Here, we use seismotectonic analogue models to investigate the effect of subduction interface roughness on seismicity in subduction zones, which allow us to observe the seismogenic behavior over multiple seismic cycles. We compared rupture source parameters and slip distributions for two roughness endmembers. Models characterized by a very rough interface have lower interface frictional strength and lower initial- and interseismic coupling than models with a very smooth interface. Overall, ruptures in the rough models are smaller in terms of rupture area and duration, as well as maximum displacement and laboratory moment magnitudes. Individual rupture evolutions and slip distributions indicate a segmentation of the subduction interface by the rough geometry. We propose that the alternation of tensional and compressional bending forces as a result of the flexure of the overriding plate is one of the mechanisms that can create a very heterogeneous strength distribution, resulting in the segmentation of the interface.

5.1. Introduction

Just as in strike-slip fault systems (e.g., Wesnousky, 2006), fault geometry is thought to play an important role in the occurrence of earthquakes along the subduction megathrust (e.g., Kelleher & McCann, 1976). The geometry of the subduction thrust fault, usually referred to as its roughness, is caused by topographic features on the seafloor, such as seamounts, ridges, fracture zones, or plateaus. Many studies have already addressed the influence of subducting topography on the spatial occurrence of megathrust earthquakes (e.g., Das & Watts 2009; Kopp 2013; Wang & Bilek 2014), but a detailed understanding of how this roughness affects the state of stress at the subduction interface, and therefore its seismogenic potential, is still debated. By focusing on the spatial distribution of individual ruptures in nature, several studies have shown that a subducting seamount, ridge or fracture zone has acted as a barrier to rupture propagation (e.g., Das & Watts, 2009; Geersen et al., 2015; Henstock et al., 2016; Kodaira et al., 2000; Mochizuki et al., 2008; Robinson et al., 2006; Singh et al., 2011). However, contradicting theories exist as well, suggesting that a subducting feature may act as an asperity and therefore promote the occurrence of megathrust earthquakes instead (Cloos 1992; Scholz & Small 1997; Husen et al. 2002; Bilek et al. 2003). Recent studies have addressed this issue with a global approach and all suggest that a smooth subduction interface is more prone to host large- to mega-earthquakes than a rough interface (Wang & Bilek 2014; Bassett & Watts 2015a; Lallemand et al. 2018; van Rijnsingen et al. 2018). Possible explanations for this are the promotion of rupture propagation on smooth interfaces due to the absence of interruptions such as topographic features, a local decrease in mechanical coupling when rough seafloor subducts (i.e., due to the development of a fracture network around a subducting high; Wang & Bilek, 2011), or a local increase in coupling when rough seafloor subducts (i.e., due to increased normal stress; Kodaira et al., 2000).

In addition to natural data studies, models can be useful to study the process of subducting seafloor roughness systematically and over longer timescales ($\gg 100$ yrs). This is not feasible with natural data, since recurrence times for (very) large earthquakes often exceed the natural record of roughly 100 years. Among the first models of subducting seafloor topography were the sand box experiments performed by Dominguez et al. (1998a; 2000),

which show a fracture network that develops in the overriding plate during single seamount subduction. Since then, models that address this question have been mainly numerical, such as the 2D sinusoidal fault models by Ritz & Pollard (2012), or the scale independent fault roughness models by Zielke et al. (2017), which both show that increasing fault roughness leads to smaller ruptures.

In this study, we address the problem by using seismotectonic analogue models (Corbi et al., 2013) that allow us to study the effect of fault roughness in a physically self-consistent, realistic and three-dimensional subduction setting, over the course of multiple seismic cycles. These models have been used before to study the role of subduction velocity and the width of the seismogenic zone on the seismogenic behavior (Corbi et al., 2017a), as well as the synchronization of asperities on the interface by spatially varying the frictional properties from velocity weakening to velocity strengthening (Corbi et al., 2017b).

Here we keep the frictional properties constant, but instead we introduce a 3D printed geometry that can be added to the subduction interface. By reproducing scales of roughness that are in line with large topographic features we observe in nature (Lallemand et al. 2018), we test if and how a rough interface influences the size and spatial distribution of megathrust earthquakes. Instead of focusing on a single seamount, we aim to look at a broader scale, allowing comparison with natural subduction zones that are characterized by a very rough- (e.g., Mariana) or very smooth (e.g., Kuril) subducting seafloor. The analogue setup allows us to only focus on the role of roughness of the interface, while keeping all other subduction parameters constant.

We will first discuss the new 3D printing approach as well as the model setup, after which we will analyze two sets of endmember roughness models (i.e., very rough and very smooth interfaces) in terms of source parameters such as rupture duration, rupture area and moment magnitude, as well as interseismic coupling and spatial slip distribution with respect to the geometry of the interface. Finally, we will discuss how our results relate to the previously proposed physical mechanisms for subduction of rough seafloor (Scholz & Small, 1997; Wang & Bilek, 2011; 2014).

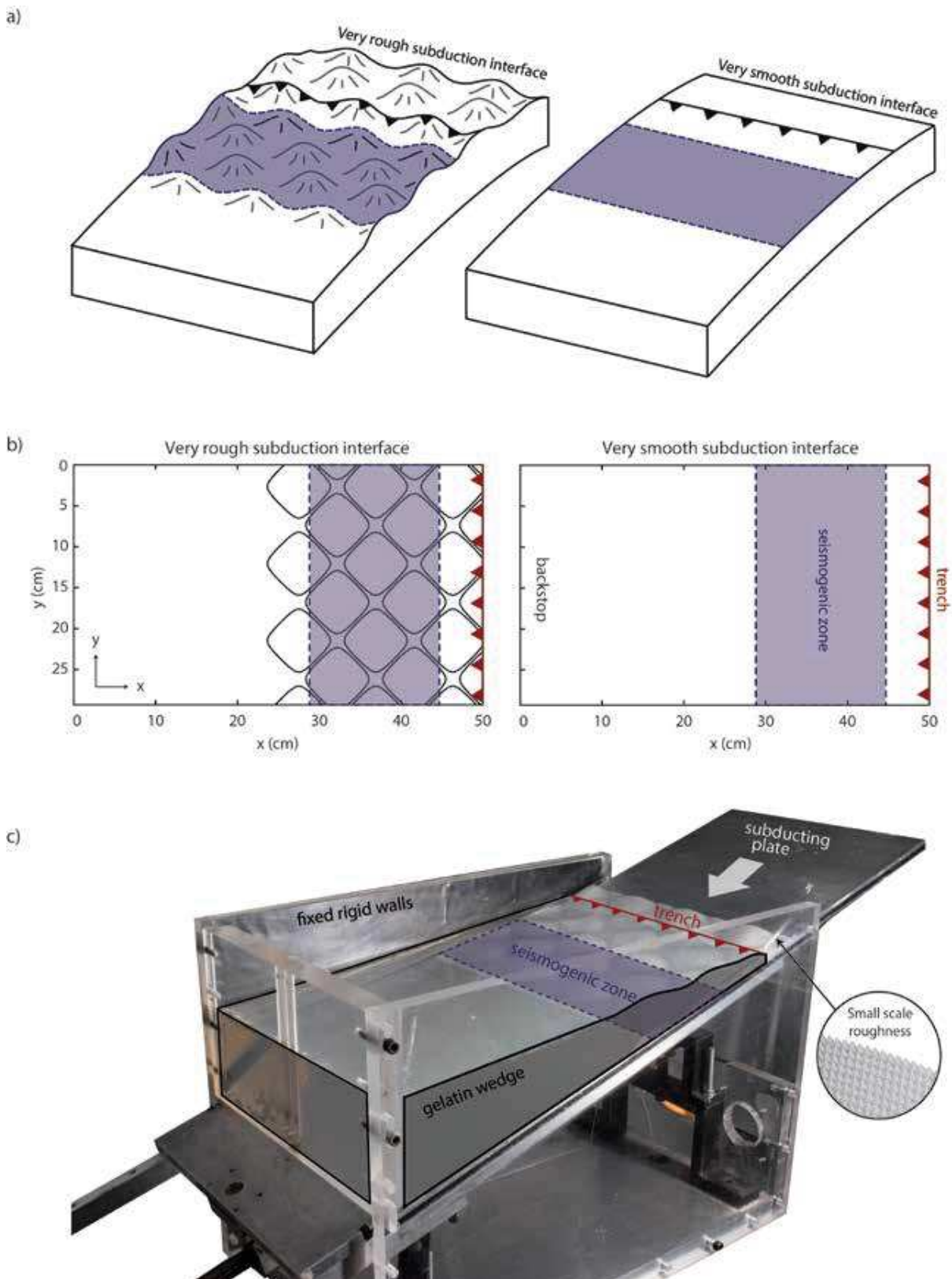


Figure 5.1. Model setup with two endmember interfaces. a) Cartoon illustrating the rough and smooth endmembers. b) Schematic representation (top view) of the experimental setup. The rough interface (black squares), the seismogenic zone (blue shaded rectangle) and the trench (red triangles) are indicated. c) Photograph of the experimental apparatus (oblique view). The gelatin wedge (highlighted with black lines) has a size of 34 x 52 cm² in trench parallel- and orthogonal direction respectively, which is equivalent to a natural convergent margin of 216 x 330 km². The rough interface is characterized by large seamounts (i.e., the large scale roughness) and a small scale roughness (see inset) that ensures stick-slip behavior.

5.2. Methods

5.2.1. 3D-printing seafloor roughness

For studying the effect of subduction interface roughness on the occurrence of megathrust earthquakes, we create two endmember-type subduction interfaces: a planar vs. a very rough interface (Figure 5.1a & b). We 3D-print these interfaces by using a FlashForge Creator Pro 3D printer and PLA filament as printing material. With a Matlab algorithm, we can design a 3D seafloor by stacking multiple 2D sinusoidal functions that are converted to positive values only for practical reasons. Both interfaces are characterized by an isotropic, small scale roughness to ensure stick-slip behavior. It is characterized by peak amplitudes (A) of 0.8 mm and a wavelength (λ) of 1 mm and, following a benchmark test with the previously used sandpaper by Corbi et al. (2011, 2013, 2017a, 2017b), shows velocity-weakening behavior (Table 5.1). In addition to this small scale roughness, the rough interface is made up of a larger scale roughness, consisting of equally sized and homogenously distributed seamounts with amplitudes of 6.28 mm (4 km in nature) and a period of 94 mm (60 km in nature). These sizes are equivalent to large seamounts in nature, such as the seamounts in the Louisville Seamount Chain at the Tonga-Kermadec trench (Scholz & Small 1997), or the Joban Seamount Chain in the Japan trench (Lallemand et al. 1989; Mochizuki et al. 2008).

5.2.2. Model setup and monitoring

The 3D-printed subduction interfaces are attached to a rigid, 10° dipping plate that represents the shallow portion of the subducting slab (Figure 5.1b). With a velocity of 0.1 mm/s, it underthrusts a gelatin wedge (2.5 wt% Pigskin; Di Giuseppe et al., 2009), the analogue of the overriding plate (more details on

the scaling of the gelatin wedge and the model setup with nature can be found in the appendix, section A.5.1.). A plastic sheet with a window of $34 \times 16 \text{ cm}^2$ that indicates the seismogenic zone ($216 \times 102 \text{ km}^2$ in nature), is placed between the downgoing plate and the gelatin wedge. It follows the shape of the underlying topography, but stays in place during the experiment, meaning that the seismogenic zone (i.e., the window in the plastic sheet) will remain in a fixed place, while the downgoing plate passes below. Areas up- and downdip of the seismogenic zone will behave in a velocity strengthening way, due to the contact between the plastic sheet and the gelatin wedge, while the 3D printed interface arriving within the window has velocity weakening characteristics. In total, eight experiments are performed, from which four with an (identical) rough interface (Rough A-D) and four with a smooth interface (Smooth A-D). All experiments are monitored from above with a video camera that records 7.5 frames per second for a duration of 20 min, allowing us to observe multiple seismic cycles within one experiment. Images are post-processed using particle image velocimetry PIV (PIVlab, Thielicke & Stamhuis, 2014) resulting in displacement data at the top of the gelatin wedge (i.e., surface displacements). From these data, source parameters, such as rupture area, rupture duration, interseismic coupling, recurrence time and mean displacement are extracted with a Matlab algorithm (see appendix A.5.2. for details). By working with surface displacements, we implicitly assume that these displacements are representative for the displacements at the subduction interface. For the experiments with a rough subduction interface, earthquakes are classified into different categories based on their slip distribution (i.e., largest slip occurring on top of one seamount, on multiple seamounts or mainly in between seamounts).

	Amplitude A (mm)	Wavelength λ (mm)	Natural equivalent	Models
Small scale roughness	0.8	1	Provides frictional properties for stick-slip behavior	Both smooth and rough
Large scale roughness	6.28	94	Very rough seafloor characterized by large seamounts with heights of $\pm 4 \text{ km}$ and widths of $\pm 60 \text{ km}$.	Rough only

Table 5.1. Roughness properties used for the 3D printed subduction interfaces.

5.3. Results

5.3.1. General model behavior

All models go through an initial loading stage (4-8 min), during which the gelatin wedge gets elastically shortened and the trench slowly moves landward as the basal plate is underthrust (Figure 5.2). At a certain strength threshold (after 5-10 % of shortening), the system starts to behave in a stick-slip manner, showing multiple seismic cycles characterized by a phase of landward loading (i.e., stick), followed by a quick release of stress and a seaward motion of (part of) the wedge (i.e., slip).

The coupling for the initial loading stage can be calculated based on the compression of the wedge towards the backstop during the first 4 minutes of each experiment (steep initial slopes in Figure 5.2) as a ratio of the displacement of the downgoing plate (black line in Figure 5.2; see supporting information for more details). The initial loading coupling ranges from 67% (Rough D) to 82% (Smooth B) and the displacement threshold before stick-slip behavior lies between 15 mm (Rough C) and 43 mm (Smooth A). Looking at this displacement threshold, which is equivalent to the frictional strength of the interface right before failure, we can clearly observe two

groups: larger thresholds (i.e. larger interface strength) for all four smooth models, while the rough models show generally lower, and more variable displacement thresholds.

Figure 5.3 shows representative slip maps for both the smooth- and the rough models. In these figures, the seismic asperity is indicated (white line), which highlights where the largest displacement has taken place during the rupture (50% max slip contour). For the smooth models, we can distinguish between ruptures that cover the entire interface (5.3a), and ruptures that cover only a third or half of the interface (5.3b). The slip distribution within these ruptures is generally quite symmetrical, showing a seismic asperity in the center of the rupture area and decreasing slip values towards the rupture edges. Ruptures in the rough models are generally smaller, often limited to only one or several seamounts.

We analyzed all events in the rough models in terms of spatial distribution of the slip larger than 50% of the maximum slip (Figure 5.3c-e). Ruptures were divided into three different categories: the maximum slip focused on a single seamount (33%), on multiple seamounts (14%), or mainly in between a group

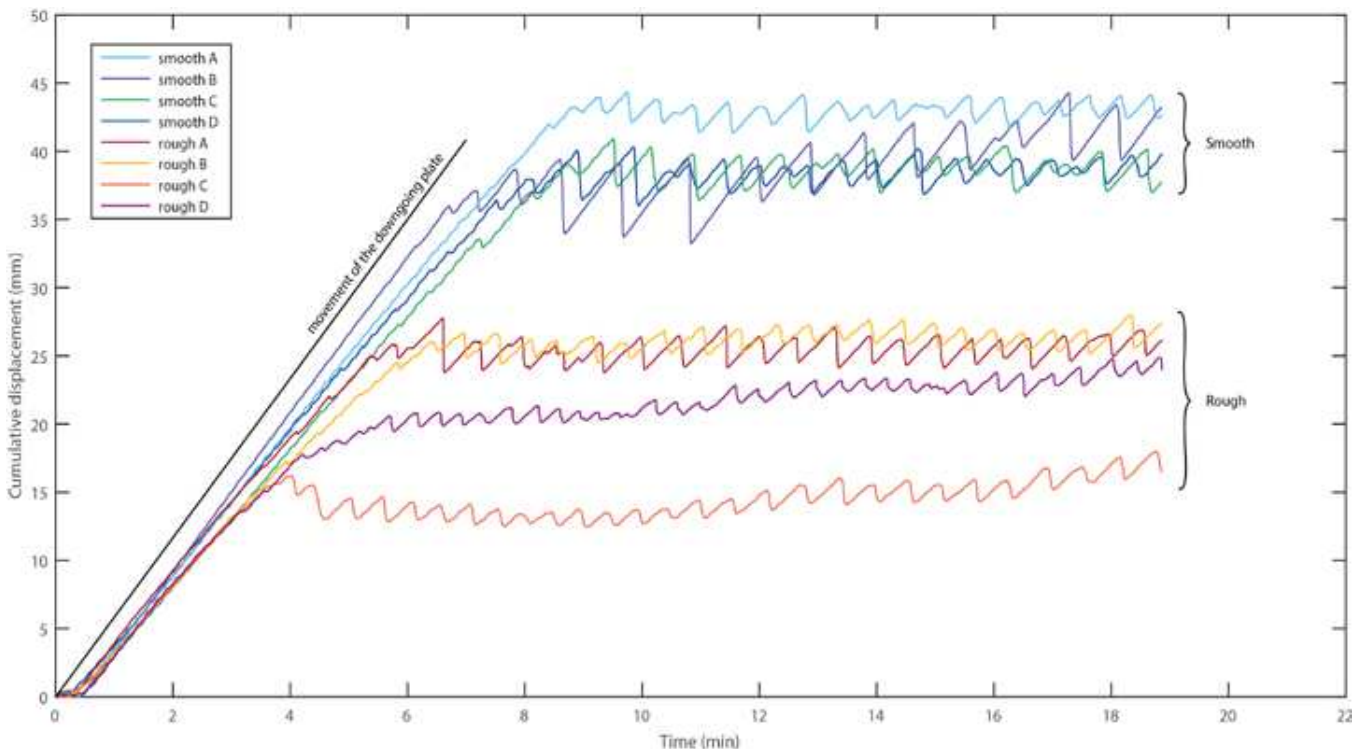


Figure 5.2. Cumulative displacement of one point centered above the seismogenic zone for each experiment. Each colored line represents one experiment, while the black line indicates the movement of the downgoing plate. The smooth- and rough experiments can clearly be distinguished into two groups.

of seamounts (53%). These percentages show that only a small number of the events clearly ruptures multiple seamounts (Figure 5.3e), while most of the events have their maximum slip concentrated either on top of a single seamount (Figure 5.3c), or at a low surrounded by seamounts (Figure 5.3d). Figure 5.4 shows an example of a multi-seamount rupture, with both incremental- and cumulative displacement evolution over time. We observe a crack-type rupture,

meaning that the nucleation region slips throughout the quake, expanding and then shrinking until the rupture stops (Marone & Richardson, 2006). The rupture starts off at a low ($t = 0$ s), followed by a large concentration of slip on a single seamount ($t = 0.4$ s), after which it slowly expands to the neighboring seamounts. The expansion of the rupture is influenced by the geometry of the interface, since the largest concentration of slip moves step-wise

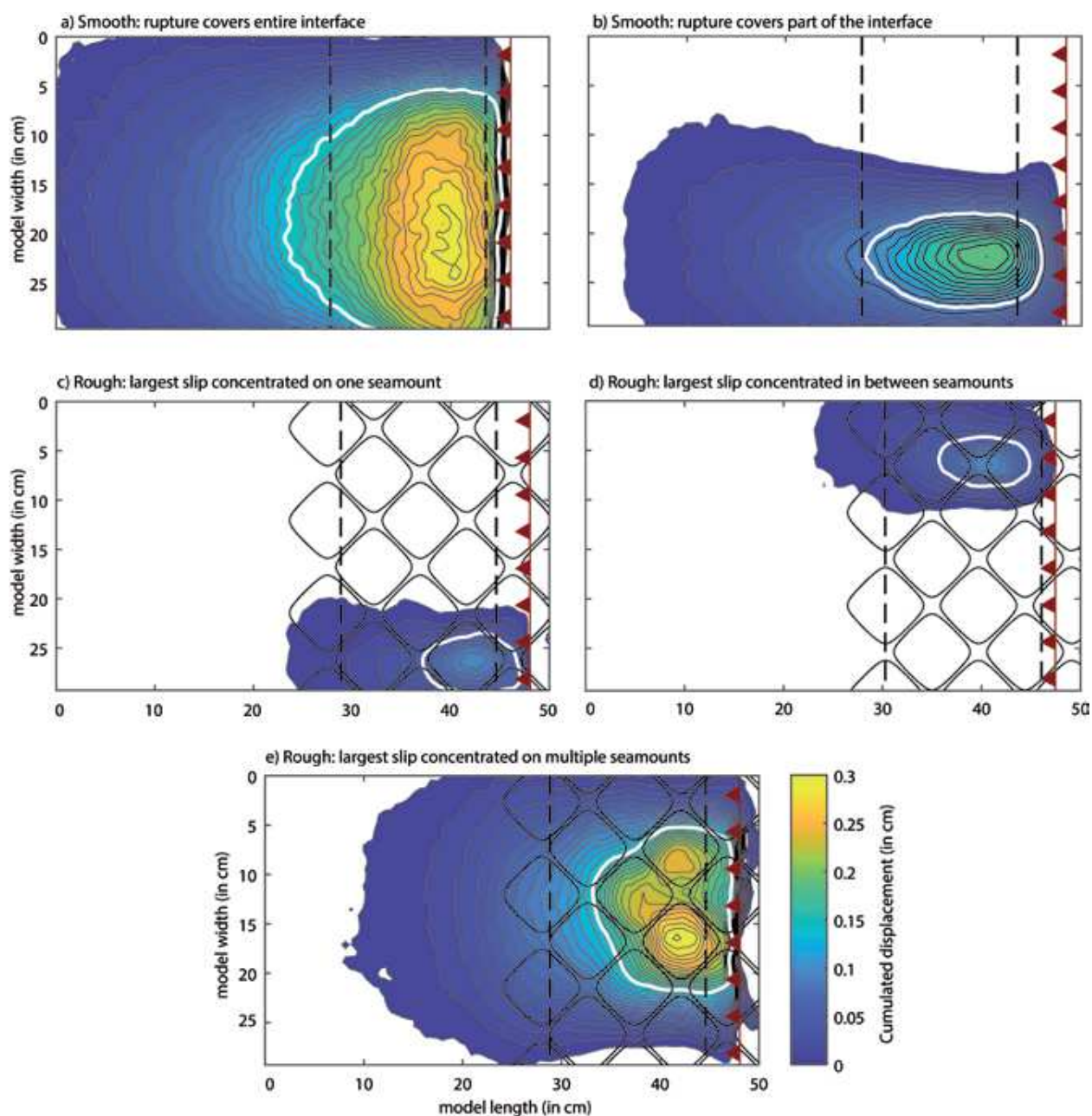


Figure 5.3. Cumulative displacement for representative coseismic events for the smooth- (a & b) and the rough models (c - e). Colors indicate cumulative slip in cm, following the colorbar on the bottom right. The white line represents the area where the maximum slip occurred (seismic asperity; 50% of maximum slip). The seismogenic zone is bounded by the dashed black lines and for the rough models, the seamount distribution is shown with solid black lines.

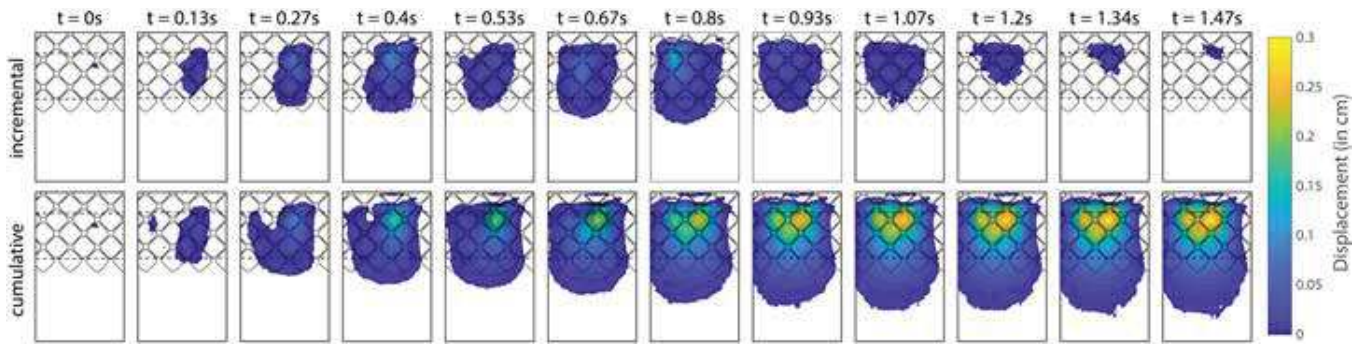


Figure 5.4. Incremental and cumulative slip distribution over time for an event rupturing multiple seamounts. The seismogenic zone (dotted black lines) and the roughness pattern (solid black lines) are indicated in each sub-figure.

from one seamount to another ($t = 0.67$ and $t = 0.8$ s), rather than growing homogeneously. Three seamounts acted as individual asperities, but synchronized during this particular rupture, and can be clearly identified from the final cumulative slip pattern (Figure 5.4, $t = 1.47$).

5.3.2. Source parameters: Rough vs. Smooth

By isolating the coseismic- from the interseismic phases in our models, several source parameters for each coseismic event can be extracted (see the appendix for details on how the source parameters are extracted). Figure 5.5 shows violin plots for earthquake duration (a), recurrence time (b), interseismic coupling (c), mean slip (d), rupture area (e) and seismic asperity (f). The smooth- and rough violin show the data distribution for all events in the smooth- (245 coseismic events) and the rough models (346 coseismic events). For earthquake duration, we observe a clear difference between the two endmembers. Rupture duration for the smooth models is generally much longer (mean = 2.27 s) compared to the rough models (mean = 0.76 s). For the recurrence time we see similar distributions for both smooth (mean = 12.28 s) and rough (mean = 11.35 s) datasets. The interseismic coupling, which indicates how much movement of the downgoing plate is transferred to the overriding plate (see appendix A.5.2. for more details on how this is calculated), is generally much higher (mean = 50.71 %) for the smooth models than for the rough models (mean = 34.49 %). When looking at the slip parameters, we observe higher mean slip (mean = 0.26 mm) for events in the smooth models, ranging

up to 2 mm. The rough models have a mean slip of 0.11 mm, with the largest values ranging up to 1 mm. A small difference can be seen for the rupture area distributions (mean smooth = 565 cm², mean rough = 395.8 cm²), while the difference for the seismic asperity area is much clearer (mean smooth = 121.4 cm², mean rough = 70.7 cm²). The seismic asperity represents the area where slip values are at least half of the maximum slip of the event, meaning that the area of the seismic asperity says something about how homogeneous the slip values are distributed within the rupture area.

The results of these source parameters show that ruptures in the smooth models generally have longer duration and higher mean slip values, that are more widely distributed within the rupture area (i.e., larger seismic asperities). In addition, smooth models show higher interseismic coupling than rough models.

5.3.3. Seismic moment vs. Duration

To better understand whether the longer durations for ruptures in the smooth models mainly result from the larger areas, or from slower rupture propagation, the seismic moment vs. rupture duration can be evaluated. Figure 5.6. shows seismic moment M_0 vs. rupture duration in a log-log representation. The seismic moment is calculated following:

$$M_0 = \mu AD$$

where μ is the gelatin's shear modulus in Pa, A the rupture area in m² and D the mean displacement in m. The seismic moment and rupture duration are

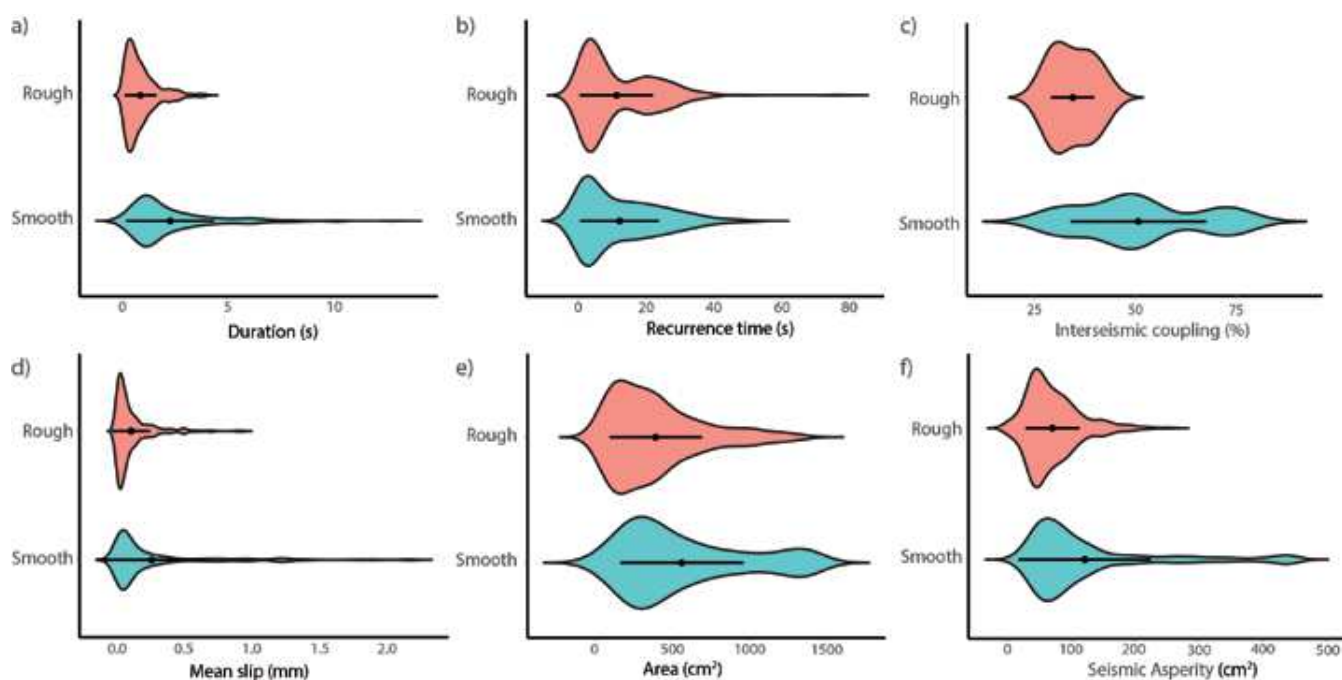


Figure 5.5. Violin plots of various source parameters for models with a smooth- (blue) and rough (red) subduction interface. The curved lines show the distribution of the data, while the black dot and bar represent the mean and standard deviation (respectively).

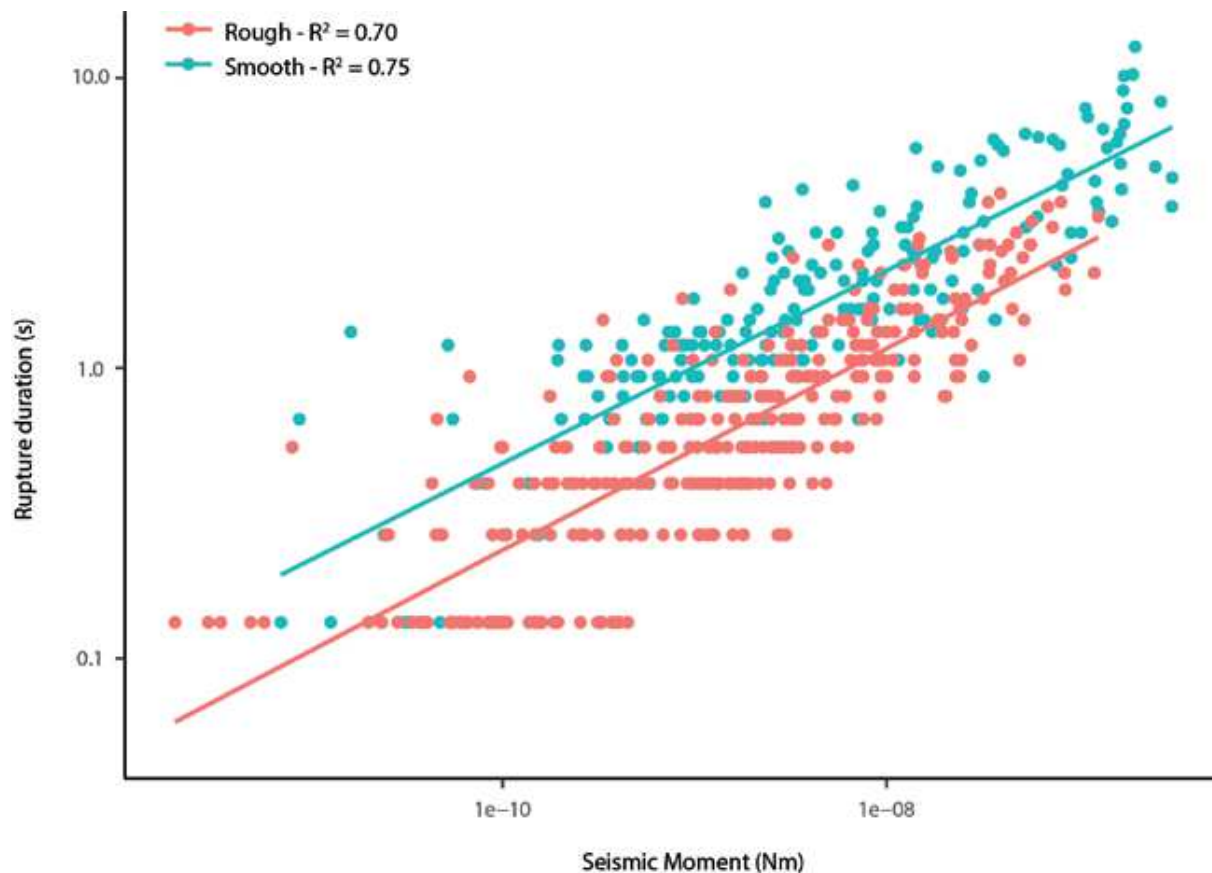


Figure 5.6. Seismic moment vs rupture duration for both the Smooth (blue) and the Rough (red) datasets in a log-log representation. Seismic moment $M_0 = \mu AD$, where μ is the gelatin's shear modulus in Pa, A the rupture area in m^2 and D the mean displacement in m. A linear regression line is plotted for both datasets, with R^2 indicated in the legend.

based on the experimental data and not converted to natural scales.

In Figure 5.6, two datasets can be clearly distinguished, with the smooth data more located towards the top-right of the plot (i.e., larger seismic moments and longer rupture durations) and the rough data more towards the bottom-left corner (i.e. smaller seismic moments and shorter rupture durations).

5.4. Discussion

In this work, we study the effect of subduction interface roughness on the occurrence of megathrust earthquakes. The advantage of using (analogue) models with respect to the analysis of natural data, is the possibility to isolate one parameter (the subduction interface roughness), while keeping all the other parameters constant. For this, we use two endmember interfaces, one very rough (characterized by many large seamounts) and one very smooth (planar) interface. We observe that the rough models have lower interface frictional strength with respect to the smooth models, meaning that they can store less elastic energy before failing in a stick-slip manner (Figure 5.2). The finding that both initial coupling (during the strain accumulation phase) and interseismic coupling are also lower for the rough models is therefore not surprising, since the ability for the interface to store elastic energy and the coupling between both plates are inherently related. From the source parameters (section 5.3.2.), we observed a general trend for smaller earthquakes in the rough models, both in terms of rupture area and duration, as well as mean slip and seismic asperity. This trend is also seen when looking at the slip patterns for the earthquakes in the rough experiments, where 33% of the ruptures has their largest displacement concentrated (i.e., seismic asperity) on a single seamount, and 53% of the events has their seismic asperity located in between a group of seamounts. Only 14% of the ruptures in the rough models are much larger, with the seismic asperity covering multiple seamounts. Here, the segmenting effect of the interface geometry can be clearly observed in the slip pattern (Figure 5.4.).

When comparing the slopes for both regression lines, they appear quite similar (i.e., 0.33 and 0.35 for the smooth and rough datasets, respectively). However, a vertical shift in the regression line can be observed, indicating that for the same seismic moment, a rupture occurring in a smooth subduction interface setting would have longer rupture duration than a rupture in a rough model.

5.4.1. Comparison with numerical modelling studies

The results from this study are in agreement with several numerical models that investigate the effect of fault roughness (Ritz & Pollard 2012; Zielke et al. 2017) or seamount subduction (Yang et al. 2013) on the occurrence of earthquakes. Ritz & Pollard (2012) use a two-dimensional displacement discontinuity method to study the amount of slip and its distribution along an infinitely long sinusoidal interface in a homogeneous and isotropic elastic material. They find that where slip on a planar fault usually has an elliptical distribution (Pollard and Segall, 1987), for the wavy fault interfaces the slip distributions are nonelliptical and reflect the sinusoidal geometry, something we see in our models as well (section 5.3.1). They also show that the mean slip decreases as the geometrical irregularity of the fault (e.g., the number of sinusoidal waves or the amplitude/wavelength ratio) increases. Zielke et al. (2017) investigated the (combined) effect of fault surface roughness and the spatial heterogeneity of fault strength on the slip distribution and moment release. They use large scale numerical simulations in which the fault roughness is parameterized as a 2D random field that follows the von Karman autocorrelation function. Since they use a self-similar roughness model, their simulations are scale-independent, meaning that the circular fault patch in their models can represent faults at any scale. Their results show that smooth faults, both for a homogeneous- and heterogeneous strength distribution, have higher seismic moment releases, and therefore larger earthquakes than rougher faults. Yang et al. (2013) do not investigate the effect of fault roughness

on the occurrence of earthquakes, but focus only on the barrier-effect (i.e., the possibility to stop a rupture from propagating) of a single subducting seamount. By using slip-weakening dynamic rupture simulations they investigate how a geometrical high under either elevated or reduced normal stress influences coseismic rupture propagation. They show that a seamount is more likely to act as a barrier when normal stress at the seamount is increased with respect to the surroundings (as suggested by Kodaira et al., 2000), for larger seamount height-to-width ratios, and for shorter seamount-to-nucleation distances. They also show that the required additional normal stress to stop rupture propagation is decreased as the seamount height-to-width ratio increases.

5.4.2. Comparison with natural observations

Our model results are also in agreement with many natural data studies that focus on the relationship between subduction interface roughness and the occurrence of megathrust earthquakes. Global studies have shown that large earthquakes ($M_w \geq 7.5$) preferably occur along a smooth subduction interface and that rough subducting seafloor is associated with lower seismic coupling and a creep-like behavior (Wang & Bilek 2014; Bassett & Watts 2015a; Lallemand et al. 2018; van Rijsingen et al. 2018). This trend can be illustrated by comparing two endmember subduction zones, the Izu-Bonin-Mariana trench versus the Japan-Kuril-Kamchatka trench. Following the classification of Lallemand et al. (2018), which is based on the seafloor characteristics prior-to-subduction, Izu-Bonin-Mariana is considered almost entirely rough, while Japan-Kuril-Kamchatka is dominantly smooth. This difference between the two endmembers is also reflected in the occurrence of $M_w \geq 7.5$ megathrust events over the past ~ 100 years (van Rijsingen et al., 2018), since 96% of the Kamchatka-Kuril trench length has ruptured (among which 10 $M_w \geq 8.0$ ruptures), while no $M_w \geq 7.5$ events have occurred in the Izu-Bonin-Mariana trench. Even though on a global scale, there seems to be a clear difference between dominantly rough- and dominantly smooth subduction zones in terms of seismogenic behaviour, on a local scale, different trends are observed. In some places, measurements of geodetic coupling above subducting topographic relief show a local

increase in interplate coupling (e.g., Kyriakopoulos & Newman 2016; Collot et al. 2017), while in other places a subducting topography is thought to cause a local decrease in coupling (Mochizuki et al. 2008; Singh et al. 2011; Geersen et al. 2015; Marcaillou et al. 2016; Collot et al. 2017). These local variations, but also the short natural record (i.e., ~ 100 years), make it challenging to come up with a mechanism that correctly explains the effect of subducting seafloor roughness on the occurrence of megathrust earthquakes.

5.4.3. Scenarios for subducting seafloor roughness

From the existing literature, two scenarios describing the effect of subducting relief on the coupling and seismogenic behaviour in subduction zones can be considered. Scholz & Small (1997) suggest that subducting seamounts are accommodated along the subduction interface by flexure of the subducting- and overriding plate, which would increase the normal stress on the interface (Turcotte and Schubert, 1982, p. 120). They argue that this local increase in normal stress would result in a higher coupling and therefore promote an asperity-like effect of subducting seamounts, meaning that (large) ruptures would preferably occur in locations where (large) seamounts are subducting. Wang and Bilek (2011; 2014) on the other hand, suggest a decrease in coupling where topographic features are subducting, due to a fracture network that is thought to develop in the overriding plate surrounding such a feature. Through this network of small faults, stresses along the interface are released, promoting a creep-like behavior rather than strain accumulation and therefore a locking of the interface. This can explain the observed barrier-effect of subducting features (e.g., Geersen et al., 2015; Mochizuki et al., 2008; Singh et al., 2011), the decrease in seismic coupling for rough subduction zones (Lallemand et al. 2018), and the observation that large earthquakes preferably occur along a smooth megathrust (van Rijsingen et al., 2018). Also fluids that are delivered to the subduction interface may play a role in this, since fluid overpressures reduce the effective friction at the subduction interface, therefore reducing the amount of elastic strain accumulation (Lallemand et al. 1994; Bangs et al. 2006).

As in most numerical models covering this topic, the rheology of our overriding plate (i.e., the gelatin wedge) is mainly elastic, and hence does not allow off-fault brittle deformation due to subducting topography. Therefore, following the two proposed scenarios, one may expect that our results will be more in line with what has been proposed by Scholz and Small (1997): an increase in coupling when a topographic feature subducts due to the flexure of the overriding plate. However, we observe a much lower interseismic coupling and interface strength for the rough models than for the smooth models (section 5.3.1 and 5.3.2). The scenario proposed by Scholz & Small however, is based on a 2D representation of the subduction of a single seamount, while we consider the effect of a 3D rough seafloor (characterized by multiple seamounts). This might explain the difference between the expected results following Scholz & Small's theory, and the observed results from our models. Another possible explanation for this discrepancy follows the reasoning of Wang and Bilek (2011), who argue that from a theoretical point of view, the tensional stresses as a result of the flexure of the overriding plate will be much larger than the normal stress, possibly resulting in local uplift of the seafloor. Despite the fact that in our models we only consider roughness of the subduction interface, without any off-fault brittle deformation, our results are still in agreement with what is proposed by Wang and Bilek (2011, 2014): lower coupling and fewer large earthquakes when rough seafloor subducts. To explain these results, we propose that in our models, due to flexure of the wedge around the rough interface, tensional stresses above the subducting seamounts arise, that lead to a heterogeneous stress distribution (Figure 5.7). At the surface of the wedge, which partly reflects the geometry of the interface, tensional stresses are observed above the top of the seamounts, while at the subduction interface, tensional stresses are larger on the leading flanks of the seamount, due to a larger dip angle (i.e., the combined result of the dipping downgoing plate and the seamount flank) and therefore a larger gravitational effect. It is possible that due to these tensional stresses within the overriding plate, the actual contact area between the two plates decreases, which would explain the lower (interseismic) coupling and interface strength.

However, even though many ruptures in the rough models are relatively small, showing a concentration

of the maximum slip on top of one seamount or in between a group of seamounts, in some cases several seamount segments synchronize, creating a much larger rupture with higher slip values. These results suggest that the segmentation of the interface due to the heterogeneous strength distribution as described above, makes it more difficult for ruptures to propagate compared to ruptures in the smooth models, but not impossible. In other words, the rough interface in our models hinders rupture propagation significantly, but does not prevent large ruptures to occur entirely (Nielsen & Knopoff 1998). The more enhanced decoupling-effect of subduction interface roughness that is often observed in nature (e.g., Geersen et al., 2015; Mochizuki et al., 2008; Singh et al., 2011), could therefore be a combined effect of deformation of the overriding plate (following the fracture network scenario of Wang and Bilek, 2011), the presence of fluids along the interface, as well as flexure of the overriding plate as proposed in this study, since they all contribute to a more heterogeneous strength distribution and therefore a segmentation of the seismogenic zone.

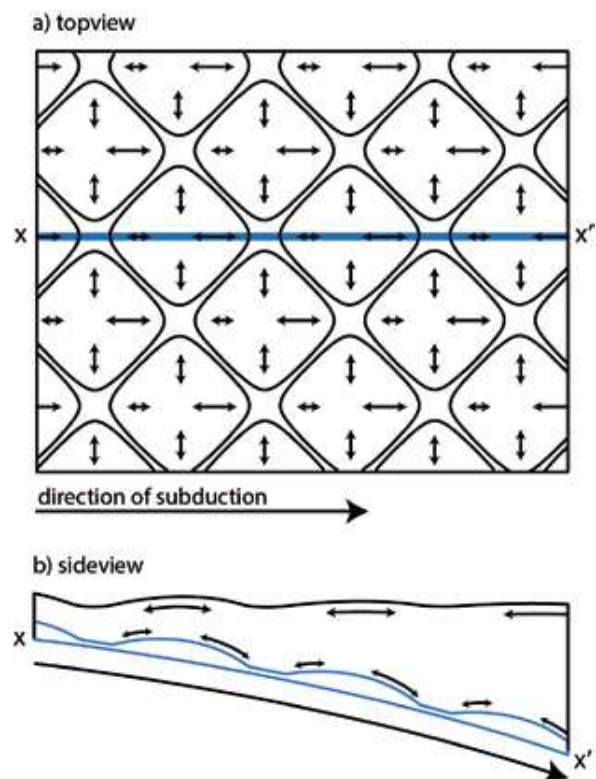


Figure 5.7. Schematic sketch of flexure of the overriding plate due to the roughness of the interface. a) Topview of stresses at the base of the wedge, showing extensional stresses on all flanks of the seamounts, resulting in a heterogeneous stress distribution. b) Sideview of the rough subduction interface (in blue) and resulting tensile stresses within the wedge.

5.5. Conclusions

In this study we investigate the effect of subduction interface roughness on seismogenic behavior in subduction zones by using seismotectonic analogue models. We compared rupture source parameters and slip distributions for two roughness endmembers. We observe that models characterized by a very rough interface have lower interface frictional strength and lower initial- and interseismic coupling than models with a very smooth interface. In addition, ruptures in the rough models are smaller in terms of rupture area and duration, as well as mean displacement and seismic asperity. Their slip distributions and rupture evolution clearly reflect the segmenting effect of the rough interface geometry.

6. Conclusions

6.1. The role of subduction interface roughness on megathrust earthquakes

6.1.1. A quantification of seafloor roughness

This Thesis starts with the quantification of seafloor roughness prior to subduction (Chapter 3), in order to provide a homogeneous, worldwide database that allows proper comparison between subduction zones. Both qualitative and quantitative descriptions of the seafloor roughness on a global scale had already been given (Morgan et al. 2008; Wang & Bilek 2014; Bassett & Watts 2015a), but these studies did not provide a complete description of which amplitudes of seafloor roughness are considered rough and smooth. In addition, the quantification performed in this study does not only take into account variations in bathymetry, but also includes gradients of bathymetry, therefore being able to distinguish between abrupt and gradual changes in elevation. Finally, the quantification of the seafloor seaward of the trench is presented at two distinct wavelengths: the short wavelength roughness R_{SW} (12-20 km) and the long wavelength roughness R_{LW} (80-100 km). Subduction zone segments are analyzed based on the relative distribution of R_{LW} amplitudes, for which thresholds for smooth (< 250 m) and rough (> 1,000m) seafloor are used. We can now distinguish subduction segments into dominantly rough, mixed and dominantly smooth subduction zones.

To better understand what the various roughness amplitudes and wavelengths mean in terms of seafloor morphology, the R_{SW} and R_{LW} amplitudes associated with features like seamounts, fracture zones and ridges have been analyzed with respect to the global roughness signal (Chapter 3). Results show that seamounts show distinct R_{SW} and R_{LW} signatures of much larger amplitudes than the global trend. Submarine ridges can only be distinguished from the global trend on the long wavelengths, which could be related to their large spatial size and the fact that they can host both regular seafloor and small seamounts at the shorter wavelengths. Surprisingly, fracture zones can statistically not be distinguished from the global seafloor at both wavelengths. This suggests that the potential role of a fracture zone on megathrust seismicity may depend more on its individual characteristics (some do have a distinct roughness pattern), or a potentially high fluid content. In addition, mylonitic zones that form due to intense shearing at lithospheric scale of a fracture zone are sometimes brought to the surface,

where they could play a role in attenuating rupture propagation (Maia et al. 2016).

6.1.2. Subduction interface roughness in relation to seismogenic behavior in subduction zones

The presence of continuous along-trench roughness measurements for all subduction zones allows for a systematic comparison with parameters describing the state of stress in subduction zones (e.g., Heuret et al., 2011). The comparison between seafloor roughness and seismic coupling performed in this study (Chapter 3), shows that relatively rough subducting seafloor is always associated with low seismic coupling and that areas with high seismic coupling have relatively low roughness amplitudes. Even though these results do not provide any information on the mechanism that might cause the decrease in seismic coupling, they are in agreement with the model proposed by Wang and Bilek (2011, 2014), who stated that a rough subduction interface is more likely to behave in a creeping manner. The mechanism they propose involves a fracture networks that develops around the subducting geometrical features and, therefore, prevents the accumulation of stresses between the two plates.

A more detailed comparison of the seafloor roughness seaward of the trench has been performed with the newly compiled SubQuake database (Chapter 4). The seafloor roughness associated with trench segments that have ruptured ($M_w \geq 7.5$) over the past 117 years is compared with the seafloor roughness facing trench segments that did not rupture. Results show that the seafloor facing rupture segments is generally smoother at long wavelengths, while at the short wavelengths, no clear difference can be observed. This could mean that roughness at wavelengths of 12-20 km does not play a significant role in rupture propagation and arrest, or that the proxy used for the comparison becomes less reliable at shorter wavelengths.

The comparison between seafloor roughness at long wavelengths and megathrust occurrence has also been performed for various moment magnitudes (Chapter 4). Results from this comparison show that the correlation between megathrust earthquakes

and smooth seafloor improves with increasing magnitude. This makes sense when considering rough seafloor as a barrier for rupture propagation, since earthquakes with large magnitudes need to grow over large distances and can do this more easily when not meeting any barriers. This is also in line with the results from Chapter 3, where it was shown that high seismic coupling is associated with smooth seafloor. Regions with high seismic coupling are regions where most of the plate convergence is accommodated by seismic slip, rather than by aseismic slip (i.e., creep). It is now shown that smooth subducting seafloor does not only correlate with regions that behave mainly seismic, but that earthquakes along smooth segments tend to be larger as well. This is additional proof that rough subducting seafloor mainly acts as a barrier to rupture propagation (Wang & Bilek 2011, 2014).

Besides information on the rupture area, the SubQuake database also provides the epicenter and seismic asperity of the ruptures, which, in turn, can also be compared with the seafloor roughness seaward of the trench (Chapter 4). Even though this comparison becomes a bit more challenging due to the smaller spatial scale on which these features occur, and therefore the possibly larger error when extrapolating roughness data seaward of the trench, some trends can still be observed. When comparing the roughness signal facing seismic asperities with the roughness associated with rupture areas in general, a slight amplification of the seismic asperity signal can be seen at low roughness amplitudes. This suggests that the smoothest patches along the subduction interface might also be the patches where the largest displacement occurs (Contreras-Reyes et al. 2010, 2017).

The conditions that favor rupture propagation might be very different from the conditions that allow rupture nucleation (e.g., Lapusta & Rice 2003; Das & Watts 2009). This can already be seen when looking at the relative position of a rupture's hypocenter and seismic asperity: in ~35% to ~50% of the cases, the hypocenter is located outside the seismic asperity. Results from the quantitative comparison in Chapter 4 show slightly rougher seafloor associated with rupture epicenters. When considering that rough seafloor subducts in a more creeping manner, regions close to subducting topographic highs might

be favorable for rupture nucleation due to the transition between locked and creeping patches of the interface (Lapusta & Rice 2003).

6.1.3. The influence of rough subducting seafloor on the state of stress within subduction zones: insights from analogue models

A limitation with respect to natural observation is the short seismic record, which in most regions does not even cover one seismic cycle. Many of the observational studies presented in section 2.6 address the interaction of a single rupture with respect to a subducting feature. The relationship that is found in these individual studies is often assumed to be characteristic, but this might not be true. Das and Watts (2009) already argued the variable behavior of subducting seafloor roughness over time, since they believe that each part of the subduction megathrust at some point must catch-up. In their view, a patch of rough seafloor might therefore act as a barrier for one earthquake, but as an asperity for the following event. Global studies addressing this issue have the advantage of looking at many regions capturing different 'snapshots' of the seismic cycle. Moreover, geodetic studies inferring the degree of coupling along specific sections of the subduction megathrust provide information of what actually happens when rough (or smooth) seafloor subducts (e.g., Geersen et al. 2015; Marcaillou et al. 2016; Collot et al. 2017). However, the degree of coupling is often assumed to be constant throughout a seismic cycle and, in turn, representative for longer timescales, which does not necessarily have to be the case.

Numerical and analogue models can overcome these intrinsic and unavoidable limitations of natural data. Modelling not only provides the possibility to investigate the relationship between subduction interface roughness and megathrust seismicity over multiple seismic cycles (i.e., longer timescales), but also allows for the isolation of a single parameter to understand its role on seismicity (e.g., Corbi et al. 2017a&b), as well as better (more direct) observations of what happens when rough seafloor subducts. Does it temporarily act as a barrier, to catch-up at a later point in the seismic cycle (Das and Watts, 2009)? Or is the barrier-effect continuous

over multiple seismic cycles due to more permanent changes in the state of stress along the interface (e.g., Wang and Bilek, 2014)? A better understanding of the mechanisms related to subducting interface roughness can provide new insights in the long-term effect (i.e. over multiple seismic cycles) on the occurrence of megathrust earthquakes.

With this in mind, a set of analogue models has been realized as a final part of this Thesis (Chapter 5). In these models, the roughness of the subduction interface is the only parameter that has been varied, namely by using two endmember interfaces (i.e. planar versus very rough). From the experimental outcomes, source parameters such as rupture- and seismic asperity area, rupture duration, recurrence time, mean displacement and interseismic coupling can be extracted and compared between the two types of models. Results based on a minimum of 15 seismic cycles show that rough models have lower interface frictional strength, lower initial- and interseismic coupling and smaller earthquakes in terms of rupture area, seismic asperity, rupture duration and mean slip. This confirms the findings from Chapters 3 and 4, showing that the results found in the global natural data analysis might also be representative over multiple seismic cycles.

An important question that results from the analogue models, is how the rough subduction interface causes this decrease in interseismic coupling and the occurrence of smaller earthquakes with respect to the smooth models. Considering the two contradicting scenarios that have been proposed for subducting seamounts (Scholz & Small 1997; Wang & Bilek 2011, 2014), the model results are more in agreement with Wang and Bilek (2011,2014). Scholz and Small (1997) argue that flexure of the subducting- and overriding plate due to seamount subduction increases the normal stress and therefore the coupling along the interface. Even though they consider the effect of a single seamount, while this study focuses on the effect of a rough interface in general (here for simplification represented as multiple large seamounts), the analogue modelling results from this study suggest that also an increase in coupling as a consequence of single seamount subduction remains questionable.

Even though the analogue modelling results are in line with what has been proposed by Wang and Bilek, the

effect the rough interface has on the state of stress along the plate interface is likely to be different. The rheology of the overriding plate in the models (i.e., the gelatin wedge) is mainly elastic, and therefore does not allow the development of a fracture network in the overriding plate. Nevertheless, the rough models still show considerably lower interseismic coupling with respect to the smooth models, suggesting that the development of a fracture network might not be the only responsible mechanism. The mechanism proposed in this study (Chapter 5) involves the development of a heterogeneous strength distribution along the subduction interface due to the tensional stresses resulting from the deformation of the overriding plate around the geometrical irregularities. This segments the interface and, in turn, inhibits the growth of ruptures that would allow them to reach larger magnitudes.

However, the occurrence of megathrust ruptures in the analogue models is not entirely limited. Even though large ruptures are less likely, smaller ruptures on top- or in between the seamounts still occur. The more enhanced decoupling-effect of subduction interface roughness that is often observed in nature (e.g., Geersen et al., 2015; Mochizuki et al., 2008; Singh et al., 2011), could be a combined effect of several processes. These include deformation of the overriding plate (following the ‘breakthrough’ scenario of Wang and Bilek, 2011,2014), heterogeneous strength distribution of the overriding plate (as proposed in Chapter 5), but also the effect of fluid-overpressures that may reduce the coupling along the interface (e.g., Lallemand et al. 1994; Bangs et al. 2006). The exact interplay of these three processes may have different consequences in specific regions, which could explain the occurrence of smaller ($\sim M_w 7$) earthquakes in relation to subducting features, as has been proposed for the Costa Rica margin (section 2.6.3; Bilek et al. 2003), as well as tsunami earthquakes that may occur in the wake of a single subducting seamount (e.g., Bell et al. 2014). As proposed by Collot et al (2017), the roughness amplitude, as well as the height-width ratio of specific features might affect this relative contribution of the three abovementioned processes.

To conclude, this Thesis provides insights into the behavior of the subduction thrust fault suggesting

that large- to great megathrust events mainly occur in regions where smooth seafloor subducts. It also shows, based on both global observational data

and experimental results, that interseismic coupling is significantly lower when overall rough seafloor subducts.

6.2. Suggestions for future work

The scientific community is arriving towards a general consensus regarding the overall effect of subduction interface roughness on the seismogenic behavior in subduction zones. However, a detailed understanding of what is happening in current subduction zones remains puzzling. More accurate observations and more realistic models are key ingredients to reach this challenging goal. In this section, new avenues for future investigations are discussed.

6.2.1. Natural observations

Observing what happens along the subduction megathrust remains challenging, but future technological advances will most likely make this a bit easier. More and more GPS-stations are installed, which can provide more accurate information on the state of coupling in subduction zones. Especially the remote areas, where we currently have little knowledge about the coupling along the interface (such as the Antilles or Central America), are worth exploring. Also the employment of ocean-bottom stations is very important, since this allows the possibility to measure geodetic displacements directly above the seismogenic zone (e.g., Yokota et al. 2016). This is now only possible in regions where land is located relatively close to the trench, such as the Nicoya Peninsula in Costa Rica (Kyriakopoulos & Newman 2016) and La Plata Island along the Ecuadorian coast (Collot et al. 2017). Ocean-bottom stations also proved to be valuable for slip inversion models, such as the GPS stations that were employed on the seafloor near the 2011 Tohoku rupture area (Yue & Lay 2013).

Slip inversions in general also deserve more attention in the future, since the non-uniqueness of the models leads to the co-existence of many different models for the same event. More consistent and detailed models of a rupture's slip evolution might provide more insights in how a rupture behaves with respect to the properties of the interface. Also

the relationships between rupture complexity and subduction interface roughness are worth exploring (Ye et al. 2018).

Technological advances in the field of seismic reflection and refraction, such as the use of dense OBS arrays and waveform inversion techniques (e.g., Górszczyk et al. 2017), will literary provide a better image of the subduction interface, allowing for a better estimate of the degree of interface roughness. Also the role of sediments could be addressed with these techniques, since they might provide better insights in the relationship between subducting sediments and sediments that accrete at the trench. This is important, since the amount of sediments that subduct might modify the roughness at the interface.

In order to understand subduction zones in the most complete and accurate way possible, it is important to share data among scientists. This can be done by using homogeneous and continuously updated online databases and/or platforms, where externals can not only access data, but contribute as well.

6.2.2. Seismotectonic modelling

In terms of both numerical- and analogue seismotectonic models, the employment of more complex rheologies is necessary to model the deformation along the subduction interface in a more realistic way. Many numerical models covering the topic of fault roughness only include an elastic rheology, and also the analogue models presented in this Thesis have limitations in terms of rheology, such as the lack of a brittle response in the viscoelastic models presented in Chapter 5. Extensive rheometric analyses, in collaboration with material scientists, are needed to calibrate these new analogue materials. The development from 2D numerical models to 3D will most likely provide some important new insights, since the geometry of the interface (and its effect on along-trench propagation of ruptures) can

be modeled in a more realistic way. Also analogue models with longer trench-parallel lengths can be used to study the influence of various subduction parameters on rupture propagation in a more realistic way. Modelling of rupture propagation in the trench-parallel direction is very important for hazard assessment, since knowing how far ruptures may propagate, gives important insights in a region's maximum earthquake magnitude.

In terms of seafloor roughness would it be interesting to test the influence of height-to-width ratios of subducting features, as well as extending the study in Chapter 5 by testing systematically various roughness amplitudes and wavelengths, finally arriving to a more complex and thus realistic subduction interface roughness (e.g., by incorporating roughness at all wavelengths). In addition, ruptures developing in the wake of seamounts, therefore possibly becoming tsunami earthquakes, deserve more attention, especially given the associated tsunami hazard. This requires more detailed modeling of the stress distributions surrounding subducting seamounts in the interseismic phase, as well as surface deformations as a result of coseismic rupture that will trigger possible tsunami runups. Besides subduction interface roughness, other proposed subduction parameters, such as along-dip curvature of the downgoing plate (Bletery et al. 2016), or fore-arc structure (Heuret et al. 2011; Schellart & Rawlinson 2013; Bassett et al. 2016), are worth exploring as well.

As already discussed in Chapter 5 and 6, understanding how the short- and long term behavior of subducting seafloor roughness are related, is crucial for earthquake forecasting. Since the limited seismic record prevents a good observation of multiple seismic cycles in nature, this needs to be mainly addressed with modelling. New technologies, such as machine learning, can provide important insights in how the seismogenic behavior for a specific region (i.e., where a seamount subducts) might vary over time, and thus how the associated hazard might change. This can also be addressed with statistical studies, which use the large number of data from all subduction zones to still discover certain patterns in terms of seismogenic behavior.

A more general note related to future research comprises the need for more interdisciplinary collaborations. Earthquake research will benefit from more- and better communication between disciplines like seismology, seismotectonic modelling and rock mechanics. However, besides collaborations within the fields of geology and geophysics, collaborating with more external disciplines like tribology or material science, i.e., by using their knowledge to address our questions, is crucial for moving forward as scientific community.

References

- Abercrombie, R.E. et al., 2001. The 1994 Java tsunami earthquake: Slip over a subducting seamount. *Journal of Geophysical Research: Solid Earth*, 106(B4), pp.6595–6607. Available at: <http://doi.wiley.com/10.1029/2000JB900403>.
- Acharya, H.K., 1980. Seismic slip on the Philippine fault and its tectonic implications. *Geology*, 8(1), pp.40–42.
- Adam, J. et al., 2005. Shear localisation and strain distribution during tectonic faulting - New insights from granular-flow experiments and high-resolution optical image correlation techniques. *Journal of Structural Geology*, 27(2), pp.299–301.
- Adamek, S., Tajima, F. & Wiens, D.A., 1987. Seismic rupture associated with subduction of the Cocos Ridge. *Tectonics*, 6(6), pp.757–774.
- Adams, J., 1990. Paleoseismicity of the Cascadia subduction zone: Evidence from turbidites off the Oregon-Washington margin. *Tectonics*, 9(4), pp.569–583.
- Allen, T.I. & Hayes, G.P., 2017. Alternative rupture-scaling relationships for subduction interface and other offshore environments. *Bulletin of the Seismological Society of America*, 107(3), pp.1240–1253.
- Alshibli, K.A. & Roussel, L.E., 2006. Experimental investigation of slip-stick behaviour in granular materials. *International Journal for Numerical and Analytical Methods in Geomechanics*, 30(14), pp.1391–1407.
- Ammon, C.J. et al., 2005. Rupture process of the 2004 Sumatra-Andaman earthquake. *Science (New York, N.Y.)*, 308(5725), pp.1133–1139. Available at: <http://www.ncbi.nlm.nih.gov/pubmed/15905393>.
- Ando, M., 1975. Source mechanisms and tectonic significance of historical earthquakes along the Nankai trough, Japan. *Tectonophysics*, 27(2), pp.119–140.
- Anthony, J.L. & Marone, C., 2005. Influence of particle characteristics on granular friction. *Journal of Geophysical Research: Solid Earth*, 110(8), pp.1–14.
- Archuleta, R.J. & Brune, J.N., 1975. Surface strong motion associated with a stick-slip event in a foam rubber model of earthquakes. *Bulletin of the Seismological Society of America*, 65(5), pp.1059–1071.
- Atwater, B.F., 1987. Evidence for Great Holocene Earthquakes Along the Outer Coast of Washington State. *Science*, 236(4804), pp.942–944. Available at: <http://science.sciencemag.org/content/236/4804/942.abstract>.
- Baba, T. et al., 2002. The slip distribution of the 1946 Nankai earthquake estimated from tsunami inversion using a new plate model. *Physics of the Earth and Planetary Interiors*, 132(1–3), pp.59–73.
- Bangs, N.L.B., Gulick, S.P.S. & Shipley, T.H., 2006. Seamount subduction erosion in the Nankai Trough and its potential impact on the seismogenic zone. *Geology*, 34(8), pp.701–704.
- Barrientos, S.E. & Ward, S.N., 1990. The 1960 Chile earthquake: Inversion for slip distribution from surface deformation. *Geophys. J. Int.*, 103, pp.589–598.
- Bassett, D. et al., 2016. Upper-plate controls on co-seismic slip in the 2011 magnitude 9.0 Tohoku-oki earthquake. *Nature*, 531(7592), pp.92–96. Available at: <http://dx.doi.org/10.1038/nature16945>.
- Bassett, D. & Watts, A., 2015a. Gravity Anomalies, crustal structure, and seismicity at subduction zones: 1. Seafloor roughness and subducting relief. *Geochemistry Geophysics Geosystems*, pp.1508–1540.
- Bassett, D. & Watts, A., 2015b. Gravity anomalies, crustal structure, and seismicity at subduction zones: 2. Interrelationships between fore-arc structure and seismogenic behavior. *Geochemistry Geophysics Geosystems*, 18(1–2), pp.1541–1576.
- Baumberger, T., Caroli, C. & Ronsin, O., 2003. Self-healing slip pulses and the friction of gelatin gels. *European Physical Journal E*, 11(1), pp.85–93.
- Baumberger, T., Heslot, F. & Perrin, B., 1994. Crossover from creep to inertial motion in friction dynamics. *Nature*, 367(6463), pp.544–546.
- Beck, S. et al., 1998. Source characteristics of historic earthquakes along the central Chile subduction zone. *Journal of South American Earth Sciences*, 11(2), pp.115–129.
- Beck, S.L. & Christensen, D.H., 1991. Rupture process of the February 4, 1965, Rat Islands Earthquake. *Journal of Geophysical Research*, 96(B2), pp.2205–2221. Available at: <http://doi.wiley.com/10.1029/90JB02092>.
- Beck, S.L. & Ruff, L.J., 1989. Great earthquakes and subduction along the Peru trench. *Physics of the Earth and Planetary Interiors*, 57(3–4), pp.199–224.
- Beck, S.L. & Ruff, L.J., 1987. Rupture Process of the Great 1963 Kurile Islands Earthquake Sequence: Asperity Interaction and Multiple Event Rupture. *Journal of Geophysical Research*, 92(B13), p.14,123-14,138.
- Beck, S.L. & Ruff, L.J., 1984. The rupture process of the Great 1979 Colombia Earthquake: Evidence for the asperity model. *Journal of Geophysical Research: Solid Earth*, 89(B11), pp.9281–9291.
- Becker, J.J. et al., 2009. Global Bathymetry and Elevation Data at 30 Arc Seconds Resolution: SRTM30_PLUS. *Marine Geodesy*, 32(4), pp.355–371.
- Beeler, N.M., Tullis, T.E. & Weeks, J.D., 1994. The roles of time and displacement in the evolution effect in rock friction. *Geophysical Research Letters*, 21(18), pp.1987–1990.
- Bell, R. et al., 2014. Hikurangi margin tsunami earthquake generated by slow seismic rupture over a subducted seamount. *Earth and Planetary Science Letters*, 397, pp.1–9. Available at: <http://dx.doi.org/10.1016/j>.

- epsl.2014.04.005.
- Benioff, H., Press, F. & Smith, S., 1961. Excitation of the free oscillations of the Earth by earthquakes. *Journal of Geophysical Research*, 66(2), p.605. Available at: <http://doi.wiley.com/10.1029/JZ066i002p00605>.
- Beroza, G., Rial, J.A. & McNally, K.C., 1984. Source mechanisms of the June 7, 1982 ometepac, Mexico earthquake. *Geophysical Research Letters*, 11(8), pp.689–692.
- Bilek, S.L., 2007. Influence of Subducting Topography on Earthquake Rupture. In T. Dixon & C. Moore, eds. *The seismogenic zone of subduction thrust faults*. Columbia University Press - New York, pp. 123–146.
- Bilek, S.L., 2010a. Invited review paper: Seismicity along the South American subduction zone: Review of large earthquakes, tsunamis, and subduction zone complexity. *Tectonophysics*, 495(1–2), pp.2–14. Available at: <http://dx.doi.org/10.1016/j.tecto.2009.02.037>.
- Bilek, S.L., 2010b. The role of subduction erosion on seismicity. *Geology*, 38(5), pp.479–480.
- Bilek, S.L., Elliott, C.E. & Lithgow-Bertelloni, C., 2009. Triggered seismicity associated with the 1990 Nicoya, Costa Rica, Mw= 7.0 earthquake. *Geochemistry, Geophysics, Geosystems*, 10(4), pp.1–13.
- Bilek, S.L. & Engdahl, E.R., 2007. Rupture characterization and aftershock relocations for the 1994 and 2006 tsunami earthquakes in the Java subduction zone. *Geophysical Research Letters*, 34(20), pp.1–5.
- Bilek, S.L. & Lay, T., 1998. Variation of interplate fault zone properties with depth in the Japan subduction zone. *Science*, 281(5380), pp.1175–1178.
- Bilek, S.L. & Lay, T., 1999. Rigidity variations with depth along interplate megathrust faults in subduction zones. *Nature*, 400(6743), pp.443–446.
- Bilek, S.L. & Lay, T., 2002. Tsunami earthquakes possibly widespread manifestations of frictional conditional stability. *Geophysical Research Letters*, 29(14), pp.1–4.
- Bilek, S.L., Schwartz, S.Y. & DeShon, H.R., 2003. Control of seafloor roughness on earthquake rupture behavior. *Geology*, 31(5), pp.455–458.
- Bilham, R. et al., 2005. Partial and Complete Rupture of the Indo-Andaman Plate Boundary 1847-2004. *Seismological Research Letters*, 76(3), pp.299–311.
- Bletery, Q. et al., 2014. A detailed source model for the Mw9.0 Tohoku-Oki earthquake reconciling geodesy, seismology, and tsunami records. *Journal of Geophysical Research B: Solid Earth*, 119(10), pp.7636–7653.
- Bletery, Q. et al., 2016. Mega-earthquake rupture flat megathrusts. *Science*, 354(6315), pp.1027–1031.
- Boyd, T.M., Engdahl, E.R. & Spence, W., 1995. Seismic Cycles Along the Aleutian Arc - Analysis of Seismicity from 1957 through 1991. *Journal of Geophysical Research-Solid Earth*, 100(B1), pp.621–644.
- Brace, W.F. & Byerlee, J.D., 1966. Stick-Slip as a Mechanism for Earthquakes. *Science*, 153(3739), pp.990–992. Available at: <http://dx.doi.org/10.1126/science.153.3739.990>.
- Brizzi, S. et al., 2018. Multivariate statistical analysis to investigate the subduction zone parameters favoring the occurrence of giant megathrust earthquakes. *Tectonophysics*, 728–729(January), pp.92–103. Available at: <http://linkinghub.elsevier.com/retrieve/pii/S0040195118300398>.
- Brune, J.N., 1973. Earthquake modeling by stick-slip along pre-cut surfaces in stressed foam rubber. *Bulletin of the Seismological Society of America*, 63(6), pp.2105–2119.
- Brune, J.N., 1968. Seismic moment, seismicity, and rate of slip along major fault zones. *Journal of Geophysical Research*, 73, pp.777–784.
- Burridge, R. & Knopoff, L., 1967. Model and theoretical seismicity. *Bulletin of the Seismological Society of America*, 57, pp.341–371.
- Byerlee, J.D., 1970. The mechanics of stick-slip. *Tectonophysics*, 9(5), pp.475–486.
- Byrne, D.E., Davis, M. & Sykes, R., 1988. Loci and Maximum Size of Thrust Earthquakes and the Mechanics of the Shallow Region of Subduction Zones. *Tectonics*, 7(4), pp.833–857.
- Byrne, D.E., Sykes, L.R. & Davis, D.A.N.M., 1992. Great Thrust Earthquakes and Aseismic Slip Along the Plate Boundary of the Makran Subduction Zone. *Journal of geophysical Research*, 97(91), pp.449–478.
- Caniven, Y. et al., 2015. A new multilayered visco-elasto-plastic experimental model to study strike-slip fault seismic cycle. , pp.232–264.
- Caniven, Y. et al., 2017. Relationships between along-fault heterogeneous normal stress and fault slip patterns during the seismic cycle: Insights from a strike-slip fault laboratory model. *Earth and Planetary Science Letters*, 480(November), pp.147–157. Available at: <https://doi.org/10.1016/j.epsl.2017.10.009>.
- Carena, S., 2011. Subducting-plate Topography and Nucleation of Great and Giant Earthquakes along the South American Trench. *Seismological Research Letters*, 82(5), pp.629–637. Available at: <http://srl.geoscienceworld.org/cgi/doi/10.1785/gssrl.82.5.629>.
- Chen, T. et al., 2009. Slip distribution from the 1 April 2007 Solomon Islands earthquake: A unique image of near-trench rupture. *Geophysical Research Letters*, 36(16), pp.6–11.
- Chlieh, M. et al., 2014. Distribution of discrete seismic asperities and aseismic slip along the Ecuadorian megathrust. *Earth and Planetary Science Letters*, 400, pp.292–301. Available at: <http://dx.doi.org/10.1016/j.epsl.2014.05.027>.
- Chlieh, M. et al., 2011. Interseismic coupling and seismic

- potential along the Central Andes subduction zone. *Journal of Geophysical Research: Solid Earth*, 116(12), pp.1–21.
- Christensen, D.H. & Lay, T., 1988. Large Earthquakes in the Tonga Region Associated With Subduction of the Louisville Ridge. *Journal of Geophysical Research: Solid Earth*, 93(B11), pp.13367–13389. Available at: <http://dx.doi.org/10.1029/JB093iB11p13367>.
- Christensen, D.H. & Ruff, L.J., 1983. Outer-Rise Earthquakes and Seismic Coupling. *Geophysical Research Letters*, 10(8), pp.697–700.
- Clague, J.J., 2002. The Earthquake Threat in Southwestern British Columbia: A Geological Perspective. *Natural Hazards*, 26, pp.7–34.
- Clévéde, E. et al., 2012. Long-period spectral features of the Sumatra-Andaman 2004 earthquake rupture process. *Geophysical Journal International*, 191(3), pp.1215–1225.
- Cloos, M., 1992. Thrust-type subduction-zone earthquakes and seamount asperities: A physical model for seismic rupture. *Geology*, 20, pp.601–604.
- Collot, J.-Y. et al., 2017. Subducted oceanic relief locks the shallow megathrust in central Ecuador. *Journal of Geophysical Research: Solid Earth*, 122, pp.1–20.
- Collot, J.-Y. et al., 2001. The giant Ruatoria debris avalanche on the northern Hikurangi margin, New Zealand: Result of oblique seamount subduction. *Journal of Geophysical Research: Solid Earth*, 106(B9), pp.19271–19297. Available at: <http://doi.wiley.com/10.1029/2001JB900004>.
- Collot, J.-Y., Daniel, J. & Burne, R.V., 1985. Recent tectonics associated with the subduction of the D'Entrecasteaux zone in the central new Hebrides. *Tectonophysics*, 112(1–4), pp.325–356.
- Collot, J.Y. et al., 2005. Seafloor margin map helps in understanding subduction earthquakes. *Eos*, 86(46), pp.463–465.
- Comte, D. et al., 1986. The 1985 Central Chile Earthquake: A Repeat of Previous Great Earthquakes in the Region? *Science*, 233(4762), pp.449–453. Available at: <http://www.sciencemag.org/content/233/4762/449.abstract>.
- Contreras-Reyes, E. et al., 2017. On the relationship between structure, morphology and large coseismic slip: A case study of the Mw8.8 Maule, Chile 2010 earthquake. *Earth and Planetary Science Letters*, 478, pp.27–39. Available at: <http://dx.doi.org/10.1016/j.epsl.2017.08.028>.
- Contreras-Reyes, E. & Carrizo, D., 2011. Control of high oceanic features and subduction channel on earthquake ruptures along the Chile-Peru subduction zone. *Physics of the Earth and Planetary Interiors*, 186(1–2), pp.49–58. Available at: <http://dx.doi.org/10.1016/j.pepi.2011.03.002>.
- Contreras-Reyes, E., Flueh, E.R. & Grevemeyer, I., 2010. Tectonic control on sediment accretion and subduction off south central Chile: Implications for coseismic rupture processes of the 1960 and 2010 megathrust earthquakes. *Tectonics*, 29(6), pp.1–27.
- Corbi, F. et al., 2017a. Control of asperities size and spacing on seismic behavior of subduction megathrusts. *Geophysical Research Letters*, 44(16), pp.8227–8235.
- Corbi, F. et al., 2011. Seismic variability of subduction thrust faults: Insights from laboratory models. *Journal of Geophysical Research: Solid Earth*, 116(6), pp.1–14.
- Corbi, F. et al., 2013. The seismic cycle at subduction thrusts: 1. Insights from laboratory models. *Journal of Geophysical Research: Solid Earth*, 118(4), pp.1483–1501.
- Corbi, F., et al., 2017b. Controls of seismogenic zone width and subduction velocity on interplate seismicity: Insights from analog and numerical models. *Geophysical Research Letters*, 44(12), pp.6082–6091.
- Cummins, P.R., et al., 1999. Subduction zone structure and earthquake deformation in the Nankai Through. *EOS*, 80 (fall suppl.), 738.
- Das, S. & Kostrov, B. V., 1990. Inversion for seismic slip rate history and distribution with stabilizing constraints: Application to the 1986 Andeanof Islands Earthquake. *Journal of Geophysical Research*, 95(B5), pp.6899–6913. Available at: <http://doi.wiley.com/10.1029/JB095iB05p06899>.
- Das, S. & Watts, A.B., 2009. Effect of Subducting Seafloor Topography on the Rupture Characteristics of Great Subduction Zone Earthquakes. In *Subduction Zone Geodynamics*. pp. 103–118. Available at: <http://link.springer.com/10.1007/978-3-540-87974-9>.
- Davies, G.F. & Brune, J.N., 1971. Regional and Global Fault Slip Rates from Seismicity. *Nature Physical Science*, 229(4), pp.101–107. Available at: [papers2://publication/doi/doi:10.1038/1038physci229101a0](https://doi.org/10.1038/1038physci229101a0).
- Davies, G.F. & Richard, M.A., 1992. Mantle convection. *Journal of Geology*, 100(2), pp.151–206.
- DeMets, C., Gordon, R.G. & Argus, D.F., 2010. Geologically current plate motions. *Geophysical Journal International*, 181(1), pp.1–80.
- Deschamps, A. & Lallemand, S., 2002. The West Philippine Basin: An Eocene to early Oligocene back arc basin opened between two opposed subduction zones. *Journal of Geophysical Research: Solid Earth*, 107(B12), p.EPM 1-1-EPM 1-24. Available at: <http://doi.wiley.com/10.1029/2001JB001706>.
- Deschamps, A.E., Lallemand, S.E. & Collot, J.-Y., 1998. A detailed study of the Gagua Ridge: A fracture zone ridge uplifted during a plate reorganisation in the mid-Eocene. *Marine Geophysical Researches*, 20(5), pp.403–423.
- Dewey, J. & Byerly, P., 1969. The Early History of Seismometry (to 1900). *Bulletin of the Seismological Society of America*, 59(1), pp.183–227.
- Dieterich, J.H., 1972. Time-dependent friction in rocks. *Journal*

- of *Geophysical Research*, 77(20), pp.3690–3697. Available at: <http://doi.wiley.com/10.1029/JB077i020p03690>.
- Dieterich, J.H., 1979. Modeling of rock friction: 1. Experimental results and constitutive equations. *Journal of geophysical research*, 84(B5), pp.2161–2168. Available at: <http://dx.doi.org/10.1007/BF00876539>.
- Dominguez, S. et al., 2015. Modeling subduction megathrust earthquakes: Insights from a visco-elasto-plastic analog model. *Geophysical Research Abstracts*, 17(EGU2015–15200).
- Dominguez, S., Lallemand, S., et al., 1998. Oblique subduction of the Gagua Ridge beneath the Ryukyu accretionary wedge system: Insights from marine observations and sandbox experiments. *Marine Geophysical Researches*, 20(5), pp.383–402.
- Dominguez, S., Lallemand, S.E., et al., 1998. Upper plate deformation associated with seamount subduction. *Tectonophysics*, 293(3–4), pp.207–224.
- Dominguez, S., Malavieille, J. & Lallemand, S.E., 2000. Deformation of accretionary wedges in response to seamount subduction: Insights from sandbox experiments. *Tectonics*, 19(1), pp.182–196.
- Duda, S.J. & Nuttli, O.W., 1974. Earthquake Magnitude Scales. *Geophysical Surveys*, 1, pp.429–458.
- Dunham, E.M. et al., 2011. Earthquake ruptures with strongly rate-weakening friction and off-fault plasticity, part 2: Nonplanar faults. *Bulletin of the Seismological Society of America*, 101(5), pp.2308–2322.
- Duong, N.A. et al., 2009. Assessment of bathymetry effects on tsunami propagation in Vietnam. *Advances in Natural Sciences*, 10(4), pp.457–468.
- Elsasser, W.M., 1971. Sea-floor spreading as thermal convection. *Journal of Geophysical Research*, 76(5), pp.1101–1112. Available at: <http://doi.wiley.com/10.1029/JB076i005p01101>.
- Engdahl, E.R. & Scholz, C.H., 1977. A double Benioff Zone beneath the central Aleutians: An unbending of the lithosphere. *Geophysical Research Letters*, 4(10), pp.473–476.
- Fedotov, S.A., Solomatin, A. V. & Chernyshev, S.D., 2011. A long-term earthquake forecast for the Kuril-Kamchatka arc for the period from September 2010 to August 2015 and the reliability of previous forecasts, as well as their applications. *Journal of Volcanology and Seismology*, 5(2), pp.75–99. Available at: <http://link.springer.com/10.1134/S0742046311020023>.
- Feng, L. et al., 2012. Active deformation near the Nicoya Peninsula, northwestern Costa Rica, between 1996 and 2010: Interseismic megathrust coupling. *Journal of Geophysical Research: Solid Earth*, 117(6), pp.1–23.
- Fisher, M.A., Collot, J.-Y. & Geist, E.L., 1991. Structure of the collision zone between Bougainville guyot and the accretionary wedge of the New Hebrides island arc, southwest Pacific. *Tectonics*, 10(5), pp.887–903.
- Forsyth, D. & Uyeda, S., 1975. On the relative importance of the driving forces of plate motion. *Geophys. J. R. astr. Soc.*, 43(August), pp.163–200.
- Fox, C.G. & Hayes, D.E., 1985. Quantitative methods for analysing the roughness of the seafloor. *Reviews of Geophysics*, 23(1), pp.1–48.
- Franco, A. et al., 2012. Fault kinematics in northern Central America and coupling along the subduction interface of the Cocos Plate, from GPS data in Chiapas (Mexico), Guatemala and El Salvador. *Geophysical Journal International*, 189(3), pp.1223–1236.
- Furlong, K.P., Lay, T. & Ammon, C.J., 2009. A great earthquake rupture across a rapidly evolving three-plate boundary. *Science*, 324(5924), pp.226–229.
- Gao, X. & Wang, K., 2014. Strength of stick-slip and creeping subduction megathrusts from heat flow observations. *Science*, 345(6200), pp.1038–1041. Available at: <http://www.sciencemag.org/content/345/6200/1038.abstract>.
- Gardner, T.W., 1992. Quaternary uplift astride the aseismic Cocos Ridge, Pacific coast, Costa Rica. *Geological Society of America Bulletin*, 104(2), pp.219–232.
- Geersen, J. et al., 2015. Subducting seamounts control interplate coupling and seismic rupture in the 2014 Iquique earthquake area. *Nature Communications*, 6, p.8267. Available at: <http://www.nature.com/doifinder/10.1038/ncomms9267>.
- Ghosh, A. et al., 2008. Interface locking along the subduction megathrust from b-value mapping near Nicoya Peninsula, Costa Rica. *Geophysical Research Letters*, 35(1), pp.1–6.
- Di Giuseppe, E. et al., 2009. Gelatins as rock analogs: A systematic study of their rheological and physical properties. *Tectonophysics*, 473, pp.391–403.
- Goebel, T.H.W. et al., 2017. What allows seismic events to grow big?: Insights from b-value and fault roughness analysis in laboratory stick-slip experiments. *Geology*, 45(9), pp.815–818.
- Goldfinger, C. et al., 2012. Turbidite Event History — Methods and Implications for Holocene Paleoseismicity of the Cascadia Subduction Zone. U.S. Geological Survey Professional Paper, 1661–F, pp.1–20.
- Górszczyk, A., Operto, S. & Malinowski, M., 2017. Toward a robust workflow for deep crustal imaging by FWI of OBS data: The eastern Nankai Trough revisited. *Journal of Geophysical Research: Solid Earth*, 122(6), pp.4601–4630.
- Gutenberg, B., 1945. Amplitudes of surface waves and magnitudes of shallow earthquakes. *Bulletin of the Seismological Society of America*, 35(3), pp.3–12.
- Gutenberg, B., 1945. Magnitude Determination for Deep-

- Focus Earthquakes. *Bulletin of the Seismological Society of America*, 35(3), pp.117–130.
- Gutenberg, B. & Richter, C.F., 1944. Frequency of earthquakes in California. *Bulletin of the Seismological Society of America*, 34, pp.185–188.
- Gutscher, M.-A. & Peacock, S.M., 2003. Thermal models of flat subduction and the rupture zone of great subduction earthquakes. *Journal of Geophysical Research: Solid Earth*, 108(B1), p.ESE 2-1-ESE 2-16. Available at: <http://doi.wiley.com/10.1029/2001JB000787>.
- Gutscher, M.-A. & Westbrook, G.K., 2009. Great Earthquakes in Slow-Subduction, Low-Taper Margins. In S. Lallemand & F. Funiciello, eds. *Subduction Zone Geodynamics*. Springer-Verlag, pp. 119–133. Available at: <http://link.springer.com/10.1007/978-3-540-87974-9>.
- Gutscher, M.A. et al., 1999. Tectonic segmentation of the North Andean margin: Impact of the Carnegie Ridge collision. *Earth and Planetary Science Letters*, 168(3–4), pp.255–270.
- Gutscher, M.-A. et al., 2000. Geodynamics of flat subduction: Seismicity and tomographic constraints from the Andean margin. *Tectonics*, 19(5), pp.814–833.
- Hager, B.H., 1984. Subducted Slabs and the Geoid: Constraints on Mantle Rheology and Flow. *Journal of Geophysical Research*, 89(B7), pp.6003–6015.
- Hamilton, T. & McCloskey, J., 1997. Breakdown in power-law scaling in an analogue model of earthquake rupture and stick-slip. *Geophysical Research Letters*, 24(4), pp.465–468.
- Hamilton, T. & McCloskey, J., 1998. The predictability of large earthquakes: evidence from an analogue model of earthquake rupture. *Pure and Applied Geophysics*, 152(1), pp.23–35.
- Hanks, T.C. & Kanamori, H., 1979. A Moment Magnitude Scale. *Journal of Geophysical Research*, 84(B5), pp.2348–2350.
- Harris, R.N. & Wang, K., 2002. Thermal models of the Middle America Trench at the Nicoya Peninsula, Costa Rica. *Geophysical Research Letters*, 29(21), pp.1–4.
- Hartzell, S. & Langer, C., 1993. Importance of Model Parameterization in Finite Fault Inversions - Application To the 1974 Mw 8.0 Peru Earthquake. *Journal of Geophysical Research-Solid Earth*, 98(B12), pp.22123–22134.
- Hashimoto, C. et al., 2009. Interplate seismogenic zones along the Kuril–Japan trench inferred from GPS data inversion. *Nature Geoscience*, 2(2), pp.141–144. Available at: <http://www.nature.com/doi/10.1038/ngeo421>.
- Hayes, G.P., 2017. The finite, kinematic rupture properties of great-sized earthquakes since 1990. *Earth and Planetary Science Letters*, 468(June 2016), pp.94–100. Available at: <http://linkinghub.elsevier.com/retrieve/pii/S0012821X17301826>.
- Hayes, G.P., Wald, D.J. & Johnson, R.L., 2012. Slab1.0: A three-dimensional model of global subduction zone geometries. *Journal of Geophysical Research: Solid Earth*, 117(1), pp.1–15.
- Heise, W. et al., 2017. Mapping subduction interface coupling using magnetotellurics: Hikurangi margin, New Zealand. *Geophysical Research Letters*, 44(18), pp.9261–9266.
- Henstock, T.J. et al., 2016. Downgoing plate topography stopped rupture in the A.D. 2005 Sumatra earthquake. *Geology*, 44(1), pp.71–74.
- Herrendorfer, R. et al., 2015. Earthquake supercycle in subduction zones controlled by the width of the seismogenic zone. *Nature Geosci*, 8(6), pp.471–474. Available at: <http://dx.doi.org/10.1038/ngeo2427%5Cn10.1038/ngeo2427%5Cnhttp://www.nature.com/ngeo/journal/v8/n6/abs/ngeo2427.html#supplementary-information>.
- Heslot, F. et al., 1994. Creep, stick-slip, and dry-friction dynamics: Experiments and a heuristic model. *Physical Review E*, 49(6), pp.4973–4988.
- Heuret, A. & Lallemand, S., 2005. Plate motions, slab dynamics and back-arc deformation. *Physics of the Earth and Planetary Interiors*, 149(1–2 SPEC. ISS.), pp.31–51.
- Heuret, A. et al., 2012. Relation between subduction megathrust earthquakes, trench sediment thickness and upper plate strain. *Geophysical Research Letters*, 39(5), pp.1–6.
- Heuret, A. et al., 2011. Physical characteristics of subduction interface type seismogenic zones revisited. *Geochemistry, Geophysics, Geosystems*, 12(1), pp.1–26.
- Hirata, K. et al., 2003. Slip distribution of the 1952 Tokachi-Oki earthquake (M 8.1) along the Kuril Trench deduced from tsunami waveform inversion. *J. Geophys. Res.* 108, 108 (B4)(May 2002), pp.2196–2212.
- Holdahl, S.R. & Sauber, J., 1994. Coseismic slip in the 1964 Prince William Sound earthquake: A new geodetic inversion. *Pure and Applied Geophysics PAGEOPH*, 142(1), pp.55–82.
- House, L.S. & Jacob, K.H., 1983. Earthquakes, Plate Subduction, And Stress Reversals in the Eastern Aleutian Arc. *Journal of Geophysical Research*, 88(B11), pp.9347–9373.
- Huang, J. & Turcotte, D.L., 1989. Fractal mapping of digitized images: Application to the topography of Arizona and comparisons with synthetic images. *Journal of Geophysical Research*, 94(B6), pp.7491–7495.
- Huang, J. & Turcotte, D.L., 1990. Are earthquakes an example of deterministic chaos? *Geophysical Research Letters*, 17, pp.223–226.
- Hubbert, M.K., 1937. Theory of scale models as applied to the study of geologic structures. *Bulletin of the Geological Society of America*, 48, pp.1459–1520.
- von Huene, R. et al., 1995. Morphotectonics of the Pacific convergent margin of Costa Rica. In P. Mann, ed. *Geologic and tectonic development of the Caribbean Plate boundary in southern Central America*. The Geological Society of America, Inc., pp. 291–308.

- von Huene, R. et al., 2000. Quaternary convergent margin tectonics of Costa Rica, segmentation of the Cocos Plate, and Central American volcanism. *Tectonics*, 19(2), pp.314–334.
- von Huene, R. & Lallemand, S., 1990. Tectonic erosion along the Japan and Peru convergent margins. *Geological Society of America Bulletin*, 102(6), pp.704–720.
- von Huene, R., Ranero, C.R. & Vannucchi, P., 2004. Generic model of subduction erosion. *Geology*, 32(10), pp.913–916.
- von Huene, R. & Scholl, D.W., 1991. Observations at convergent margins concerning sediment subduction, subduction erosion, and the growth of continental crust. *Reviews of Geophysics*, 29(3), pp.279–316.
- Husen, S., Kissling, E. & Quintero, R., 2002. Tomographic evidence for a subducted seamount beneath the Gulf of Nicoya, Costa Rica: The cause of the 1990 Mw = 7.0 Gulf of Nicoya earthquake. *Geophysical Research Letters*, 29(8), pp.79-1-79-4. Available at: <http://doi.wiley.com/10.1029/2001GL014045>.
- Hyndman, R.D., 2007. The Seismogenic Zone of Subduction Thrust Faults - What We Know and Don't Know. In T. H. Dixon & J. C. Moore, eds. *The Seismogenic Zone of Subduction Thrust Faults*. Columbia University Press - New York, pp. 15–40.
- Ide, S., 2007. Slip Inversion. In G. Schubert, ed. *Treatise on Geophysics*. Elsevier B.V., pp. 193–223. Available at: <http://dx.doi.org/10.1016/B978-0-444-53802-4.00076-2>.
- Ide, S., 2010. Striations, duration, migration and tidal response in deep tremor. *Nature*, 466(7304), pp.356–359.
- Ishizuka, O. et al., 2013. Upwelling, rifting, and age-progressive magmatism from the Oki-Daito mantle plume. *Geology*, 41(9), pp.1011–1014.
- Jarrard, R.D., 1986. Relations among subduction parameters. *Reviews of Geophysics*, 24(2), pp.217–284.
- Ji, C., Wald, D.J. & Helmberger, D. V., 2002. Source description of the 1999 Hector Mine, California, earthquake, part I: Wavelet domain inversion theory and resolution analysis. *Bulletin of the Seismological Society of America*, 92(4), pp.1192–1207.
- Johnson, J.M. et al., 1994. The 1957 great Aleutian earthquake. *Pure and Applied Geophysics PAGEOPH*, 142(1), pp.3–28.
- Johnson, J.M. & Satake, K., 1999. Asperity Distribution of the 1952 Great Kamchatka Earthquake and its Relation to Future Earthquake Potential in Kamchatka. *Pure and Applied Geophysics*, 154(3–4), pp.541–553.
- Johnson, J.M. & Satake, K., 1994. Rupture extent of the 1938 Alaskan earthquake as inferred from tsunami waveforms. *Geophysical Research Letters*, 21(8), pp.733–736.
- Kanamori, H., 1983. Magnitude scale and quantification of earthquakes. *Tectonophysics*, 93(3–4), pp.185–199.
- Kanamori, H., 1977. The Energy Release in Great Earthquakes. *Journal of Geophysical Research*, 82(20), pp.2981–2987.
- Kato, T., & Ando, M., 1997. Source mechanisms of the 1944 Tonankai and 1946 Nankaido earthquakes: Spatial heterogeneity of rise times. *Geophysical Research Letters*, 24, 2055.
- Kelleher, J. et al., 1974. Why and where great thrust earthquakes occur along island arcs. *Journal of Geophysical Research*, 79(32), pp.4889–4899. Available at: <http://doi.wiley.com/10.1029/JB079i032p04889>.
- Kelleher, J. & McCann, W., 1976. Buoyant Zones, Great Earthquakes, and Unstable Boundaries of Subduction to a low level Marianas-Bonins the tions of subduction appear interact with Tonga-Kermadec arc Katsumata and offsets in the Sykes of active depth and of the margin, lithosphere Pac. *Journal of Geophysical Research*, 81(26), pp.4885–4896.
- Kelleher, J., Sykes, L. & Oliver, J., 1973. Possible criteria for predicting earthquake locations and their application to major plate boundaries of the Pacific and the Caribbean. *Journal of Geophysical Research*, 78(14), pp.2547–2585.
- Kelleher, J.A., 1972. Rupture zones of large South American earthquakes and some predictions. *Journal of Geophysical Research*, 77(11), pp.2087–2103.
- Kikuchi, M. & Kanamori, H., 1982. Inversion of complex body waves. *Bulletin of the Seismological Society of America*, 72(2), pp.491–506.
- Kim, S.S. & Wessel, P., 2011. New global seamount census from altimetry-derived gravity data. *Geophysical Journal International*, 186(2), pp.615–631.
- King, C.-Y., 1991. Multicycle Slip Distribution Along a Laboratory Fault. *Journal of geophysical Research*, 96(B9), pp.14377–14381. Available at: <http://www.agu.org/pubs/crossref/1991/91JB01313.shtml%5Cnpapers2://publication/doi/10.1029/91JB01313>.
- King, C., 1994. Earthquake Mechanism and Predictability Shown by a.pdf. *PAGEOPH*, 134(1/2/3), pp.457–482.
- King, C., 1975. Model Seismicity and Faulting Parameters. *Bulletin of the Seismological Society of America*, 65(1), pp.245–259.
- Kirby, S.H. et al., 1996. Metastable mantle phase transformations and deep earthquakes in subducting oceanic lithosphere. *Reviews of Geophysics*, 34(2), pp.261–306.
- Klinkmüller, M. et al., 2016. Properties of granular analogue model materials: A community wide survey. *Tectonophysics*, 684, pp.23–38. Available at: <http://dx.doi.org/10.1016/j.tecto.2016.01.017>.
- Kobayashi, K., Kasuga, S. & Okino, K., 1995. Shikoku Basin and its Margins. In B. Taylor, ed. *Backarc Basins: Tectonics and Magmatism*. Plenum Press, New York, pp. 381–405.
- Kodaira, S. et al., 2000. Subducted Seamount Imaged in the

- Rupture Zone of the 1946 Nankaido Earthquake. *Science*, 289(5476), pp.104–106.
- Konca, A.O. et al., 2008. Partial rupture of a locked patch of the Sumatra megathrust during the 2007 earthquake sequence. *Nature*, 456(7222), pp.631–635.
- Kopp, H., 2013. Invited review paper: The control of subduction zone structural complexity and geometry on margin segmentation and seismicity. *Tectonophysics*, 589, pp.1–16. Available at: <http://dx.doi.org/10.1016/j.tecto.2012.12.037>.
- Kowalik, Z. et al., 2005. Numerical Modeling of The Global Tsunami: Indonesian Tsunami of 26 December 2004. *Science of Tsunami Hazards*, 23(1), pp.40–56.
- Kyriakopoulos, C. & Newman, A. V., 2016. Journal of Geophysical Research: Solid Earth Structural asperity focusing locking and earthquake. *Journal of Geophysical Research: Solid Earth*, pp.1–16.
- LaFemina, P. et al., 2009. Fore-arc motion and Cocos Ridge collision in Central America. *Geochemistry, Geophysics, Geosystems*, 10(5), pp.1–21.
- Laigle, M. et al., 2013. Seismic structure and activity of the north-central Lesser Antilles subduction zone from an integrated approach: Similarities with the Tohoku forearc. *Tectonophysics*, 603, pp.1–20. Available at: <http://dx.doi.org/10.1016/j.tecto.2013.05.043>.
- Lallemant, S., 2016. Philippine Sea Plate inception, evolution, and consumption with special emphasis on the early stages of Izu-Bonin-Mariana subduction. *Progress in Earth and Planetary Science*, 3(1), pp.1–26. Available at: <http://progearthplanetsci.springeropen.com/articles/10.1186/s40645-016-0085-6>.
- Lallemant, S. et al., 1990. Impact of oceanic asperities on the tectonogenesis of modern convergent margins. *Oceanologica Acta*, 10, 17-30.
- Lallemant, S., Culotta, R. & von Huene, R., 1989. Subduction of the Daiichi Kashima Seamount in the Japan Trench. *Tectonophysics*, 160(1–4), pp.231–241.
- Lallemant, S. et al., 2018. Roughness Characteristics of Oceanic Seafloor Prior to Subduction in Relation to the Seismogenic Potential of Subduction Zones. *Geochemistry, Geophysics, Geosystems*, 19, pp.1–26. Available at: <http://doi.wiley.com/10.1029/2018GC007434>.
- Lallemant, S. & Heuret, A., 2017. Subduction Zones Parameters. In *Reference Module in Earth Systems and Environmental Sciences*. Elsevier Inc., pp. 1–15. Available at: <http://linkinghub.elsevier.com/retrieve/pii/B9780124095489094951>.
- Lallemant, S., Schnurle, P. & Malavieille, J., 1994. Coulomb theory applied to accretionary and nonaccretionary wedges: Possible causes for tectonic erosion and/or frontal accretion. *Journal of Geophysical Research*, 99(B6), p.12,033-12,055.
- Lallemant, S.E., Malavieille, J. & Calassou, S., 1992. Effects of oceanic ridge subduction on accretionary wedges: experimental modeling and marine observations. *Tectonics*, 11(6), pp.1301–1313.
- Lallemant, S.E., Schnurle, P. & Manoussis, S., 1992. Reconstruction of subduction zone paleogeometries and quantification of upper plate material losses caused by tectonic erosion. *Journal of Geophysical Research*, 97(B1), p.217. Available at: <http://doi.wiley.com/10.1029/91JB02342>.
- Lallemant, S. et al., 1989. Zenisu Ridge: a deep intraoceanic thrust related to subduction, off southwest Japan. *Tectonophysics*, 160(1–4), pp.151–174.
- Landgrebe, T.C.W. & Müller, R.D., 2015. Uncovering the relationship between subducting bathymetric ridges and volcanic chains with significant earthquakes using geophysical data mining. *Australian Journal of Earth Sciences*, 62(2), pp.171–180. Available at: <http://www.tandfonline.com/doi/abs/10.1080/08120099.2015.1003145>.
- Lapusta, N. & Rice, J.R., 2003. Nucleation and early seismic propagation of small and large events in a crustal earthquake model. *Journal of Geophysical Research: Solid Earth*, 108(B4), pp.1–18. Available at: <http://doi.wiley.com/10.1029/2001JB000793>.
- Latour, S. et al., 2013. Effect of fault heterogeneity on rupture dynamics: An experimental approach using ultrafast ultrasonic imaging. *Journal of Geophysical Research: Solid Earth*, 118(11), pp.5888–5902.
- Lay, T., 2017. A review of the rupture characteristics of the 2011 Tohoku-oki Mw 9.1 earthquake. *Tectonophysics*, 733(September 2017), pp.4–36. Available at: <https://doi.org/10.1016/j.tecto.2017.09.022>.
- Lay, T. et al., 2012. Depth-varying rupture properties of subduction zone megathrust faults. *Journal of Geophysical Research: Solid Earth*, 117(4), pp.1–21.
- Lay, T., 2015. The surge of great earthquakes from 2004 to 2014. *Earth and Planetary Science Letters*, 409, pp.133–146. Available at: <http://dx.doi.org/10.1016/j.epsl.2014.10.047>.
- Lay, T. & Bilek, S.L., 2007. Anomalous Earthquake Ruptures at Shallow Depths on Subduction Zone Megathrusts. In T. H. Dixon & J. C. Moore, eds. *The seismogenic zone of subduction thrust faults*. Columbia University Press - New York, pp. 476–511.
- Lay, T. & Kanamori, H., 1981. An asperity model of large earthquake sequences. *Earthquake Prediction - An International Review*, 4, pp.579–592.
- Lay, T. & Kanamori, H., 1980. Earthquake doublets in the Solomon Islands. *Physics of the Earth and Planetary Interiors*, 21(4), pp.283–304.

- Lay, T., Kanamori, H. & Ruff, L., 1982. The Asperity Model and the Nature of Large Subduction Zone Earthquakes. *Earthquake prediction Research*, 1, pp.3–71.
- Lewis, K.B., Collot, J.Y. & Lallemand, S.E., 1998. The dammed Hikurangi Trough: A channel-fed trench blocked by subducting seamounts and their wake avalanches (New Zealand-France GeodyNZ Project). *Basin Research*, 10(4), pp.441–468.
- Lewis, K.B., Lallemand, S.E. & Carter, L., 2004. Collapse in a quaternary shelf basin off East Cape, New Zealand: Evidence for passage of a subducted seamount inboard of the ruatoria giant avalanche. *New Zealand Journal of Geology and Geophysics*, 47(3), pp.415–429.
- Lin, W. et al., 2013. Stress State in the Largest Displacement Area of the 2011 Tohoku-Oki Earthquake. *Science*, 339(April), pp.687–690.
- Lockner, D.A. et al., 1991. Quasi-static fault growth and shear fracture energy in granite. *Nature*, 350(6313), pp.39–42.
- Lonsdale, P. & Klitgord, K.D., 1978. Structure and tectonic history of the eastern Panama Basin. *Geological Society of America Bulletin*, 89(80703), pp.981–999.
- Loveless, J.P., Pritchard, M.E. & Kukowski, N., 2010. Testing mechanisms of seismic segmentation with slip distributions from recent earthquakes along the Andean margin. *Tectonophysics*, 495, pp.15–33. Available at: <http://dx.doi.org/10.1016/j.tecto.2009.05.008>.
- Lu, X., Lapusta, N. & Rosakis, A.J., 2009. Analysis of supershear transition regimes in rupture experiments: The effect of nucleation conditions and friction parameters. *Geophysical Journal International*, 177(2), pp.717–732.
- Mai, P.M. & Thingbaijam, K.K.S., 2014. SRCMOD: An Online Database of Finite-Fault Rupture Models. *Seismological Research Letters*, 85(6), pp.1348–1357. Available at: <http://srl.geoscienceworld.org/cgi/doi/10.1785/0220140077>.
- Maia, M. et al., 2016. Extreme mantle uplift and exhumation along a transpressive transform fault. *Nature Geoscience*, 9(8), pp.619–623.
- Mair, K., Frye, K.M. & Marone, C., 2002. Influence of grain characteristics on the friction of granular shear zones. *Journal of Geophysical Research: Solid Earth*, 107(B10), p.ECV 4-1-ECV 4-9. Available at: <http://doi.wiley.com/10.1029/2001JB000516>.
- Manaker, D.M. et al., 2008. Interseismic plate coupling and strain partitioning in the Northeastern Caribbean. *Geophysical Journal International*, 174(3), pp.889–903.
- Marcaillou, B. et al., 2016. Seamount subduction at the North-Ecuadorian convergent margin: Effects on structures, interseismic coupling and seismogenesis. *Earth and Planetary Science Letters*, 433, pp.146–158. Available at: <http://dx.doi.org/10.1016/j.epsl.2015.10.043>.
- Marone, C., 1998. Laboratory-Derived Friction Laws and Their Application To Seismic Faulting. *Annual Review of Earth and Planetary Sciences*, 26(1), pp.643–696.
- Marone, C. & Richardson, E., 2006. Do Earthquakes Rupture Piece by Piece or All Together? *Science*, 313(5794), pp.1748–1749.
- Marone, C. & Scholz, C.H., 1988. The Depth of Seismic Faulting and the Upper Transition from Stable to Unstable Slip Regimes. *Geophysical Research Letters*, 15(6), pp.621–624.
- Masson, D.G. et al., 1990. Subduction of seamounts at the Java Trench: a view with long-range sidescan sonar. *Tectonophysics*, 185(1–2), pp.51–65.
- Matsuda, T. et al., 1978. Fault mechanism and recurrence time of major earthquakes in southern Kanto district, Japan, as deduced from coastal terrace data. *Bulletin of the Geological Society of America*, 89(11), pp.1610–1618.
- McCaffrey, R., 1994. Dependence of earthquake size distributions on convergence rates at subduction zones. *Geophysical Research Letters*, 21(21), pp.2327–2330.
- McCaffrey, R., 2008. Global frequency of magnitude 9 earthquakes. *Geology*, 36(3), pp.263–266.
- Mendoza, C. & Hartzell, S., 1989. Slip distribution of the 19 September 1985 Michoacan, Mexico, earthquake: Near-source and teleseismic constraints. *Bulletin of the Seismological Society of ...*, 79(3), pp.655–669. Available at: <http://www.bssaonline.org/content/79/3/655.short>.
- Mendoza, C., Hartzell, S. & Monfret, T., 1994. Wide-band analysis of the 3 March 1985 central Chile earthquake: Overall source process and rupture history. *Bulletin of the Seismological Society of America*, 84(2), pp.269–283. Available at: <http://www.bssaonline.org/content/84/2/269.short>.
- Métois, M., Socquet, A. & Vigny, C., 2012. Interseismic coupling, segmentation and mechanical behavior of the central Chile subduction zone. *Journal of Geophysical Research: Solid Earth*, 117(3), pp.1–16.
- Mochizuki, K. et al., 2008. Weak Interplate Coupling by Seamounts and Repeating M ~ 7 Earthquakes. *Science*, 321(5893), pp.1194–1197.
- Moeremans, R.E. & Singh, S.C., 2015. Fore-arc basin deformation in the Andaman-Nicobar segment of the Sumatra-Andaman subduction zone: Insight from high-resolution seismic reflection data. *Tectonics*, 34(8), pp.1736–1750.
- Moeremans, R.E. & Singh, S.C., 2014. Seismic evidence of continental margin influence on the NinetyEast Ridge in the Bay of Bengal. *Geophysical Research Letters*, 41(20), pp.7143–7150.
- Moreno, M. et al., 2018. Chilean megathrust earthquake recurrence linked to frictional contrast at depth. *Nature Geoscience*. DOI: 10.1038/s41561-018-0089-5
- Morgan, E.C., McAdoo, B.G. & Baise, L.G., 2008. Quantifying geomorphology associated with large subduction zone earthquakes. *Basin Research*, 20(4), pp.531–542.

- Morgan, P.M. et al., 2017. Sibling earthquakes generated within a persistent rupture barrier on the Sunda megathrust under Simeulue Island. *Geophysical Research Letters*, 44(5), pp.2159–2166.
- Müller, R.D. et al., 2008. Age, spreading rates, and spreading asymmetry of the world's ocean crust. *Geochemistry, Geophysics, Geosystems*, 9(4), pp.1–19.
- Müller, R.D. & Landgrebe, T.C.W., 2012. The link between great earthquakes and the subduction of oceanic fracture zones. *Solid Earth*, 3(2), pp.447–465.
- Myhill, R., 2013. Slab buckling and its effect on the distributions and focal mechanisms of deep-focus earthquakes. *Geophysical Journal International*, 192(2), pp.837–853.
- Nagai, R., Kikuchi, M. & Yamanaka, Y., 2001. Comparative study on the source process of recurrent large earthquakes in Sanriku-Oki region: The 1968 Tokachi-Oki earthquake and the 1994 Sanriku-oki earthquake (in Japanese with English abstract). *Journal of Seismological Society Japan*, 52, pp.267–289.
- Namiki, A. et al., 2014. Earthquake model experiments in a viscoelastic fluid: A scaling of decreasing magnitudes of earthquakes with depth. *Journal of Geophysical Research: Solid Earth*, 119(4), pp.3169–3181.
- Nasuno, S. et al., 1998. Time-resolved studies of stick-slip friction in sheared granular layers. *Physical Review E*, 58(2), pp.2161–2171.
- Natawidjaja, D.H. et al., 2004. Paleogeodetic records of seismic and aseismic subduction from central Sumatran microatolls, Indonesia. *Journal of Geophysical Research B: Solid Earth*, 109(4), pp.1–34.
- Needham, J., 1959. *Science and Civilization in China* 3rd ed., Cambridge.
- Newcomb, K.R. & McCann, W.R., 1987. Seismic history and seismotectonics of the Sunda Arc. *Journal of Geophysical Research*, 92(B1), pp.421–439. Available at: <http://doi.wiley.com/10.1029/JB092iB01p00421>.
- Newman, A. V. et al., 2002. Along-strike variability in the seismogenic zone below Nicoya Peninsula, Costa Rica. *Geophysical Research Letters*, 29(20), pp.38-1-38-4. Available at: <http://doi.wiley.com/10.1029/2002GL015409>.
- Nielsen, S.B. & Knopoff, L., 1998. The equivalent strength of geometrical barriers to earthquakes. *Journal of Geophysical Research: Solid Earth*, 103(B5), pp.9953–9965. Available at: <http://doi.wiley.com/10.1029/97JB03293>.
- Nishenko, S.P., 1991. Circum-Pacific seismic potential: 1989–1999. *Pure and Applied Geophysics PAGEOPH*, 135(2), pp.169–259.
- Nishikawa, T. & Ide, S., 2014. Earthquake size distribution in subduction zones linked to slab buoyancy. *Nature Geoscience*, 7(12), pp.904–908.
- Nishizawa, A. et al., 2009. Seismic structure of the subducting seamounts on the trench axis: Erimo Seamount and Daiichi-Kashima Seamount, northern and southern ends of the Japan Trench. *Earth, Planets and Space*, 61(3), pp.e5–e8. Available at: <http://earth-planets-space.springeropen.com/articles/10.1186/BF03352912>.
- Nishizawa, A. et al., 2014. Wide-angle refraction experiments in the daito ridges region at the northwestern end of the philippine sea plate. *Earth, Planets and Space*, 66(1), pp.1–16.
- Nocquet, J.-M. et al., 2016. Supercycle at the Ecuadorian subduction zone revealed after the 2016 Pedernales earthquake. *Nature Geoscience*, 10(December 2016). Available at: <http://www.nature.com/doi/10.1038/ngeo2864>.
- Nocquet, J.M. et al., 2014. Motion of continental slivers and creeping subduction in the northern Andes. *Nature Geoscience*, 7(4), pp.287–291.
- Norabuena, E. et al., 2004. Geodetic and seismic constraints on some seismogenic zone processes in Costa Rica. *Journal of Geophysical Research: Solid Earth*, 109(11), pp.1–25.
- Ohnaka, M., 2000. A Physical Scaling Relation Between the Size of an Earthquake and its Nucleation Zone Size. *Pure and Applied Geophysics*, 157(11), pp.2259–2282. Available at: <http://link.springer.com/10.1007/PL00001084>.
- Okal, E.A., 2012. The south of Java earthquake of 1921 September 11: A negative search for a large interplate thrust event at the Java Trench. *Geophysical Journal International*, 190(3), pp.1657–1672.
- Okal, E.A., Borrero, J. & Synolakis, C.E., 2004. The earthquake and tsunami of 1865 November 17: Evidence for far-field tsunami hazard from Tonga. *Geophysical Journal International*, 157(1), pp.164–174.
- Okal, E.A. & Hartnady, C.J., 2009. The South Sandwich Islands earthquake of 27 June 1929: Seismological study and inference on tsunami risk for the South Atlantic. *South African Journal of Geology*, 112(3–4), pp.359–370.
- Okino, K. & Kato, Y., 1995. Geomorphological study on an accretionary prism: The Nankai Trough. *The Island Arc*, 4, pp.182–198.
- Oleskevich, D.A., Hyndman, R.D. & Wang, K., 1999. The updip and downdip limits to great subduction earthquakes: Thermal and structural models of Cascadia, south Alaska, SW Japan, and Chile. *Journal of Geophysical Research*, 104(B7), p.14,956-14,991.
- Olson, A.H. & Apsel, R.J., 1982. Finite faults and inverse theory with applications to the 1979 Imperial Valley earthquake. *Bulletin of the Seismological Society of America*, 72(6), pp.1969–2001.
- Pacheco, J.F. & Sykes, L.R., 1992. Seismic moment catalog of large shallow earthquakes, 1900 to 1989. *Bulletin of the Seismological Society of America*, 82(3), pp.1306–

1349. Available at: <http://www.bssaonline.org/content/82/3/1306.abstract>.
- Pacheco, J.F., Sykes, L.R. & Scholz, C.H., 1993. Nature of seismic coupling along simple plate boundaries of the subduction type. *Journal of Geophysical Research: Solid Earth*, 98(B8), pp.14133–14159. Available at: <http://doi.wiley.com/10.1029/93JB00349>.
- Park, J.O. et al., 2004. A subducted oceanic ridge influencing the Nankai megathrust earthquake rupture. *Earth and Planetary Science Letters*, 217(1–2), pp.77–84.
- Park, J.O., Hori, T. & Kaneda, Y., 2009. Seismotectonic implications of the Kyushu-Palau ridge subducting beneath the westernmost Nankai forearc. *Earth, Planets and Space*, 61(8), pp.1013–1018.
- Park, S.C. & Mori, J., 2007. Are asperity patterns persistent? Implication from large earthquakes in Papua New Guinea. *Journal of Geophysical Research: Solid Earth*, 112(3), pp.1–16.
- Peacock, S.M. & Hyndman, R.D., 1999. Hydrous minerals in the mantle wedge and the maximum depth of subduction thrust earthquakes. *Geophysical Research Letters*, 26(16), pp.2517–2520.
- Pedley, K.L. et al., 2010. Seafloor structural geomorphic evolution of the accretionary frontal wedge in response to seamount subduction, Poverty Indentation, New Zealand. *Marine Geology*, 270(1–4), pp.119–138. Available at: <http://dx.doi.org/10.1016/j.margeo.2009.11.006>.
- Pelayo, A.M. & Wiens, D.A., 1990. The November 20, 1960 Peru Tsunami Earthquake: Source mechanism of a slow event. *Geophysical Research Letters*, 17(6), pp.661–664.
- Pelletier, B. & Dupont, J., 1990. Effets de la subduction de la ride de Louisville sur l'arc de Tonga-Kermadec. *Oceanologica Acta*, 10(January 1990), pp.57–76.
- Pennington, W.D., 1981. Subduction of the Eastern Panama Basin and Seismotectonics of Northwestern South America. *Journal of Geophysical Research*, 86(B11), pp.10753–10770.
- Perez, O.J., 2000. Kuril Islands Arc: Two Seismic Cycles of Great Earthquakes during which the Complete History of Seismicity ($M_s > 6$) Is Observed. *Bulletin of the Seismological Society of America*, 90(4), pp.1096–1100.
- Perron, J.T., Kirchner, J.W. & Dietrich, W.E., 2008. Spectral signatures of characteristic spatial scales and nonfractal structure in landscapes. *Journal of Geophysical Research: Earth Surface*, 113(4), pp.1–14.
- Peterson, E.T. & Seno, T., 1984. Factors Affecting Seismic Moment Release Rates in Subduction Zones. *Journal of Geophysical Research*, 89(B12), p.10,233–10,248.
- Le Pichon, X. et al., 1996. Structure and evolution of the backstop in the Eastern Nankai trough area (Japan): implications for the soon to come Tokai earthquake. *Island Arc*, 5, pp.440–454. Available at: <http://www.blackwell-synergy.com/doi/abs/10.1111/j.1440-1738.1996.tb00164.x>.
- Popov, V.L. et al., 2012. Rate and state dependent friction laws and the prediction of earthquakes: What can we learn from laboratory models? *Tectonophysics*, 532–535, pp.291–300.
- Press, F., Ben-Menahem, A. & Toksöz, M.N., 1961. Experimental Determination of Earthquake Fault Length and Rupture Velocity. *Journal of Geophysical Research*, 66(10), pp.3471–3485.
- Protti, M. et al., 2014. Nicoya earthquake rupture anticipated by geodetic measurement of the locked plate interface. *Nature Geoscience*, 7(2), pp.117–121. Available at: <http://dx.doi.org/10.1038/ngeo2038>.
- Protti, M. et al., 1995. The March 25, 1990 ($M_w=7.0$, $M_l=6.8$), earthquake at the entrance of the Nicoya Gulf, Costa Rica: Its prior activity, foreshocks, aftershocks, and triggered seismicity. *Journal of Geophysical Research*, 100(B10), p.20,345–20,358.
- Rabinowicz, E., 1951. The nature of the static and kinetic coefficients of friction. *Journal of Applied Physics*, 22(11), pp.1373–1379.
- Ranero, C.R. et al., 2008. Hydrogeological system of erosional convergent margins and its influence on tectonics and interplate seismogenesis. *Geochemistry, Geophysics, Geosystems*, 9(3), pp.1–18.
- Ranero, C.R. & von Huene, R., 2000. Subduction erosion along the Middle America convergent margin. *Nature*, 404(6779), pp.748–752. Available at: <http://www.ncbi.nlm.nih.gov/pubmed/10783885>.
- Reber, J.E., Lavier, L.L. & Hayman, N.W., 2015. Experimental demonstration of a semi-brittle origin for crustal strain transients. *Nature Geoscience*, 8(9), pp.712–715.
- Reid, H.F., 1911. The elastic-rebound theory of earthquakes. University of California Publication Department in Geological Sciences.
- Renard, F., Candela, T. & Bouchaud, E., 2013. Constant dimensionality of fault roughness from the scale of microfractures to the scale of continents. *Geophysical Research Letters*, 40(1), pp.83–87.
- Richter, C.F., 1935. An instrumental earthquake magnitude scale. *Bulletin of the Seismological Society of America*, 25(1), pp.1–32.
- van Rijnsingen, E. et al., 2018. How subduction interface roughness influences the occurrence of large interplate earthquakes. *Geochemistry Geophysics Geosystems*, 19, pp.1–29.
- Ritz, E. & Pollard, D.D., 2012. Stick, slip, and opening of wavy frictional faults: A numerical approach in two dimensions. *Journal of Geophysical Research: Solid Earth*, 117(3), pp.1–16.
- Rivera, L. a et al., 2002. A comparative study of the 1935 and

- 1984 Sumatran subduction earthquakes. *Eos, Transactions, American Geophysical Union*, 81(48, Suppl.), pp.1721–1736.
- Robinson, D.P., Das, S. & Watts, A.B., 2006. Earthquake Rupture Stalled by a Subducting Fracture Zone. *Science*, 312(2006), pp.1203–1204.
- Rodriguez, M. et al., 2013. Mode of opening of an oceanic pull-apart: The 20°N Basin along the Owen Fracture Zone (NW Indian Ocean). *Tectonics*, 32(5), pp.1343–1357.
- Rosenau, M. et al., 2010. Experimental insights into the scaling and variability of local tsunamis triggered by giant subduction megathrust earthquakes. *Journal of Geophysical Research: Solid Earth*, 115(9), pp.1–20.
- Rosenau, M., Corbi, F. & Dominguez, S., 2017. Analogue earthquakes and seismic cycles: Experimental modelling across timescales. *Solid Earth*, 8(3), pp.597–635.
- Rosenau, M., Lohrmann, J. & Oncken, O., 2009. Shocks in a box: An analogue model of subduction earthquake cycles with application to seismotectonic forearc evolution. *Journal of Geophysical Research: Solid Earth*, 114(1), pp.1–20.
- Rubinstein, J.L. et al., 2012. Fixed recurrence and slip models better predict earthquake behavior than the time-and slip-predictable models: 1. Repeating earthquakes. *Journal of Geophysical Research: Solid Earth*, 117(2), pp.1–13.
- Ruff, L. & Kanamori, H., 1983. Seismic coupling and uncoupling at subduction zones. *Tectonophysics*, 99(2–4), pp.99–117.
- Ruff, L. & Kanamori, H., 1980. Seismicity and the subduction zone process. *Physics of the Earth and Planetary Interiors*, 23, pp.240–252.
- Ruff, L.J., 1992. Asperity distributions and large earthquake occurrence in subduction zones. *Tectonophysics*, 211(1–4), pp.61–83.
- Ruff, L.J., 1989. Do trench sediments affect great earthquake occurrence in subduction zones? *Pure and Applied Geophysics PAGEOPH*, 129(1–2), pp.263–282.
- Ruff, L.J. & Miller, A.D., 1994. Rupture process of large earthquakes in the northern Mexico subduction zone. *Pure and Applied Geophysics PAGEOPH*, 142(1), pp.101–172.
- Ruff, L.J. & Tichelaar, B.W., 1996. What Controls The Seismogenic Plate Interface In Subduction Zones? In G. E. Bebout et al., eds. *Subduction: Top to Bottom*. American Geophysical Union, pp. 105–111.
- Ruh, J.B. et al., 2016. Crustal deformation dynamics and stress evolution during seamount subduction: High-resolution 3-D numerical modeling. *Journal of Geophysical Research: Solid Earth*, 121(9), pp.6880–6902.
- Ruina, A., 1983. Slip instability and state variable friction laws. *Journal of Geophysical Research*, 88(B12), p.10,359–10,370.
- Saffer, D.M., 2017. Mapping fluids to subduction megathrust locking and slip behavior. *Geophysical Research Letters*, 44(18), pp.9337–9340.
- Saffer, D.M. & Tobin, H.J., 2011. Hydrogeology and Mechanics of Subduction Zone Forearcs: Fluid Flow and Pore Pressure. *Annual Review of Earth and Planetary Sciences*, 39(1), pp.157–186. Available at: <http://www.annualreviews.org/doi/10.1146/annurev-earth-040610-133408>.
- Sage, F., Collot, J.Y. & Ranero, C.R., 2006. Interplate patchiness and subduction-erosion mechanisms: Evidence from depth-migrated seismic images at the central Ecuador convergent margin. *Geology*, 34(12), pp.997–1000.
- Saillard, M. et al., 2017. From the seismic cycle to long-term deformation: linking seismic coupling and Quaternary coastal geomorphology along the Andean megathrust. *Tectonics*, 36(2), pp.241–256.
- Sallarès, V. et al., 2005. Seismic structure of the Carnegie ridge and the nature of the Galápagos hotspot. *Geophysical Journal International*, 161(3), pp.763–788.
- Sandwell, D.T., Gille, S.T. & Smith, W.H.F., 2002. Bathymetry from space: Oceanography, geophysics, and climate, geoscience professional services. Maryland: Bethesda.
- Satake, K., 2003. Fault slip and seismic moment of the 1700 Cascadia earthquake inferred from Japanese tsunami descriptions. *Journal of Geophysical Research*, 108(B11), pp.2535–2552. Available at: <http://doi.wiley.com/10.1029/2003JB002521>.
- Satake, K., 2015. Geological and historical evidence of irregular recurrent earthquakes in Japan. *Philosophical Transactions of the Royal Society A: Mathematical, Physical and Engineering Sciences*, 373(2053), pp.1–15. Available at: <http://rsta.royalsocietypublishing.org/lookup/doi/10.1098/rsta.2014.0375>.
- Schallamach, A., 1971. How Does Rubber Slide? *Rubber Chemistry and Technology*, 44(5), pp.1147–1158. Available at: <https://doi.org/10.5254/1.3544797>.
- Schellart, W.P. & Rawlinson, N., 2013. Global correlations between maximum magnitudes of subduction zone interface thrust earthquakes and physical parameters of subduction zones. *Physics of the Earth and Planetary Interiors*, 225, pp.41–67. Available at: <http://dx.doi.org/10.1016/j.pepi.2013.10.001>.
- Schlaphorst, D. et al., 2016. Water, oceanic fracture zones and the lubrication of subducting plate boundaries—insights from seismicity. *Geophysical Journal International*, 204(3), pp.1405–1420.
- Scholl, D.W. et al., 2015. Great (\geq Mw8.0) megathrust earthquakes and the subduction of excess sediment and bathymetrically smooth seafloor. *Geosphere*, 11(2), pp.236–265.
- Scholz, C., Molnar, P. & Johnson, T., 1972. Detailed studies of frictional sliding of granite and implications for the earthquake mechanism. *Journal of Geophysical Research*, 77(10), pp.5113–5126.

- 77(32), pp.6392–6406. Available at: <http://doi.wiley.com/10.1029/JB077i032p06392>.
- Scholz, C.H., 1998. Earthquakes and friction laws. *Nature*, 391(6662), pp.37–42. Available at: <http://dx.doi.org/10.1038/34097>.
- Scholz, C.H., Aviles, C.A. & Wesnousky, S.G., 1986. Scaling Differences between Large Interplate and Intraplate Earthquakes. *Bulletin of the Seismological Society of America*, 76(1), pp.65–70.
- Scholz, C.H. & Campos, J., 2012. The seismic coupling of subduction zones revisited. *Journal of Geophysical Research: Solid Earth*, 117(5), pp.1–22.
- Scholz, C.H. & Engelder, J.T., 1976. The Role of Asperity Indentation and Ploughing in Rock Friction - I Asperity Creep and Stick-Slip. *International Journal of Rock Mechanics and Mining Sciences & Geomechanics Abstracts*, 13, pp.149–154.
- Scholz, C.H. & Small, C., 1997. The effect of seamount subduction on seismic coupling. *Geology*, 25(6), pp.487–490.
- Schulze, D., 2003. Time- and velocity-dependent properties of powders effecting slip-stick oscillations. *Chemical Engineering and Technology*, 26(10), pp.1047–1051.
- Schwartz, S.Y. & DeShon, H.R., 2007. Distinct Updip Limits to Geodetic Locking and Microseismicity at the Northern Costa Rica Seismogenic Zone: Evidence for Two Mechanical Transitions. In T. Dixon & C. Moore, eds. *The seismogenic zone of subduction thrust faults*. Columbia University Press - New York, pp. 567–599.
- Schwartz, S.Y. & Ruff, L.J., 1987. Asperity distribution and earthquake occurrence in the southern Kurile Islands arc. *Physics of the Earth and Planetary Interiors*, 49(1–2), pp.54–77.
- Schwartz, S.Y. & Ruff, L.J., 1985. The 1968 Tokachi-Oki and the 1969 Kurile Islands earthquakes: Variability in the rupture process. *Journal of Geophysical Research: Solid Earth*, 90, pp.8613–8626.
- Scuderi, M.M. et al., 2015. Poromechanics of stick-slip frictional sliding and strength recovery on tectonic faults. *Journal of Geophysical Research: Solid Earth*, 120, pp.6895–6912.
- Shulgin, A. et al., 2011. Structural architecture of oceanic plateau subduction offshore Eastern Java and the potential implications for geohazards. *Geophysical Journal International*, 184(1), pp.12–28.
- Singh, S.C. et al., 2011. Aseismic zone and earthquake segmentation associated with a deep subducted seamount in Sumatra. *Nature Geoscience*, 4(5), pp.308–311. Available at: <http://dx.doi.org/10.1038/ngeo1119>.
- Singh, S.K., Suárez, G. & Domínguez, T., 1985. The Oaxaca, Mexico, earthquake of 1931: lithospheric normal faulting in the subducted Cocos plate. *Nature*, 317(5), pp.56–58.
- Sladen, A. & Trevisan, J., 2018. Shallow megathrust earthquake ruptures betrayed by their outer-trench aftershocks signature. *Earth and Planetary Science Letters*, 483, pp.105–113. Available at: <https://doi.org/10.1016/j.epsl.2017.12.006>.
- Smith, W.H.F. & Sandwell, D.T., 1997. Global Sea Floor Topography from Satellite Altimetry and Ship Depth Soundings. *Science*, 277(26 SEPTEMBER 1997), pp.1956–1962.
- Song, T.R.A. & Simons, M., 2003. Large trench-parallel gravity variations predict seismogenic behavior in subduction zones. *Science*, 301(5633), pp.630–633.
- Sparkes, R. et al., 2010. Subducted seafloor relief stops rupture in South American great earthquakes: Implications for rupture behaviour in the 2010 Maule, Chile earthquake. *Earth and Planetary Science Letters*, 298(1–2), pp.89–94. Available at: <http://dx.doi.org/10.1016/j.epsl.2010.07.029>.
- Spence, W. et al., 1999. Seismic subduction of the Nazca Ridge as shown by the 1996–97 Peru earthquakes. *Pure and Applied Geophysics*, 154, pp.753–776.
- Spinelli, G.A. & Saffer, D.M., 2004. Along-strike variations in underthrust sediment dewatering on the Nicoya margin, Costa Rica related to the updip limit of seismicity. *Geophysical Research Letters*, 31(4), pp.1–5.
- Stein, S. & Okal, E.A., 2011. The Size of the 2011 Tohoku Earthquake Need Not Have Been a Surprise. *Eos, Transactions, American Geophysical Union*, 92(27). Available at: <http://geology.gsapubs.org/content/43/8/751.full?etoc>.
- Stein, S. & Okal, E.A., 2007. Ultralong period seismic study of the December 2004 Indian Ocean earthquake and implications for regional tectonics and the subduction process. *Bulletin of the Seismological Society of America*, 97(1A), pp.S279–S295.
- Storchak, D.A. et al., 2013. Public release of the ISC-GEM global instrumental earthquake catalog (1900–2009). *Seismological Research Letters*, (October), pp.810–815. Available at: http://www.seismosoc.org/publications/SRL/SRL_84/srl_84-5_es/.
- Strasser, F.O., Arango, M.C. & Bommer, J.J., 2010. Comparison of Seismicity Rates in the New Madrid and Wabash Valley Seismic Zones. *Seismological Research Letters*, 81(6), pp.951–954.
- Sveen, J.K., 2004. An introduction to MatPIV v. 1.6.1. Eprint no. 2, ISSN 0809-4403, pp.1–27. Available at: <http://folk.uio.no/jks/matpiv/>.
- Swenson, J.L. & Beck, S.L., 1996. Historical 1942 Ecuador and 1942 Peru subduction earthquakes, and earthquake cycles along Colombia-Ecuador and Peru subduction segments. *Pure and Applied Geophysics*, 146(1), pp.67–101.
- Sykes, L.R., 1971. Aftershock sequences of great earthquakes, seismicity gaps, and earthquake prediction for Alaska and Aleutians. *J. Geophys. Res.*, 76(32), pp.8021–8041.

- Tajima, F. & Kanamori, H., 1985. Aftershock area expansion and mechanical heterogeneity of fault zone within subduction zones. *Geophysical Research Letters*, 12(6), pp.345–348.
- Tanioka, Y. & Satake, K., 2001. Detailed coseismic slip distribution of the 1944 Tonankai earthquake estimated from tsunami waveforms. *Geophysical Research Letters*, 28(6), pp.1075–1078.
- Theunissen, T. et al., 2012. Crustal deformation at the southernmost part of the Ryukyu subduction (East Taiwan) as revealed by new marine seismic experiments. *Tectonophysics*, 578(June), pp.10–30. Available at: <http://dx.doi.org/10.1016/j.tecto.2012.04.011>.
- Theunissen, T. et al., 2010. The largest instrumentally recorded earthquake in Taiwan: Revised location and magnitude, and tectonic significance of the 1920 event. *Geophysical Journal International*, 183(3), pp.1119–1133.
- Thielicke, W. & Stamhuis, E.J., 2014. PIVlab – Towards User-friendly, Affordable and Accurate Digital Particle Image Velocimetry in MATLAB. *Journal of Open Research Software*, 2(30), pp.2–10. Available at: <http://openresearchsoftware.metajnl.com/articles/10.5334/jors.bl/>.
- Thompson, B.D., Young, R.P. & Lockner, D.A., 2006. Fracture in Westerly granite under AE feedback and constant strain rate loading: Nucleation, quasi-static propagation, and the transition to unstable fracture propagation. *Pure and Applied Geophysics*, 163(5–6), pp.995–1019.
- Thompson, B.D., Young, R.P. & Lockner, D.A., 2005. Observations of premonitory acoustic emission and slip nucleation during a stick slip experiment in smooth faulted Westerly granite. *Geophysical Research Letters*, 32(10), pp.1–4.
- Thompson, B.D., Young, R.P. & Lockner, D.A., 2009. Premonitory acoustic emissions and stick-slip in natural and smooth-faulted Westerly granite. *Journal of Geophysical Research: Solid Earth*, 114(2), pp.1–14.
- Trifunac, M.D., 1974. A three-dimensional dislocation model for the San Fernando, California, earthquake of February 9, 1971. *Bulletin of the Seismological Society of America*, 64(1), pp.149–172. Available at: <http://www.bssaonline.org/content/64/1/149.short>.
- Tsutsumi, A. & Shimamoto, T., 1997. High-velocity frictional properties of gabbro. *Geophysical Research Letters*, 24(6), pp.699–702.
- Turcotte, D.L., 1992. Fractals, chaos, self-organized criticality and tectonics. *Terra Nova*, 4, pp.4–12.
- Turcotte, D.L., 1997. Fractals and chaos in geology and geophysics, New York: Cambridge Univ. Press.
- Uyeda, S., 1987. Chilean vs. Mariana type subduction zones with remarks on arc volcanism and collision tectonics. In J. W. H. Monger & J. Francheteau, eds. *Circum-Pacific orogenic belts and evolution of the Pacific Ocean basin*, Geodynamic Series 18. *Int. Lith. Pr. Contrib.*
- Vallée, M. et al., 2013. Intense interface seismicity triggered by a shallow slow slip event in the Central Ecuador subduction zone. *Journal of Geophysical Research: Solid Earth*, 118(6), pp.2965–2981.
- Varamashvili, N., Chelidze, T. & Lursmanashvili, O., 2008. Phase synchronization of slips by periodical (tangential and normal) mechanical forcing in the spring-slider model. *Acta Geophysica*, 56, pp.357–371.
- Vargas, C.A. et al., 2008. Sliding size distribution in a simple spring-block system with asperities. *Physica A: Statistical Mechanics and its Applications*, 387(13), pp.3137–3144.
- Voisin, C., Renard, F. & Grasso, J.R., 2007. Long term friction: From stick-slip to stable sliding. *Geophysical Research Letters*, 34(13), pp.1–5.
- Voss, R.F., 1988. Fractals in nature: From characterization to simulation. In H. O. Peitgen & D. Saupe, eds. *The science of fractal images*. New-York: Springer, pp. 21–70.
- Wada, I. & Wang, K., 2009. Common depth of slab-mantle decoupling: Reconciling diversity and uniformity of subduction zones. *Geochemistry, Geophysics, Geosystems*, 10(10), pp.1–36.
- Wallace, L.M., Ellis, S. & Mann, P., 2009. Collisional model for rapid fore-arc block rotations, arc curvature, and episodic back-arc rifting in subduction settings. *Geochemistry, Geophysics, Geosystems*, 10(5), pp.1–50.
- Wang, K. & Bilek, S.L., 2011. Do subducting seamounts generate or stop large earthquakes? *Geology*, 39(9), pp.819–822.
- Wang, K. & Bilek, S.L., 2014. Invited review paper: Fault creep caused by subduction of rough seafloor relief. *Tectonophysics*, 610, pp.1–24. Available at: <http://dx.doi.org/10.1016/j.tecto.2013.11.024>.
- Wang, K. & Tréhu, A.M., 2016. Invited review paper: Some outstanding issues in the study of great megathrust earthquakes—The Cascadia example. *Journal of Geodynamics*, 98, pp.1–18. Available at: <http://dx.doi.org/10.1016/j.jog.2016.03.010>.
- Weatherall, P. et al., 2015. A new digital bathymetric model of the world's oceans. *Earth and Space Science*, 2, pp.331–345.
- Wells, R.E., 2003. Correction to “Basin-centered asperities in great subduction zone earthquakes: A link between slip, subsidence, and subduction erosion?” *Journal of Geophysical Research*, 108(B12), p.2562. Available at: <http://doi.wiley.com/10.1029/2003JB002880>.
- Wesnousky, S.G., 2006. Predicting the endpoints of earthquake ruptures. *Nature*, 444(7117), pp.358–360. Available at: <http://www.nature.com/doi/10.1038/nature05275>.
- Wessel, P. et al., 2013. Generic Mapping Tools: Improved Version Released. *Eos, Transactions American Geophysical Union*, 94(45), pp.409–410. Available at: <http://doi.wiley.com/10.1002/2013EO450001>.

- Wessel, P., 2001. Global distribution of seamounts inferred from gridded Geosat/ERS-1 altimetry. *Journal of Geophysical Research: Solid Earth*, 106(B9), pp.19431–19441. Available at: <http://doi.wiley.com/10.1029/2000JB000083>.
- Wood, H.O., 1912. The elastic-rebound theory of Earthquakes. *Bulletin of the Seismological Society of America*, 2, pp.98–100.
- Wood, H.O. & Neumann, F., 1931. Modified Mercalli Intensity Scale of 1931. *Bulletin of the Seismological Society of America*, 21(4), pp.277–283.
- Wyss, M., 1976. Local sea level changes before and after the hyuganada, Japan, Earthquakes. *Journal of Geophysical Research*, 81(29), pp.5315–5321.
- Yamaguchi, T. et al., 2011. Gutenberg-Richter's law in sliding friction of gels. *Journal of Geophysical Research: Solid Earth*, 116(12), pp.1–8.
- Yamamoto, Y. et al., 2013. Imaging of the subducted kyushu-palau ridge in the hyuga-nada region, western nankai trough subduction zone. *Tectonophysics*, 589, pp.90–102. Available at: <http://dx.doi.org/10.1016/j.tecto.2012.12.028>.
- Yamanaka, Y. & Kikuchi, M., 2004. Asperity map along the subduction zone in northeastern Japan inferred from regional seismic data. *Journal of Geophysical Research B: Solid Earth*, 109(7), pp.1–14.
- Yamazaki, T. & Okamura, Y., 1989. Subducting seamounts and deformation of overriding forearc wedges around Japan. *Tectonophysics*, 160(1–4), pp.207–229.
- Yang, H., Liu, Y. & Lin, J., 2012. Effects of subducted seamounts on megathrust earthquake nucleation and rupture propagation. *Geophysical Research Letters*, 39(24), pp.2–7.
- Yang, H., Liu, Y. & Lin, J., 2013. Geometrical effects of a subducted seamount on stopping megathrust ruptures. *Geophysical Research Letters*, 40(10), pp.2011–2016.
- Ye, L. et al., 2016. Rupture characteristics of major and great ($M_w \geq 7.0$) megathrust earthquakes from 1990 to 2015: 1. Source parameter scaling relationships. *Journal of Geophysical Research: Solid Earth*, pp.826–844.
- Ye, L., Kanamori, H. & Lay, T., 2018. Global variations of large megathrust earthquake rupture characteristics. *Science Advances*, 4, pp.1–8.
- Yepes, H. et al., 2016. A new view for the geodynamics of Ecuador: Implication in seismogenic source definition and seismic hazard assessment. *Tectonics*, 35(5), pp.1249–1279.
- Yokota, Y. et al., 2016. Seafloor geodetic constraints on interplate coupling of the Nankai Trough megathrust zone. *Nature*, 534(7607), pp.4–6. Available at: <http://www.nature.com/doi/10.1038/nature17632>.
- Yue, H. & Lay, T., 2013. Source rupture models for the Mw 9.0 2011 Tohoku earthquake from joint inversions of high-rate geodetic and seismic data. *Bulletin of the Seismological Society of America*, 103(2 B), pp.1242–1255.
- Zang, A. et al., 2000. Fracture process zone in granite. *Journal of Geophysical Research-Solid Earth*, 105(B10), pp.23651–23661.
- Zielke, O., Galis, M. & Mai, P.M., 2017. Fault roughness and strength heterogeneity control earthquake size and stress drop. *Geophysical Research Letters*, 44(2), pp.777–783.

Appendix Chapter 3 (A3)

Introduction

This file includes a methodological appendix which better develops the details of computation and a series of figures that supports or complement our study.

Additional Supporting Information (Files uploaded separately)

http://www.gm.univ-montp2.fr/lallemant/Supp_material_G3_roughness_Lallemant.zip

Text A3.1. Methodological Appendix

Roughness in spatial domain

The dispersion of the elevation around its mean value is just the 2nd statistical moment of topography. Taking the L2-norm, a simple mathematical estimator for roughness is the root-mean-square (rms) of the elevation z over the study area Ω (Equation A3.1).

$$R_{\Omega} = \left(\int_{\Omega} (z - \bar{z})^2 d\Omega \right)^{1/2} \quad (\text{A3.1})$$

It has the same unit as elevation.

One way to compute this disparity is to consider the autocorrelation function of the elevation, which correlates the bathymetry with itself spatially shifted by some vectors. In practice, on discrete datasets with limited spatial extent, the autocorrelation function is estimated by means of semi-variograms that are directly built in the spatial-domain. They exhibit the distribution of elevation dissemblance with distance. At large distances, they converge towards the variance of the data. This plateau, called “sill” is attained at some distance called “range”. Various mathematical models are used for fitting the semi-variograms and consequently estimating these parameters. This approach has been adopted for estimating the roughness of the bathymetry in some subduction zones (e.g. Morgan et al., 2008).

Power spectral density

A computationally more efficient way to compute this autocorrelation function is to move into the frequency domain via Fourier transform. The Wiener-Khinchine theorem states that the power

spectral density (*PSD*) of a stationary process is the Fourier transform of its autocorrelation function.

If the variable z is stationary with zero mean, then the *PSD* of R_{Ω} is:

$$PSD(f) = \mathcal{F}(R_{\Omega}) = Z(f) \cdot Z^*(f)$$

where $Z = \mathcal{F}(z)$ is the Fourier Transform of z and f is the spatial frequency (inverse of the spatial wavelength). It provides a measure of how the variance of the bathymetry evolves with spatial frequency. Putting another way, the *PSD* measures the contribution of each specific frequency (or wavelength) to the total energy of the bathymetric signal.

In practice, on a finite number of z samples, the *PSD* is estimated with a Discrete Fourier Transform (DFT) periodogram. In 2-dimensions we get:

$$PSD(f_x, f_y) = \frac{\Delta x \Delta y}{N_x N_y} |Z(f_x, f_y)|^2$$

where, Δx and Δy are the spatial sampling intervals in two horizontal directions, f_x and f_y the frequencies, and N_x and N_y the corresponding number of samples used for the DFT.

Roughness in the frequency domain

The *PSD* relates with the initial definition of roughness (Equation A3.1) through the Parseval theorem which states that the total energy of one signal is the same both in the spatial domain and the frequency domain. Therefore, one can define the roughness in the frequency domain as follows:

$$R_f = \left[\iint_0^{+\infty} PSD(f_x, f_y) df_x df_y \right]^{1/2} \quad (\text{A3.2})$$

Bandwidth roughness

We can also define a “bandwidth roughness” (e.g. Dunham et al., 2011) which only considers the contribution of one specific frequency band (or wavelength band) to the complete disparity of the signal around its zero mean value. It expresses in two directions as follows :

$$R_{\Delta f_x \Delta f_y} = \left[\iint_{f_{min}}^{f_{max}} PSD(f_x, f_y) df_x df_y \right]^{1/2}$$

This integral over 2 directions can be reduced to 1 dimension by considering only radial frequencies (Figure 3.1). Doing so, we implicitly assume that the bathymetry disparity is isotropic, or alternatively, we must acknowledge that we measure a mean roughness value which may vary with orientation. In this study, we work with radial frequencies, but also provide information about the roughness disparity with orientation.

Consequently, the mathematical expression of the bandwidth roughness, expressed in term of radial frequency, is:

$$R_{\Delta f} = \left[\int_{f_{\min}}^{f_{\max}} PSD(f) df \right]^{1/2} \quad (\text{A3.3})$$

We fit the discrete *PSD* measurements (over a specific radial frequency bandwidth) with 2 distinct models. One takes into account the fractal structure of topography, while the other simply takes the average.

PSD and fractals

It has been shown that global topography on Earth can be considered as a fractal object. That is to say that the distribution of elevation is similar whatever scale analysis is performed (Turcotte, 1992). It means that the *PSD* of topography exhibits a power-law dependence with radial frequency (e.g. Fox and Hayes, 1985; Voss, 1988; Huang and Turcotte, 1989 and 1990; Turcotte, 1997).

$$PSD(f) \propto |f|^{-(\beta+1)} \quad (\text{A3.4})$$

In a log-log representation, $(\beta+1)$ is the slope (in absolute value) of the theoretical dependence of the *PSD* values with radial frequency (Fig. 3.1). This exponent can also be expressed in terms of other parameters that are commonly used in the literature. They are the fractal dimension D , the Hurst coefficient H or the Hausdorff measure H_a . Their relationships, in a 3-dimensional space, are the following:

$$\begin{cases} \beta = 2 H_a + 1 \\ \beta = 2 H - 1 \\ D = 3 - H_a \end{cases}$$

Therefore,

$$D = \frac{7 - \beta}{2}$$

For a 2D spectra, a slope value of 3 indicates that amplitude is directly proportional to wavelength (self-similar) (Voss, 1988). Conversely, slopes that are different from 3 reveal self-affine dependence. Slope higher (respectively, smaller) than 3 indicates that shorter wavelength features have smaller (respectively, higher) height-to-width ratios.

Since the fractal dimension D of a surface in a 3-dimensional space (e.g. bathymetry) must be comprised between 2 (a plane) and 3 (a very rough surface which almost completely occupies a volume), then the admissible parameter intervals are:

$$\begin{cases} \text{slope} \in [2, 4] \\ \beta \in [1, 3] \\ H_a \in [0, 1] \\ H \in [1, 2] \end{cases}$$

The slopes that are measured in this study globally fall within these ranges.

Using this fractal model, Equation A3.3 becomes:

$$R_{\Delta f // \text{fractal}} = \left[\int_{f_{\min}}^{f_{\max}} C f^{-(\beta+1)} df \right]^{1/2}$$

Where C is a constant (amplitude of the *PSD* at $f=1$ Hz) that needs to be estimated in conjunction with β .

Therefore (for $\beta > 0$),

$$R_{\Delta f // \text{fractal}} = \left[\frac{C}{\beta} \right]^{1/2} (f_{\min}^{-\beta} - f_{\max}^{-\beta})^{1/2}$$

And finally, with $\lambda = \frac{1}{f}$ the spatial wavelength,

$$R_{\Delta \lambda // \text{fractal}} = \left[\frac{C}{\beta} \right]^{1/2} (\lambda_{\max}^{\beta} - \lambda_{\min}^{\beta})^{1/2} \quad (\text{A3.5})$$

These estimates of the roughness are dominated by the longest wavelength. The longer the wavelength is, the higher the roughness will be. Nevertheless, when considering one single frequency (or frequency band), one can compare these roughness values from one zone to another, highlighting geographical

zones where roughness at these frequencies is more or less important.

Roughness considering an average model over the frequency band

In the case of limited frequency bandwidth, the PSD function can be approximated by a constant value equal to its mean within the considered frequency band (Figure 3.1). Although this approach seems, at least on its principle, less precise than the fractal approach, in practice, it appears, globally, to be steadier since the fractal hypothesis may not be valid everywhere, and particularly when considering a narrow bandwidth.

Equation A3.3 now becomes:

$$R_{\Delta f / \text{mean}} = \left[\int_{f_{\min}}^{f_{\max}} \overline{PSD} df \right]^{1/2}$$

Where (\overline{PSD}) is the mean value of PSD over the frequency band $[f_{\min}, f_{\max}]$.

Finally:

$$R_{\Delta f / \text{mean}} = [\overline{PSD}]^{1/2} (f_{\max} - f_{\min})^{1/2}$$

or

$$R_{\Delta \lambda / \text{mean}} = [\overline{PSD}]^{1/2} \left(\frac{1}{\lambda_{\min}} - \frac{1}{\lambda_{\max}} \right)^{1/2} \quad (\text{A3.6})$$

where (\overline{PSD}) is the mean value of PSD over the wavelength band $[\lambda_{\min}, \lambda_{\max}]$.

Uncertainties

All the aforementioned estimators for the bathymetric roughness are associated with some uncertainties. We provide here two crude approaches for determining proxies for these uncertainties. We say crude in the sense that we do not take explicitly into account the uncertainty associated with elevation. We saw that this latter uncertainty is on the order of a few hundreds of meters, but nothing more. So, we consider that the disparity that we measure over the window of analysis reflects, in a reliable way, these uncertainties on elevation values. But, this can only be considered at first order.

A straightforward way to estimate uncertainty for roughness measurements using the average approach over some frequency bands is to measure

the standard deviation of the PSD values σ_{PSD} . Then, from Equation A3.6, we get:

$$\sigma_R = \frac{1}{2} [\overline{PSD}]^{-1/2} (f_{\max} - f_{\min})^{1/2} \sigma_{PSD} \quad (\text{A3.7})$$

A similar approach can be led for the fractal model approach. However, the standard deviations of the slope and intercept parameters are less easy to derive. An alternative approach may consist in computing the disparity of PSD relatively to the fractal model. For simplicity, we implemented a third approach which is adapted to both average and fractal models, and that consists in the determination of the variance of roughness values over spatial orientation.

In this study, we have taken the decision to collect all PSD values within some frequency bandwidths, whatever their orientation. This choice is justified by our search for a single global parameter, and by the fact that, if some significant roughness exists in a specific orientation, then the global roughness should also be high, even though it may be attenuated by the contributions of other directions. Nevertheless, in a very few cases, working in radial frequencies make us miss the information of orientation of dominant roughness.

We have thus used the complete 2D PSD information for (1) getting an additional proxy of the roughness disparity, and for (2) complementing the roughness database with more detailed information related to orientation.

To determine the roughness along all possible orientations, we have used 12 orientations with 15° wide opening to cover the $0-180^\circ$ azimuth range. It allows us to estimate their variance over orientation. This is what is plotted on Figure A3.1 (middle). Then, we retain the orientation that exhibits the highest roughness value. If the roughness disparity, at a given location, is above some threshold, then one may consider that there is, in this vicinity, a preferential orientation for roughness. This is notably the case for linear structures of morphological patterns. Seaward of Japan, our procedure highlights normal bending structures at high frequencies, whereas the Joban seamount chain is the main structure where anisotropy in low frequency roughness is found (Figure A3.1).

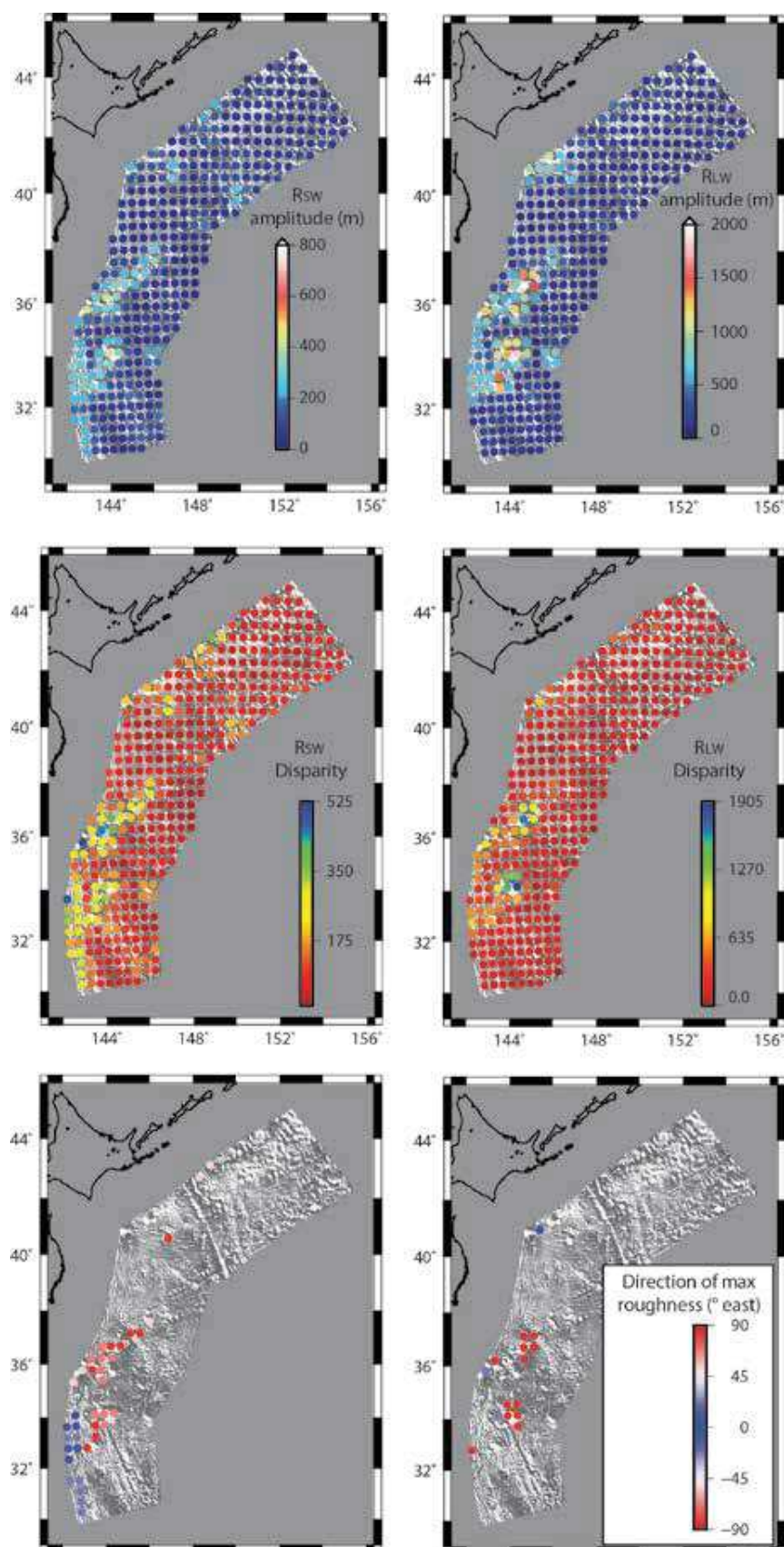


Figure A3.1. Illustration of roughness anisotropy (average method) for high frequencies (left) and low frequencies (right) seaward Japan. (Top) Roughness spatial distribution. (Middle) Roughness disparity over directions. (Bottom) Direction of maximum roughness at nodes where roughness disparity is higher than its spatial mean plus its standard deviation as estimated over the whole Japan area (hence, about 15% of nodes are selected).

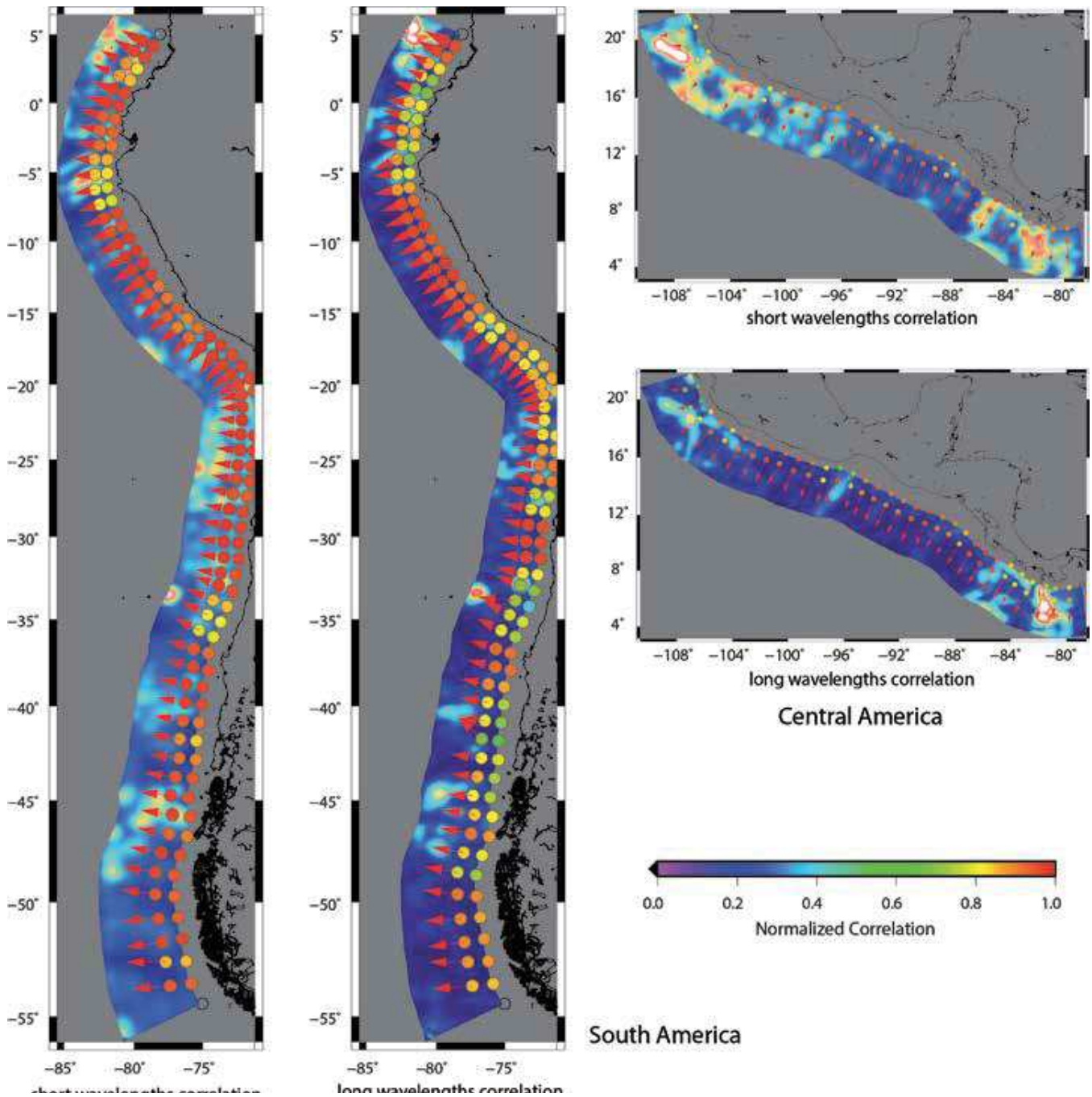


Figure A3.2. Two examples of correlation processing between 200 km-wide squared trench-side areas with similar sized ocean-side areas either in a direction normal to the trench or oblique to it (up to $\pm 45^\circ$). The roughness shape disparity is quantified from 0 (maximum disparity) to 1 (minimum disparity). Left: Andean trench (left: correlation using R_{SW} , right: correlation using R_{LW}). Right: Middle America trench (top: correlation using R_{SW} , bottom: correlation using R_{LW}). Colored dots along trenches represent the normalized correlation in a direction normal to the trench whereas colored dots aside from the trench line give the best correlation associated with the direction along which the fit is the best (red arrows).

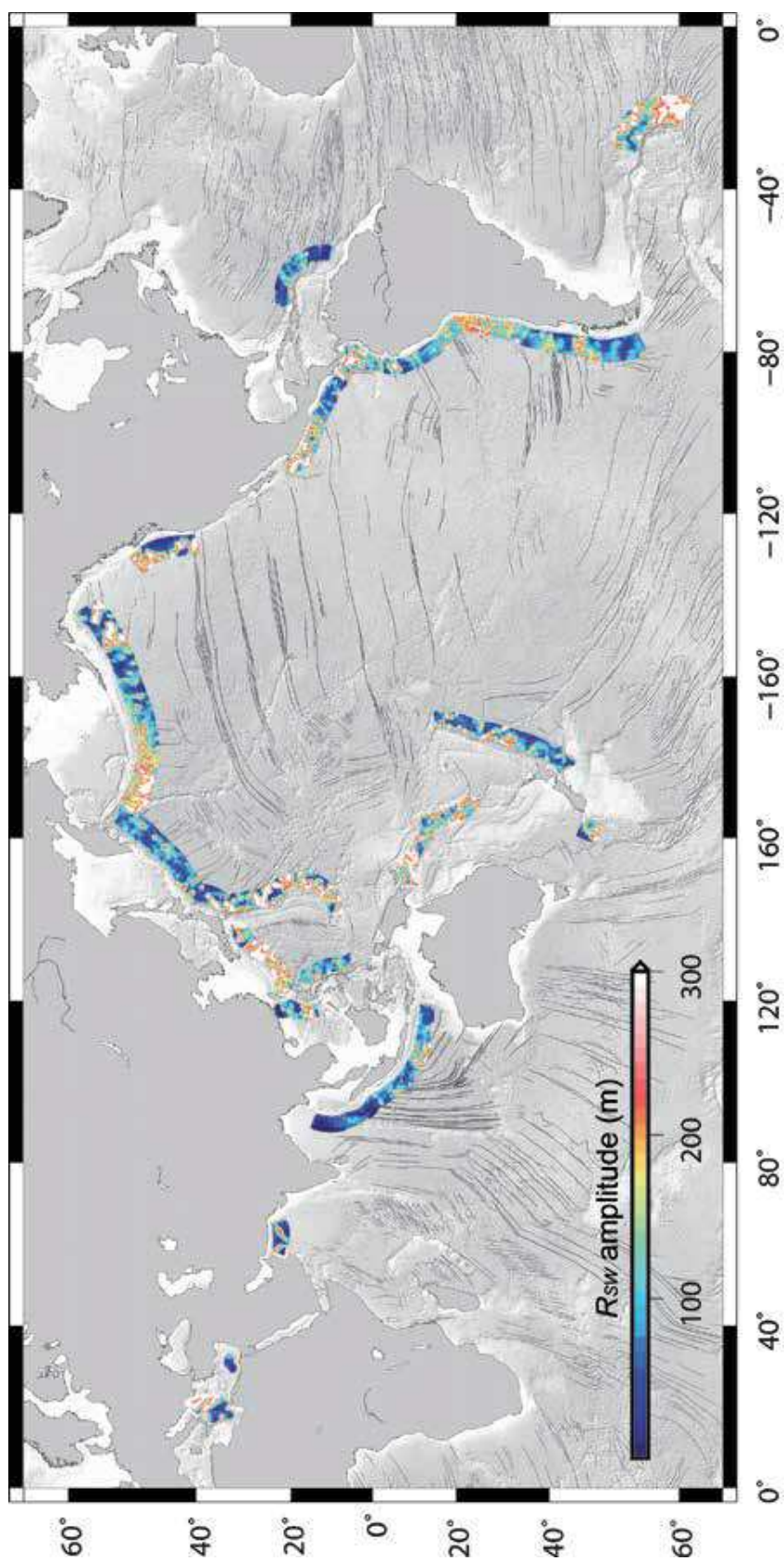


Figure A3.3. Global map of roughness R_{sw} estimated from the average of the PSD at short wavelengths between 12 and 20 km over a 400 km strip along subduction trenches. The white dotted line at a distance of 260 km from the trench represent the seaward limit of the proxy area used in this study. Amplitudes are in meters.

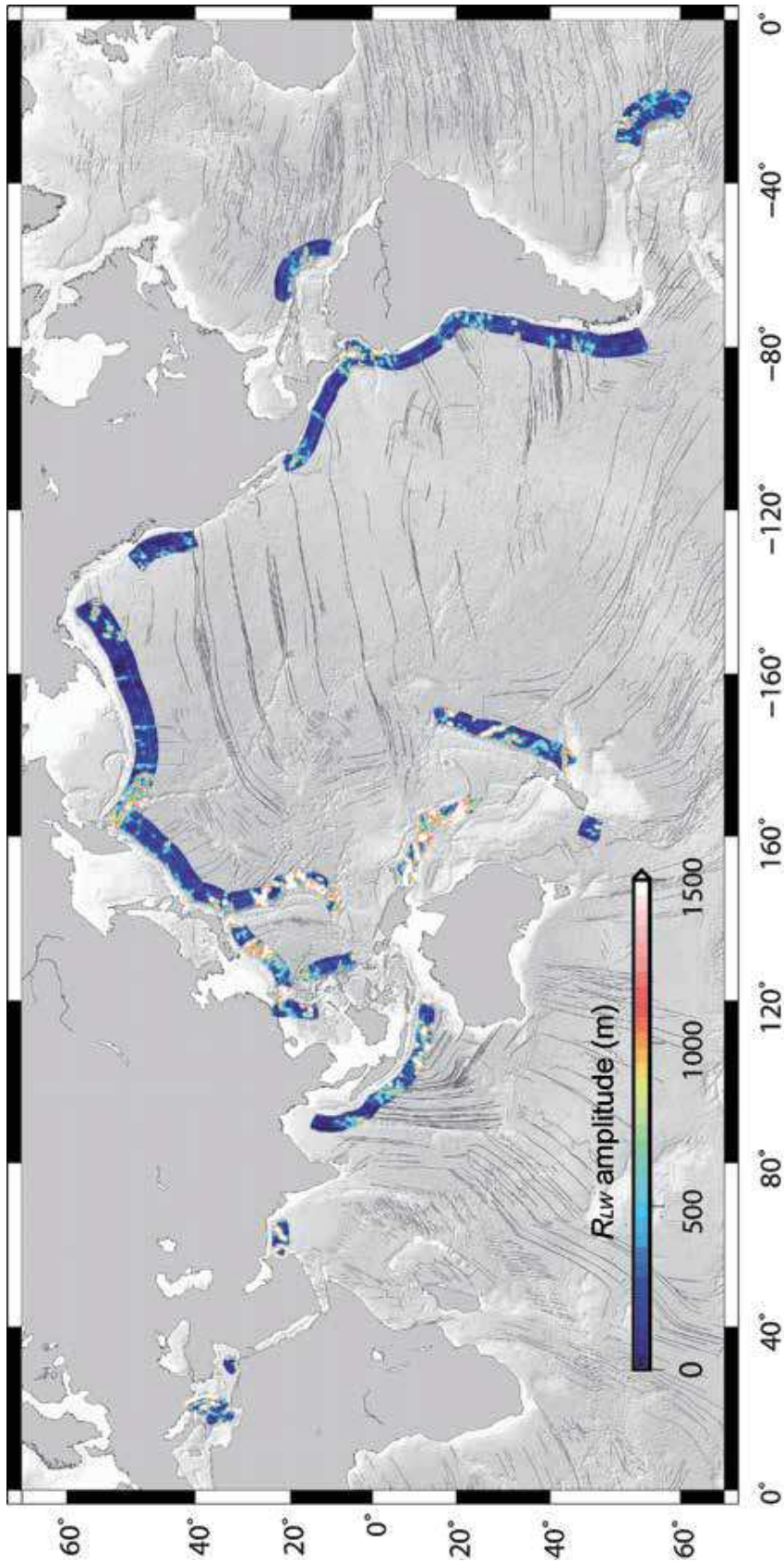


Figure A4.4. Global map of roughness R_{LW} estimated from the average of the PSD at long wavelengths between 80 and 100 km.

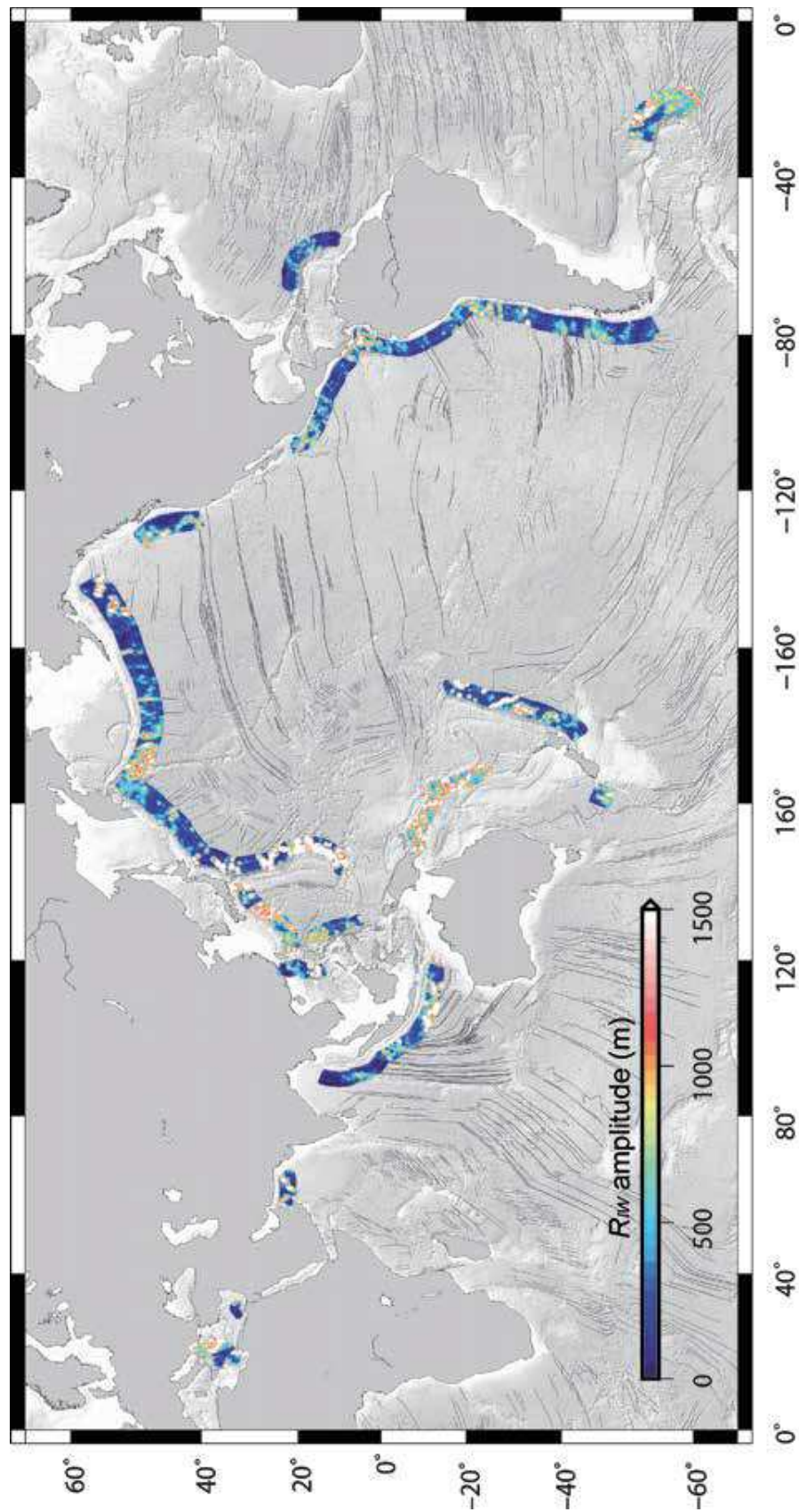


Figure A3.5. Global map of roughness R_W estimated from the fractal model over the PSD graph between wavelengths 20 and 80 km.

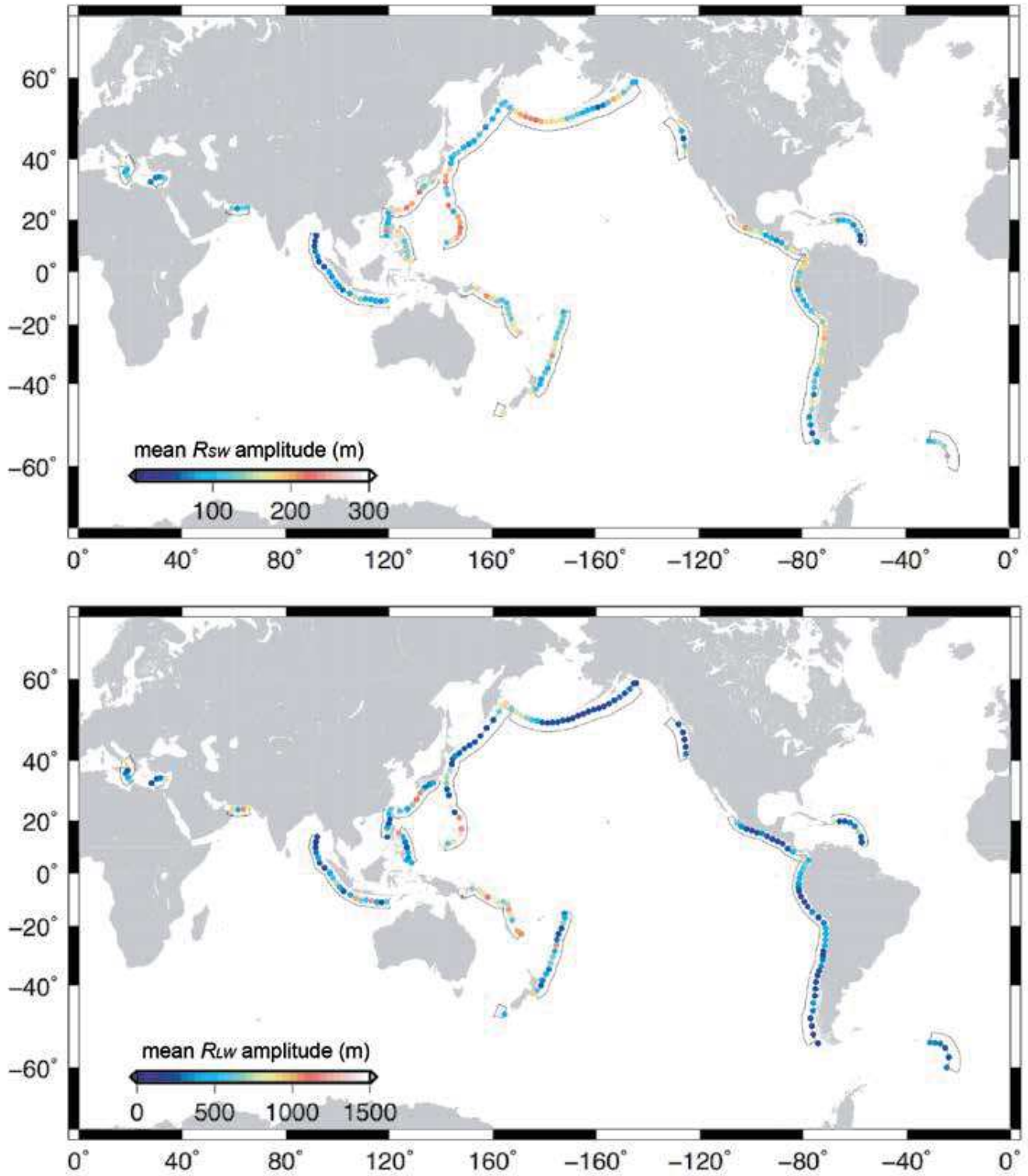


Figure A3.6. For both roughness databases (short and long wavelengths, top and bottom respectively), a mean spatial value is computed over a 200 km wide square facing each node from the Heuret et al.'s SubMap database (2011).

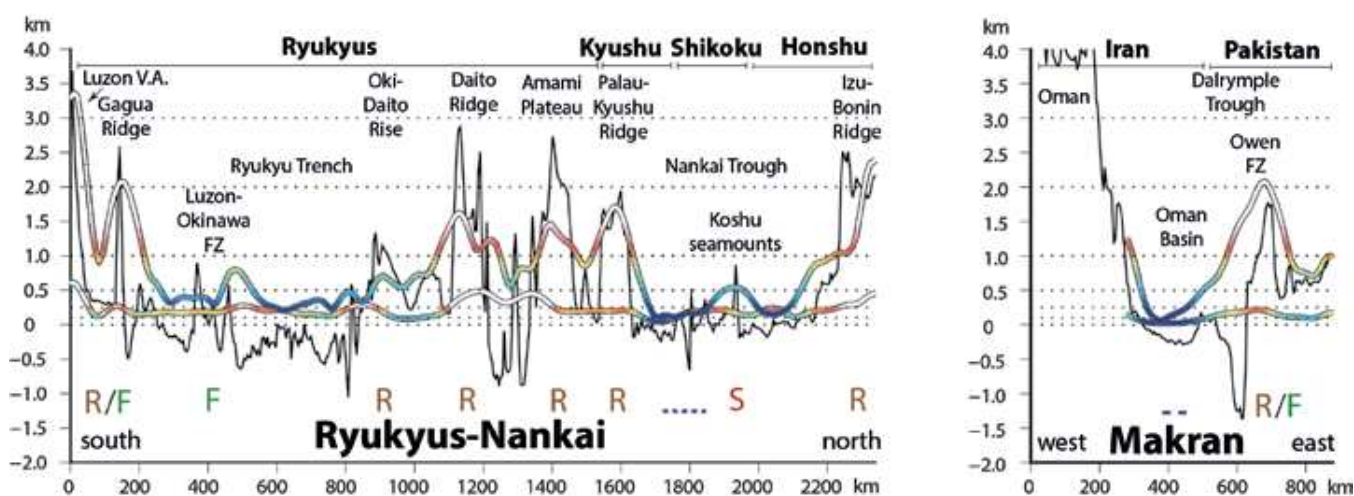
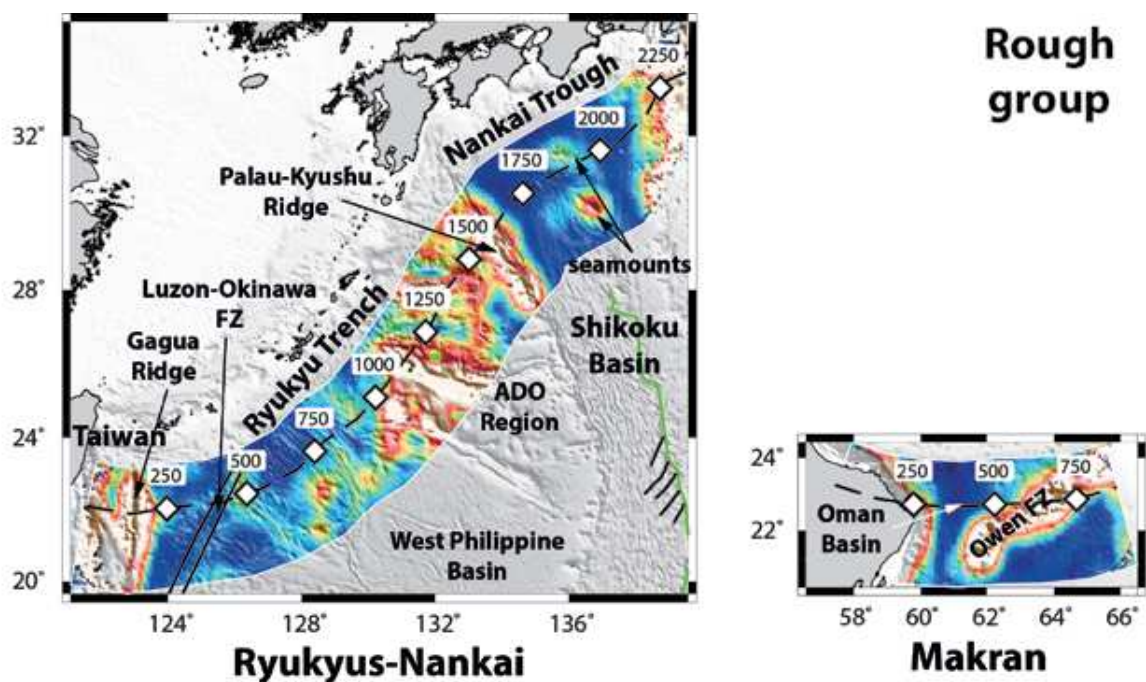


Figure A3.7. R_{LW} maps of two subduction zones: Ryukyu-Nankai and Makran, classified as dominantly rough and plotted at the same scale. Along-strike profiles, plotted as a black dashed line on map views, show the relative bathymetry (black line), acquired at a distance of 135 km seaward of the trench (see Figure 3.2), and associated R_{SW} and R_{LW} . Diamonds are plotted every 250 km in order to facilitate the comparison with the main features on the profiles. Horizontal tiny dotted lines are rules at 0, 100, 250, 500, 1000, 2000 and 3000 m. S indicates the location of major seamounts or seamount chains or seamount massifs. R indicates the location of major aseismic or active ridges. F indicates the location of major fracture zones. Continuous dark blue lines below the profiles indicates the very smooth regions characterized by R_{SW} and $R_{LW} < 100$ m. The dotted dark blue lines outline areas with moderately smooth seafloor, e.g., R_{SW} and $R_{LW} < 250$ m.

Mixed group

Tonga-Kermadec

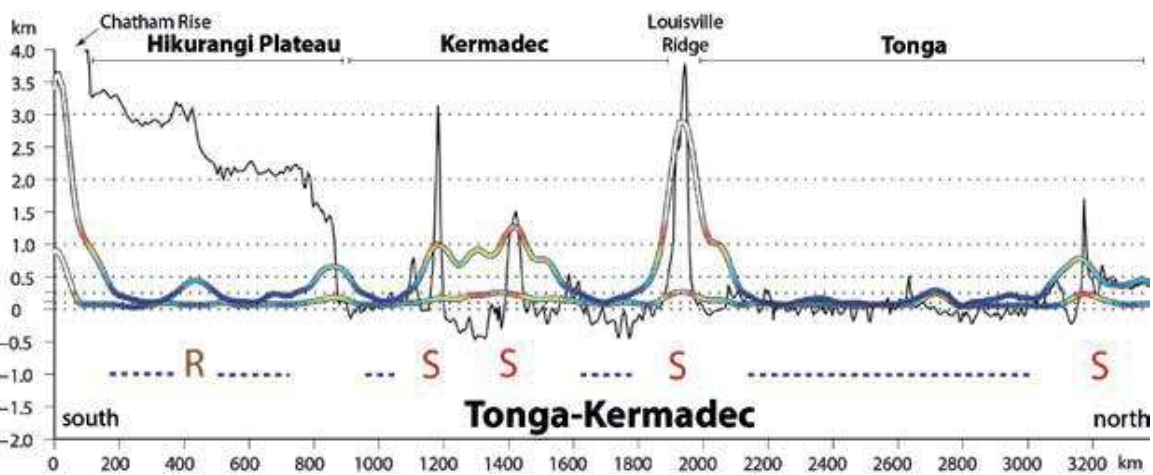
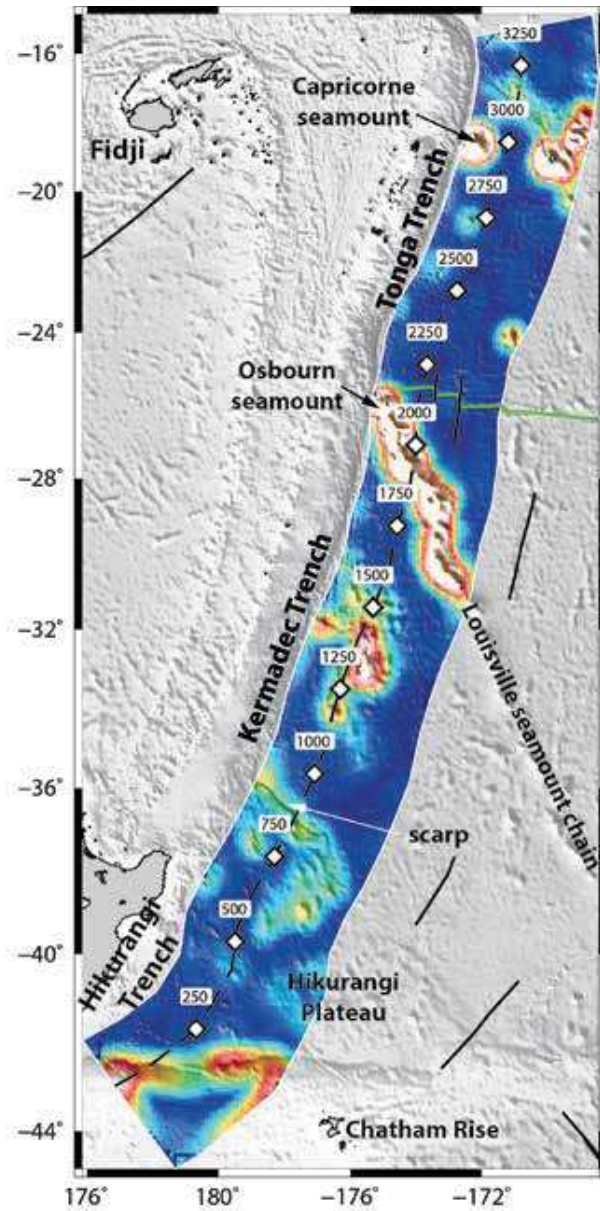


Figure A3.8. R_{LW} map and along-strike profiles of the Tonga-Kermadec subduction zones which belongs to the mixed group. See figure caption of Figure A3.7 for details.

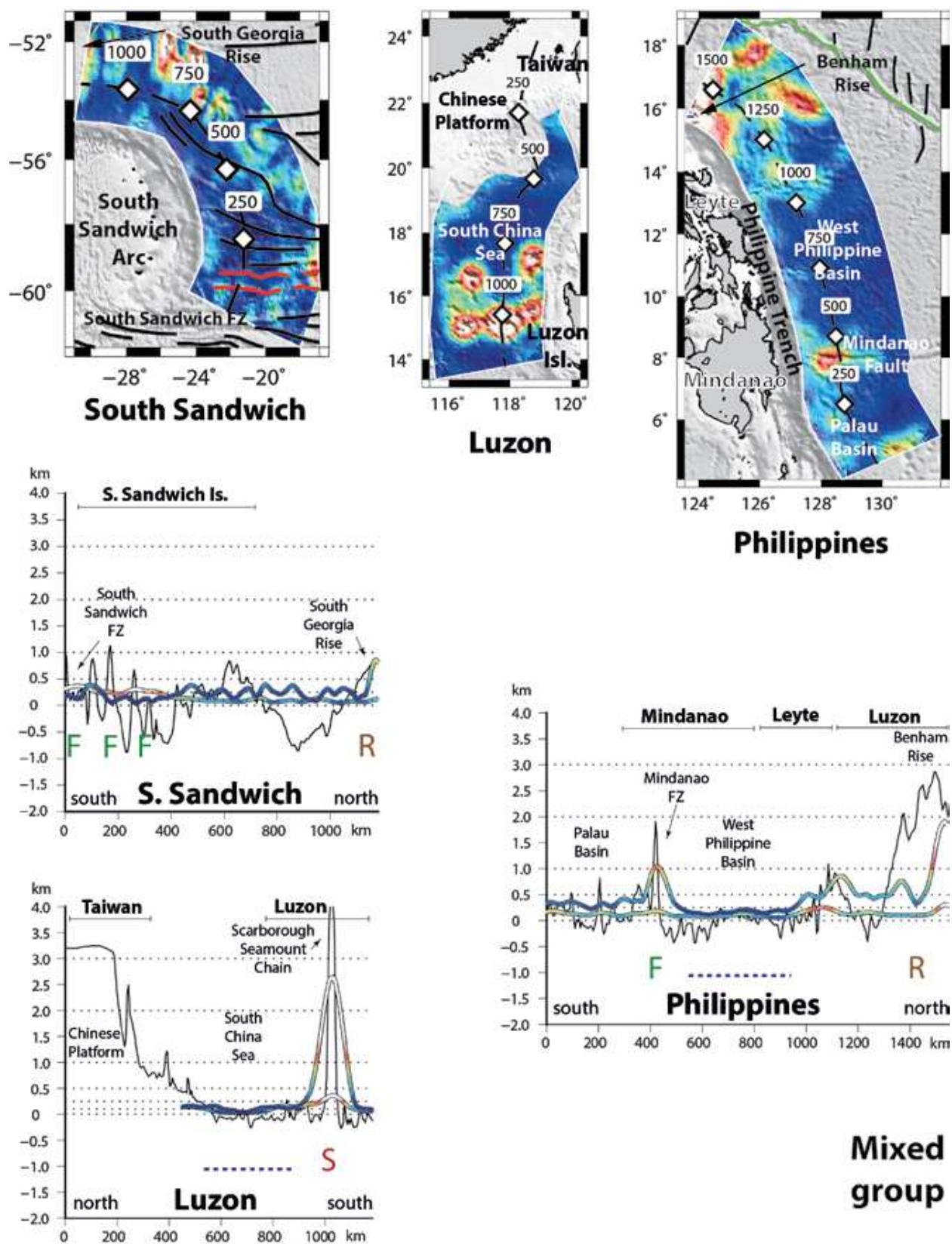


Figure A3.9. R_{LW} maps and along-strike profiles of the South Sandwich, Luzon and Philippines subduction zones which belong to the mixed group. See figure caption of Figure A3.7 for details.

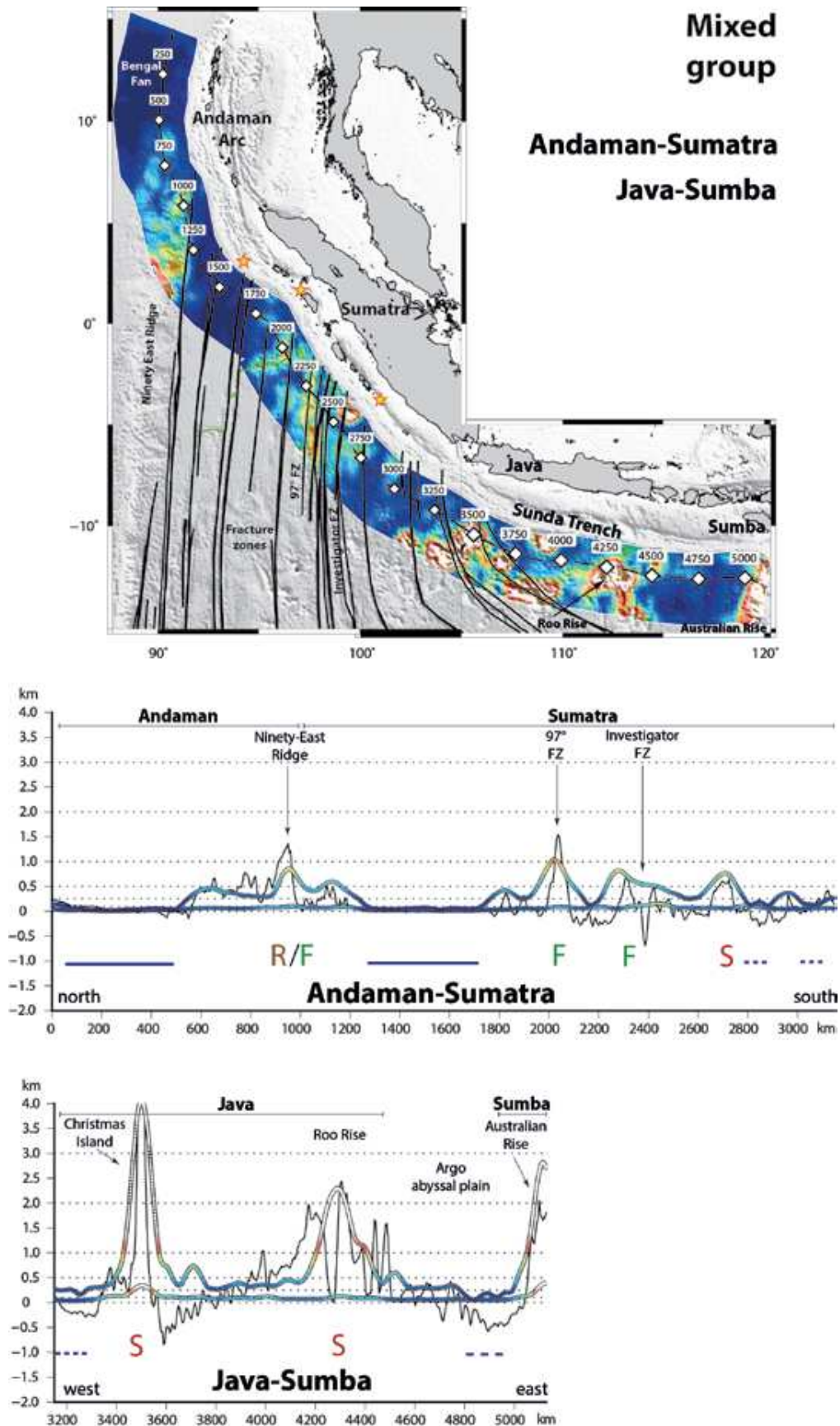


Figure A3.10. R_{LW} maps and along-strike profiles of the Andaman-Sumatra-Java-Sumba subduction zones which belong to the mixed group. See figure caption of Figure A3.7 for details.

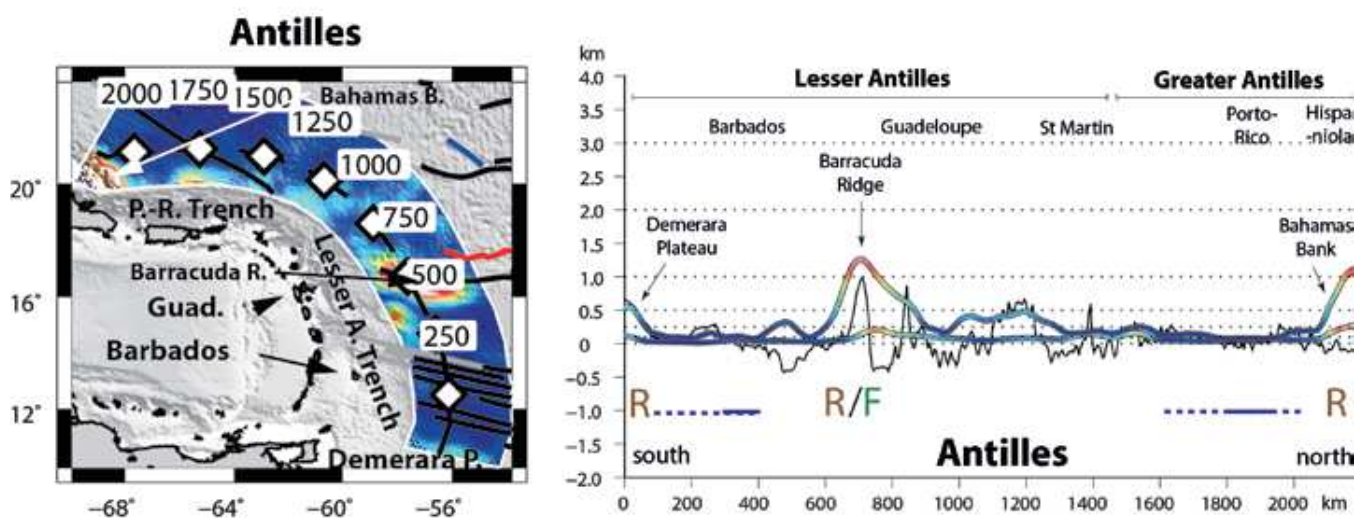
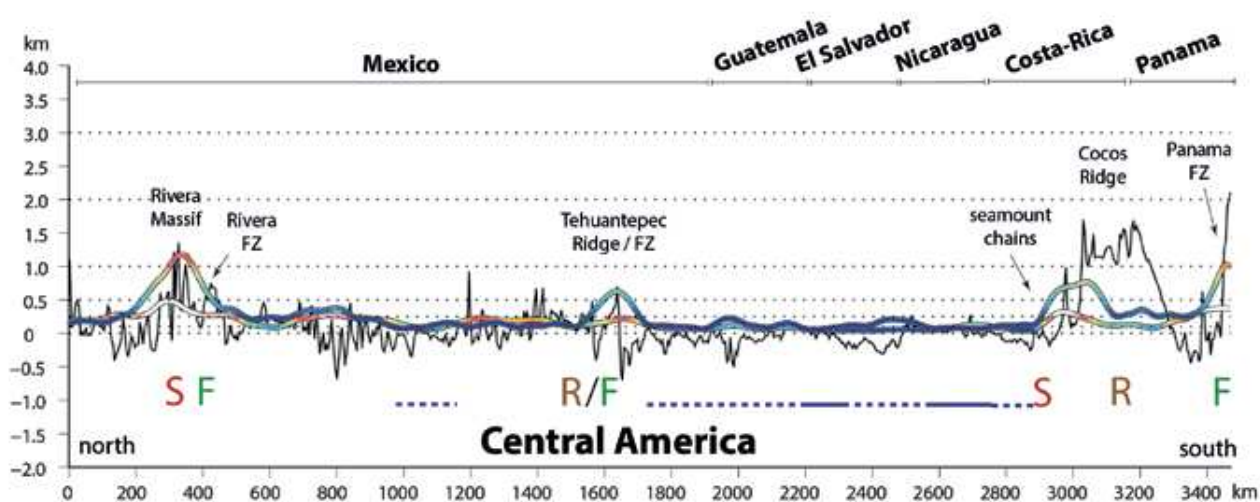
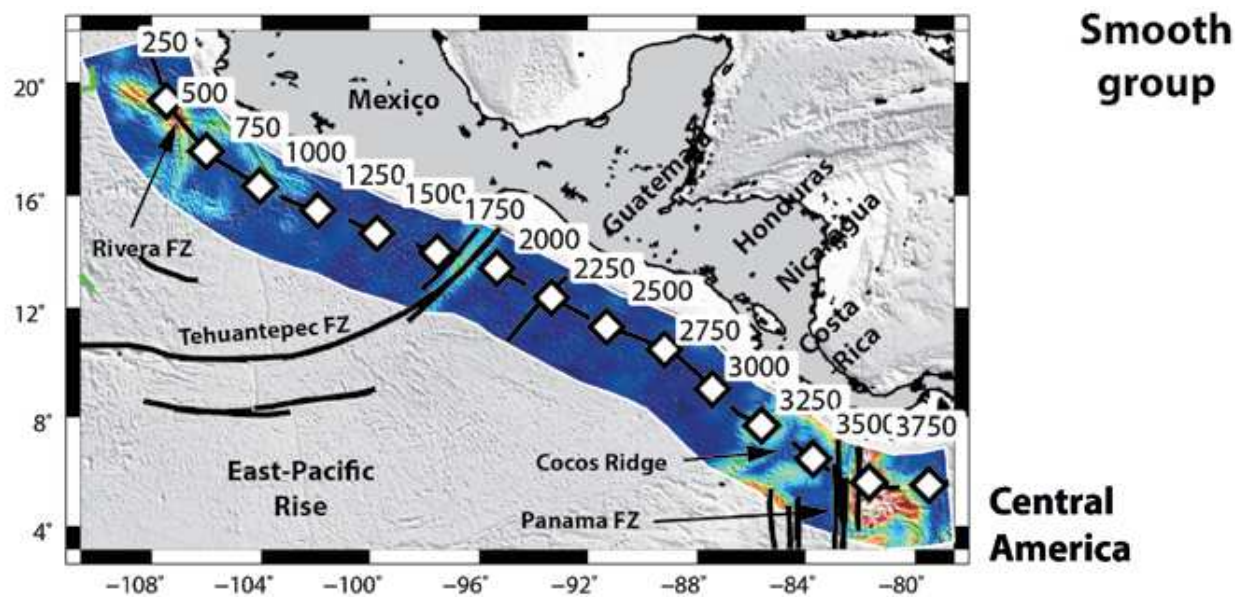


Figure A3.11. R_{LW} maps and along-strike profiles of the Central America and Antilles subduction zones which belong to the mixed group. See figure caption of Figure A3.7 for details.

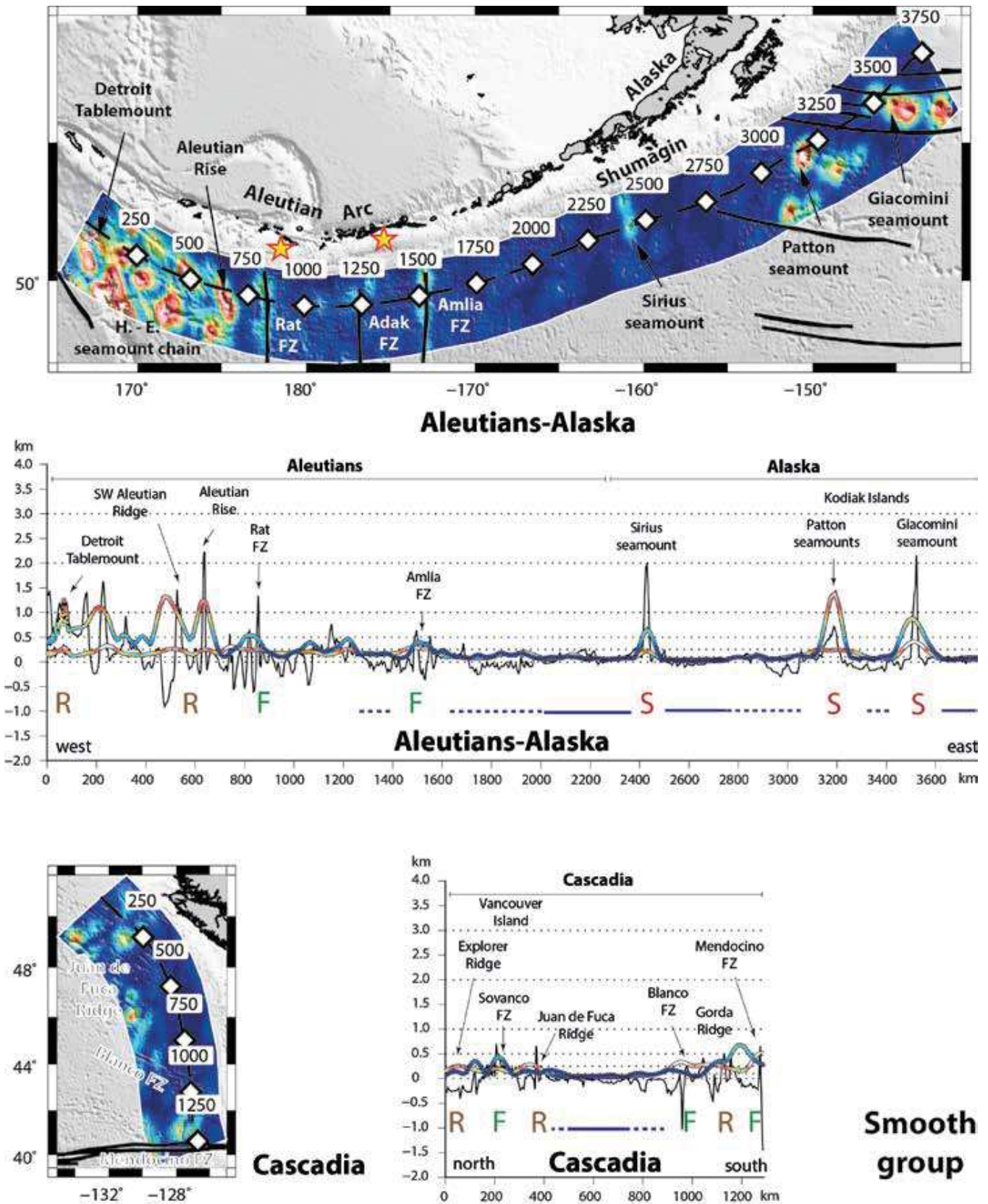


Figure A3.12. R_{LW} maps and along-strike profiles of the Aleutians-Alaska and Cascadia subduction zones which belong to the smooth group. See figure caption of Figure A3.7 for details.

Appendix Chapter 4 (A4)

Introduction

The supporting information contains additional information on the methodology of the study, and some additional analyses for the SubQuake database. It also provides maps and density plots for all subduction zones presented in the manuscript. For the methodology, the compilation of the SubQuake grid (text A4.1) and the correlation algorithms used (text A4.2 and A4.3) are described in more detail. Figures A4.1 to A4.15 show the SubQuake grid for each region, as well as the short- and long wavelength roughness seaward of the trench. Figure A4.16 shows the density plots for all regions that have not been discussed in the main text. Figure A4.17 accompanies text A4.3 by illustrating the obtained result when only taking into account category 1 earthquakes for the global correlation.

Text A4.1. Additional information on the compilation of the SubQuake grid

Since the SubQuake grid represents the surface projection of the seismogenic zone, the horizontal distances between the trench and the updip- and downdip limits of the seismogenic zone (U_x and D_x , respectively; Heuret et al., 2011), are used to constrain the trench-perpendicular extent of the grid. However, after reviewing the extent of the SubQuake ruptures, we decided to set U_x to 0, meaning that our grid always starts at the trench. We observed that large ruptures often extend all the way or very close to the trench, demonstrated very well by the Tohoku rupture, for which even the largest amount of slip occurred near the trench (Yue & Lay 2013; Sladen & Trevisan 2018).

Since the D_x information for all subduction zones is based on the locations of epicenters, the rupture contours sometimes exceed this downdip limit. In those cases, we manually adjusted D_x in order to include all rupture areas in our grid. Hence, by our definition, the seismogenic zone (represented by our SubQuake grid), defines not only the region along the subduction interface where ruptures nucleate, but also where they propagate. For some older ruptures, the relocated ISC-GEM epicenter did not correlate with the rupture contour. In those cases, we manually adjusted the rupture contour to include the location of the relocated epicenter.

Trench nodes separated by 1 degree from Heuret et al. (2011) are used as a basis for the SubQuake grid. In trench-parallel direction, interpolated grid nodes are separated by 0.1 degree, while in the trench-perpendicular direction, the dip of the seismogenic zone (i.e., Θ ; Heuret et al., 2011) is used to calculate the grid distance at the surface, assuming a 10 km distance between the nodes on the actual seismogenic zone. The grid therefore consists of trench-perpendicular lines for all interpolated trench nodes (i.e., separated by 0.1 degree), for which the length of those lines depends on the width of the seismogenic zone projection.

Text A4.2. Additional information on the correlation algorithms

A4.1.1 Subquake grid

Based on the three different types of segments, the SubRough data seaward of the trench, for both the short wavelength R_{SW} and the long wavelength R_{LW} , can be selected and evaluated. For this, we assume a trench-perpendicular continuation of the seafloor roughness, because in this way we use the seafloor closest to the segment of the seismogenic zone as a proxy, rather than choosing something which is further away. One could assume that seafloor right next to each other went through similar processes since their formation and therefore might be similar in terms of roughness. In some cases, we had information about a specific linear feature extending into the trench, so we used the azimuth of these features for roughness extrapolation into the seismogenic zone (i.e. for the Joban Seamount chain in Japan, the Louisville ridge in Tonga and the Murray Ridge in Makran). In the case of the Joban Seamount chain and the Murray Ridge, using an adjusted azimuth considerably improves the correlation, since then it becomes clear that the rupture most likely occurred on a smooth patch right next to the oblique relief. In those cases, a perpendicular correlation would have weakened our global correlation. This probably still happens in some areas, like for the seafloor in front of the 1906 Ecuador earthquake. Due to the Malpelo Ridge and the adjacent Yaquina Trough, the roughness amplitudes in this area are very high. Since these are not necessarily a features with a linear trend continuing into the trench, it is likely that they are not representative for the

roughness of the subduction interface.

A4.1.2. Epicenter correlation

All 182 epicenters have been correlated with R_{SW} and R_{LW} seaward of the trench. For each epicenter, the closest trench node has been selected based on a spherical approximation with great circles (Global Mapping Tools, Wessel et al. 2013). For these trench nodes, roughness data perpendicular to the trench are selected within a strip of 50 km wide and 250 km long (i.e., the complete width of the roughness bands). A smaller area closer to the trench (e.g., limited to a length of 100 km) might show more similarity to the actual roughness of the subduction interface, but due to the small sampling area more disparities could arise. Such roughness sampling might only reflect a very local feature, rather than a representative value that can be extrapolated into the subduction interface. The latter may also hold for a strip with the chosen length of 250 km, so results from such a correlation should be handled with care. Also the width of the roughness strip selected for each epicenter (now chosen to be 50 km), can influence the roughness signal. By choosing a width of 50 km, we aim to find a balance between taking into account possible uncertainty in the epicenter location, and not averaging out the roughness signal too much.

A4.1.3. Synthetic tests for epicenter correlation

To test the robustness of the epicenter correlation algorithm, 100 synthetic sets of 182 (randomly selected) trench nodes have been correlated with the roughness as well. This means that, besides the original epicenter dataset containing 182 events, 100 synthetic datasets have been created. Each of these 100 datasets contains 182 'fake epicenters', for which roughness data is selected in the same manner as for the original epicenter dataset. Since for the epicenter correlation, the closest trench nodes are used for the selection of the roughness data, the 100 synthetic datasets each contain 182 randomly selected trench nodes, rather than

randomly selected grid nodes that should depict the synthetic epicenters. Each grey line in figure 12a and b represents one synthetic dataset, showing the distribution of roughness data selected for the 182 random trench nodes.

In this way, we test the deviation that arises from simply selecting a subset of the total dataset 100 times. If the roughness distribution related to the epicenters shows similar deviations as the distributions that arise from the 100 synthetic tests, we can conclude that a possible deviation is mainly related to the limited size of the dataset sample and not to a physical phenomenon.

Text A4.3. Global correlation with Category 1 only events

The global correlation between the rupture occurrence and the seafloor roughness has also been done for the 45 category 1 ruptures only (i.e., younger than 1990), since the location of these rupture areas is assumed to be more robust than for older ruptures in the SubQuake database. As for the correlations discussed in the previous section, the selection of the no-rupture areas has not changed, meaning that previous rupture segments based on category 2-4 ruptures are now completely excluded from the analysis (and not converted into no-rupture areas). The correlation has been done for R_{LW} only, since the short wavelength roughness does not seem to correlate with the occurrence of megathrust ruptures on a global scale. Figure A4.15 shows the results from this category 1 rupture correlation, taking into account the different M_w classes. We observe a higher density at low roughness amplitudes for the category 1 $M_w > 8.5$ rupture segments, as observed in section 4.3.2.3. (by including events from all categories). Looking at the two other magnitude classes, they show a very different roughness distribution. They appear to have higher roughness amplitudes than the no-rupture segments. Since for this category 1 correlation, a smaller number of ruptures has been used, it is more difficult to statistically compare the rupture and no-rupture groups.

Japan - Kuril - Kamchatka

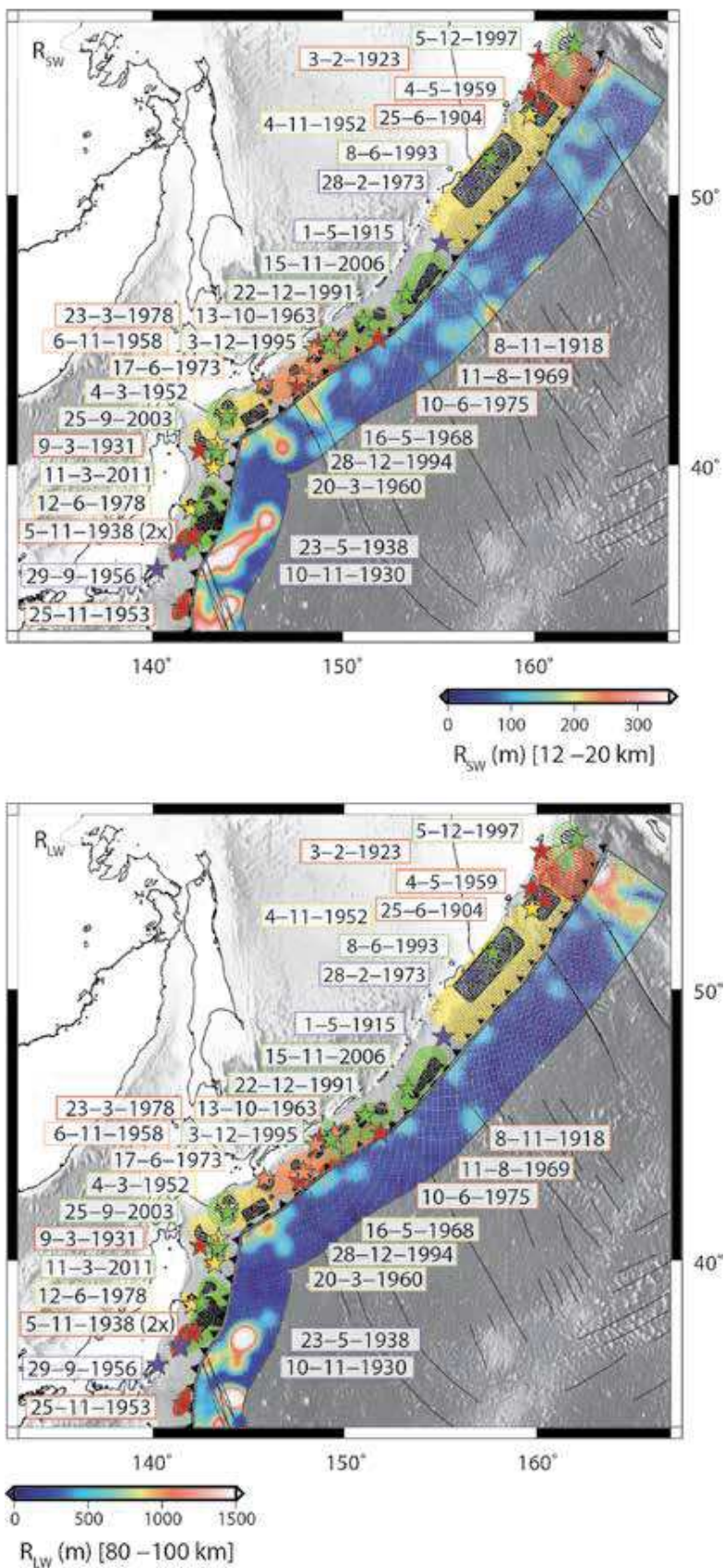


Figure A4.1. Japan-Kuril-Kamchatka. Short wavelength (R_{SW}) and long wavelength (R_{LW}) roughness data seaward of the trench and the SubQuake ruptures landward of the trench, color-coded according to the categories introduced in Figure 4.2.

Andes

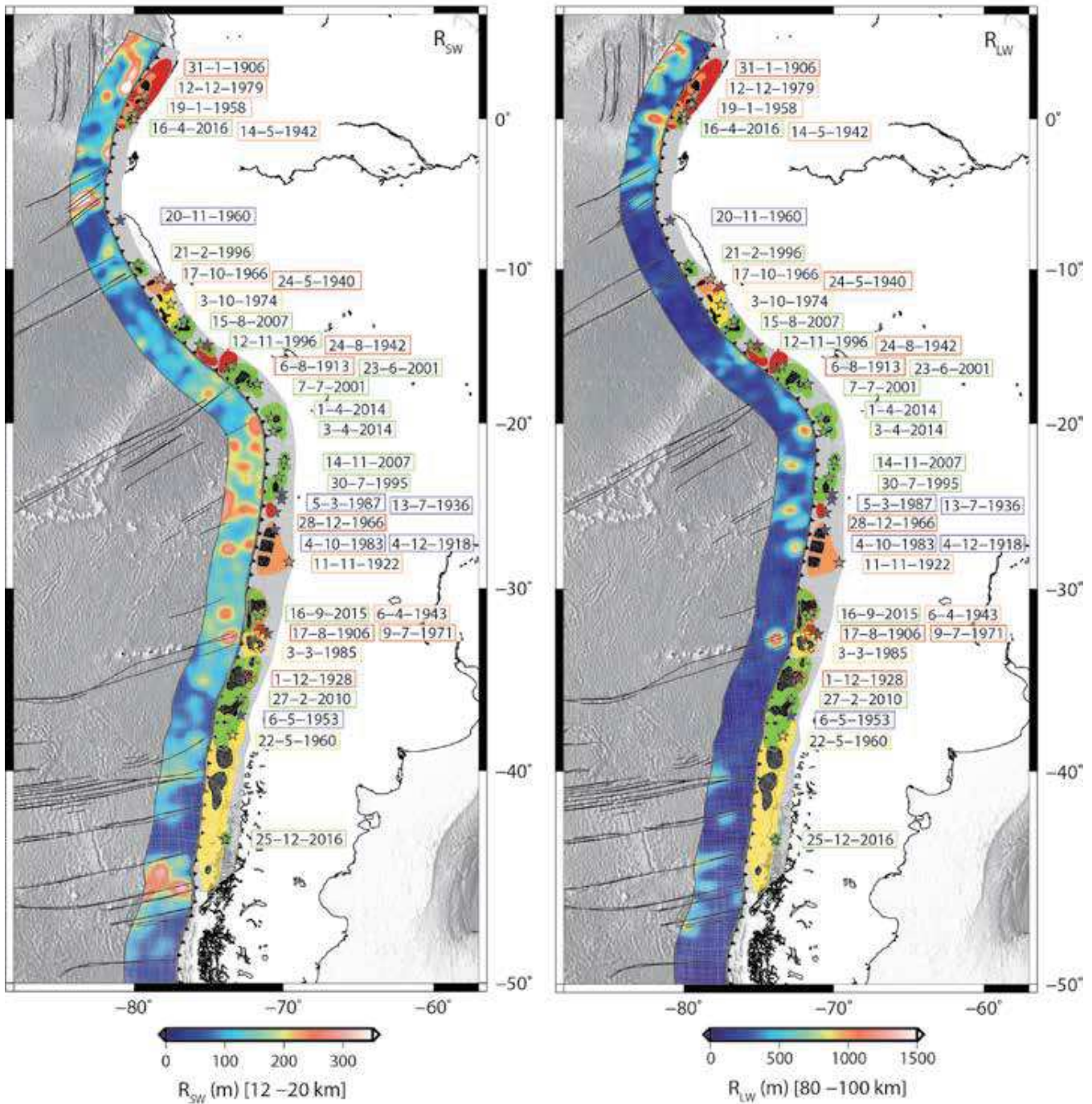


Figure A4.2. Andes. Short wavelength (R_{SW}) and long wavelength (R_{LW}) roughness data seaward of the trench and the SubQuake ruptures landward of the trench, color-coded according to the categories introduced in Figure 4.2.

Alaska-Aleutian

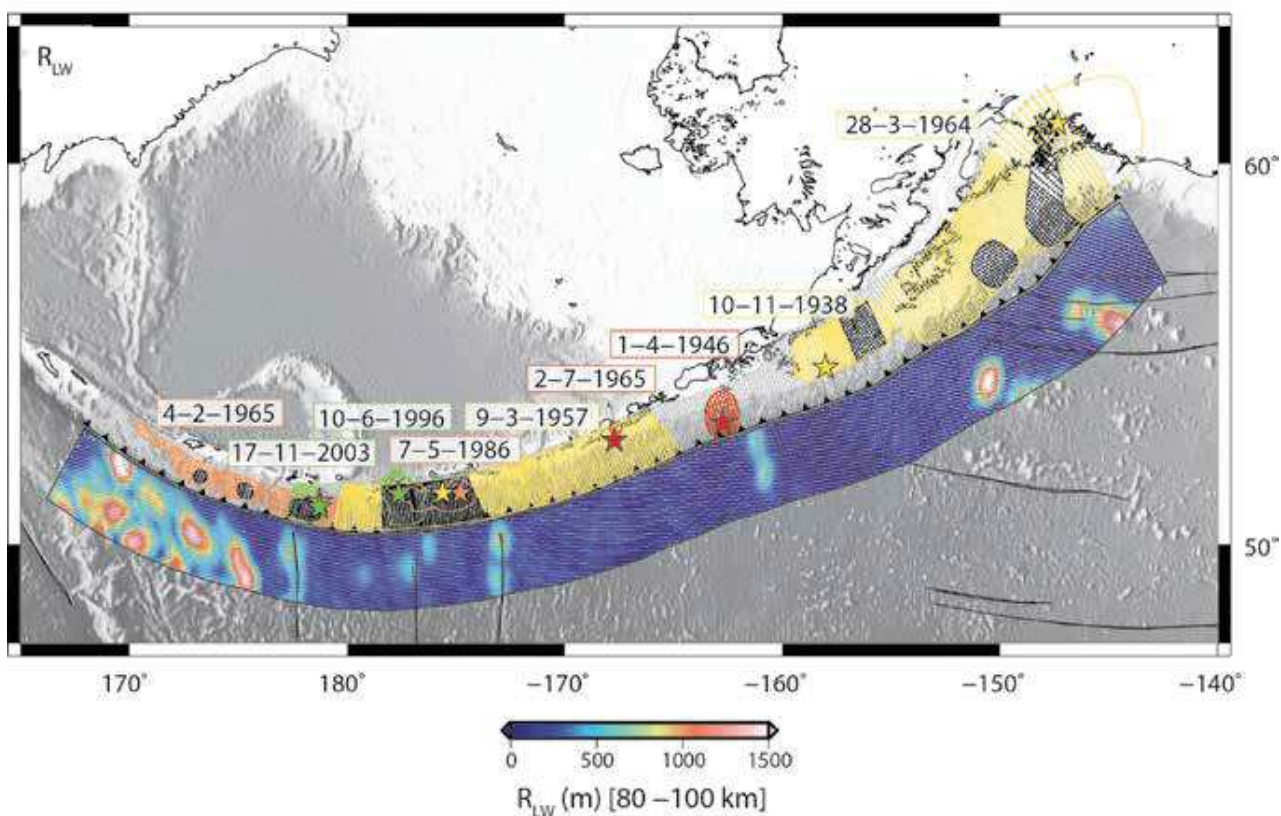
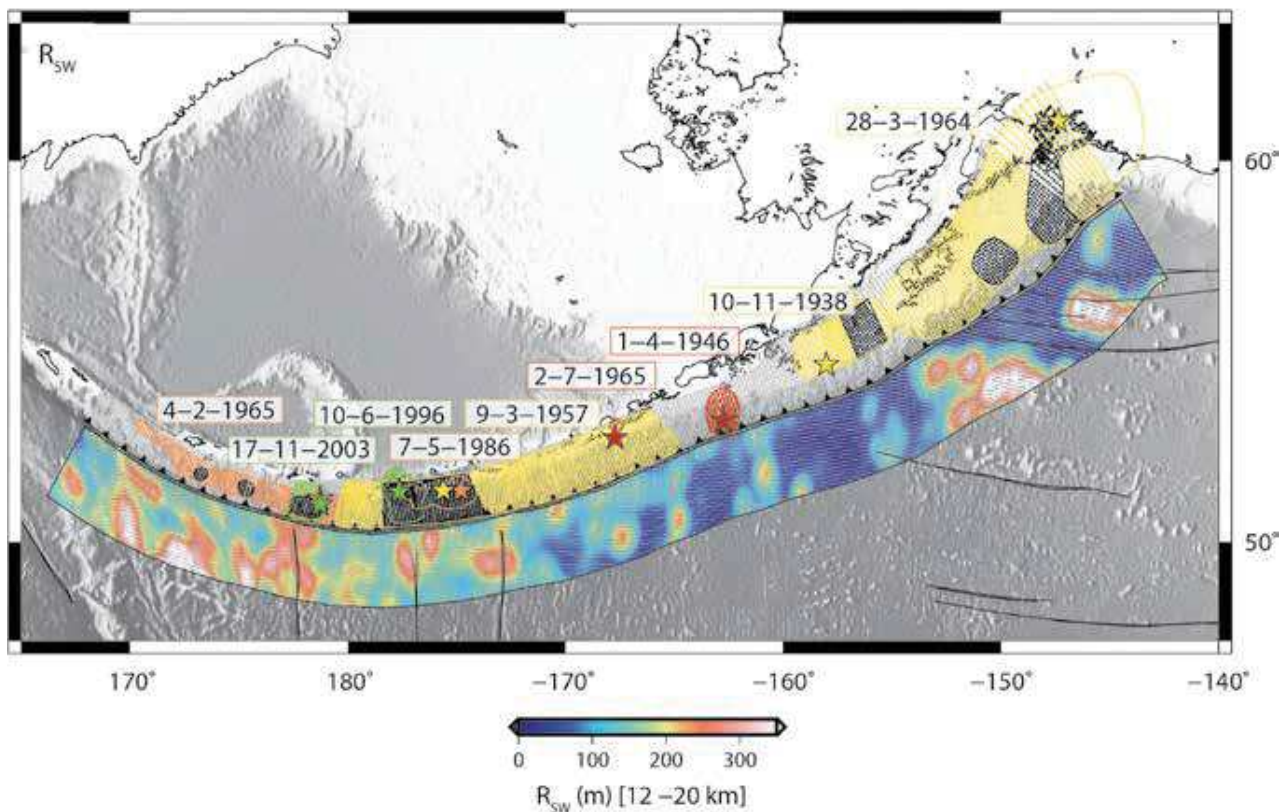


Figure A4.3. Alaska-Aleutian. Short wavelength (R_{SW}) and long wavelength (R_{LW}) roughness data seaward of the trench and the SubQuake ruptures landward of the trench, color-coded according to the categories introduced in Figure 4.2.

Sumatra-Java

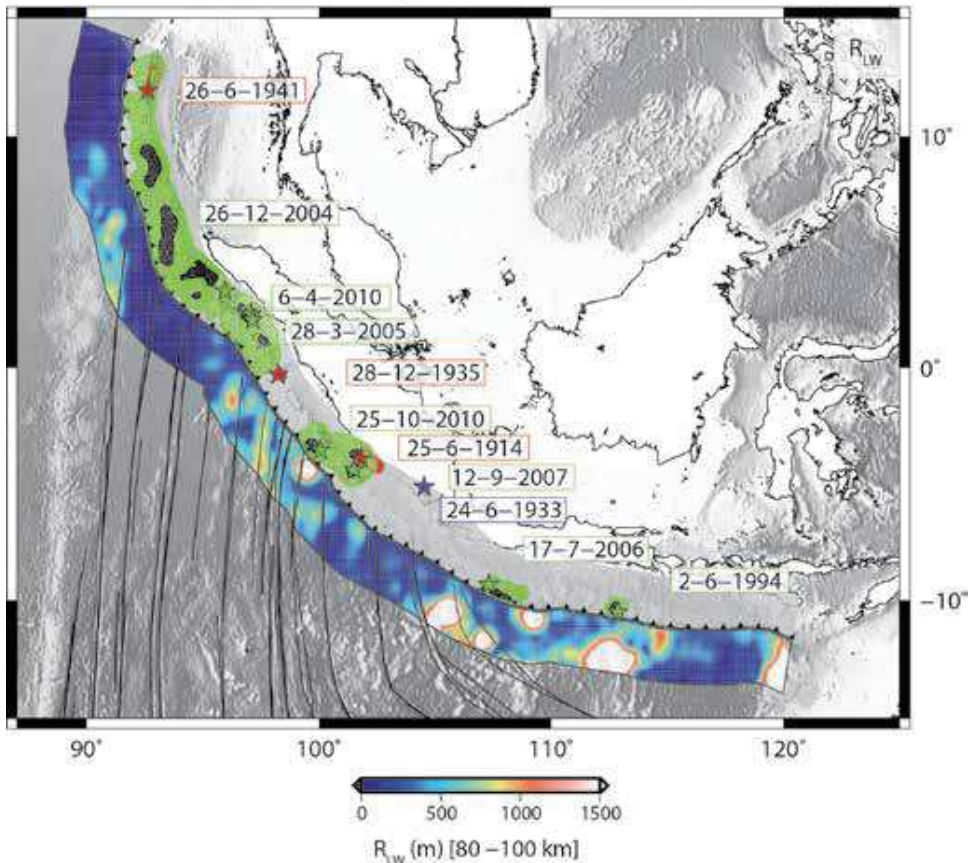
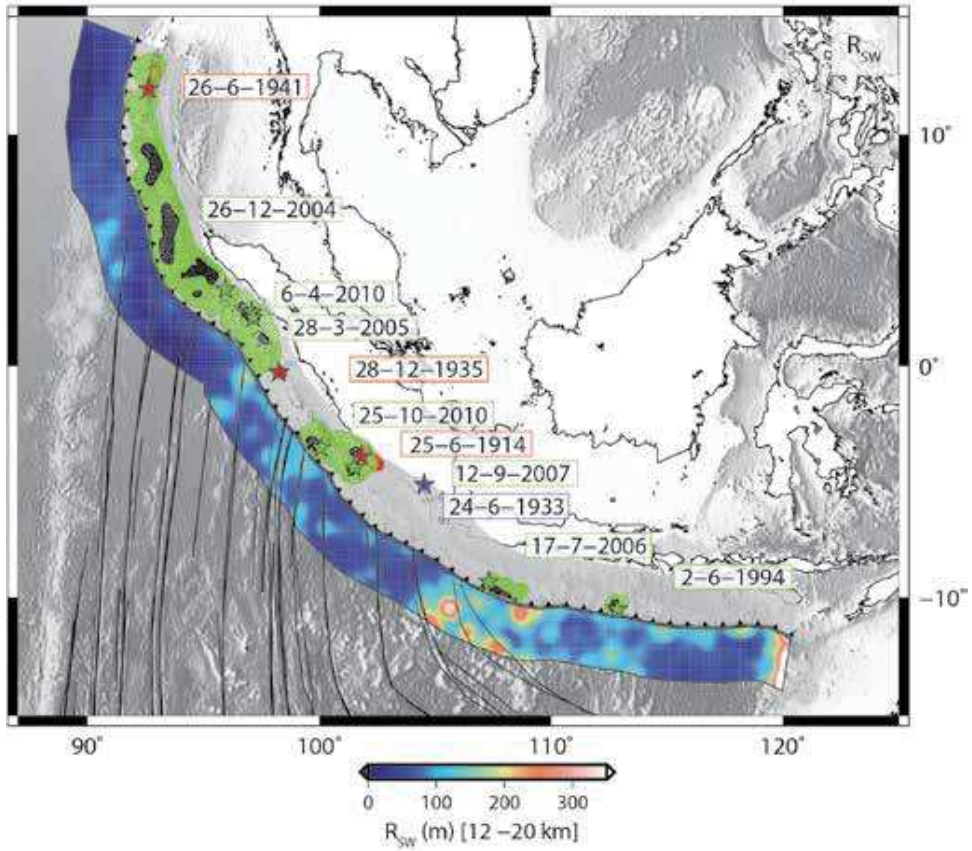
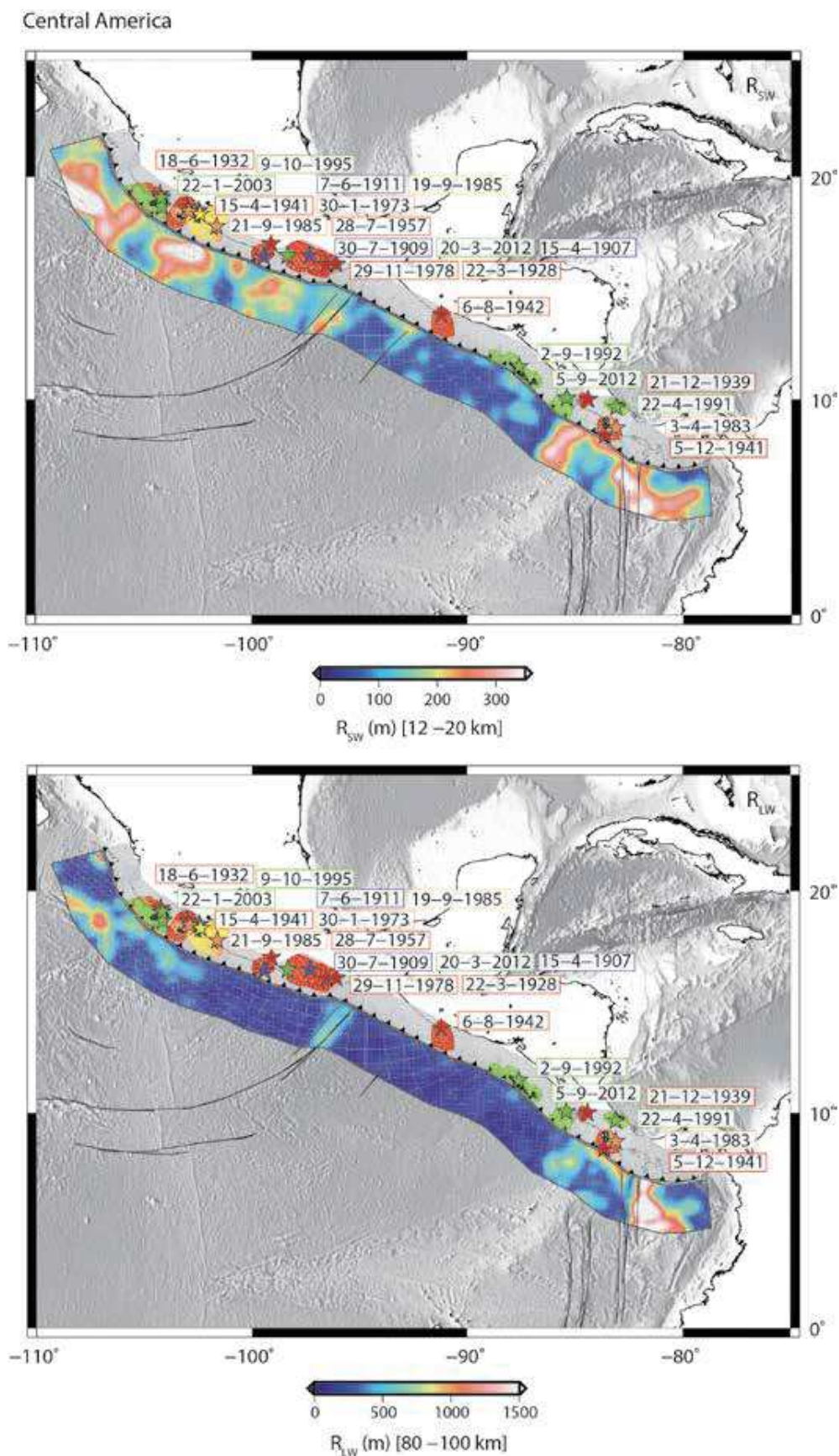


Figure A4.4. Sumatra-Java. Short wavelength (R_{SW}) and long wavelength (R_{LW}) roughness data seaward of the trench and the SubQuake ruptures landward of the trench, color-coded according to the categories introduced in Figure 4.2.



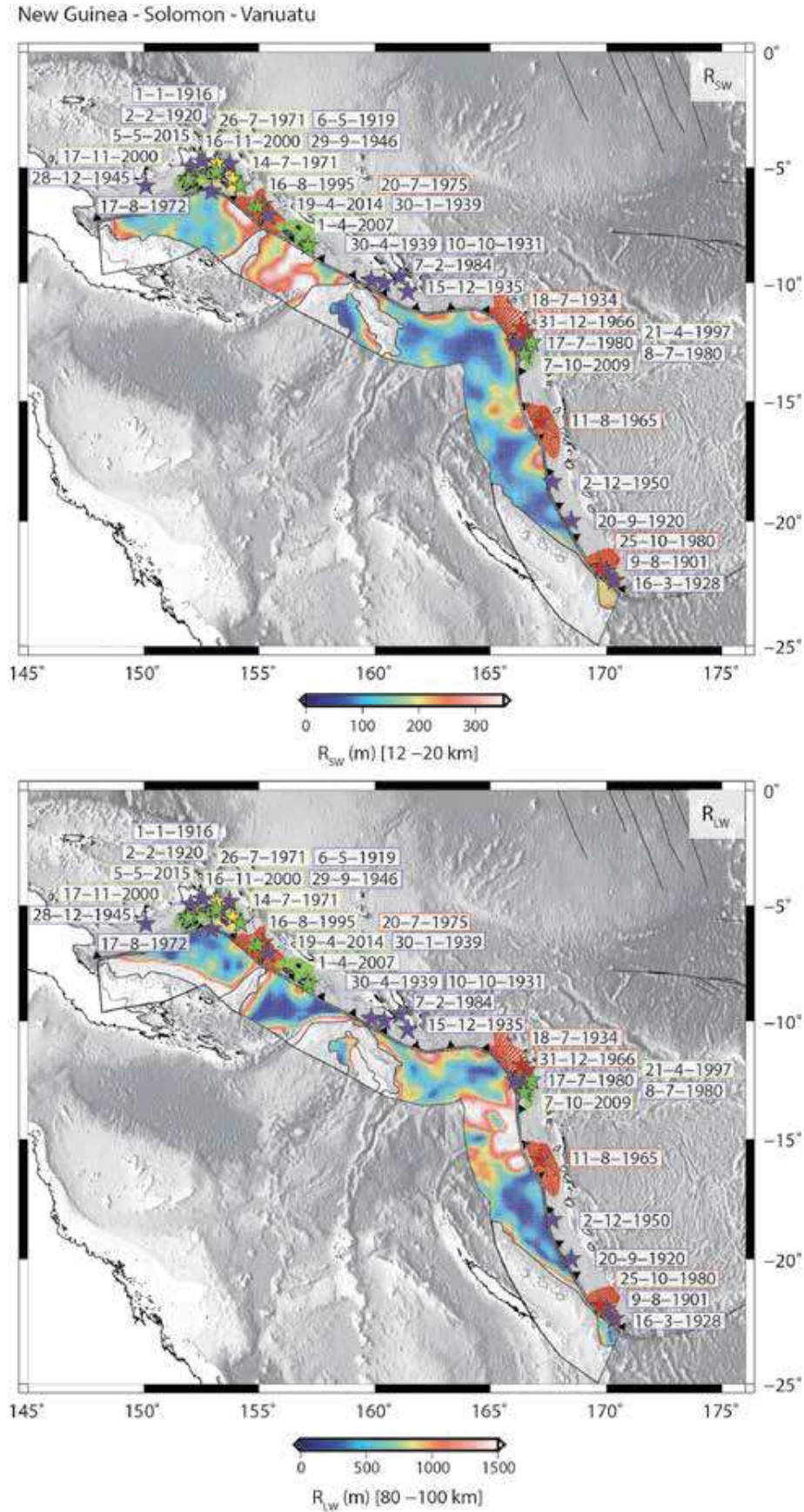


Figure A4.6. New Guinea - Solomon - Vanuatu. Short wavelength (R_{sw}) and long wavelength (R_{lw}) roughness data seaward of the trench and the SubQuake ruptures landward of the trench, color-coded according to the categories introduced in Figure 4.2.

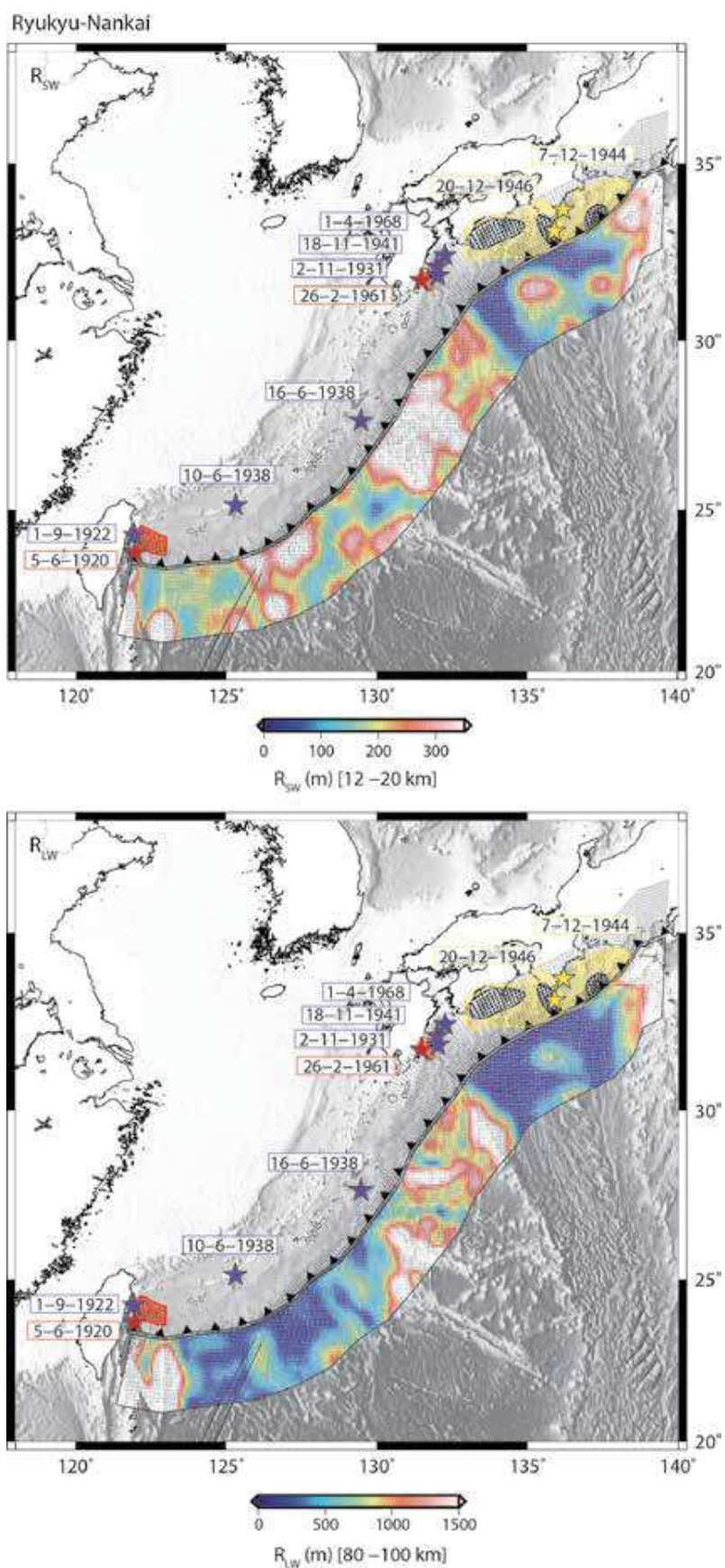


Figure A4.7. Ryukyu-Nankai. Short wavelength (R_{SW}) and long wavelength (R_{LW}) roughness data seaward of the trench and the SubQuake ruptures landward of the trench, color-coded according to the categories introduced in Figure 4.2.

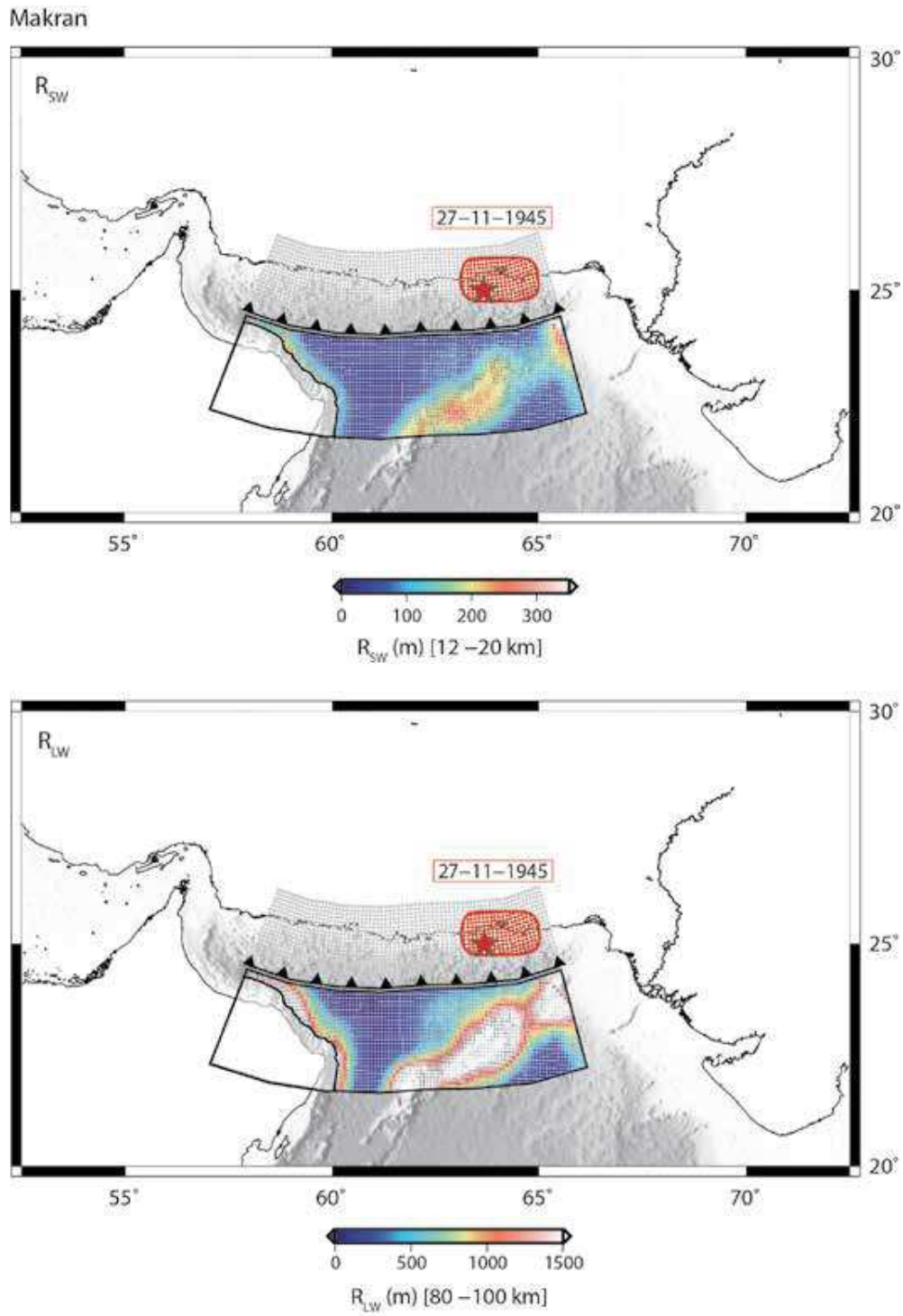


Figure A4.8. Makran. Short wavelength (R_{SW}) and long wavelength (R_{LW}) roughness data seaward of the trench and the SubQuake ruptures landward of the trench, color-coded according to the categories introduced in Figure 4.2.

Tonga - Kermadec

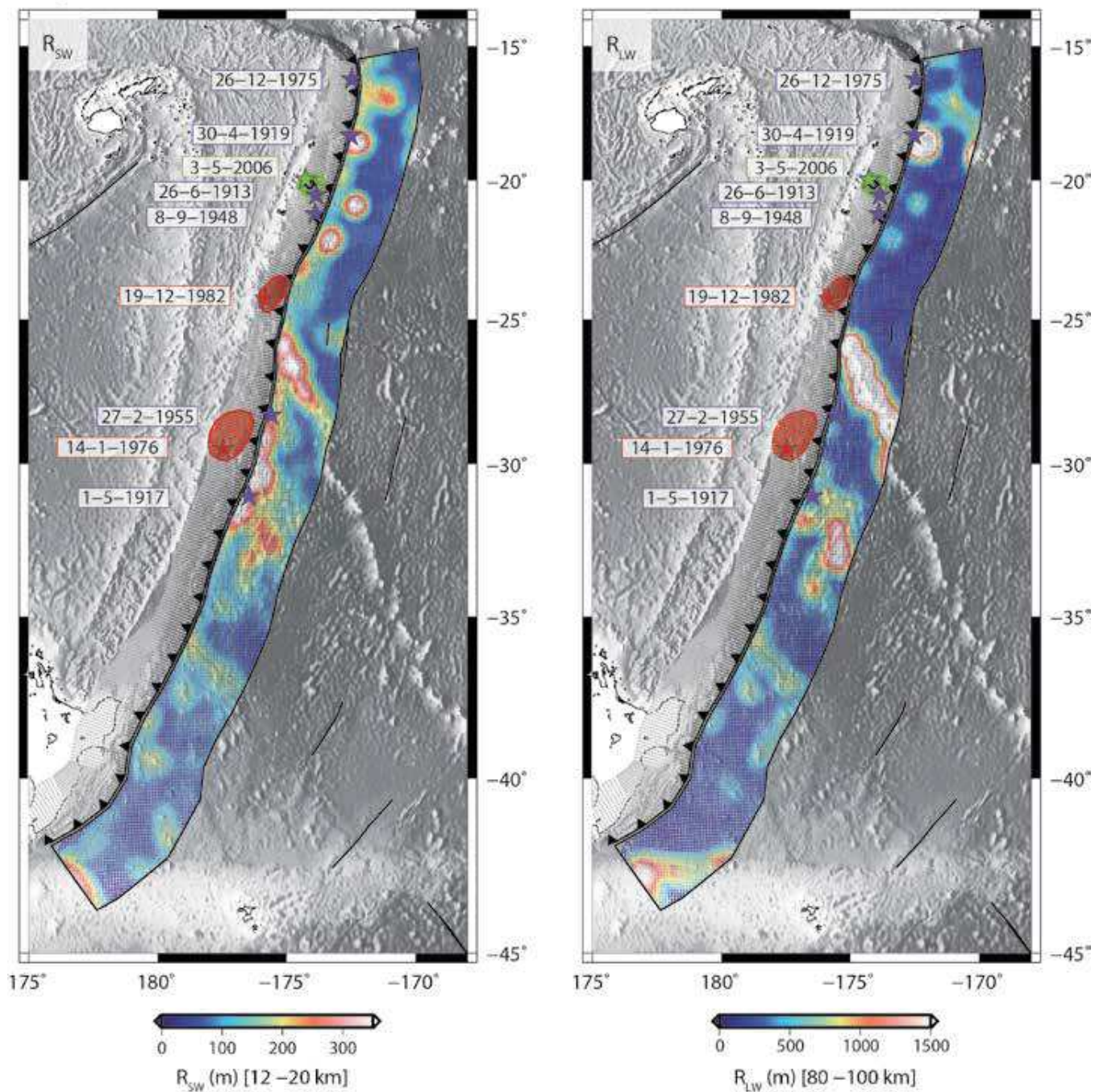


Figure A4.9. Tonga-Kermadec. Short wavelength (R_{SW}) and long wavelength (R_{LW}) roughness data seaward of the trench and the SubQuake ruptures landward of the trench, color-coded according to the categories introduced in Figure 4.2.

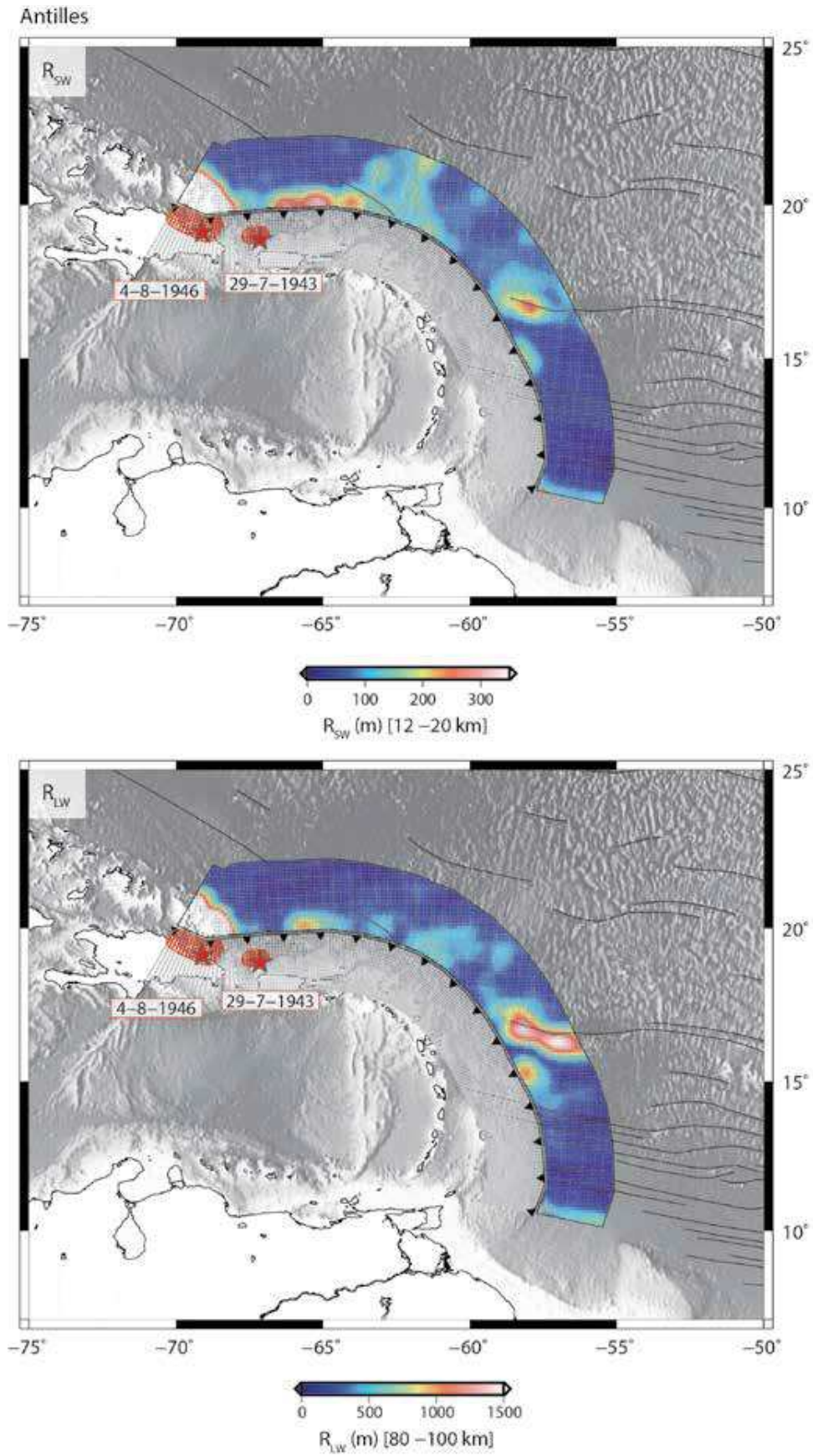


Figure A4.10. Antilles. Short wavelength (R_{SW}) and long wavelength (R_{LW}) roughness data seaward of the trench and the SubQuake ruptures landward of the trench, color-coded according to the categories introduced in Figure 4.2.

Philippines

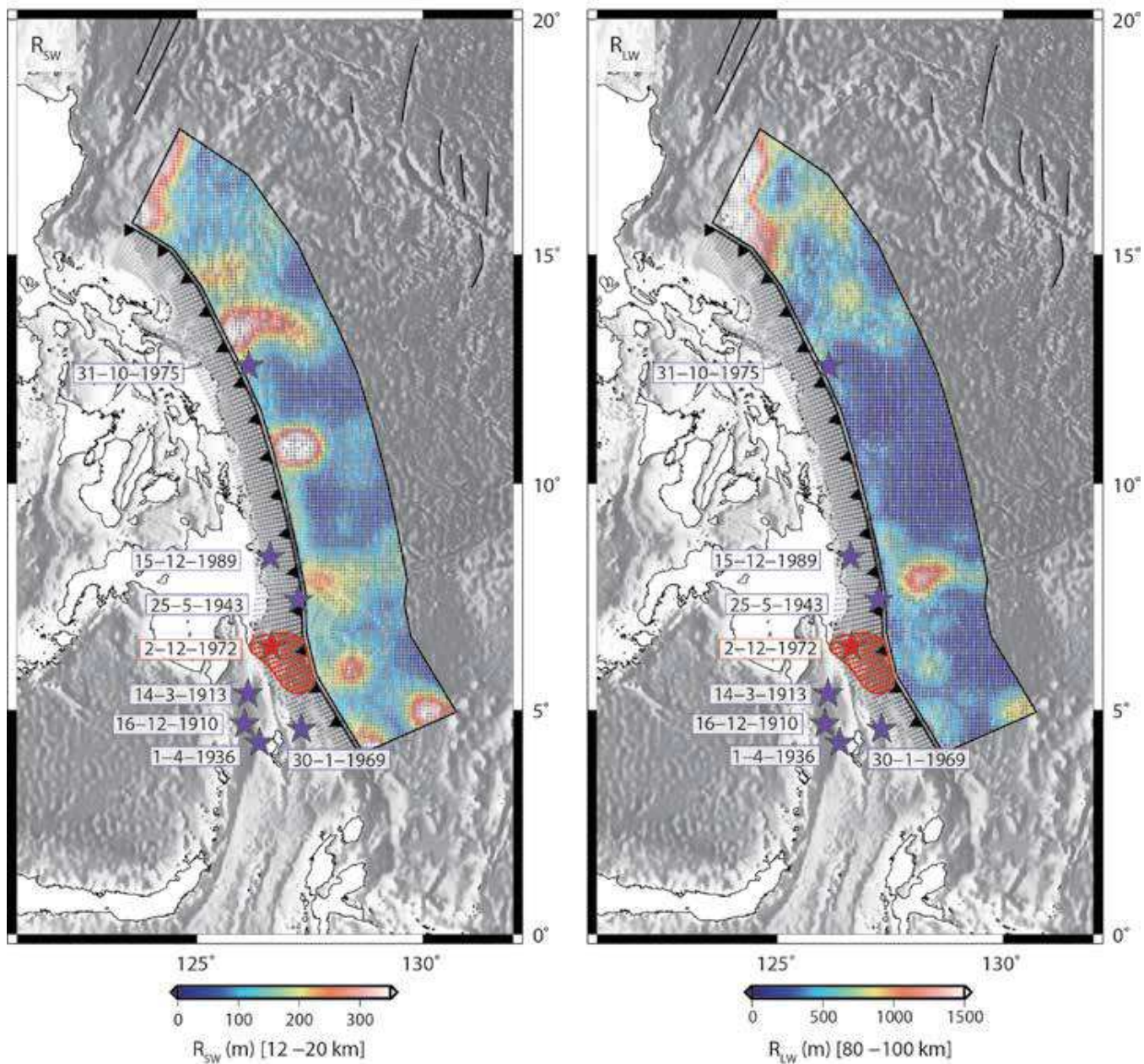


Figure A4.11. Philippines. Short wavelength (R_{SW}) and long wavelength (R_{LW}) roughness data seaward of the trench and the SubQuake ruptures landward of the trench, color-coded according to the categories introduced in Figure 4.2.

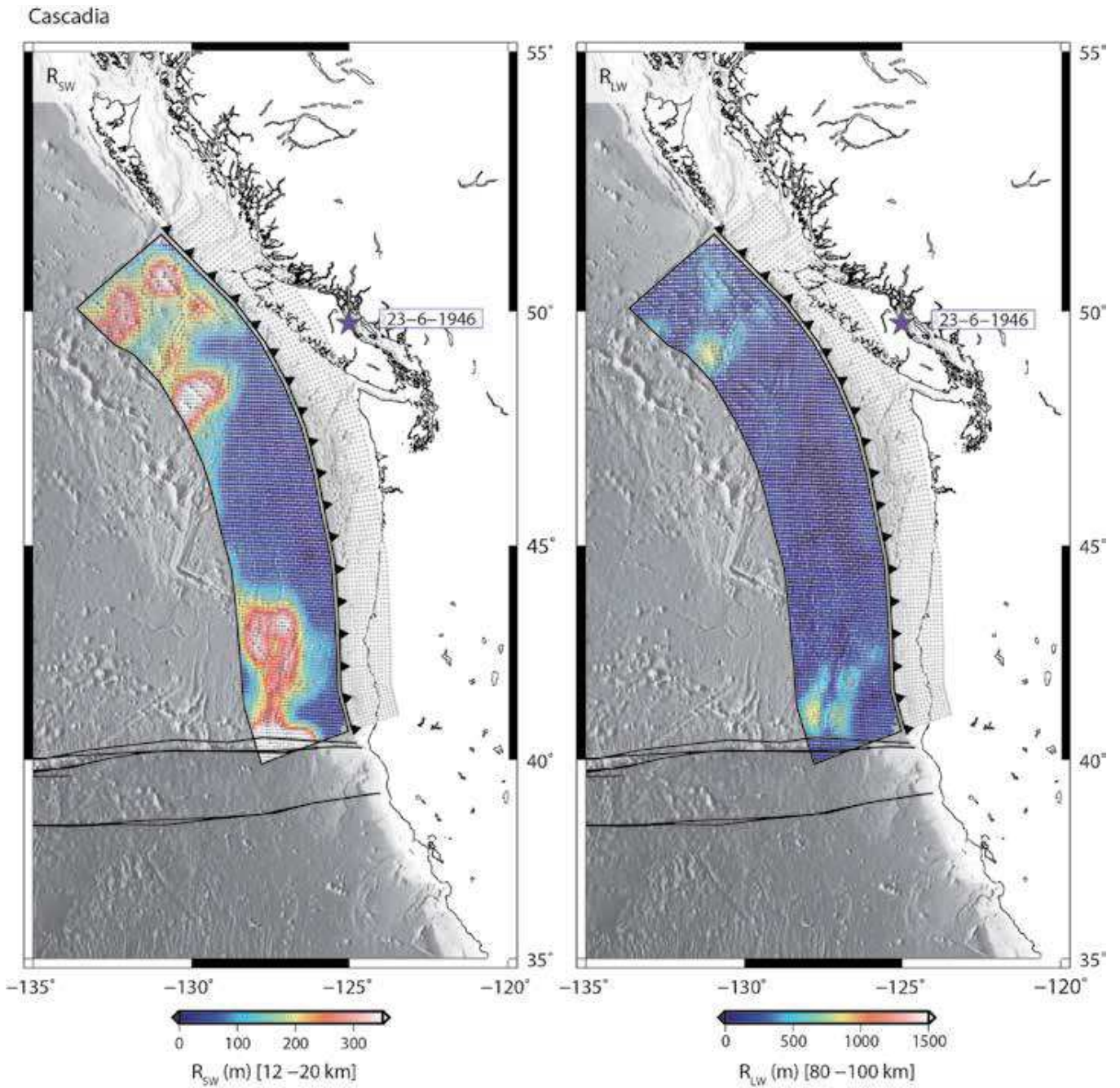


Figure A4.12. Cascadia. Short wavelength (R_{SW}) and long wavelength (R_{LW}) roughness data seaward of the trench and the SubQuake ruptures landward of the trench, color-coded according to the categories introduced in Figure 4.2.

Izu-Bonin-Mariana

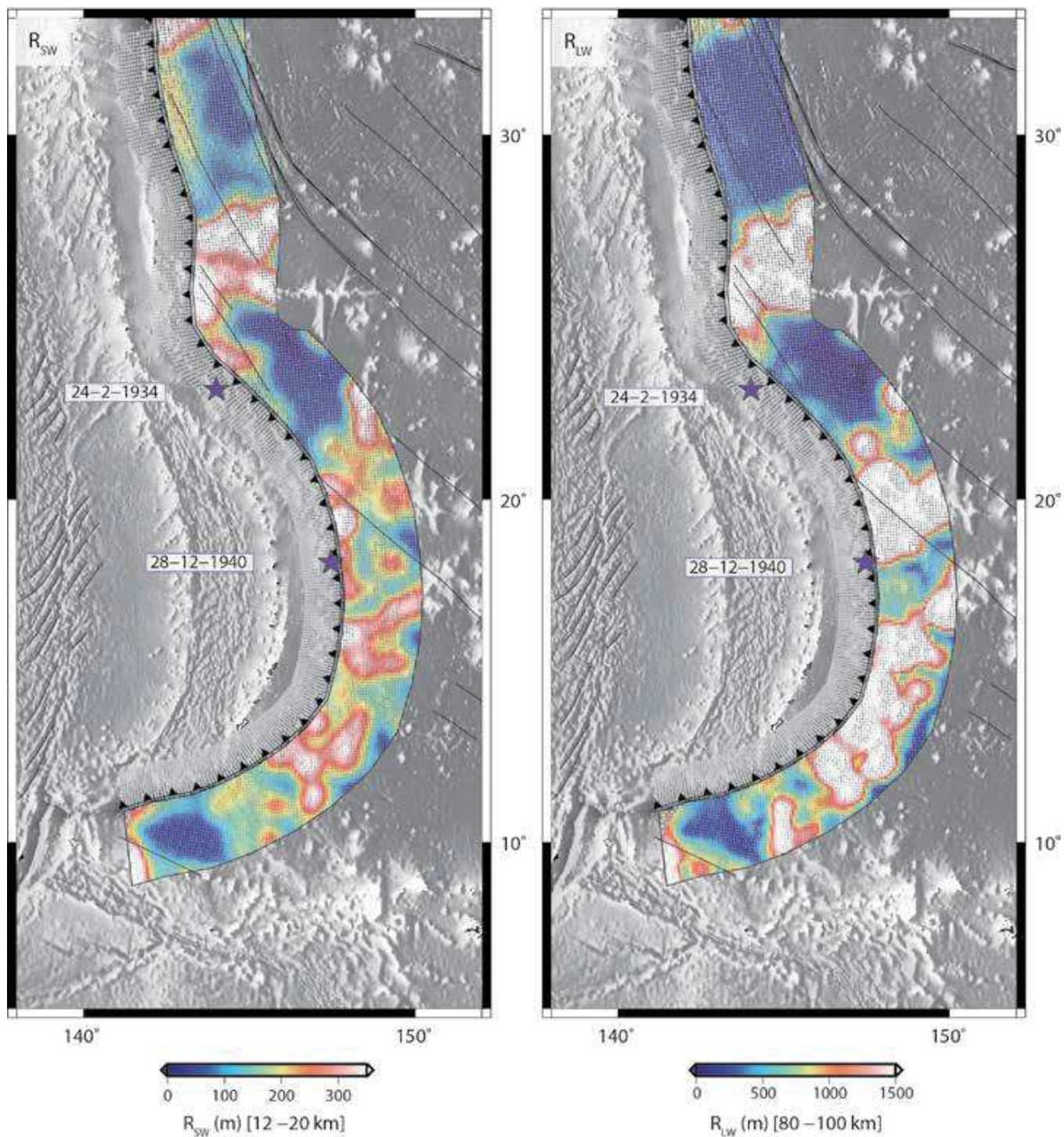


Figure A4.13. Izu-Bonin-Mariana. Short wavelength (R_{SW}) and long wavelength (R_{LW}) roughness data seaward of the trench and the SubQuake ruptures landward of the trench, color-coded according to the categories introduced in Figure 4.2.

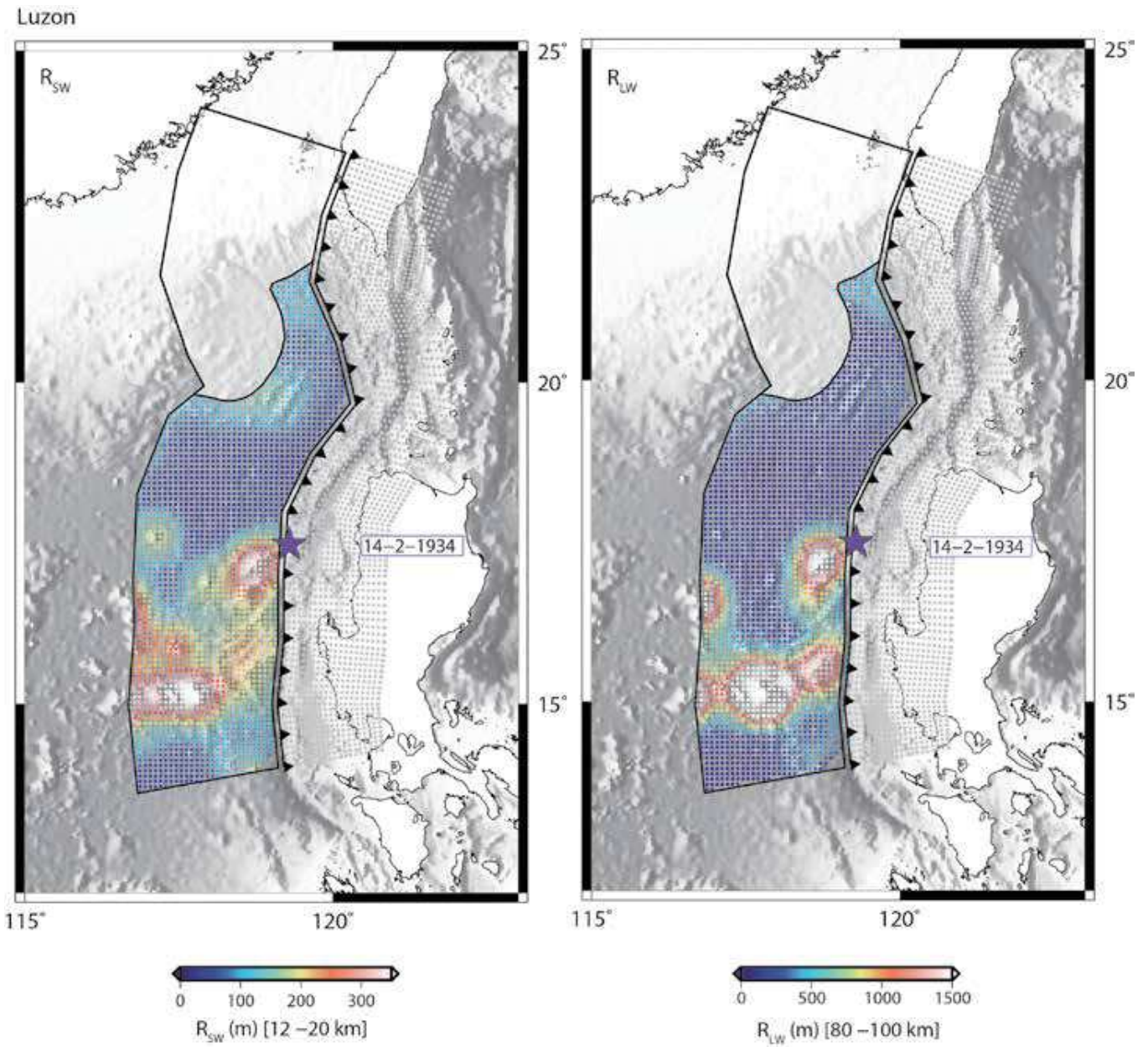


Figure A4.14. Luzon. Short wavelength (R_{SW}) and long wavelength (R_{LW}) roughness data seaward of the trench and the SubQuake ruptures landward of the trench, color-coded according to the categories introduced in Figure 4.2.

South Sandwich

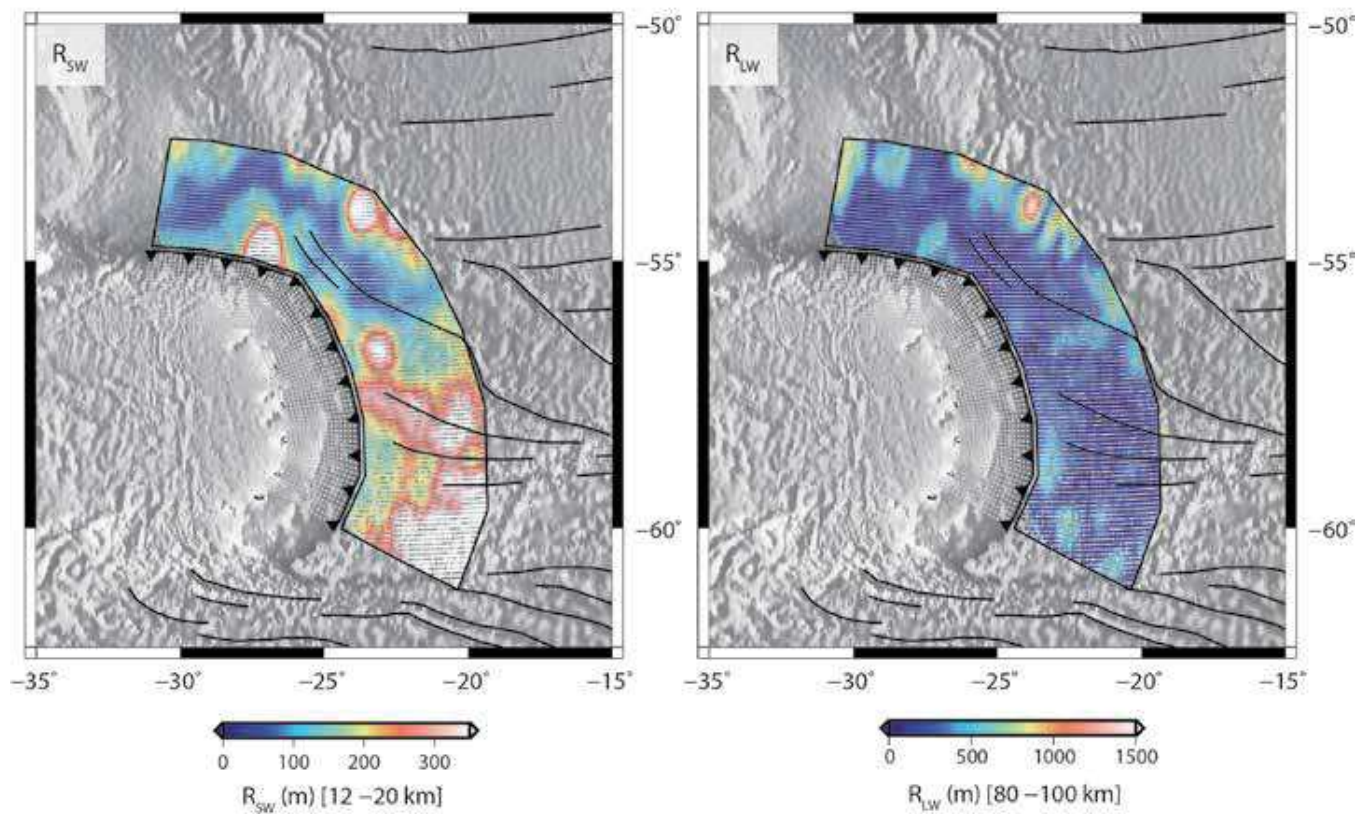


Figure A4.15. South Sandwich. Short wavelength (R_{SW}) and long wavelength (R_{LW}) roughness data seaward of the trench and the SubQuake ruptures landward of the trench, color-coded according to the categories introduced in Figure 4.2.

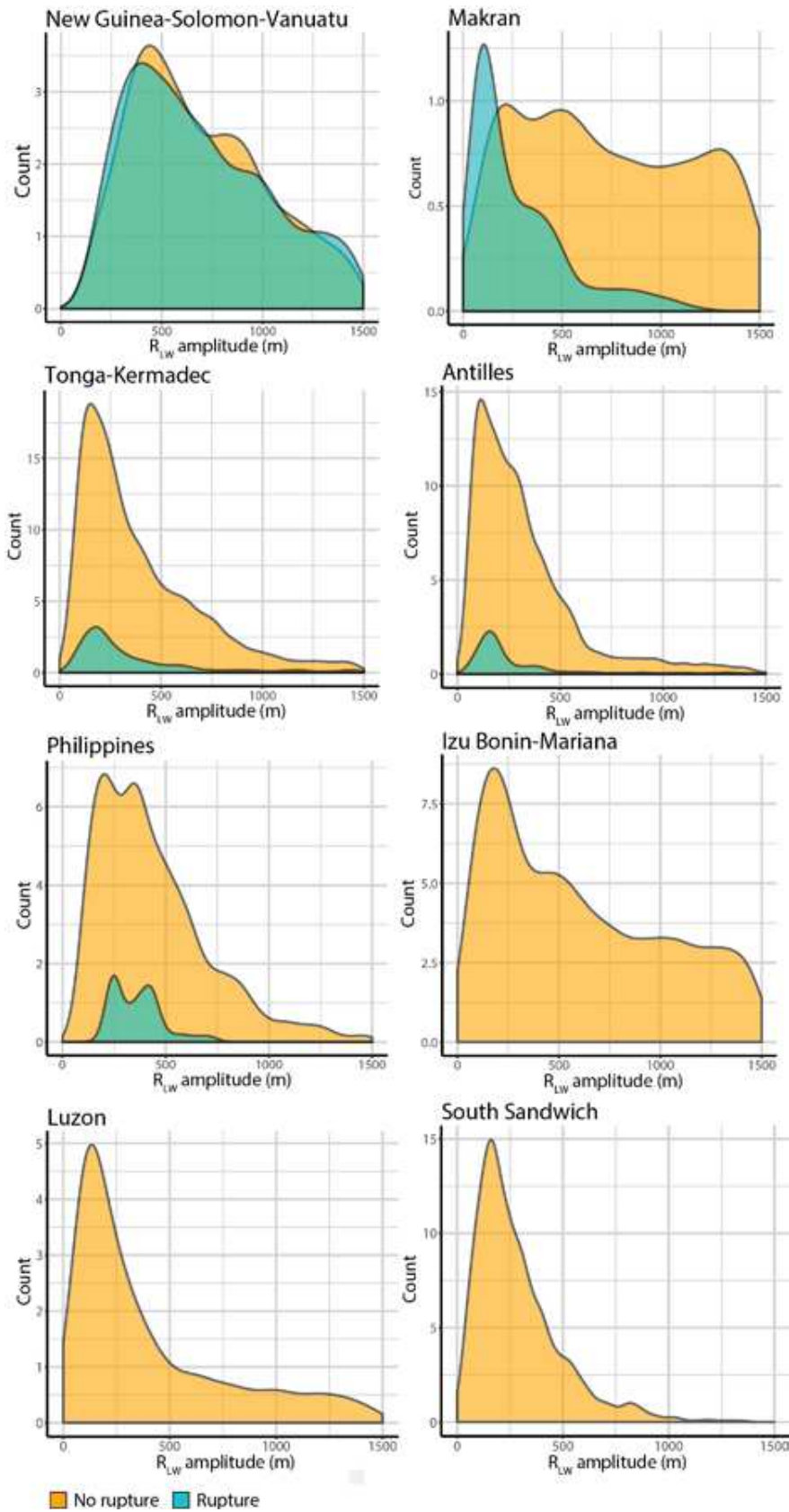


Figure A4.16. Long wavelength (R_{LW}) density plots for the eight remaining regions from Table 4.2. Orange and blue shades represent roughness data related to no-rupture and rupture segments, respectively.

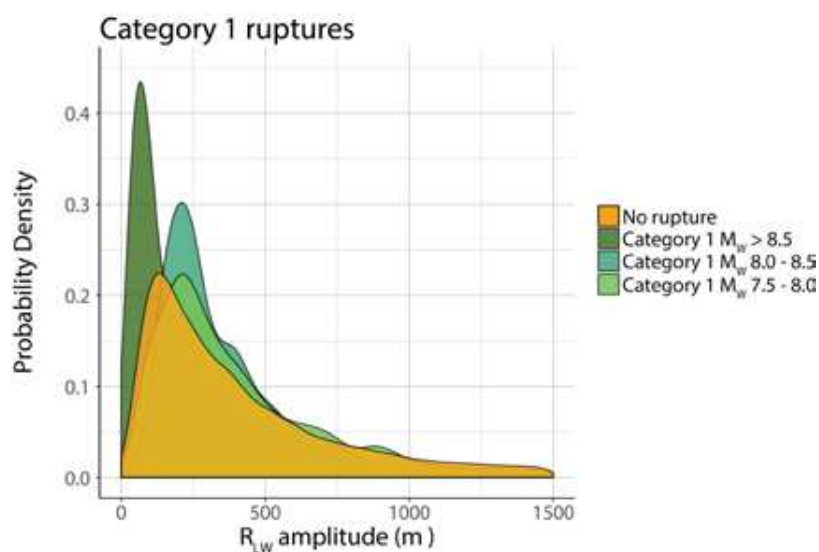


Figure A4.17. Long wavelength roughness probability density for category 1 only. Orange curve indicates the roughness data selected for the no-rupture segments and remains unvaried. Green curves indicate the roughness data selected for different magnitude groups.

Appendix Chapter 5 (A5)

Introduction

The appendix of Chapter 5 contains additional information on the scaling of the analogue material and the experimental setup (text A5.1) and how the source parameters are extracted from the experiments (text A5.2).

Text A5.1. Scaling of experimental setup

A5.1.1. Scaling principle

The analogue experiments are scaled to nature based on the principals of geometric, kinematic, dynamic, and rheological similarity (e.g., Hubbert, 1937). Each important physical dimension (i.e., length, time, and weight) is scaled to nature with a constant scaling factor (*). This is a dimensionless number that represents the ratio between model (M) and nature (N). Scaling factors for length (L^*), density (ρ^*) and viscosity (η^*) are determined independently based on representative natural values, while scaling factors for stress (σ^*) and time (T^*) are derived from the other scaling factors. For time, two different scaling factors are used due to the very small experimental interseismic/coseismic time ratio: an interseismic- and a coseismic scaling factor (i.e., T_i^* and T_c^* , respectively; Rosenau et al., 2009).

A5.1.2. Scaling of analogue material

The gelatin wedge used in the seismotectonic models is made out of 2.5 wt% Pig Skin gelatin. Di Giuseppe et al. (2009) explored the use of gelatin for analogue modelling, in order to have a single analogue material that can reproduce the complex rheological behavior of rocks. In their gel-state (i.e., solid-like behavior), gelatins show a visco-elasto-brittle rheology, while having a viscous rheology in their sol-state (i.e., fluid-like behavior). By varying gelatin composition, concentration, temperature, ageing and applied strain rate, Giuseppe et al. (2009) found that pig skin 2.5 wt% at 10°C has the best rheological properties to serve as an analogue of the earth's crust, with a shear modulus (G) of 1×10^3 to 1×10^4 Pa, a viscosity (η) of 3×10^5 Pa s and a density (ρ) of 1000 kg/m³.

A5.1.3. Scaling principal applied to the experimental setup

The experimental setup is scaled with a length scaling factor L^* of 1.57×10^{-6} (i.e., 1 cm in the model corresponds to 6.4 km in nature). From the density of the Pig Skin 2.5 wt% (i.e., 1000 kg/m³), we can obtain density scaling factor ρ^* of 3.45×10^{-1} (assuming a natural density of 2900 kg/m³), and

following the relation:

$$\sigma^* = \rho^* \cdot L^*$$

a stress scaling factor σ^* of 5.42×10^{-7} can be determined (i.e., 1 Pa in the model corresponds to 1.85 MPa in nature). The shear modulus G follows the same scaling factor and scales with natural values ranging from 1.85×10^9 – 1.85×10^{10} Pa. The coseismic scaling factor is determined by assuming an instantaneous elastic response with a constant Froude number (i.e., the ratio of a body's inertia to gravitational forces). This results in a coseismic time scaling factor:

$$T_c^* = \sqrt{L^*}$$

(i.e., 1 s in the model corresponds to approximately 800 s in nature). On interseismic time scales, inertia is negligible, and viscous behavior becomes more dominant. This results in an interseismic time scaling factor:

$$T_i^* = \eta^* / \sigma^*$$

where the viscosity scaling factor, based on a natural viscosity of 5×10^{21} Pa s, is 6×10^{-17} . This results in an interseismic time scaling factor of 1.11×10^{-10} (i.e., 1 s in the model corresponds to 286 years in nature).

Text A5.2. Source parameters

The experiments are recorded from above with a video camera, recording 7.5 frames per second. Images are post-processed with Particle Image Velocimetry (PIV), resulting in a 2D velocity field for each frame (i.e., each 0.133 second), which describes the displacement of the surface of the gelatin wedge. By extracting the maximum velocity, VX_{max} (in the x-direction), for each frame, peak velocities corresponding to a coseismic event can be identified. To isolate each coseismic event, a threshold of 0.05 cm/s is used, based on a trade-off analysis that shows the sensitivity of the number of events with respect to different thresholds. In this way, each series of frames for which VX_{max} continuously exceeds this threshold is identified as one coseismic event. From this information, duration of each event can be determined by calculating the difference between the first and last frame of each event,

$$D_{eq}(i) = lastframe(i) - firstframe(i)$$

Following this, the recurrence time is calculated as the number of frames in between two consecutive events (1 frame = 0.133 s),

$$T_{rec}(i) = firstframe(i+1) - lastframe(i)$$

The velocity of each cell in the 2D velocity field can be converted into displacement and eventually cumulative displacement over the course of one coseismic event. From the cumulative displacement map, the mean- and maximum values can be extracted, which represent the mean- and maximum slip during each event, respectively. By selecting all the cells that have exceeded the velocity threshold during the event, the total rupture area is calculated (the area of one cell is approximately 0.3 cm^2).

The rupture area and mean displacement are used for calculating a laboratory moment magnitude,

$$M_w = 2/3 \log_{10}(M_o) - 6.06$$

where M_o is the seismic moment,

$$M_o = \mu AD \text{ (in Nm)}$$

μ the shear modulus (1×10^3 , Corbi et al., 2013), A the rupture area and D the average displacement (Hanks & Kanamori 1979).

To calculate the interseismic coupling, the average surface displacement of the wedge towards the backstop (i.e., landward) in between two consecutive events is calculated as a ratio of the horizontal component of the displacement of the downgoing plate during the same time interval. Then, the average and standard deviation for all interseismic coupling values for both the rough- and smooth experiments are calculated.

The initial loading coupling (i.e., before initiation of the stick-slip behavior) is calculated in a similar manner, i.e. calculating the compression of the wedge towards the backstop as a ratio of the displacement of the downgoing plate for the first 4 minutes of each experiment.

Elenora van Rijsingen

Personal

Elenora Martina van Rijsingen
Born september 12, 1992
Dutch nationality
Via Mastro Giorgio 8, Rome
+31 614592708
e.m.vanrijsingen@gmail.com



My research interests are within the fields of geodynamics and tectonics. I enjoy studying the mechanisms of large scale tectonic processes and their link with both mantle dynamics and surface processes. During my PhD project I developed a specific interest in large tectonic earthquakes and associated hazard assessment. Besides that, I have a strong interest in science outreach and teaching.

Education

Joint PhD - ITN fellow

Nov 2015 - Nov 2018

Università Roma Tre - Laboratory of Experimental Tectonics
Université de Montpellier - Géosciences Montpellier

Subduction Interface Roughness and Megathrust Earthquakes: Insights from natural data and analogue models

Supervisors: Francesca Funicello, Serge Lallemand, Fabio Corbi and Michel Peyret

In a natural data study I made a global comparison between seafloor roughness calculated seaward of the trench and the occurrence of large megathrust earthquakes. By using analogue models I continued investigating this relationship, with the advantage of being able to investigate multiple seismic cycles. A 3D-printer was used to create roughness with various wavelengths and amplitudes.

More info: <http://www.creep-itn.eu/>

Msc. Earth, Structure and Dynamics

Sept 2013 - August 2015

Utrecht University
8.0 (Out of 10) - GPA: 4.00 Cum laude

Msc Thesis: Mesozoic evolution of the Dinaric-Hellenic belt: a plate-kinematic reconstruction using Jurassic ophiolites, Greece (Paleomagnetic laboratory Fort Hoofddijk).

Msc Internship: Geothermal potential in the Lower Carboniferous Limestone group in the Netherlands (If Technology Arnhem).

Courses: Tectonophysics, Dynamics of Basins and Orogens, Paleomagnetism and Rock Magnetism, Field Research Instruction Geology, Structure and Composition of the Earth's Interior, Reflection Seismics and Petroleum Systems.

Bsc. Earth Sciences

Sept 2010 - July 2013

Utrecht University
7.5 (Out of 10) - GPA: 3.42

Contributions to conferences and workshops

11. Y. Caniven, S. Dominguez*, J. Malavieille, S. Mazzotti, M. Peyret, F. Corbi, E. van Rijsingen. Potentialities and Applications to Natural Earthquakes of 2D and 3D Subduction Foam Quake Analogue Models. Geomod 2018 (poster).
10. E. van Rijsingen*, F. Funiciello, F. Corbi, S. Lallemand (2018). How subduction interface roughness influences megathrust earthquakes: Insights from analogue models. Geomod 2018 (poster).
9. M. Peyret, S. Lallemand*, E. van Rijsingen, D. Arcay (2017). Comparative Roughness Characteristics of the Subducting Seafloor and Statistical Relationships with Seismogenic Potential with Special Emphasis on Great Earthquakes. AGU Fall meeting, session T14B (talk).
8. E. van Rijsingen*, S. Lallemand, M. Peyret, F. Corbi, F. Funiciello, D. Arcay, A. Heuret (2017). How does Subduction Interface Roughness influence Megathrust Earthquakes: Insights from Natural Data and Analogue Models. AGU Fall meeting, session T23A (poster).
7. E. van Rijsingen*, S. Lallemand, M. Peyret, D. Arcay (2017). The relation between subduction interface roughness and the occurrence of megathrust earthquakes: A global analysis of natural data. Cargèse Earthquake Summer School (talk).
6. E. van Rijsingen*, S. Lallemand, M. Peyret, D. Arcay (2017). SubRough database: Proxy of Subduction interface Roughness and its relation with seismogenic potential. Part 3 - Application. SIP conference (talk).
5. E. van Rijsingen*, S. Lallemand, M. Peyret, D. Arcay (2017). SubRough database: Proxy of Subduction interface Roughness and its relation with seismogenic potential. Part 3 - Application. SIP conference (poster).
4. S. Lallemand*, M. Peyret, E. van Rijsingen, D. Arcay (2017). SubRough database: Proxy of Subduction interface Roughness and its relation with seismogenic potential. Part 2 - Analysis. SIP conference (poster).
3. M. Peyret*, S. Lallemand, D. Arcay, E. van Rijsingen (2017). SubRough database: Proxy of Subduction interface Roughness and its relation with seismogenic potential. Part 1 - Methodology. SIP conference (poster).
2. F. Corbi*, F. Funiciello, S. Brizzi, E. van Rijsingen, S. Lallemand, S. Dominguez (2016). Control of barrier width on asperity synchronization and genesis of great megathrust earthquakes: insights from 3D analog models. GeoMod (talk).
1. E. van Rijsingen*, S. Lallemand, M. Peyret, D. Arcay, F. Funiciello, S. Dominguez, F. Corbi (2016). How does subducting seafloor roughness relate to the seismogenic behaviour of subduction zones? Geomod 2016 (poster).

*presenter

Publications

4. van Rijsingen, E., Funiciello, F., Corbi, F., Lallemand, S. (in preparation for submission). Rough subducting seafloor reduces interseismic coupling and mega-earthquake occurrence: Insights from analogue models.
3. van Rijsingen, E., Lallemand, S., Peyret, M., Arcay, D., Heuret, A., Corbi, F., Funiciello, F. (2018). How subduction interface roughness influences the occurrence of large interplate earthquakes. *Geochem. Geophys. Geosyst.* <https://doi.org/10.1029/2018GC007618>
2. Lallemand, S., Peyret, M., van Rijsingen, E., Arcay, D., Heuret, A. (2018). Roughness characteristics of oceanic seafloor prior to subduction in relation to the seismogenic potential of subduction zones. *Geochem. Geophys. Geosyst.* <https://doi.org/10.1029/2018GC007434>
1. De Groot, L.V., Béguin, A., Koster, M.A., van Rijsingen, E., Struijk, L.M., Biggin, A.J., Hurst, E.A., Langereis, C.G., Dekkers, M.J. (2015). High paleointensities for the Canary Islands constrain the Levant geomagnetic high. *Earth Planet. Sci. Lett.* 419, 154-167. <https://doi.org/10.1016/j.epsl.2015.03.020>

Teaching

- **Co-lecturer at geodynamics master course Roma Tre (november 2017, 4h)**
- **Student-assistant - Utrecht University (2012 - 2015, ~200h)**
1st and 2nd year mathematics, 2nd year geochemistry, 1st year fieldwork preparation, 1st year Ardennen fieldwork, master course 'Dynamics of basins and orogens'. Number of students ranging from 5 (fieldwork groups) to 70 (large classes with several student assistants).
- **Homework tutor - Juffrouw Julia (June - October 2013, 6h per week)**
Helping kids with daily homework, in a wide range of topics. Individual sessions or supervising groups up to 15 children.
- **Teacher exam trainings - Lyceo (2011 - 2012, 36h)**
Mathematics and physics, several 3-day training courses for classes up to 20 people.
- **Primary school English teacher at Galapagos Islands (summer 2012, 45h)**
Summer volunteering project, 5 classes of 20-30 children.

Other activities

- **Elected Representative ITN fellows (Jan 2016 - Jan 2019)**
Marie Skłodowska Curie, CREEP Innovative Training Network
Representing the CREEP ITN fellows by attending the Supervisory meetings and coordinating all the common activities which have to be done in the frame of the ITN project. More info here.
- **Editor and Writer EGU Tectonics and Structural Geology blog (July 2016 - Present)**
European Geoscience Union, TS Early Career Scientists team
Responsible for managing the blog, communication with guest authors and writing blogs.
Recently published a blog series 'Mind Your Head', focusing on coping mechanisms for mental health issues in academia.
- **Translator Planet Press (April 2016 - Present)**
European Geoscience Union
EGU press releases are re-written in children's versions and translated into several European languages to be used for children's education. I am involved in the translation from English to Dutch (translated up to 20 texts of roughly 500 words so far) and distribution of the articles in the Netherlands.
- **Role model: Women in bèta professions (Sept 2012 - Present)**
VHTO, Dutch national expert organisation on girls/women and science/technology
Giving interactive lectures at both primary and secondary schools about my study/profession. The aim of this is to change the general perspective of beta/technical professions (mainly meant for men) and to encourage girls to choose what they like to do, regardless of prejudices and expectations of others.
- **Committee Foreign Company Excursion Dubai & Abu Dhabi (Sept 2013 - Nov 2014)**
Utrecht Earth Sciences Society
With a group of 9 students we organized an excursion for 25 master students to Dubai & Abu Dhabi, where international companies related to Earth sciences were visited. Personal responsibilities: acquisition and planning
- **President Utrecht Student Bigband (Jan 2013 - Sept 2014)**
Utrecht Student Bigband
Responsible for coordinating the board and the general affairs. In addition: In charge of audition policy and outreach activities.
- **Editor in Chief 'PanGeo'- student magazine Earth Sciences (Sept 2012 - Dec 2013)**
Utrecht Earth Sciences Society
After the merge of two study societies, a new magazine had to be launched. I managed a group of 10 students to create a magazine each quarter of a year and I was responsible for the final layout.

Honors and Awards

- *2017: GeoPRISMS best student poster award*
- *2017: Outstanding Student Paper Award (American Geophysical Union)*
- *2018: Special Award of the Honorary Committee for a science outreach video submitted to the 'On the Rocks' geological video contest organized by the Geological Society of Italy*

Skills

<i>Languages</i>	Dutch (native) English (fluent) Italian (conversational) French (conversational)
<i>Acquainted with</i>	Software: Adobe Indesign, Adobe Illustrator, Matlab, Global Mapping Tools, R (statistics) Machines: Several magnetometers (cryogenic, alternating field, microwave), rheometer (Anton Paar MCR 301) , 3D printer (FlashForge Creator Pro)

